Isogeometric Analysis for Functionally Graded Plates
Using Higher Order Shear Deformation Theory

Isogeometrische analyse voor functionelegradiëntplaten
met behulp van een afschuivings-vervormingstheorie van een hogere orde

Vinh Loc Tran

Promotoren: prof. dr. ir. M. Abdel Wahab, prof. dr. H. Nguyen Xuan
Proefschrift ingediend tot het behalen van de graad van
Doctor in de Ingenieurswetenschappen: Werktuigkunde-Elektrotechniek

Vakgroep Elektrische Energie, Systemen en Automatisering
Voorzitter: prof. dr. ir. J. Melkebeek
Faculteit Ingenieurswetenschappen en Architectuur
Academiejaar 2015 - 2016

UNIVERSITEIT
GENT

ISBN 978-90-8578-884-3
NUR 978
Wettelijk depot: D/2016/10.500/16

Isogeometric Analysis for Functionally Graded Plates Using Higher-Order Shear Deformation Theory

Isogeometrische analyse voor functionelegradiëntplaten met behulp van een afschuivings-vervormingstheorie van een hogere orde

Vinh Loc Tran

Promotoren: prof. dr. ir. M. Abdel Wahab, assoc. prof. dr. H. Nguyen-Xuan

Proefschrift ingediend tot het behalen van de graad van

Doctor in de Ingenieurswetenschappen: Werktuigkunde-Elektrotechniek

Vakgroep Elektrische Energie, Systemen en Automatisering

Voorzitter: prof. dr. ir. Jan Melkebeek

Faculteit Ingenieurswetenschappen en Architectuur

Academie jaar 2015 - 2016

UNIVERSITEIT GENT

ISBN 978-90-8578-884-3
NUR 978
Wettelijk depot: D/2016/10.500/16

Promoters:

Prof. dr. ir. Magd Abdel Wahab
Assoc. prof. dr. Hung Nguyen-Xuan

Examination Committee:

Prof. dr. ir. Rik Van de Walle (Chair)
Ghent University, Belgium
Prof. dr. ir. Magd Abdel Wahab
Ghent University, Belgium
Assoc. prof. dr. Hung Nguyen-Xuan
HUTECH University, Vietnam
Prof. dr. ir. Dieter Fauconnier
Ghent University, Belgium
Prof. dr. ir. Stephan Pierre Alain Bordas
University of Luxembourg, Luxembourg
Prof. dr. ir. Joris Degrieck
Ghent University, Belgium
Prof. dr. ir. Guido De Roeck
University of Leuven, Belgium

Research Institute

Ghent University
Faculty of Engineering and Architecture
Department of Electrical Energy, Systems and Automation
Laboratory Soete http://www.soetelaboratory.ugent.be
Technologiepark 903, B-9052 Zwijnaarde, Belgium

Tel: +32 9 331 0477
Email: Loc.TranVinh@UGent.be, tranvinhlocpy@gmail.com

Dedicate to my mother

Mrs. Lưu Thị Kim Ngọc

Acknowledgements

This thesis has been carried out at Laboratory Soete, Department of Electrical Energy, Systems and Automation, Faculty of Engineering and Architecture, Ghent University funded by Special Funding of Ghent University (Bijzonder Onderzoeksfonds), in the framework of the project BOF 01N02410 and Lotus Unlimited Erasmus Mundus Action 2. The researcher gratefully acknowledges the financial supports.

First of all, I would like to express my deeply gratitude to my promoters Prof. Magd Abdel Wahab and Assoc. Prof. Nguyen Xuan Hung for their patient guidance and valuable advices through my research. Undoubtedly, without their wholehearted help, consistent support and encouragement this work would not have been completed.

I would like to sincerely thank to Dr. Thai Hoang Chien, Assoc. Prof. Nguyen Thoi Trung, Dr. Nguyen Vinh Phu and MSc. Phung Van Phuc – my former colleagues at Division of Computational Mechanics, Vietnam for their fruitful collaboration. I would like to thanks to Prof. Jaehong Lee from Sejong University, Korea for his kindly support and outstanding discussions during my short stay research at his laboratory. Many thanks are due to Dr. Nguyen Thanh Nhon from the Institute of Applied Mechanics, Technical University of Braunschweig, Germany for his help and insightful suggestions.

Furthermore, I am grateful to my colleagues at Laboratory Soete for their kindly help and friendly support.

Finally, my biggest gratitude goes to my family, especially my mother for her unconditional support, love and encouragement throughout my study.

Summary

Functionally graded materials (FGMs) are the most advanced heterogeneous composite materials, which are made of two or more constituent phases with continuous variation of material ingredients between two points in a predetermined direction. As a result, FGMs are enabled to inherit the best properties of the distinct components, e.g. low thermal conductivity, high thermal resistance, ductility, durability and superiority of fracture toughness and so on. FGMs were initially designed for the space shuttle for the thermal coating. Nowadays, they have a variety of real and potential applications in many engineering fields such as transport systems, energy conversion systems, cutting tools, machine parts, semi-conductors, optics and biomaterials, etc. Taking into account theoretical, numerical modelling and analysis of FGM, this thesis mainly focuses on predicting the response of functionally graded material plates by development with a novel and effective formulation, combining the isogeometric finite element method and higher-order shear deformation theories (HSDTs). The FGM plates were made of a mixture of two distinct material phases, namely a ceramic and a metal, which are assumed to vary continuously through the plate thickness according to a power-law distribution. To infer their effective material properties, two homogenization techniques, the rule of mixture and the Mori-Tanaka scheme, are utilized here.

In order to model these plates, beside three-dimensional elasticity theory, two-dimensional plate theories based on the equivalent single layer (ESL) model, which is concerned with the kinematics of deformation or stress state through the plate thickness, is preferred to use. In the context of the ESL model, classical plate theory (CPT) is the simplest one, which requires C^1-continuity elements and merely provides acceptable results for thin plates. The first-order shear deformation theories (FSDT), which take into account the effects of shear deformation, is therefore developed. FSDT is suitable for moderate and thick plates. However, the primary difficulty of standard FSDT-based finite elements is that thin plate behaves stiff and shear-locking phenomenon takes place. Furthermore, with the linear in-plane displacement assumption through thickness of plate, shear strains and stresses are distributed inaccurately and do not satisfy the traction free boundary conditions at the plate surfaces. The shear correction factors (SCFs), which have values that are quite dispersed through each problem, are hence required to rectify

the unrealistic shear strain energy part. In this thesis, we successfully developed the higher-order shear deformation theories (HSDTs) including Reddy's theory (TSDT), refined plate theory (RPT) and generalized shear deformation theory (GSDT). By including higher-order terms in displacement field, the HSDT models do not only describe more accurate the shear strains/stresses without requirement of SCFs but also achieve very good results for thick, moderate, thin and very thin plates. The GSDT and RPT models are presented in the general forms, which is strongly dependent on a distributed function, $f(z)$. The distributed function is chosen to satisfy zero gradients at the top and bottom surfaces, i.e. $f'(\pm h/2)=0$. Based on this condition, we propose a new inverse tangent function to enhance the accuracy of the numerical results. In addition, geometric nonlinearity is concerned with considering the strain–displacement relationship as being nonlinear. It is observed that plate is commonly modelled using small deformation assumptions. In many instances, assumptions of linearity lead to reasonable idealization of the plate behaviours. However, in some cases, e.g. small strains, moderate rotations (say 10° - 15°) and large displacements (i.e. $w/h \geq 1$), these assumptions may result in an unrealistic approximation of the response. Thus, the von Kármán nonlinear theory needs to be adopted. The plate formulations are established according to the total Lagrange description and solved by the iteration methods.

In recent years, Thomas Hughes and co-workers have introduced a powerful numerical method, called an isogeometric analysis (IGA), which has a primary original purpose to enable a tighter connection between computer aided design (CAD) and finite element analysis (FEA). Being different from the traditional finite element method (FEM), which utilizes the Lagrange basis functions in approximating the unknown solutions and the geometry, isogeometric analysis employs the same basis functions in describing the exact geometry such as: B-spline, non-uniform rational B-spline (NURBS), etc., in order to construct finite approximation for analysis. As a result, the geometric error is eliminated because the geometry is represented exactly in the first coarsest mesh. Another major advantage is that IGA achieves easily the smoothness with C^{p-1} continuity by using p^{th} order NURBS. It enables this method to naturally fulfil the C^1 continuity requirement of the HSDT models by using the higher-order NURBS basis functions.

This thesis investigates behaviours of the FGM plates, which can be classified into the following main points:

- Firstly, the bending analysis of the functionally graded material plates based on HSDT models including TSDT, RPT and GSDT under thermo-mechanical loadings is addressed. More importantly, the nonlinear equation of the plate based on von Kármán assumptions is provided and solved by Newton-Raphson method on a general framework of the isogeometric approach. The influences of gradient index, boundary condition, geometric shape, type of loading, material property on the response of FGM plate are also examined.
- Secondly, elastic instability behaviour of FGM plates under in-plane compression load is investigated. The compression results from either directly applied load or temperature change. In the former, the loading is at the neutral surface of the plates. In the latter, it is assumed that the temperature varies uniformly on the top and bottom surfaces and be considered as a constant, linear or nonlinear function through the thickness direction. Moreover, high temperature environment makes a significant change in mechanical properties of the constituent materials. Therefore, the effect of temperature-dependent thermo-elastic material properties is considered in order to accurately predict the mechanical responses of FGM structures.
- Thirdly, the dynamic problems related to free vibration and forced vibration are solved. In the former, the problem without the force vector is solved by eigenvalue analysis to estimate the natural frequencies, whilst in the latter applied loads and the von Kármán strains are considered. Thus, the equation of dynamic system, which is dependent upon not only time domain but also unknown displacements, is solved by the Newmark’s integration scheme in association with the Picard methods.
- Finally, cracked FGM plate is modelled based on GSDT. Herein, a novel procedure based on integrating the enrichment functions into isogeometric finite element is proposed in order to model the discontinuous phenomenon in the cracked structure. In this concept, the Heaviside function is incorporated with NURBS basis to capture the discontinuous phenomenon at the crack faces, while at the crack tip, the asymptotic functions obtained from analytical solution are used as the enrichment functions to model the singular field, i.e. displacement field.

Samenvatting

Functionele gradiënt materialen (FGM’s) zijn de meest geavanceerde heterogene composietmaterialen die bestaan uit twee of meer samenstellende onderdelen waarbij tussen twee punten in een vooraf bepaalde richting materiaalingrediënten continu variëren. Hierdoor kunnen FGM’s de beste eigenschappen van de verschillende componenten gebruiken, zoals onder meer lage thermische geleidbaarheid, hoge thermische weerstand, buigzaamheid, duurzaamheid en de superioriteit van breuktaaiheid. FGM’s werden in eerste instantie ontworpen voor de thermische bekleding van ruimteveren. Tegenwoordig hebben ze verschillende reële en potentiële toepassingen in vele technische gebieden, zoals transportsystemen, energieconversiesystemen, snijgereedschappen, machineonderdelen, halfgeleiders, optica en biomaterialen. Rekening houdend met theoretische en numerieke modellen en analyses van FGM’s, richt dit proefschrift zich vooral op het voorspellen van de respons van functionele gradiënt platen via de ontwikkeling van een nieuwe en effectieve formulering die een combinatie maakt van de isogeometrische eindige-elementenmethode en de hogere-orde theorie voor afschuifvervorming. De functionele gradiënt platen zijn gemaakt van een mengsel van twee afzonderlijke materialen: een keramische en een metalen die continu variëren doorheen de plaatdikte volgens een machtsfunctieverdeling. Om hun effectieve materiaaleigenschappen af te leiden worden twee homogenisatietechnieken gebruikt: de mengregelsmengregelsen de regel van Mori-Tanaka.

Om deze platen te modelleren wordt, naast de driedimensionale elasticiteitstheorie, de voorkeur gegeven aan de tweedimensionale plaattheorieën gebaseerd op het evenwicht van het éénlaagmodel, dat zicht bezighoudt met de kinematica van vervorming of de spanningstoestand langs de plaatdikte. In het kader van het éénlaagmodel, is de klassieke plaattheorie de eenvoudigste, waarbij C^1-contunïteitselementen gerespecteerd worden en aanvaardbare resultaten voor dunne platen worden bekomen. De afschuivingsvervormingstheorieën van de eerste orde, die rekening houden met de effecten van afschuifvervorming, werden daarom ontwikkeld. Deze theorieën zijn geschikt voor middelmatige en dikke platen. De moeilijkheid van deze theorieën is evenwel dat, als ze gecombineerd worden met eindige elementen, dunne platen stijf worden en het shear-locking fenomeen plaatsvindt. Bovendien worden, indien uitgegaan wordt van lineaire vlakke verplaatsing doorheen de plaatdikte, afschuifrekken en

spanningen onnauwkeurig verdeeld en wordt niet voldaan aan de vrije tractie randvoorwaarden bij de plaatoppervlakken. De afschuivingscorrectiefactor, die voor elk probleem varieert, dient dus de onrealistische energie van de afschuifrekken te rectifiëren. In dit proefschrift hebben we met succes de hogere-orde theorieën voor afschuifvervorming inclusief de theorie van Reddy, de verfijnde plaattheorie en de gegeneraliseerde afschuivingsvervormingstheorie ontwikkeld. Door het opnemen van termen van hogere orde in het verplaatsingsveld, beschrijven de modellen van de hogere-orde theorie voor afschuifvervorming zowel afschuifrekken als spanningen nauwkeuriger, zonder de vereisten van de afschuivingscorrectiefactoren. Bovendien bekomen ze zeer goede resultaten voor dikke, midddelmatige, dunne en zeer dunne platen. De modellen van de gegeneraliseerde afschuivingsvervormingstheorie en de theorie van Reddy worden in algemene vormen uitgedrukt, die sterk afhankelijk zijn van een specifieke functie. Deze functie wordt gekozen om aan de nulwaarden van de gradiënt te voldoen aan de boven- en onderoppervlakken. Gelet op deze voorwaarde, stellen we een nieuwe inverse trigonometrische functie voor om de nauwkeurigheid van de numerieke resultaten te verbeteren. Bovendien wordt de geometrische niet-lineariteit in rekening gebracht om de rekverplaatsingsrelatie als niet-lineair te beschouwen. Er kan opgemerkt worden dat een plaat wordt gemodelleerd vanuit de veronderstelling van minimale vervorming. In veel gevallen leidt deze veronderstelling van niet-lineariteit tot een redelijke modellering van de plaat. Echter, in sommige gevallen, namelijk bij kleine rekken, matige rotaties (bijvoorbeeld 10° - 15°) en grote verplaatsingen, leidt deze veronderstelling tot een onrealistische respons. Vandaar dat de von Kármán niet-lineaire theorie moet worden aangepast. De plaatformuleringen worden vastgesteld op basis van de totale beschrijving van Lagrange en worden opgelost door iteratie werkwijzen.

Recent hebben Thomas Hughes en medewerkers een krachtige numerieke methode ontwikkeld, genoemd isogeometrische analyse (IGA). IGA heeft als oorspronkelijk doel een nauwere verbinding tussen computerondersteund ontwerp of computer aided design (CAD) en eindige-elementenanalyse te bekomen. Anders dan de traditionele eindige-elementenmethode, die de Lagrange basisfuncties gebruikt voor zowel de onbekende parameters als de geometrie, maakt IGA gebruik van dezelfde basisfuncties in de beschrijving van de precieze geometrie, zoals B-spline en niet-uniforme rationele B-spline (NURBS). Hierdoor wordt de geometrische fout geëlimineerd omdat de geometrie met een grove verdeling goed wordt benaderd. Een ander groot voordeel is dat IGA gemakkelijk C^{p-1} continuïteit bereikt door gebruik van NURBS van de p^{de} orde. Dit zorgt ervoor dat deze methode ruim voldoet aan de C^1 continuïteitseis van de modellen van de hogere-orde theorieën voor afschuifvervorming door NURBS basisfuncties van hogere orde toe te passen.

Dit proefschrift onderzoekt het gedrag van functionele gradiënt platen, dat als volgt kan worden ingedeeld:

- Ten eerste wordt de buiganalyse van de functioneel ingedeelde platen onder thermomechanische belasting beschreven, gebaseerd op de hogere-orde theorieën voor afschuifvervorming, de theorie van Reddy, de verfijnde plaattheorie en de gegeneraliseerde afschuivingsvervormingstheorie. Wat nog belangrijker is, is dat de niet-lineaire vergelijking van de plaat op basis van de veronderstelling van von Kármán beschreven wordt en opgelost wordt door de Newton-Raphson methode in het algemene kader van de isogeometrische aanpak. De invloeden van de gradiëntindex, de randvoorwaarden, de geometrische vorm, het type van belasting en de materiële eigenschappen op de respons van de functionele gradiënt platen wordt eveneens onderzocht.
- Ten tweede wordt het elastische instabiliteitsgedrag van functionele gradiënt platen onder drukbelasting in het vlak onderzocht. De drukspanning komt van de rechtstreeks opgelegde belasting of temperatuursverandering. In het eerste geval ligt de belasting op het neutrale oppervlak van de platen. In het tweede geval wordt verondersteld dat de temperatuur gelijkmatig verdeeld is over de bovenste en onderste oppervlakken en wordt het in de dikterichting beschouwd als een constante, lineaire of niet-lineaire functie. Bovendien brengt hoge temperatuur een significante verandering teweeg in de mechanische eigenschappen van de samenstellende materialen. Dus wordt het effect van de temperatuurafhankelijke thermo-elastische materiaaleigenschappen in aanmerking genomen om de mechanische respons te voorspellen.
- Ten derde worden de dynamische problemen verbonden aan vrije trillingen en gedwongen trillingen opgelost. In het geval van vrije trilling wordt het probleem zonder de krachtvector opgelost door eigenwaardeanalyse om de eigenfrequenties in te schatten, terwijl in het geval van gedwongen trilling de toegepaste belasting

en de von Kármán rekken in aanmerking worden genomen. Op die manier wordt de vergelijking van het dynamische systeem, dat niet alleen van het tijdsdomein, maar ook van ongekende verplaatsingen afhankelijk is, opgelost door Newmark's integratieschema samen met de Picard methoden.

- Tot slot worden gescheurde functionele gradiënt platen gemodelleerd op basis van de gegeneraliseerde theorie voor afschuifvervorming. Hierbij wordt een nieuwe numerieke procedure voorgesteld om het discontinue fenomeen in de gescheurde structuur te modelleren, gebaseerd op de integratie van de Heaviside functie met isogeometrische eindige elementen. De Heaviside functie wordt verrijkt om het discontinue fenomeen bij de scheurvlakken vast te leggen, terwijl de asymptotische functies van de analytische oplossing worden geïncorporeerd met NURBS om de singulariteit bij de scheurtip te simuleren.

Table of Contents

Heading **Page**

List of Figures

List of Tables

Nomenclature

Latin Symbols

a	crack length
E	Young modulus
f_i	distribution force according to *i*-direction
$f(z)$	distributed function
G	shear modulus
h	plate thickness
K	bulk modulus
k	thermal conductivity
L	length
n	gradient index
p, q	order of shape function
t	time
T	temperature
u_0, v_0, w_0	displacement components
V	the volume fraction
W	width
N_i^p	i^{th} B-Spline basic function
R_i^p	i^{th} NURBS basis function
x, y, z	Cartersian coordinate
$\mathbf{B}$	strain matrix
$\mathbf{F}$	force vector
$\mathbf{J}$	Jacobian matrix
$\mathbf{K}$	global stiffness matrix
$\mathbf{K}_g$	geometric stiffness matrix
$\mathbf{K}_L$	linear stiffness matrix
$\mathbf{K}_{NL}$	nonlinear stiffness matrix
$\mathbf{M}$	global mass matrix
$\mathbf{P}$	control point coordinate
$\mathbf{q}$	unknown variable vector
$\mathbf{u}$	displacement field
$\dot{\mathbf{u}}$	velocity field
$\ddot{\mathbf{u}}$	acceleration field

Greek symbols

α	the coefficient of thermal expansion
β_x, β_y	rotations

ξ, η	parametric coordinates
ζ	weigh value
λ	load factor
μ	shear modulus
ν	Poission’s ratio
ρ	mass density
θ	angle skew
∇	gradient operator
ω	natural frequency
$\boldsymbol{\varepsilon}$	in-plane strain field
$\boldsymbol{\varepsilon}_{L}$	linear strain field
$\boldsymbol{\varepsilon}_{NL}$	non-linear strain field
$\boldsymbol{\varepsilon}^{th}$	thermal strain field
$\boldsymbol{\gamma}$	shear strain vector
$\boldsymbol{\sigma}$	Stress field

Abbreviations

CAD	Computer Aided Design
CCCC	Fully clamped support
CPT	Classical plate theory
DOF	Degree of freedom
DQM	Differential quadrature method
ELS	Equivalent single layer
FEA	Finite element analysis
FEM	Finite element method
FGM	Functionally graded material
FGP	Functionally graded plate
FSDT	First-order shear deformation theory
FSM	Finite strip method
GSDT	Generalized shear deformation theory
HSDT	Higher-order shear deformation theory
IGA	Isogeometric analysis
MLPG	Mesh-less local Petrov-Galerkin
NURBS	Non-Uniform Rational B-splines
RPT	Refined plate theory
SCF	Shear correction factor
SIF	Stress intensity factor
SSSS	Fully simply support
TSDT	Third-order shear deformation theory
XFEM	Extended finite element method
XIGA	Extended isogeometric analysis

Chapter 1 Introduction

1.1 History of FGM

Materials play an important role in the development of science and technology. Based on available materials for different inorganic and organic compounds, many advanced materials have been invented such as, the advanced polymers, memory alloys, structural ceramics, etc. An illustration of development of modern materials is given in Figure 1.1 [1], in which, functionally graded materials (FGMs) are the most advanced heterogeneous composite materials made of two or more constituent phases with gradual variation of material ingredients between two points in a predetermined direction [2].

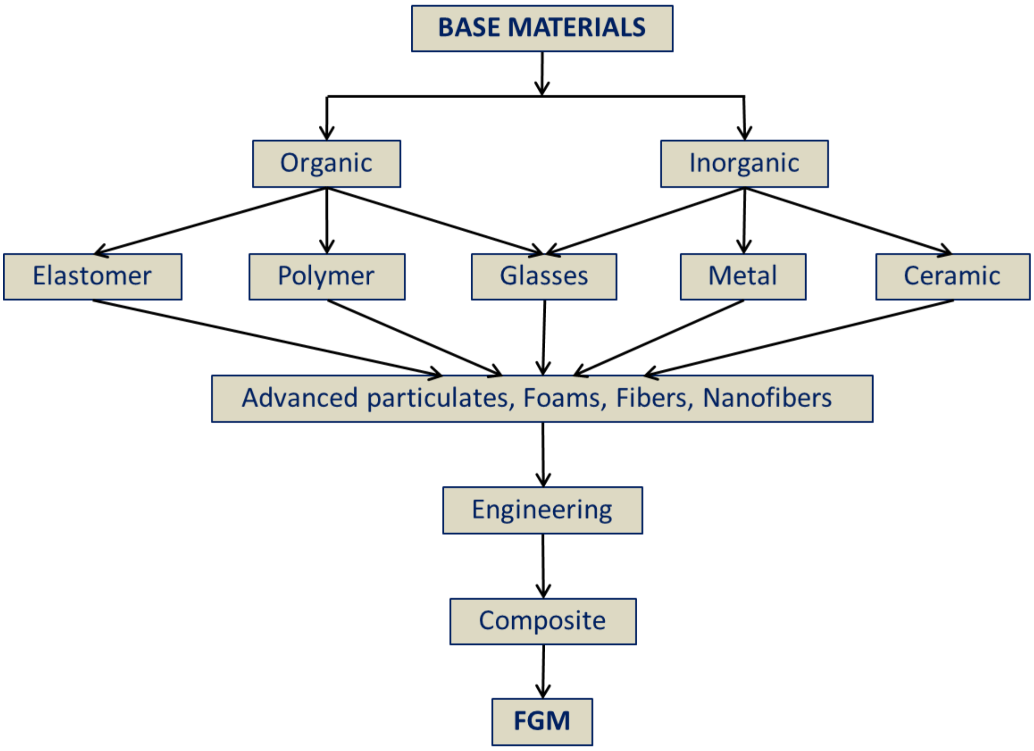

Figure 1.1 Representation of advance material hierarchy.

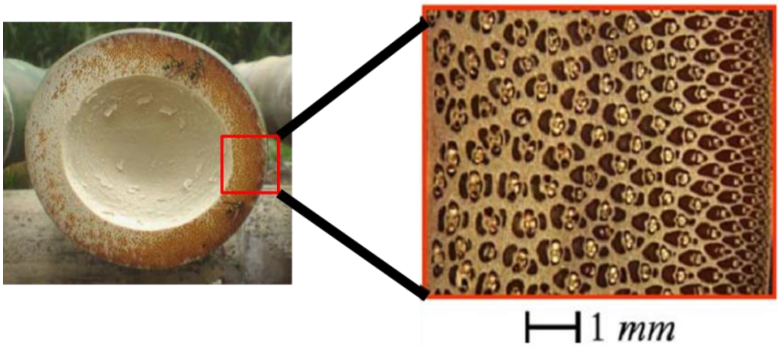

a) Cross section of bamboo tree

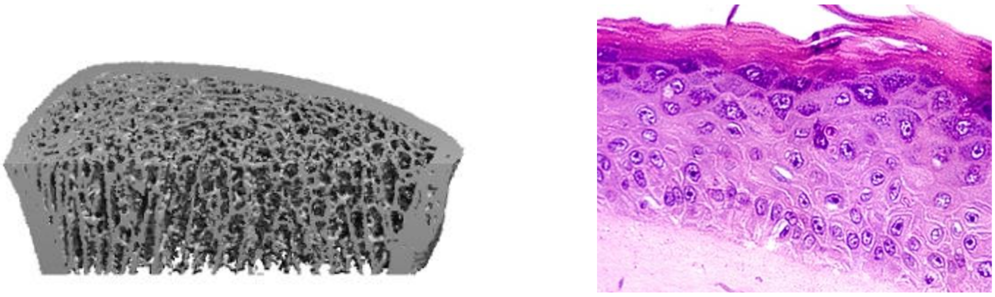

b) Bone (http://www.ncbi.nlm.nih.gov/pubmed/21424265)

c) Skin (http://www.igb.fraunhofer.de/en/press-media/press-releases/1999/skin-cosmetic-research.html)

Figure 1.2 Some examples of natural FGMs.

The concept of FGMs is easily observed in the nature. For example, bamboo is an excellent illustration. As seen in Figure 1.2a, such materials possess continuously graded properties and are characterized by spatially varying microstructures created by non-uniform distributions of the constituent phases [3]. Bone, illustrated in Figure 1.2b, is functionally graded and even human skin, as shown in Figure 1.2c, is graded. In 1972, this general idea was firstly mentioned for composites and polymeric materials [4, 5]. However, there were no actual investigations into their design, fabrication, manufacture, etc. Until 1985, the concept of FGM was proposed by a group of scientist in Sendai, Japan as a mean of developing the thermal barrier coating for the rocket engine [6]. However, most of the research works have been published in the last ten years. Noda and Tsuji [7] studied the steady thermal stresses in a FGM plate. Tanaka et al. [8, 9] employed direct sensitivity analysis and optimization techniques to design optimal thermo-elastic materials to reduce thermal stresses in FGMs. Jin and Noda [10] discussed the transient thermal stress intensity factors for a semi-infinite crack FGM plate under thermal shock loading. The modelling and analysis of FGM structures were reviewed by Birman and Byrd [11] and Swaninathan et al. [12]. From the literature, it is observed that the most common FGMs are the mixtures of two distinct material phases, e.g. a ceramic and a metal, for which their material properties vary smoothly and continuously from one surface to another. An example of FGM, e.g. Yttria Stabilized Zirconia (YSZ) / NiCoCrAlY is shown in Figure 1.3 [13]. As a result, FGMs usually inherit the best properties of the distinct components, e.g. low thermal conductivity, high thermal resistance by ceramic part, ductility, durability and superiority of fracture toughness of metal part. Therefore, they have great potential for many applications.

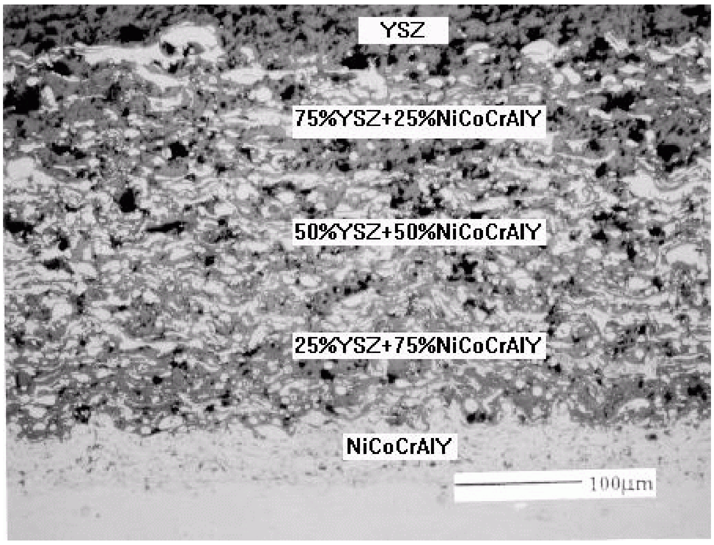

Figure 1.3 Microstructure of cross-section of YSZ/NiCoCrAlY [13].

1.2 Application of FGMs

FGMs have a variety of real and potential applications in many fields, such as transport systems, energy conversion systems, cutting tools, machine parts, semi-conductors, optics and biomaterials as described in Figure 1.4.

An example of their application can be seen in the space shuttles, for which surfaces always experience very high temperature. As known, space vehicles flying at hypersonic speeds experience extremely rapid temperature rise in very short time from aerodynamic heating due to friction between the vehicle surface and the atmosphere. For example, in U.S. space shuttles, the temperature on their outside surface increases to an attitude of 1500°C in a few minutes [14]. Hence, this required an advanced material, for which surfaces could withstand very high temperature and temperature differences. Firstly, the laminate composites with a discrete layer of ceramic material, which was bonded to a metallic structure as a conventional thermal barrier coating, were introduced. However, the abrupt transition in material properties across the interface between distinct layers can cause large inter-laminar stresses and may lead to de-bond. Furthermore, the difference in thermal coefficients of the materials may result in residual stresses. These problems can be mitigated by replacing conventionally used laminated composites with FGMs with continuously and smoothly varying material properties in the thickness direction. This application was firstly realised during space plane project in1984 in National Aerospace Laboratory of Japan to avoid the stress peaks at interfaces in coated panels for the space shuttle [2]. Herein, two important research material systems in fabrication technology of FGM are: Aluminium ‘Al_2O_3’ [15] and Zirconia ‘ZrO_2’ [16] exterior protective ceramic layers to improve thermal, oxidation and corrosion resistance. The used materials here served the temperature resistance of 2000 K with a temperature gradient of 1000 K across a 10 mm thick section [1]. Later on, their applications have been expanded to some structures in high temperature environment, such as plasma wall of fusion reactor, nuclear reactor components, heat exchangers, etc. The application of FGMs also increased in biomaterials, e.g. the artificial joints in orthopaedic implant. These implants made of the titanium/hydroxyapatite (Ti/HAP) with the concentration changed gradually in the longitudinal direction are designed to provide more titanium for the outer part subjected to directly applied forces. The main advantages of using such a FGM implant are [17]: 1) reduce the stress effect surrounding the bones; 2) improve the biocompatibility with bone tissues; 3) prevent the thermal-mechanical failure at the interface of the implants and 4) enhance the bone re-modelling, hereby maintaining the bone’s health status. In thermal-electric field, the concept of FGM has been implemented in actuators and transducers with metal-semiconductor transition with improved efficiency [16]. In engineering application, FGMs are observed in the high-performance cutting tools. Functionally-graded cutting tool, a graded FGM WC/Co, causes the hardness at the cutting tool’s surface to be higher than its interior [18]. Consequently, this graded tool results in both considerably higher damage resistance and higher wear resistance as compared to a homogeneous one. Other applications of FGMs can be found in optical materials with piezoelectric and thermoelectric devices, vehicle and space light structures. The deeply detail of the FGM’s applications can be found in the excellent book by Miyamoto et al. [14].

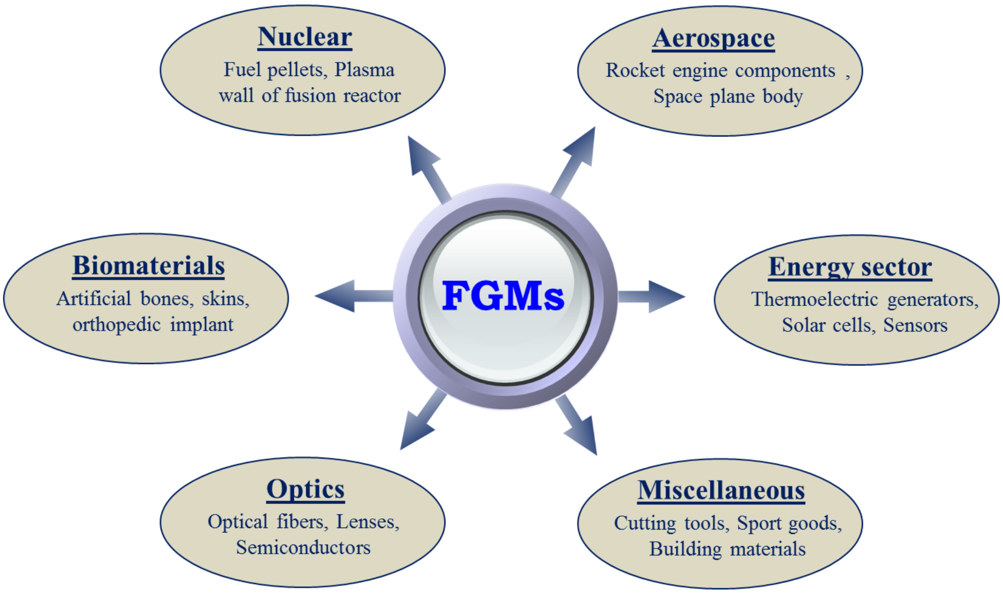

Figure 1.4 Various applicable fields for FGMs.

1.3 A brief review of researches into FGM plates

It is concluded in previous section that FGMs have a variety of real and potential applications in many engineering fields corresponding to extremely high temperature environment such as aerospace and aircraft structures, high-speed vehicle frames, nuclear fusion reactors, etc., which can be decomposed into plate/shell structures. In order to design, manufacture and operate them efficiently, a clear understanding of the behaviour of each structural component as plate/shell element, such as deformable characteristic, stress distribution, natural frequency and critical buckling of load under various conditions is therefore required. Moreover, many methodologies are proposed to predict exactly the behaviours of the FGM structures. They can be classified into two main categories: (1) the three-dimensional (3D) elasticity theory and (2) the two-dimensional (2D) plate theories.

1.3.1 3D elasticity theory

Pagano [19] initially investigated the analytical 3D elasticity method to predict the exact solution of simple static analysis. Noor [20, 21] has further developed 3D elasticity solution formulas for dynamic and stability analysis of multi-layered composite plates. For the FGM structures, Pan [22] has extended Pagano’s solution to derive a 3D exact solution for exponentially graded rectangular plates under simply supported boundary constraint. Vel and Batra obtained the 3D exact solutions for thermo-mechanical behaviours [23], as well as, the free and forced vibrations [24] of a simply supported FGM rectangular plate under mechanical and thermal loads. Reddy and Cheng [25] studied the harmonic vibration problem of functionally graded material plates by means of a 3D asymptotic theory formulated in terms of transfer matrix. It was found that the solutions are mathematically complex and just applicable to simple geometries and boundary conditions. Furthermore, the exact solutions were very hard to find for the FGM plates, for which material properties varied in another non-exponential pattern. In contrast to former work, the numerical methods were also applied to analyse some 3D FGM plate problems, e.g., differential quadrature method (DQM) by Malekzadeh [26], mesh-less local Petrov-Galerkin (MLPG) method by Mojdehi et al. [27] and Dong [28], etc. … It is well known that such an exact 3D approach has most potential to attain the exact solutions of FGM plates. However, it is not easy to solve practical problems with complex (or even slightly complicated) geometries under arbitrary boundary conditions. Moreover, it is necessary to use 3D elements in modelling 3D solid so that the storage, as well as, the computational cost will be increased significantly, as discretized mesh becomes finer. Furthermore, it is challenging that the 3D elastic solutions are sometime impossible and too hard for eigenvalue problems [12]. Hence, the 3D theory can be simplified to 2D plate theory by making suitable assumptions based on the equivalent single layer (ESL) [29] and layer-wise (LW) [30] theories.

1.3.2 2D plate theories

In the LW model [31], the displacements are assumed to be different for each layer. Therefore, there is an increase in storage and computational cost due to increased number of unknowns, which is proportional to the number of lamina. While with the ESL model, the number of displacement variables is kept constant through the thickness. In the context of the ESL model, there are three common classes: classical plate theory (CPT), first-order shear deformation theory (FSDT) and higher-order shear deformation theory (HSDT).

The classical plate theory (CPT): This is the simplest theory among the ELS theories and is based on Kirchhoff-Love hypothesis [32, 33], in which the straight lines normal to the mid-surface before deformation remains straight and perpendicular to the mid-plane after deformation (see Figure 1.5). This assumption omits both the shear and normal strains. In CPT, it is apparent that the displacement field is C^1-continuous, which numerically inconvenient in finite element formulation. Thus, the analytical [34-36] or numerical methods using Hermit interpolation functions or differential quadrature approximation in mesh-free methods [37-39] must be employed. It is observed that CPT merely provides acceptable results for the thin plate problems (length to thickness ratio $L/h \geq 100$) and becomes inadequate for the analysis of thick plates due to ignoring the transverse shear deformation.

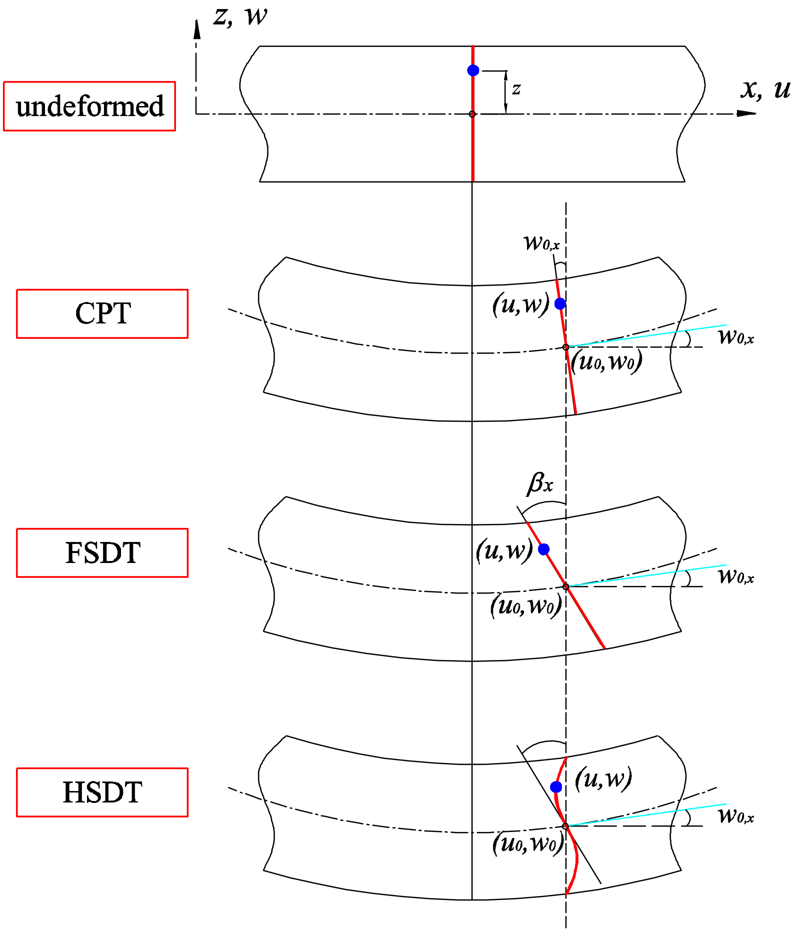

Figure 1.5 Deformation of a transverse normal.

The first-order shear deformation theory (FSDT): The next theory in the hierarchy of ELS is FSDT. It was firstly proposed by Reissner [40, 41] and then developed by Mindlin [42] by taking into account the shear deformation effect by the way of a linear variation of the in-plane displacements through the thickness. This theory assumes that the transverse normal is still straight but is not necessary perpendicular to the mid-surface after deformation (see Figure 1.5). Because of its simple implementation compared to CPT, the FSDT was widely used to model the FGM plates. Praveen and Reddy [43] studied the nonlinear transient responses of FGM plates under thermal and mechanical loadings using FEM and FSDT with von Kármán assumptions. Using an eight-node quadrilateral plate element based on consistency approach, Sundararajan et al. [44] analysed the large amplitude free flexural vibration behaviour of FGM plates. KM Liew et al. utilized combination of the element-free *kp*-Ritz method with FSDT to study thermo-elastic analysis [45], free vibration analysis [46] and geometrically nonlinear analysis [47] of FGM plates. Herein, the shear correction factor (SCF) was required to adjust the shear energy part. Nguyen-Xuan et al. developed the edge-based smoothed finite element method (ESFEM) [48] and node-based smoothed finite element method (NS-FEM) [49] to study bending static, free vibration and elastic stability of FGM plates. In this work, the strain smoothing technique was applied to the triangular plate elements to enhance the accuracy of the existing finite element methods. An isogeometric approach (IGA) was employed to study the bending, free vibration, buckling and supersonic flutter responses [50] and geometrically nonlinear analysis [51] of FGM plates based on FSDT. From the literature, it is found that FSDT model enables us to provide acceptable results for moderate and thick plate. However, when the plate becomes thin, the FSDT model is necessary to combine with some improved techniques such as reduced integration (RI) [52], mixed interpolation of tensorial components (MITC) [53], Mindlin-type plate element with improved transverse shear (MIN) [54], discrete shear gap (DSG) [55] elements and so on to overcome the shear locking phenomenon. Furthermore, based on the linear in-plane displacement assumption through the plate thickness, the FSDT yields inaccurate shear strain/stress distributions, which do not satisfy the traction free boundary conditions at the plate surfaces. It is hence required to amend the unrealistic shear strain energy part by SCF valued at a usual number of 5/6 or by a complex variable [56], which is computed so that the strain energy due to the true transverse stresses can be predicted by the 3D elastic theory [29].

The higher-order shear deformation theory (HSDT): To overcome the limitation of the CPT and FSDT, various kinds of HSDTs have then been devised [57-65]. The HSDT models take into account higher-order variations of the in-plane displacements through thickness. Consequently, they enable to more exactly describe shear strain/stress distributions with nonlinear paths and traction-free boundary conditions at the top and bottom surfaces of the plate. Moreover, the HSDT models provide better results and yield more accurate and stable solutions (e.g. inter-laminar stresses and displacements).

Furthermore, the SCFs are not required. Among HSDTs, third-order shear deformation theory (TSDT) by Reddy [57] is the most famous model and is widely used by many researchers. Reddy [66] studied both analytical solutions based on the Navier solutions and numerical ones based on finite element method for FGM plates based on the TSDT. The formulations took into account thermo-mechanical coupling, time dependency and geometric nonlinearity. Yang et al. [67] investigated the buckling, free vibration and dynamic stability of sandwich FGM plates subjected to thermo-mechanical loadings by temperature change and a periodic in-plane compression using TSDT and a semi-analytical method. Javaheri and Eslami [68] presented analytical solutions for the critical buckling temperature of simply supported FGM plates under four types of temperature rise using the TSDT and Navier solution. To extend this formulation, Najafizadeh and Heydari [69] derived the buckling in-plane load for clamped FG circular plates. Ferreira et al. utilized the mesh-less collocation method with multi-quadric radial basis functions to analyse static deformations [70, 71] and natural frequencies [72] of a simply supported plates modelled by TSDT. Tran et al. [73] employed isogeometric analysis to study the static bending behaviour, buckling load and also natural frequency and then extended their previous work for thermal buckling analysis with three types of temperature distribution [74]. However, TSDT requires the C^1-continuity that causes the obstacles in the standard finite element formulations. Several C^0 continuous elements [63, 75, 76] were proposed. GulshanTaj et al. [77] developed a nine-node isoparametric Lagrangian finite element for bending analysis of FGM plates under mechanical and thermal loadings using the C^0 HSDT with seven DOFs per node. Phung-Van et al. [78] employed the same C^0 HSDT plate formula for static and free vibration analyses of functionally graded material plates using a cell-based smoothed discrete shear gap method (CS-DSG3) and combined with von Kármán assumptions [79] to study nonlinear displacement – loading curves in FGM plates by a cell-based smoothed three-node plate element (CS-MIN3).

1.4 A review of isogeometric analysis

In engineering design, there is an intimate relation between two stages: design drawing stage generated by computer aid design (CAD) and analysis stage by finite element analysis (FEA).

Let us firstly study the evolution of CAD representation. In the past, before existence of computer graphic, designers could draw some simple geometries by hand with the drafting tools as rulers, compasses, protractors, etc. Some complex geometries such as the freeform curves of aircraft wing, ship's bow, automobile body, etc. were also handled by hand with splines. The spline comes from the nature shape of long flexible strip of timber bent by hanging a number of hooked metal weights, called ducks [80]. By moving the ducks around, the shape of spline was change accordingly. Until 1946, the spline curve was introduced in the mathematic by a mathematician, Schoenberg [81] and derived from the piecewise polynomial functions, known as B-spline basis functions. Up to 1960s, with the invention of computers, two French engineers, Pierre Bézier and de Casteljau developed a computer aided geometric design tool, called UNISURF, which could generate the spline curves and surfaces by computer (https://en.wikipedia.org/wiki/Non-uniform_rational_B-spline). After that, numerous researches on B-spline was implemented in Riesenfeld's PhD thesis [82] and rational B-splines by Versprille [83]. There are many efficient and numerically stable algorithms, which have been developed for completeness of the B-spline properties, such as the Cox-de Boor recursion [84, 85], the de Boor algorithm [86], the Oslo algorithms [87], polar forms and blossoms [88], etc. B-Splines are now extensively used in commercial software for creating smooth curves and surfaces as in AutoCAD, CATIA, 3D max, SolidWorks, LS-DYNA, etc.

In the 1970s, non-uniform rational B-splines (NURBS) were developed and become the dominant techniques in engineering design. The major reason why NURBS were introduced was that unlike B-splines, they could exactly describe all conic sections such as circles, cylinders, spheres, ellipsoids, etc. Another major advantage is that the smoothness of NURBS basis functions is controlled easily as C^{p-1} continuity for p^{th}-order. NURBS are ubiquitous in CAD but they have some shortcomings, i.e., the inability to produce watertight geometries with no gaps and overlaps, which often complicate mesh generation. The major drawback comes from the tensor product of NURBS, where refinement is applied globally. It leads to an excessive overhead number of control points with increase in refinement for some discontinuous problems. To overcome the limitations of NURBS, some technologies have been recently developed to manage the local refinement such as: T-spline [89, 90], PHT-spline (polynomial splines over hierarchical T-meshes) [91]. Thereafter, Nguyen-Thanh et al. presented PHT-spline formulations for 2D elastic solids [92] and thin shell structures [93].

In analysis stage, the initial geometries in CAD will be translated into analysis-suitable geometries such as: elements, nodal coordinates, connectivity, etc. by mesh generators in order to introduce them to large-scale finite element codes for analysis. For some complex engineering designs, this task estimated to take over 80% of the overall analysis time [94]. In 2005, Hughes and co-workers [95] introduced NURBS-based isogeometric analysis (IGA) with the primary purpose to enable a tighter connection between CAD and FEA. The main idea of this method is to use directly the shape functions from geometric description, e.g. B-spline or NURBS to approximate the unknown fields. It helps the mesh for analysis to be represented exactly even though in the coarsest mesh and finer mesh can be obtained directly from previous mesh without further communication with CAD representation. As a result, IGA simplifies the cost-intensive computational model generation procedure, especially in shape optimization [96]. Up to now, IGA has been widely applied to various engineering fields for examples, fluid mechanics [97-99], fluid-structure interaction problems [100-102], contact problems [103-105], optimization problems [106], solving PDEs having higher derivatives of the field variable such as the Hill-Cahnard equation [107], explicit gradient damage models [108] and gradient elasticity [109]. IGA has shown some advantages for structure vibration [110] and was applied to fracture problems [111-113]. So far, NURBS-based IGA has been used to analyse and simulate practical structures including beam [114, 115], plates using FSDT [50, 116, 117] and HSDT [73, 118-120], layer-wise theory [121, 122], shell structures [123, 124] and so on.

As pointed out in [125], with a fixed number of DOFs, higher-order continuity offered by NURBS requires the drastically increase in CPU time and RAM to solve the problems when using a direct solver. Whereas, solids in CAD are modelled by only the actual surfaces not the interior. Therefore, Sevilla et al. [126, 127] proposed NURBS-enhanced finite element method (NEFEM), which only requires the boundary representation provided completely by CAD. In this method, specific interpolation and numerical integration were proposed at the elements intersecting the NURBS boundary, while traditional FE was utilized otherwise. Another way, isogeometric boundary element method (IGABEM), which just considers the truly boundary representation, was proposed by Simpson et al. [128, 129]. It was found that the IGABEM based on NURBS is more accurate than classical boundary element method (BEM) with polynomial interpolations.

Recently, Natarajan et al. [130] combined the concept of IGA into the scale boundary finite element method. The unknown fields on element boundary were discretized by NURBS basis functions, while analytical solution is sought in the radial direction.

1.5 Motivation and objectives

As mentioned in the previous section, FGM plate structures are widely used in various engineering fields. Several two dimensional plate theories are provided to predict accurately the responses of the structures. Among ESL plate theories, CPT requires C^1-continuity elements and merely provides acceptable results for the thin plate, whilst FSDT is suitable for moderate and thick plates. However, the standard FSDT-based finite elements usually get too stiff and lead to shear locking in analysis of thin and very thin plates. Furthermore, the obtained results are also dependent on the SCF, which is quite dispersed through many problems. In this thesis, we focus on development of HSDT with higher-order terms in displacement field in order to describe more realistic shear energy part without SCF requirement.

Beside plate methodologies, the approximated numerical methods were developed rapidly to solve the partial differential equations (PDEs) described for these structures. Among them, the Finite Element Method (FEM) developed in the 1950s to 1960s, has been known as the most powerful and popular tool for numerical simulations in various engineering fields. However, finite element approximation of the plate structures using HSDT is not a trivial task because of using low-continuous order elements. Other drawbacks of FEM are: a) the reduction of accuracy by distortion mesh in large deformation analysis and b) the requirement of intensive re-meshing for discontinuous problems [131]. To solve the bottleneck, a family of mesh-free methods has been developed and successfully applied in engineering applications. In these methods, interpolation and nodal integration are entirely based on a set of scattered nodes instead of meshes. A comprehensive review of the mesh-free methods can be found in [132] by Belytschko et al. and in [133] by Li and Liu. Regarding direct nodal integration in mesh-free method, it was observed in Ref. [134] that the vanishing derivatives of the shape functions at the nodes cause numerical instability and low accuracy. Furthermore, shape functions are rational functions, which require high-order integration scheme and usually do not satisfied the Kronecker delta property [135]. Therefore, essential boundary conditions cannot be directly imposed as conveniently as in the traditional FEM. In recent years, a novel numerical method, the so-called Isogeometric Analysis (IGA), which yields higher-order continuity naturally and easily, has been proposed by Hughes et at. [95]. Thus, it enables to satisfy easily the stringent continuity requirement of the HSDT model without any additional variables. The second aim of this thesis is to apply isogeometric finite element method in order to integrate modelling and simulation of functionally graded material plates using higher-order shear deformation theories [62, 73, 136].

In order to use FGM plates efficiently, a clear understanding of their behaviours such as deformable characteristic, stress distribution, natural frequencies, dynamic response and elastic instability under thermal and mechanical loads is studied. Based on small displacement and strain assumptions, the plate formulation may be reduced to a linear problem. Linear solution can be obtained easily with low computational cost and sometime is a reasonable idealization. However, linear solution usually deviates from real response of structures [66, 137-139]. In some cases, assumption of nonlinearity is the only option for analyst, e.g., post buckling phenomenon [140, 141]. As safety and economy are the main goals, nonlinear analysis needs to be considered. Therefore, in this thesis, beside linear analysis, geometrically nonlinear analysis is employed to fully investigate the plate behaviour in the large deformation regime.

1.6 Thesis outline

This thesis is divided into eight chapters including the introduction and is organized as follows:

Chapter 2 describes physical representation of the functionally graded material plates. Firstly, FGM is introduced as an inhomogeneous isotropic material. In this thesis, two types of homogenization techniques: the rule of mixture and the Mori-Tanaka scheme are utilized to homogenize this material. Then, we exhibited theoretical formulations of FGM plates based on three types of HSDT: TSDT, RPT and GSDT. Herein, the general governing equations of plate structure are described in total Lagrange method with nonlinear effect related to von Kármán assumptions.

Chapter 3 introduces a framework of isogeometric analysis for plate structure based on higher-order shear deformation theories. The concept of isogeometric analysis based on NURBS basis function is reviewed. Thereafter, this method is implemented into the plate formulations. NURBS-based IGA attains higher-order continuity, which naturally satisfies C^1 continuity requirement of the HSDT models. The numerical integration technique and treatment of boundary constraints in IGA are also presented in this chapter.

Chapter 4 concentrates on static analysis of FGM plates under various boundary conditions. The governing equations for bending problems are established for both cases of linear analysis and geometrically nonlinear bending analysis, which considers nonlinear strain – displacement relation. The nonlinear governing equation is solved by employing the Newton-Raphson method. The obtained results of the thermo-mechanical deformations of the plates show the excellent performance of the present method.

Chapter 5 discusses buckling and post-buckling analyses of the FGM plates under in-plane compression. The compressive stress comes from the directly applied load or temperature change. In the former, the loading is applied at the neutral surface of the plates, while it is assumed in the latter that the temperature varies uniformly on the top and bottom surfaces and only variously through the thickness direction, i.e. constant, linear or nonlinear functions. Furthermore, the effect of temperature-dependent thermo-elastic material properties is considered in order to accurately predict the mechanical responses of FGM structures.

Chapter 6 describes the procedure for dynamic problems, which can be categorized into two groups: free vibration and force vibration. The former, without force vector, is solved by eigenvalue analysis to estimate the natural frequencies, while the latter considers the applied loads and the von Kármán nonlinear strain. Thus, the equation of dynamic system, which depends on not only time domain, but also unknown displacements, is solved by the Newmark's integration scheme in association with the Picard methods.

Chapter 7 presents the results of modal analysis for cracked FGM plates. In this chapter, a novel numerical procedure based on integrating the enrichment functions through the partition of unity method (PUM) into isogeometric finite element in order to model the discontinuous phenomenon in the cracked structures. The fact is that the Heaviside function is enriched to capture the discontinuous phenomenon at the crack faces, while the asymptotic functions from analytical solution are incorporated with NURBS to model the singular field at the crack tips. This method shows good validations for 2D in-plane structures and then extends to various shapes of FGM plates in the numerical example section.

Finally, chapter 8 closes this thesis with some concluding remarks and suggestions for future research.

Chapter 2 Functionally Graded Material Plate

2.1 Functionally graded material

We assume that the plate is made of functionally graded material, which is an inhomogeneous isotropic material as shown in Figure 2.1. FGM is fabricated by mixing two distinct material phases, e.g. ceramic and metal, for which their properties are constant in *xy*-plane (isotropic behaviour) and vary along thickness (*z*-direction).

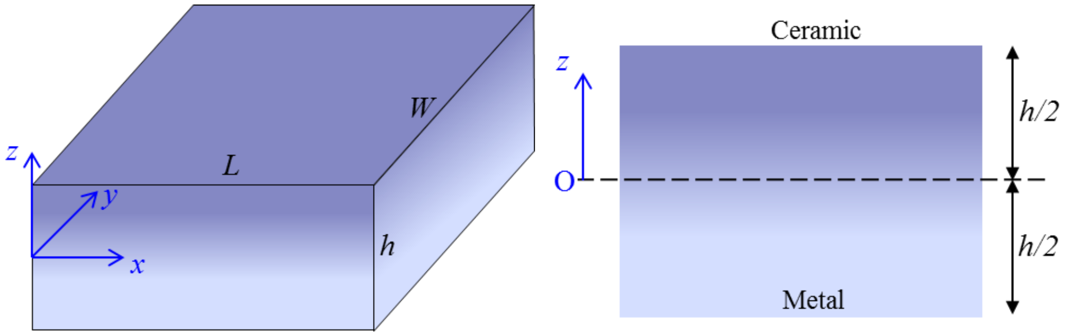

Figure 2.1 A functionally graded material layer.

Because of gradual variation of each phase along the plate thickness, the effective properties of FGM also gradually vary along the *z*-direction. In order to model FGM, there are two common approaches, in which material ingredients can be changed in a stepwise gradation as illustrated in Figure 2.2a or a continuous way as revealed in Figure 2.2b, respectively. In the former, the FGM plate works as a laminated plate, which is stacked sequentially by many isotropic lamina having different material properties. The effective material coefficient can be calculated following Reddy's text book [29]. In the latter, the material ingredients are represented as their volume fractions, which are assumed to distribute as a power-law function

$$V_c(z) = \left(\frac{1}{2} + \frac{z}{h}\right)^n \tag{2.1}$$

$$V_c + V_m = 1 \tag{2.2}$$

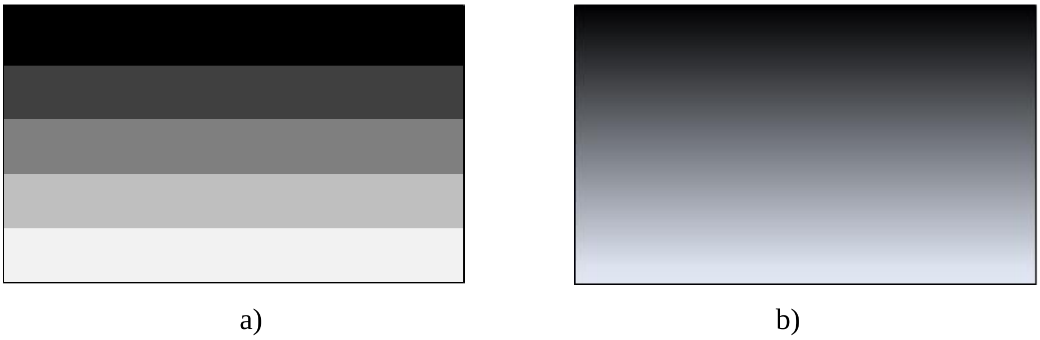
a) b)

Figure 2.2 a) Stepwise gradual and b) continuous variation.

where V_c and V_m are ceramic and metal volume fractions, respectively. It is noted that the sum of them is always unity and $n \in \mathbb{R}^+$ is the power index or gradient index. The advantage of this function is that it is simple and by changing of the power index, n, a wide range of distribution shape of the material phases can be represented, as shown in Figure 2.3 for distribution of the ceramic volume fraction. As observed, $n = 0 \rightarrow V_c = 1, V_m = 0$, the structure is fully ceramic and when $n = \infty \rightarrow V_c = 0, V_m = 1$, the homogeneous metal is retrieved. Furthermore, $V_c(h/2) = 1$ and $V_m(-h/2) = 1$ mean that fully ceramic and metal phase on the top and the bottom surfaces, respectively.

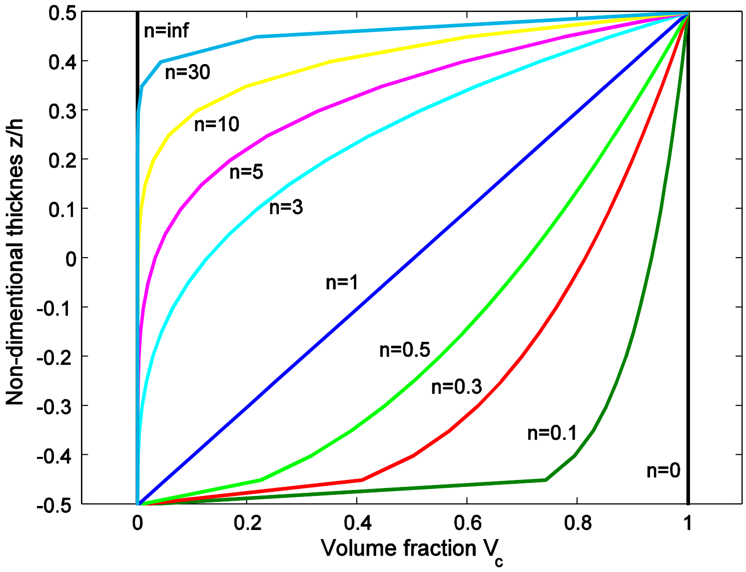

Figure 2.3 The ceramic volume fraction along the thickness.

In order to homogenize this material, several analytical approaches available in the literature [1] are briefly presented in the following section.

2.1.1 The rule of mixture

In this homogenization, the effective material properties, P_e, including Young's modulus (E), shear modulus (μ), Poisson's ratio (ν), the density (ρ), thermal conductivity (k) and thermal expansion (α) are given by:

$$P_e = P_c V_c + P_m V_m \tag{2.3}$$

where subscripts *m*, *c* and *e* refer to the metal, ceramic and effective constituents, respectively. This approach is the easiest without consider the interactions among the constituents [142] and more common in the stress analysis of FGM.

2.1.2 The Mori-Tanaka scheme

The Mori–Tanaka scheme [143, 144] works well for estimating the effective material properties of the graded microstructure, that have a clearly defined continuous matrix and a discontinuous particulate phase. It takes into account the interaction of the elastic fields between neighbouring inclusions with the effective bulk (K) and shear (μ) moduli defined as follows:

$$\begin{aligned} \frac{K_e - K_m}{K_c - K_m} &= \frac{V_c}{1 + V_m \frac{K_c - K_m}{K_m + 4/3\mu_m}} \\ \frac{\mu_e - \mu_m}{\mu_c - \mu_m} &= \frac{V_c}{1 + V_m \frac{\mu_c - \mu_m}{\mu_m + f_1}} \end{aligned} \tag{2.4}$$

where $f_1 = \mu_m(9K_m + 8\mu_m)/6(K_m + 2\mu_m)$. From the obtained effective bulk and shear moduli, the effective values of Young's modulus (E) and Poisson's ratio (ν) are given by:

$$E_e = \frac{9K_e\mu_e}{3K_e + \mu_e}, \qquad \nu_e = \frac{3K_e - 2\mu_e}{2(3K_e + \mu_e)} \tag{2.5}$$

While, the effective thermal conductivity is determined by [145]:

$$\frac{k_e - k_m}{k_c - k_m} = \frac{V_c}{1 + (1 - V_c)(K_c - K_m)/K_m} \tag{2.6}$$

and the coefficient of thermal expansion is estimated from [146]:

$$\frac{\alpha_e - \alpha_m}{\alpha_c - \alpha_m} = \frac{1/K_e - 1/K_m}{1/K_c - 1/K_m} \tag{2.7}$$

2.1.3 Other approaches

Besides the two approaches presented above, there are several micromechanics models developed over the years to infer the effective properties of macroscopically homogeneous functionally graded materials: self-consistent estimate [147], composite sphere assemblage model [148], composite cylindrical assemblage model [149], the simplified strength of materials method [150], the methods of cells [151], micromechanical models [152] and the exponential law method [153].

In this study, we adopt two popular methods for estimating the effective FGM properties: the Mori-Tanaka scheme and the rule of mixture. For Aluminium-Zirconia FGM (Al/ZrO_2-1), for which properties are tabulated in Table 2.1, Figure 2.4 shows comparison of the effective Young's modulus of plate calculated by the two homogenization schemes via the power index *n*. As it can be seen, the two models produce the same modulus for homogeneous material ($n = 0$). As material becomes inhomogeneous, the effective property through the thickness of the former is higher than that of the latter.

Table 2.1 Material property

	E (GPa)	ν	k (W/mK)	$\alpha \times 10^{-6}$ (C^{-1})	ρ (kg/m^3)
Al	70	0.3	204	23	2707
ZrO_2-1	200	0.3	2.09	10	5700
ZrO_2-2	151	0.3	2.09	10	3000
Al_2O_3	380	0.3	10.4	7.4	3800
SiC	427	0.17	120	4.0	3100

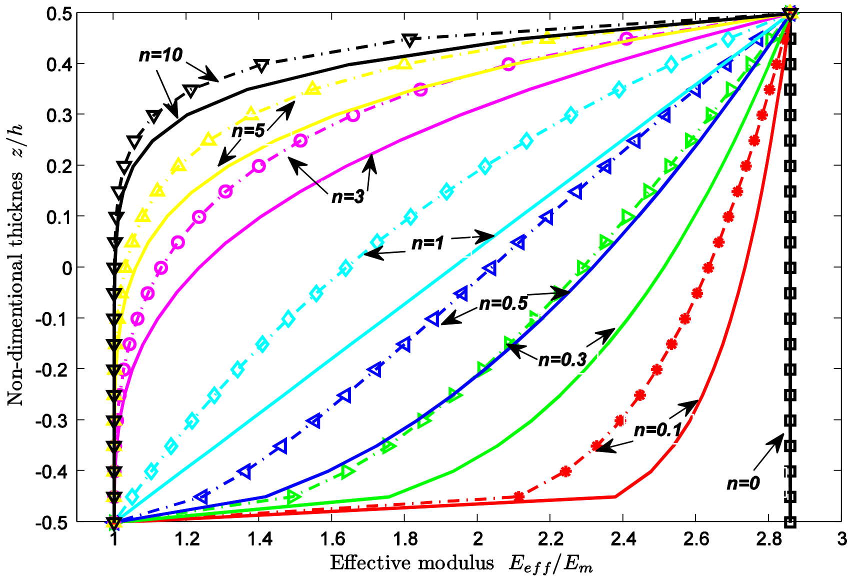

Figure 2.4 The effective modulus of Al/ZrO$_2$-1 FGM plate computed by the rule of mixture (in solid line) and the Mori-Tanaka (in dash dot line).

2.1.4 Thermal effect

FGMs are mainly made from a mixture of ceramic and metal. And they are most commonly used in the high-temperature environment. To calculate thermal load, it is assumed that the temperature varies uniformly on the top and bottom surfaces and non-uniformly through the thickness direction. Therefore, the temperature field is obtained by solving one-dimensional equation of heat conduction in the thickness direction:

$$-\frac{\mathrm{d}}{\mathrm{dz}}\left(k(z)\frac{\mathrm{d}T}{\mathrm{dz}}\right)=0 \tag{2.8}$$

The solution of Eq. (2.8) is given in analytical form [154] as:

$$T(z)=T_c-\frac{T_c-T_m}{\int_{-t/2}^{t/2}1/k_e(z)dz}\int_z^{t/2}1/k_e(\tau)d\tau \tag{2.9}$$

or expressed by polynomial series [69, 155] as:

$$T(z)=T_m+\eta(z)(T_c-T_m) \tag{2.10}$$

where

$$\eta(z)=\left(\frac{z}{h}+\frac{1}{2}\right)\sum_{i=0}^{\infty}\frac{1}{ni+1}\left(\frac{z}{h}+\frac{1}{2}\right)^{ni}\left(\frac{k_m-k_c}{k_m}\right)^{i}\Big/\sum_{i=0}^{\infty}\frac{1}{ni+1}\left(\frac{k_m-k_c}{k_m}\right)^{i} \tag{2.11}$$

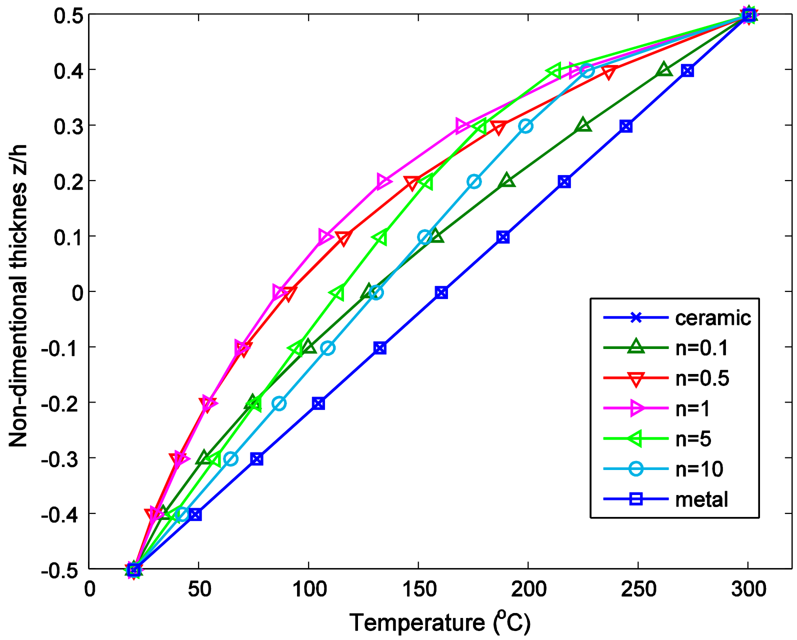

Figure 2.5 Temperature distributions through the thickness of Al/ZrO$_2$-1 FGM plate.

Figure 2.5 illustrates the effect of the gradient index *n* on the temperature distribution through the thickness of the Al/ZrO$_2$-1 FGM plate subjected to a thermal load, where the top and bottom surfaces are held at 300°C and 20°C, respectively. It is evident that the temperature in the FGM plates varies nonlinearly and is always lower than that in the homogenous plates except for two top and bottom points.

Moreover, high temperature environment makes a significant change in mechanical properties of the constituent materials. Therefore, it is essential to take into account the temperature-dependent material property to predict accurately the mechanical responses of FGM structures. According to Ref. [156], the properties of the common structural ceramics and metals are expressed as a nonlinear function of temperature:

$$P=P_0\left(P_{-1}T^{-1}+1+P_1T+P_2T^2+P_3T^3\right) \tag{2.12}$$

where P_0, P_{-1}, P_1, P_2 and P_3 are the coefficients of temperature, which can be found in Ref. [157] as the unique parameters for each constituent material.

2.2 Motion and deformation gradient

When a deformable body is under the action of external forces and given boundary constraints, the body undergoes motion and deformation and takes a definitive shape at the end of load application. In a rectangular Cartesian coordinate, let us consider two points P (*x*, *y*, *z*) and Q (*x*+*dx*, *y*+*dy*, *z*+*dz*) in un-deformed configuration of a body Ω. The length of line PQ is $ds = \sqrt{d\mathbf{x}^T d\mathbf{x}}$, where $d\mathbf{x} = [dx \quad dy \quad dz]^T$. During deformation, the points P and Q move to new positions of P* (*X*, *Y*, *Z*) and Q* (*X*+*dX*, *Y*+*dY*, *Z*+*dZ*) at deformed configuration Ω*, respectively (as shown in Figure 2.6) by adding a finite displacement as follows:

$$\mathbf{X} = \mathbf{x} + \mathbf{u} \tag{2.13}$$

The two points are now separated by an infinitesimal distance, $dS = \sqrt{d\mathbf{X}^T d\mathbf{X}}$, where $d\mathbf{X} = [dX \quad dY \quad dZ]^T$. The standard strain measure, namely the Green-Lagrange strain, **E**, is defined by the change in the differential length as [29]:

$$2d\mathbf{x}^T \mathbf{E} d\mathbf{x} = dS^2 - ds^2 = d\mathbf{X}^T d\mathbf{X} - d\mathbf{x}^T d\mathbf{x} \tag{2.14}$$

Herein, the total differential length is given by:

$$d\mathbf{X} = \mathbf{J} d\mathbf{x} \tag{2.15}$$

where **J** is the Jacobian matrix:

$$\mathbf{J} = \begin{bmatrix} \frac{\partial X}{\partial x} & \frac{\partial X}{\partial y} & \frac{\partial X}{\partial z} \\ \frac{\partial Y}{\partial x} & \frac{\partial Y}{\partial y} & \frac{\partial Y}{\partial z} \\ \frac{\partial Z}{\partial x} & \frac{\partial Z}{\partial y} & \frac{\partial Z}{\partial z} \end{bmatrix} = \mathbf{I} + \nabla \mathbf{u} \tag{2.16}$$

where $\nabla(\bullet) = \frac{\partial(\bullet)}{\partial x} + \frac{\partial(\bullet)}{\partial y} + \frac{\partial(\bullet)}{\partial z}$ denotes the gradient operator.

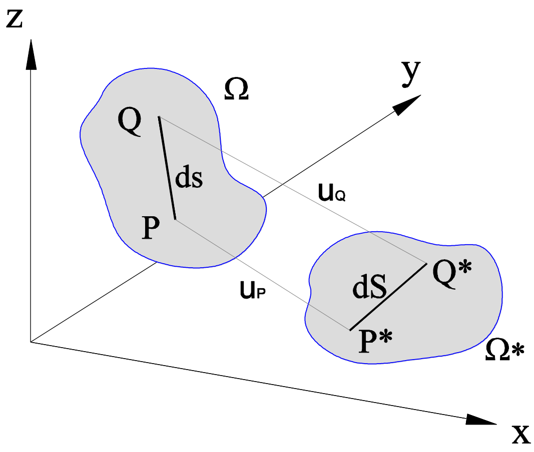

Figure 2.6 Deformation of an elastic body.

Substituting Eq. (2.15) into Eq. (2.14), the Green-Lagrange strain tensor is:

$$\mathbf{E}=\frac{1}{2}\left[\left(\mathbf{I}+\nabla\mathbf{u}\right)^{T}\left(\mathbf{I}+\nabla\mathbf{u}\right)-\mathbf{I}\right]=\frac{1}{2}\left(\nabla\mathbf{u}^{T}+\nabla\mathbf{u}\right)+\frac{1}{2}\nabla\mathbf{u}.\nabla\mathbf{u}^{T} \tag{2.17}$$

or we can rewrite it in the index form as:

$$E_{ij}=\frac{1}{2}\left(\frac{\partial u_i}{\partial x_j}+\frac{\partial u_j}{\partial x_i}\right)+\frac{1}{2}\frac{\partial u_k}{\partial x_i}\frac{\partial u_k}{\partial x_j} \tag{2.18}$$

It should be noted that if the displacement gradient is small, the Green-Lagrange tensor reduces to the infinitesimal strain tensor by eliminating the second-order infinitesimal term:

$$\boldsymbol{\varepsilon}=\frac{1}{2}\left(\nabla\mathbf{u}^{T}+\nabla\mathbf{u}\right) \quad \text{or} \quad \varepsilon_{ij}=\frac{1}{2}\left(\frac{\partial u_i}{\partial x_j}+\frac{\partial u_j}{\partial x_i}\right) \tag{2.19}$$

2.3 Two-dimensional plate theory

A plate is a three-dimensional solid with a small thickness as compared to the other dimensions [158]. To facilitate the solution, the 3D theory can be simplified to the equivalent single layer (ESL) plate theory by making assumption of kinematics of deformation. Among the ESL, the CPT and the FSDT are simple and adequate to describe the behaviour of most plates. However, they cannot yield accurate inter-laminar stress distributions. Therefore, HSDTs, which involve the higher-order stress resultants, are proposed to represent the kinematic behaviour. In these models, the higher-order terms are incorporated into the displacement field in order to consider the effect of shear deformation directly. In this section, we consider three HSDT models.

2.3.1.1 Third-order shear deformation theory (TSDT)

This is a simple and famous theory for bending plate proposed by Reddy [29], in which the displacements of an arbitrary point are given by:

$$\begin{aligned} u(x,y,z) &= u_0 + z\beta_x - \frac{4z^3}{3h^2}\left(\beta_x + w_{0,x}\right) \\ v(x,y,z) &= v_0 + z\beta_y - \frac{4z^3}{3h^2}\left(\beta_y + w_{0,y}\right) \quad , \quad \left(\frac{-h}{2} \le z \le \frac{h}{2}\right) \\ w(x,y) &= w_0 \end{aligned} \tag{2.20}$$

where u_0, v_0, w_0 are the displacement components of a point on the mid-surface through *x*, *y* and *z* directions, respectively, β_x, β_y are the rotations in the *xz* and *yz* planes, respectively, *h* is the plate thickness and $z \in [-h/2 \; h/2]$ is distance from the considered point to the mid-surface. Based on the kinematic of displacement, $\varepsilon_z = \partial w / \partial z = 0$, the infinitesimal strain tensor in Eq. (2.19) can be simplified using two separates vectors: in-plane and shear strains, respectively

$$\begin{Bmatrix} \varepsilon_{xx} \\ \varepsilon_{yy} \\ \gamma_{xy} \end{Bmatrix} = \begin{bmatrix} u_{,x} \\ v_{,y} \\ u_{,y} + v_{,x} \end{bmatrix} \tag{2.21}$$

$$\begin{Bmatrix} \gamma_{xz} \\ \gamma_{yz} \end{Bmatrix} = \begin{Bmatrix} u_{,z} + w_{0,x} \\ v_{,z} + w_{0,y} \end{Bmatrix} = \left(1 - \frac{4z^2}{h^2}\right) \begin{Bmatrix} \beta_x + w_{0,x} \\ \beta_y + w_{0,y} \end{Bmatrix} \tag{2.22}$$

It is seen that the shear strains are equal to zero at $z = \pm h/2$. It means that traction-free boundary conditions at the top and bottom surfaces of plate are automatically satisfied. In numerical computation, using the same interpolated functions makes the unequal order in the approximation of the rotations β_x, β_y and derivative of deflection $w_{0,x}$, $w_{0,y}$. In thin plate, as the length-to-thickness ratio becomes large, Eq. (2.22) does not become zero. It leads to invalid zero-transverse shear strains. Consequently, the stiffness matrix becomes stiff and yields erroneous results for the general displacements. This phenomenon is known as shear-locking, which also exists in FSDT model.

2.3.1.2 Refined plate theory (RPT)

The displacement field of RPT is established by adding those assumptions given by Senthilnathan et al. [59]:

- The transverse displacement is separated into two parts: bending and shear components denoted as w_b and w_s, respectively.

- The bending components of in-plane displacements, in conjunction with w_b, are given by classical plate theory (CPT):

$$\beta_x = -w_{b,x}, \quad \beta_y = -w_{b,y} \tag{2.23}$$

- The shear components of the in-plane displacements give rise, in conjunction with w_s, to the parabolic variations of shears trains/stresses through the plate in such a way that the shear strains/stresses vanish on the top and bottom surfaces of the plate. Substituting Eq. (2.23) into Eq. (2.20), the following displacement field can be obtained as:

$$\begin{aligned} u(x,y,z) &= u_0 - zw_{b,x} - \frac{4z^3}{3h^2}w_{s,x} \\ v(x,y,z) &= v_0 - zw_{b,y} - \frac{4z^3}{3h^2}w_{s,y} \\ w(x,y) \quad &= w_b + w_s \end{aligned} \tag{2.24}$$

As it is observed, the current unknown variable is $\mathbf{q} = \left[u_0 \; v_0 \;\; w_b \;\; w_s\right]^T$, one reduced variable as compared with FSDT and TSDT. In general, we introduce a generalized refined plate theory based on shape functions, which determine the distribution of the transverse shear strains/stresses across the plate thickness:

$$\begin{aligned} u(x,y,z) &= u_0 - zw_{b,x} + g(z)w_{s,x} \\ v(x,y,z) &= v_0 - zw_{b,y} + g(z)w_{s,y} \\ w(x,y) \quad &= w_b + w_s \end{aligned} \tag{2.25}$$

where $g(z) = f(z) - z$, in which $f(z)$ is a so-called distributed function which is clearly introduced in the next sub-section.

Substituting Eq. (2.25) into Eq. (2.22), the shear strain is derived as:

$$\boldsymbol{\gamma} = \begin{Bmatrix} \gamma_{xz} \\ \gamma_{yz} \end{Bmatrix} = f'(z) \begin{Bmatrix} w_{s,x} \\ w_{s,y} \end{Bmatrix} \tag{2.26}$$

As mention in Ref. [159], as the plate becomes thinner ($L/h \geq 100$), the effect of shear component on the transverse displacement is significantly small and can be eliminated. Consequently, the shear strains/stresses may tend to zero and this theory reduces to the CPT.

2.3.1.3 Generalized shear deformation theory (GSDT)

Another way to treat the shear-locking phenomenon naturally, a generalized higher-order shear deformation theory derived from the CPT is defined as follows:

$$\begin{aligned} u(x,y,z) &= u_0 - zw_{0,x} + f(z)\beta_x \\ v(x,y,z) &= v_0 - zw_{0,y} + f(z)\beta_y \\ w(x,y) &= w_0 \end{aligned} \tag{2.27}$$

or in vector form:

$$\mathbf{u} = \mathbf{u}_1 + z\mathbf{u}_2 + f(z)\mathbf{u}_3 \tag{2.28}$$

where $\mathbf{u}_1 = \{u_0 \;\, v_0 \;\, w_0\}^T$, $\mathbf{u}_2 = -\{w_{0,x} \;\, w_{0,y} \;\, 0\}^T$ and $\mathbf{u}_3 = \{\beta_x \;\, \beta_y \;\, 0\}^T$. And the function $f(z)$ is chosen to satisfy the tangential zero value on the top and bottom faces, i.e., $f'(\pm h/2) = 0$. Based on this condition, various distributed functions $f(z)$ are listed in Table 2.2 including: third-order polynomials by Reddy [57] and Shimpi [160, 161], exponential function by Karama [162], sinusoidal function by Touratier [163] and Arya [164], fifth-order polynomial by Nguyen [118], trigonometric function by Thai [165] and our proposed function in inverse tangent form [136] as shown in Figure 2.7. This plate theory is also called generalized shear deformation theory (GSDT), which does not only satisfy the traction free boundary condition at the plate surfaces, but also overcome shear-locking phenomenon naturally.

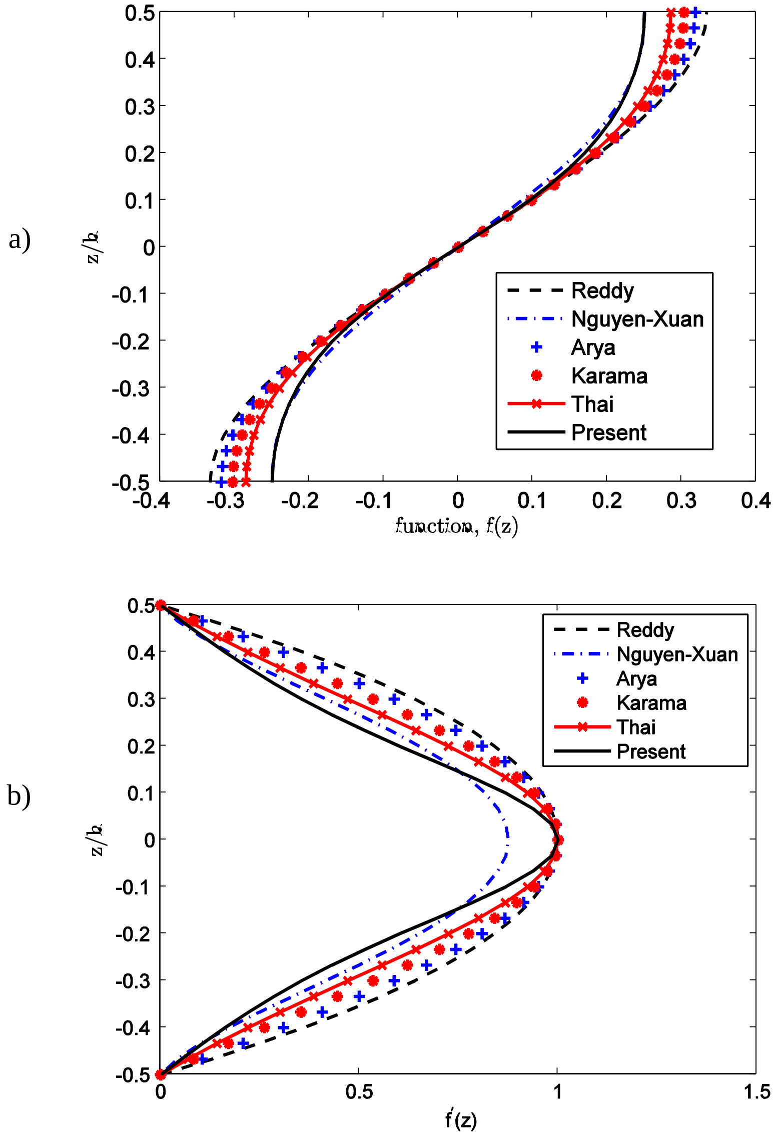

Figure 2.7 a) The shape functions and b) their derivative through the plate thickness.

Table 2.2 The forms of distributed functions and their first derivative.

Model	$f(z)$	$f'(z)$
Reddy (TSDT)	$z-\frac{4}{3}z^3/h^2$	$1-4z^2/h^2$
Shimpi	$\frac{5}{4}z-\frac{5}{3}z^3/h^2$	$\frac{5}{4}\left(1-4z^2/h^2\right)$
Karama (ESDT)	$ze^{-2(z/h)^2}$	$(1-\frac{4}{h^2}z^2)e^{-2(z/h)^2}$
Touratier (SSDT)	$\frac{h}{\pi}\sin(\frac{\pi}{h}z)$	$\cos(\frac{\pi}{h}z)$
Nguyen-Xuan	$\frac{7}{8}z-\frac{2}{h^2}z^3+\frac{2}{h^4}z^5$	$\frac{7}{8}-\frac{6}{h^2}z^2+\frac{10}{h^4}z^4$
Thai (ITSDT)	$h\arctan(\frac{2}{h}z)-z$	$(1-(\frac{2}{h}z)^2)/(1+(\frac{2}{h}z)^2)$
Present model	$\frac{h}{\pi}\arctan(\sin(\frac{\pi}{h}z))$	$\cos(\frac{\pi}{h}z)/(1+\sin^2(\frac{\pi}{h}z))$

Herein, by setting $f(z)=0$ we adopt the CPT as follows:

$$\begin{aligned} u(x,y,z) &= u_0 - zw_{0,x} \\ v(x,y,z) &= v_0 - zw_{0,y} \\ w(x,y) \ &= w_0 \end{aligned} \tag{2.29}$$

Similarly, the Reissner–Mindlin theory is obtained by setting $f(z)=z$ and assigning $\beta_{\mathbf{x}} \equiv -w_{,\mathbf{x}} + \beta_{\mathbf{x}}$

$$\begin{aligned} u(x,y,z) &= u_0 + z\beta_x \\ v(x,y,z) &= v_0 + z\beta_y \\ w(x,y) \ &= w_0 \end{aligned} \tag{2.30}$$

2.4 Strain and stress

The plate is a bending structure, in which the in-plane displacements are much smaller than the transverse one (deflection). Thus, the components of the in-plane displacement gradients $u_{,x}$, $u_{,y}$, $v_{,x}$, $v_{,y}$ are of the order ε, and the terms of the higher-order ε^2 can be neglected in the strains. Whereas, for the moderate rotations of transverse displacement (say 10°− 15°), the following terms $w_{,x}^2,\ w_{,y}^2,\ w_{,x}w_{,y}$ are small but not negligible [166]. Due to independence of transverse displacement on *z* coordinate in Eq. (2.27), the zero transverse normal strain condition $\varepsilon_z = 0$ is fulfilled. Thus, the Green-Lagrange tensor in (2.18) is simplified in the form of the von Kármán strains with five elements as follows:

$$\begin{Bmatrix} \varepsilon_x \\ \varepsilon_y \\ \gamma_{xy} \\ \gamma_{xz} \\ \gamma_{yz} \end{Bmatrix} = \begin{Bmatrix} u_{,x} \\ v_{,y} \\ u_{,y}+v_{,x} \\ u_{,z}+w_{,x} \\ v_{,z}+w_{,y} \end{Bmatrix} + \frac{1}{2} \begin{Bmatrix} w_{,x}^2 \\ w_{,x}^2 \\ 2w_{,x}w_{,y} \\ 0 \\ 0 \end{Bmatrix} \tag{2.31}$$

Substituting the assumed displacement field in (2.27) into Eq. (2.31), the strain vector with separated in-plane strain $\boldsymbol{\varepsilon}$ and shear strain $\boldsymbol{\gamma}$ parts are given by:

$$\begin{Bmatrix} \boldsymbol{\varepsilon} \\ \boldsymbol{\gamma} \end{Bmatrix} = \begin{Bmatrix} \boldsymbol{\varepsilon}_m \\ 0 \end{Bmatrix} + \begin{Bmatrix} z\boldsymbol{\kappa}_1 \\ 0 \end{Bmatrix} + \begin{Bmatrix} f(z)\boldsymbol{\kappa}_2 \\ f'(z)\boldsymbol{\beta} \end{Bmatrix} \tag{2.32}$$

where the in-plane , the mid-plane curvatures and the bending shear strain are defined as:

$$\boldsymbol{\varepsilon}_m = \begin{bmatrix} u_{0,x} \\ v_{0,y} \\ u_{0,y} + v_{0,x} \end{bmatrix} + \frac{1}{2}\begin{bmatrix} w_{0,x}^2 \\ w_{0,x}^2 \\ 2w_{0,x}w_{0,y} \end{bmatrix} = \boldsymbol{\varepsilon}_L + \boldsymbol{\varepsilon}_{NL}$$

$$\boldsymbol{\kappa}_1 = -\begin{bmatrix} w_{0,xx} \\ w_{0,yy} \\ 2w_{0,xy} \end{bmatrix}, \quad \boldsymbol{\kappa}_2 = \begin{bmatrix} \beta_{x,x} \\ \beta_{y,y} \\ \beta_{x,y} + \beta_{y,x} \end{bmatrix}, \quad \boldsymbol{\beta} = \begin{bmatrix} \beta_x \\ \beta_y \end{bmatrix} \tag{2.33}$$

The nonlinear component of in-plane strain can be rewritten as:

$$\boldsymbol{\varepsilon}_{NL} = \frac{1}{2}\mathbf{A}_\theta \boldsymbol{\theta} \tag{2.34}$$

where

$$\mathbf{A}_\theta = \begin{bmatrix} w_{0,x} & 0 \\ 0 & w_{0,y} \\ w_{0,y} & w_{0,x} \end{bmatrix} \quad \text{and} \quad \boldsymbol{\theta} = \begin{Bmatrix} w_{0,x} \\ w_{0,y} \end{Bmatrix} \tag{2.35}$$

Considering thermal effect, the thermal strain is given by:

$$\boldsymbol{\varepsilon}^{th} = \begin{Bmatrix} \varepsilon_x^{th} \\ \varepsilon_y^{th} \\ \varepsilon_{xy}^{th} \end{Bmatrix} = \alpha_e(z)\Delta T \begin{Bmatrix} 1 \\ 1 \\ 0 \end{Bmatrix} \tag{2.36}$$

with $\alpha_e(z)$ is the effective thermal coefficient and ΔT is the temperature change defined as:

$$\Delta T(z) = T(z) - T_i \tag{2.37}$$

where T_i is the initial temperature and $T(z)$ is the current temperature varied through the plate thickness as given in Eq. (2.9).

In general, the transverse normal stress σ_z is not zero. However, from practical consideration, a plate is in a state of plane stress due to thickness dimension being very small compared with the other dimensions [29]. Consequently, the transverse normal stress σ_z is assumed to be zero and eliminated in the virtual work statement. Hence, the plane-stress state reduces the constitutive relation with five elements as follows:

$$\begin{Bmatrix} \sigma_x \\ \sigma_y \\ \tau_{xy} \\ \tau_{xz} \\ \tau_{yz} \end{Bmatrix} = \begin{bmatrix} \mathbf{C} & \mathbf{0} \\ \mathbf{0} & \mathbf{G} \end{bmatrix} \begin{Bmatrix} \varepsilon_x - \varepsilon_x^{th} \\ \varepsilon_y - \varepsilon_y^{th} \\ \gamma_{xy} - \varepsilon_{xy}^{th} \\ \gamma_{xz} \\ \gamma_{yz} \end{Bmatrix} \tag{2.38}$$

or the simplified form with separated in-plane and shear stresses

$$\begin{Bmatrix} \boldsymbol{\sigma} \\ \boldsymbol{\tau} \end{Bmatrix} = \begin{bmatrix} \mathbf{C} & \mathbf{0} \\ \mathbf{0} & \mathbf{G} \end{bmatrix} \begin{Bmatrix} \boldsymbol{\varepsilon} - \boldsymbol{\varepsilon}^{th} \\ \boldsymbol{\gamma} \end{Bmatrix} \tag{2.39}$$

where the material matrices are given by:

$$\mathbf{C} = \frac{E_e}{1-\nu_e^3} \begin{bmatrix} 1 & \nu_e & 0 \\ \nu_e & 1 & 0 \\ 0 & 0 & (1-\nu_e)/2 \end{bmatrix} \tag{2.40}$$

$$\mathbf{G} = \frac{E_e}{2(1+\nu_e)} \begin{bmatrix} 1 & 0 \\ 0 & 1 \end{bmatrix} \tag{2.41}$$

The in-plane forces, moments and shear forces are calculated as follows:

$$\begin{Bmatrix} N_{ij} \\ M_{ij} \\ P_{ij} \end{Bmatrix} = \int_{-h/2}^{h/2} \sigma_{ij} \begin{Bmatrix} 1 \\ z \\ f(z) \end{Bmatrix} \mathrm{d}z \quad \text{and} \quad \begin{Bmatrix} Q_x \\ Q_y \end{Bmatrix} = \int_{-h/2}^{h/2} f'(z) \begin{Bmatrix} \tau_{xz} \\ \tau_{yz} \end{Bmatrix} \mathrm{d}z \tag{2.42}$$

Substituting Eq. (2.39) into Eq. (2.42), stress resultants are rewritten in matrix form

$$\underbrace{\begin{Bmatrix} \mathbf{N} \\ \mathbf{M} \\ \mathbf{P} \\ \mathbf{Q} \end{Bmatrix}}_{\hat{\boldsymbol{\sigma}}} = \underbrace{\begin{bmatrix} \mathbf{A} & \mathbf{B} & \mathbf{E} & \mathbf{0} \\ \mathbf{B} & \mathbf{D} & \mathbf{F} & \mathbf{0} \\ \mathbf{E} & \mathbf{F} & \mathbf{H} & \mathbf{0} \\ \mathbf{0} & \mathbf{0} & \mathbf{0} & \mathbf{D}^S \end{bmatrix}}_{\hat{\mathbf{D}}} \underbrace{\begin{Bmatrix} \boldsymbol{\varepsilon}_m \\ \boldsymbol{\kappa}_1 \\ \boldsymbol{\kappa}_2 \\ \boldsymbol{\beta} \end{Bmatrix}}_{\hat{\boldsymbol{\varepsilon}}} - \underbrace{\begin{Bmatrix} \mathbf{N}^{th} \\ \mathbf{M}^{th} \\ \mathbf{P}^{th} \\ 0 \end{Bmatrix}}_{\hat{\boldsymbol{\sigma}}_{th}} \tag{2.43}$$

in which

$$\begin{gathered} A_{ij}, B_{ij}, D_{ij}, E_{ij}, F_{ij}, H_{ij} = \int_{-h/2}^{h/2} (1, z, z^2, f(z), zf(z), f^2(z)) C_{ij} \mathrm{d}z \\ D_{ij}^s = \int_{-h/2}^{h/2} \left[f'(z) \right]^2 G_{ij} \mathrm{d}z \end{gathered} \tag{2.44}$$

and the thermal stress resultants are expressed as:

$$\left\{\mathbf{N}^{th} \quad \mathbf{M}^{th} \quad \mathbf{P}^{th}\right\} = \int_{-h/2}^{h/2} \mathbf{C} \begin{Bmatrix} \alpha_e \\ \alpha_e \\ 0 \end{Bmatrix} \{1 \quad z \quad f(z)\} \Delta T \mathrm{d}z \tag{2.45}$$

The generalized strain vector $\hat{\boldsymbol{\varepsilon}}$ in Eq. (2.43) is divided into the linear and nonlinear strain components, respectively as:

$$\hat{\boldsymbol{\varepsilon}} = \begin{Bmatrix} \boldsymbol{\varepsilon}_L \\ \boldsymbol{\kappa}_1 \\ \boldsymbol{\kappa}_2 \\ \boldsymbol{\beta} \end{Bmatrix} + \begin{Bmatrix} \boldsymbol{\varepsilon}_{NL} \\ \mathbf{0} \\ \mathbf{0} \\ \mathbf{0} \end{Bmatrix} = \hat{\boldsymbol{\varepsilon}}_L + \hat{\boldsymbol{\varepsilon}}_{NL} \tag{2.46}$$

2.5 Variational equation of equilibrium

The governing equations of the plate structure are derived from the principle of virtual displacement as:

$$\int_0^t \left(\delta U + \delta V - \delta K\right) \mathrm{d}t = 0 \tag{2.47}$$

where the virtual strain energy δU is defined as:

$$\delta U = \int_V \delta \hat{\boldsymbol{\varepsilon}}^T \hat{\boldsymbol{\sigma}} \mathrm{d}V \tag{2.48}$$

Before proceeding with the discretization of the virtual strain energy in Eq. (2.48), it is necessary to consider further the variation of strain $\delta \hat{\boldsymbol{\varepsilon}}$ due to the virtual displacements as the sum of the variation of the linear and nonlinear generalized strains as:

$$\delta \hat{\boldsymbol{\varepsilon}} = \delta \hat{\boldsymbol{\varepsilon}}_L + \delta \hat{\boldsymbol{\varepsilon}}_{NL} \tag{2.49}$$

where the variation of the nonlinear component of the in-plane strain is obtained from Eq. (2.34) as:

$$\delta \boldsymbol{\varepsilon}_{NL} = \mathbf{A}_\theta \delta \boldsymbol{\theta} \tag{2.50}$$

Substituting the stress and strain in Eq.(2.43) and (2.49), the virtual strain energy is rewritten as:

$$\delta U = \int_{\Omega} \delta\hat{\boldsymbol{\varepsilon}}^{T}\hat{\mathbf{D}}\hat{\boldsymbol{\varepsilon}} - \delta\hat{\boldsymbol{\varepsilon}}^{T}\hat{\boldsymbol{\sigma}}_{th}\mathrm{d}\Omega \tag{2.51}$$

The virtual work done by external forces

$$\delta V = -\int_{\Omega} \delta\mathbf{u}^{T}\bar{\mathbf{f}}\mathrm{d}\Omega - \int_{\Gamma} \delta\mathbf{u}^{T}\bar{\mathbf{t}}\mathrm{d}\Gamma \tag{2.52}$$

where $\bar{\mathbf{f}}$ represents the external load and $\bar{\mathbf{t}}$ is the prescribed traction on the natural boundaries.

And the virtual kinetic energy is:

$$\delta K = \int_{V} \delta\dot{\mathbf{u}}^{T}\rho_{e}\dot{\mathbf{u}}\mathrm{d}V \tag{2.53}$$

where ρ_e is the effective density of the FGM, and a dotted variable indicates its time derivative. Integrating Eq. (2.53) by part with respect to time, we obtain a new form of the virtual kinetic energy [167]:

$$\int_{0}^{t} \delta K\mathrm{d}t = -\int_{0}^{t}\left(\int_{V} \delta\ddot{\mathbf{u}}^{T}\rho\mathbf{u}\mathrm{d}V\right)\mathrm{d}t \tag{2.54}$$

Substituting by the displacement field in Eq. (2.28), the virtual kinetic energy can be reformed as:

$$\delta K = -\int_{\Omega} \delta\ddot{\tilde{\mathbf{u}}}^{T}\mathbf{m}\tilde{\mathbf{u}}\mathrm{d}\Omega \tag{2.55}$$

where $\tilde{\mathbf{u}} = \left\{\mathbf{u}_1 \;\; \mathbf{u}_2 \;\; \mathbf{u}_3\right\}^{T}$ and the mass matrix $\mathbf{m}$ is calculated according to consistent form as follows:

$$\mathbf{m} = \begin{bmatrix} I_1 & I_2 & I_4 \\ I_2 & I_3 & I_5 \\ I_4 & I_5 & I_6 \end{bmatrix} \text{ with } I_i = \int_{-h/2}^{h/2} \rho_e\left(1, z, z^2, f(z), zf(z), \left(f(z)\right)^2\right)\mathrm{d}z \tag{2.56}$$

Substituting Eqs. (2.51), (2.52) and (2.55) into Eq. (2.47), the governing equation is written as:

$$\int_{\Omega} \delta\ddot{\tilde{\mathbf{u}}}^{T}\mathbf{m}\tilde{\mathbf{u}}\mathrm{d}\Omega + \int_{\Omega} \delta\hat{\boldsymbol{\varepsilon}}^{T}\hat{\mathbf{D}}\hat{\boldsymbol{\varepsilon}}\mathrm{d}\Omega - \int_{\Omega} \delta\hat{\boldsymbol{\varepsilon}}^{T}\hat{\boldsymbol{\sigma}}_{th}\mathrm{d}\Omega - \int_{\Omega} \delta\mathbf{u}^{T}\bar{\mathbf{f}}\mathrm{d}\Omega - \int_{\Gamma} \delta\mathbf{u}^{T}\bar{\mathbf{t}}\mathrm{d}\Gamma = 0 \tag{2.57}$$

Chapter 3 Isogeometric Analysis for Plate Structures Based on Higher-Order Shear Deformation Theory

3.1 Briefly introduction of finite element method

The Finite Element Method (FEM) developed in the 1950s to 1960s, has been known as the most powerful and popular tool for numerical simulations in various engineering fields. In FEM, the domain is firstly discretized into a number of simple subdomains, called finite elements. These elements are connected by nodes, Then, over each element the unknown fields are approximated by a linear combination between unknown variables at the nodes, called degree of freedoms (DOFs) and the shape functions, commonly known as the Lagrange interpolation functions.

3.1.1 Lagrange interpolation functions

The classical univariate Lagrange interpolation functions are given by [168]:

$$L_i^p\left(\xi\right)=\prod_{j=1,\,j\neq i}^{p+1}\frac{\xi-\xi_j}{\xi_i-\xi_j} \tag{3.1}$$

where $i = 1\ldots p+1$ and p is the polynomial order. Figure 3.1 illustrates a set of quadratic Lagrange interpolation functions on a two-element parametric space, in which element boundary corresponds to value $\xi = 0.5$. It can be seen that the basis functions constitutive a partition of unity, i.e. $\sum L_i^p\left(\xi\right)=1$ and satisfy the Kronecker delta property, i.e. $L_i^p(\xi_j)=\delta_{ij}$. It helps the basis functions to be interpolatory at the nodes. Furthermore, they achieve C^0 continuity at the inter-element boundary. Thus, for the PDE having higher-order derivative of the unknown fields, e.g. the defection in Euler-Bernoulli beam theory, classical plate theory or higher-order plate theory as derived in Eq. (2.57), the Lagrange higher-order basis functions are not admissible in the finite element approximation. For these problems, such other polynomial functions known as the Hermit interpolation functions were proposed to satisfy the C^1 continuity requirement.

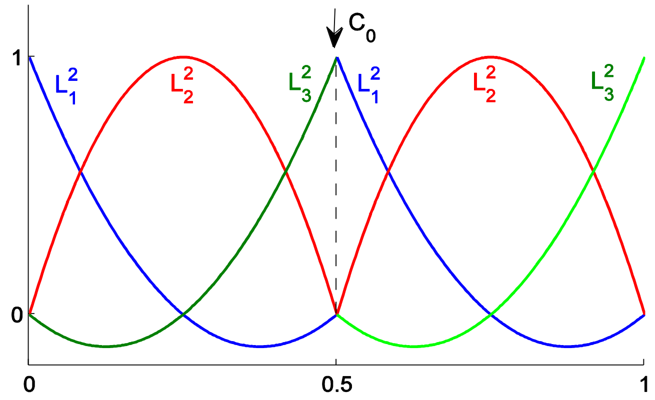

Figure 3.1 Quadratic Lagrange interpolation functions on a two-element parametric space.

3.1.2 Hermit interpolation functions

For a line element with two nodes, a set of Hermit interpolation functions is introduced as [169]:

$$\begin{aligned} H^3_{11}(\xi) &= 1-3\xi^2+2\xi^3 \qquad & H^3_{12}(\xi) &= 3\xi^2-2\xi^3 \\ H^3_{01}(\xi) &= \xi-2\xi^2+\xi^3 \qquad & H^3_{02}(\xi) &= -\xi^2+\xi^3 \end{aligned} \tag{3.2}$$

It is noted that these functions are cubic polynomial (p=3) and are separated into groups, i.e. H^3_{11}, H^3_{12} and H^3_{01}, H^3_{02}, for approximating deflection and its derivative (slope), respectively.

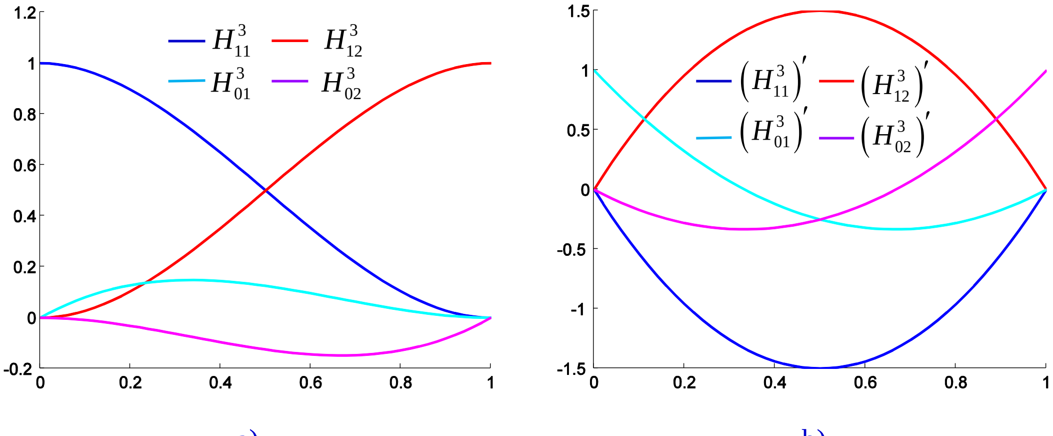

a) b)

Figure 3.2 a) Hermite cubic functions and b) their first derivative.

Figure 3.2 plots the set of Hermite cubic functions and their derivative. For a plate, a two-dimensional structure, there is a complexity in approximation. The in-plane displacement (u_0, v_0) and rotations (β_x, β_y) are approximated by the Lagrange basis functions while transverse displacement w_0 must be approximate using the Hermite interpolation functions [29]. Furthermore, it typically requires extra three unknown variables including derivatives of deflection, $w_{0,x}$, $w_{0,y}$, $w_{0,xy}$ at each node and a set of shape functions produced by tensor product, $\mathbf{H}_i$ = $[H_{1i}^3(\xi)H_{1i}^3(\eta),\ H_{0i}^3(\xi)H_{1i}^3(\eta),\ H_{1i}^3(\xi)H_{0i}^3(\eta),\ H_{0i}^3(\xi)H_{0i}^3(\eta)]$ corresponds to the variables of [w_0, $w_{0,x}$, $w_{0,y}$, $w_{0,xy}$], in which i = 1÷2.

3.2 Isogeometric analysis framework

In this section, a brief discussion about B-spline and NURBS basis functions implemented in IGA is given. Firstly, we present the basic concepts in their construction. Secondly, the most of the algorithms used to implement B-spline and NURBS are particularly summarized [94, 170].

3.2.1 B–splines basis functions

A B-splines basis of degree p is generated from a non-decreasing sequence of parameter value ξ_i, $i = 1,...m + p$, called a knot vector $\boldsymbol{\Xi} = \{\xi_1, \xi_2, ..., \xi_{m+p+1}\}$, in which $\xi_1 \le \xi_2 \le ... \le \xi_{m+p+1}$. $\xi_i \in \mathbb{R}^+$ is the i^{th} knot and m is number of the basis functions. If the knots are equally spaced in the parameter space, knot vector may be uniform and non–uniform in otherwise. In the so-called open knot, the first and the last knots are repeated by p+1times and very often get values of $\xi_1 = 0$ and $\xi_{m+p+1} = 1$. Furthermore, knot vector is divided into m-p of inner knot spans, some of which may possibly have zero length if a knot value appears more than once, the so-called a multiple knot. The B-splines basis function is C^{∞} continuous inside a knot span and C^{p-k} continuous at a knot repeated k times. As a result, it achieves C^{p-1} continuity at a single knot and C^{-1} one at the first and the last knots.

Using Cox-de Boor algorithm, the univariate B-spline basis functions $N_{i,p}(\xi)$ are defined recursively on the corresponding knot vector start with order p = 0

$$N_i^0(\xi) = \begin{cases} 1 & \text{if } \xi_i \le \xi < \xi_{i+1} \\ 0 & \text{otherwise} \end{cases} \tag{3.3}$$

as $p \ge 1$the basis functions are obtained from:

$$N_i^p(\xi)=\frac{\xi-\xi_i}{\xi_{i+p}-\xi_i}N_i^{p-1}(\xi)+\frac{\xi_{i+p+1}-\xi}{\xi_{i+p+1}-\xi_{i+1}}N_{i+1}^{p-1}(\xi) \tag{3.4}$$

Note that when evaluating these functions, ratio in the form 0/0 is assumed to be zero. An example of univariate quadratic B-spline basis functions based on an open knot vector $\Xi=\left\{0,0,0,\frac{1}{5},\frac{2}{5},\frac{3}{5},\frac{3}{5},\frac{4}{5},1,1,1\right\}$ is illustrated in Figure 3.3. The important properties of B-Spline functions are summarized as follows:

- Being piecewise polynomial functions.
- Non-negative over the domain $N_i^p(\xi)\geq 0$, $\forall \xi,\ i,\ p$
- Constitute a partition of unity $\sum N_i^p(\xi)=1$
- Linear independence, i.e., $\sum \alpha_i N_i^p(\xi)=0 \quad \Leftrightarrow \quad \alpha_i=0$
- Having local support over p+1 knot spans , i.e., $N_i^p(\xi)$ is non-zero with $\xi\in\left[\xi_i,\ \xi_{i+p+1}\right]$
- $C^{p\text{-}k}$ continuity at the interior knot having *k* repeats.
- Do not satisfy the Kronecker delta property, i.e., $N_i^p(\xi_j)\neq\delta_{ij}$ except the special case, as ξ_j repeated *p* time then $N_i^p(\xi_i)=1$.

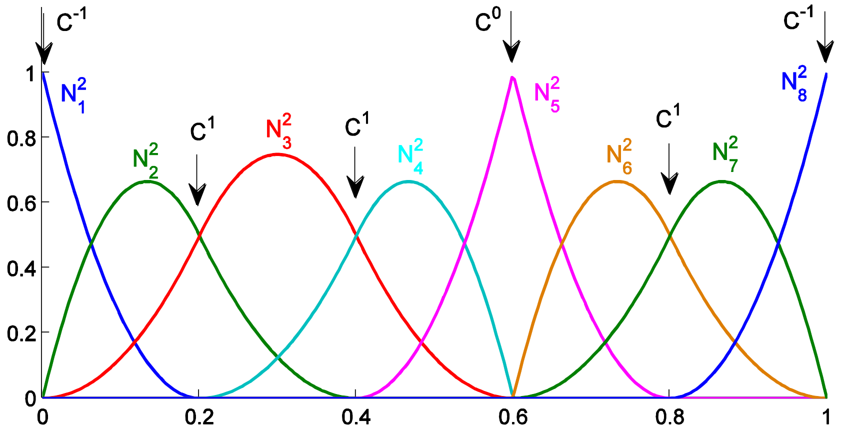

Figure 3.3 Univariate quadratic B-splines basic functions.

By a simple way, the so-called tensor product of univariate B-splines, the multivariate B-spline basis functions are generated as:

$$N_{\mathbf{i}}^{\mathbf{p}}(\boldsymbol{\xi}) = \prod_{\alpha=1}^{d} N_{i_\alpha}^{p_\alpha}(\xi^\alpha) \tag{3.5}$$

where parametric $d = 1, 2, 3$ represents 1D, 2D and 3D spaces, respectively. Figure 3.4 gives an illustration of bivariate B-splines basic based on tensor product of two knot vectors $\boldsymbol{\Xi} = \left\{0, 0, 0, \tfrac{1}{5}, \tfrac{2}{5}, \tfrac{3}{5}, \tfrac{3}{5}, \tfrac{4}{5}, 1, 1, 1\right\}$ and $\mathbf{H} = \left\{0, 0, 0, 0, \tfrac{1}{3}, \tfrac{1}{3}, \tfrac{2}{3}, \tfrac{2}{3}, 1, 1, 1, 1\right\}$ in two parametric dimensions ξ and η, respectively.

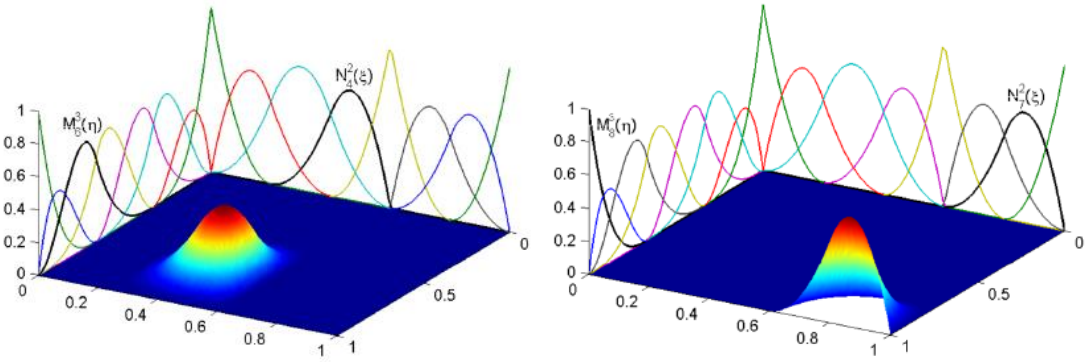

a) $N_{4,6}^{2,3}(\xi,\eta)$ b) $N_{7,8}^{2,3}(\xi,\eta)$

Figure 3.4 Bivariate B-splines basic functions.

After defining the B-spline basis functions, a domain including B-spline curve, surface or solid depending on value of parameter *d*, can be then constructed from a linear combination of them and the control points $\mathbf{P}_i$:

$$\mathbf{S}(\boldsymbol{\xi}) = \sum_{\mathbf{i}} N_{\mathbf{i}}^{\mathbf{p}}(\boldsymbol{\xi})\mathbf{P}_{\mathbf{i}} \tag{3.6}$$

3.2.2 Non-Uniform Rational B-Spline (NURBS)

B-splines are convenient for modelling the geometries with curved boundaries. However, for some simple conic shapes (e.g., circles, ellipses, spheres, etc.), we gain the ability that geometry cannot be exactly represented just by the polynomial functions. Thus, NURBS are introduced here as a generalization of B-spline in the form of rational functions, i.e.

$$R_{\mathbf{i}}^{\mathbf{p}}(\boldsymbol{\xi}) = \frac{N_{\mathbf{i}}^{\mathbf{p}}(\boldsymbol{\xi})\zeta_{\mathbf{i}}}{\sum_{\mathbf{j}} N_{\mathbf{j}}^{\mathbf{p}}(\boldsymbol{\xi})\zeta_{\mathbf{j}}} \tag{3.7}$$

where $\zeta_{\mathrm{i}} > 0$ is the so-called an individual weight corresponding to B-splines basis functions $N_{\mathrm{i}}^{\mathrm{p}}(\xi)$. The weight values can be analytically defined for simple geometries [170] or obtained from CAD software such as Rhino [171]. Figure 3.5 illustrates an examples of quadratic basis function with p = 2 corresponding to knot vector $\boldsymbol{\Xi} = \{0, 0, 0, 0.5, 1, 1, 1\}$. It is seen that the parametric domain is subdivided into two equal elements according to knot spans $[0, 0.5]$ and $[0.5, 1]$, where three non-zero functions are defined. A set of NURBS basis shapes is strongly depended on a weight vector. NURBS basis functions also inherit all the key features of their B-splines progenitors, namely, point wise non-negativity, partition of unity, continuous degree at the knot points and local support over p +1 knot spans. For the special case, in which all weights are unity, the NURBS basis reduces to the B-spline one as shown in Figure 3.5b. In a similar fashion to B-spline curve, the NURBS curved is defined according to Eq. (3.6) by replacing B-spline by NURBS.

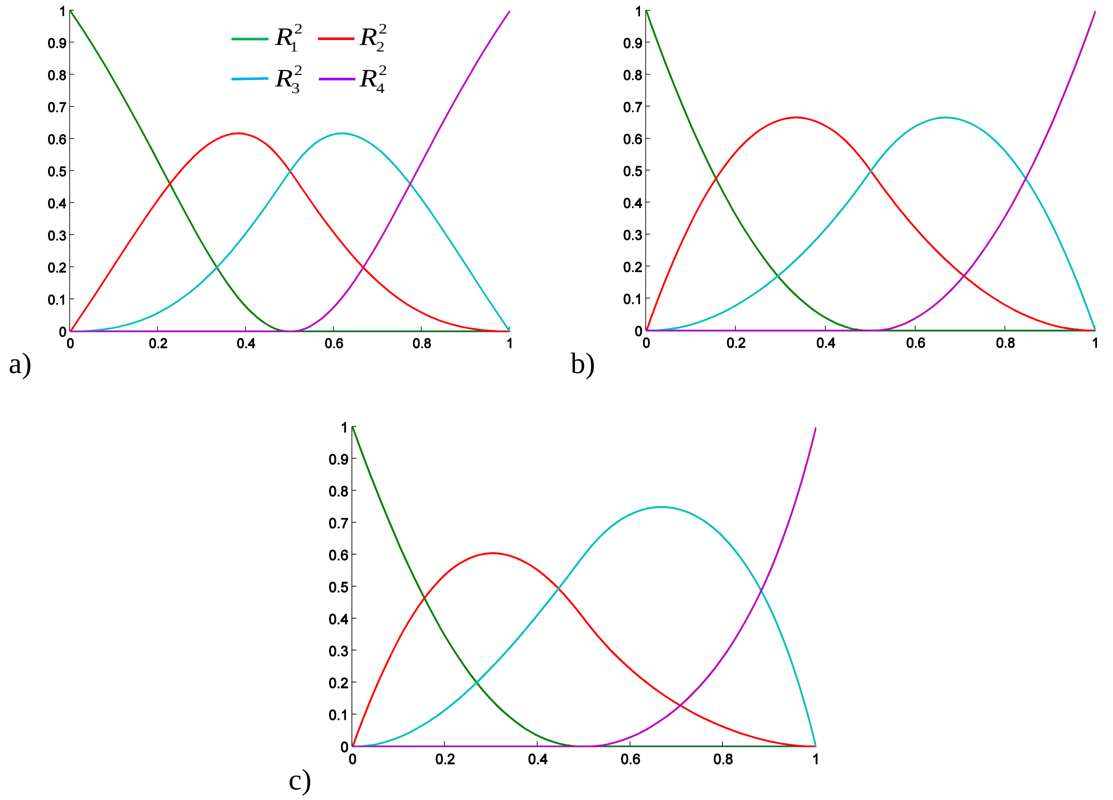

a)

b)

c)

Figure 3.5 NURBS basic functions with assigned weigth vector: a) $\zeta = \{1, 0.5, 0.5, 1\}$, *b)* $\zeta = \{1, 1, 1, 1\}$, *c)* $\zeta = \{1, 1, 1.5, 1\}$.

An example of construction for a half circle having unit radius is illustrated in Figure 3.6. For this problem, we use linear combination between three sets of quadratic NURBS basis shown in Figure 3.5 and four control points in red colour with their coordinate as shown in Figure 3.6. The red curve indicates the B-spline curve (all weights are unity) which is unable to reproduce the circle exactly, while the exact geometry is achieved by NURBS with $\zeta_1 = \zeta_4 = 1; \zeta_2 = \zeta_3 = 0.5$. As the weight at the control point $\mathbf{P}_3$ decreases the curve is pushed far away from point $\mathbf{P}_3$. In Figure 3.7, by using a set of the Lagrange interpolation functions in Figure 3.1, a half circle is approximated with two element (in blue cure) and five nodes (blue square). Because Lagrange basis functions are polynomial, they cannot describe exactly the conic geometries, e.g. a circle [95]. At the centre of arc, there is no continuity of slope at this point due to C^0 continuity at the inter-element boundary.

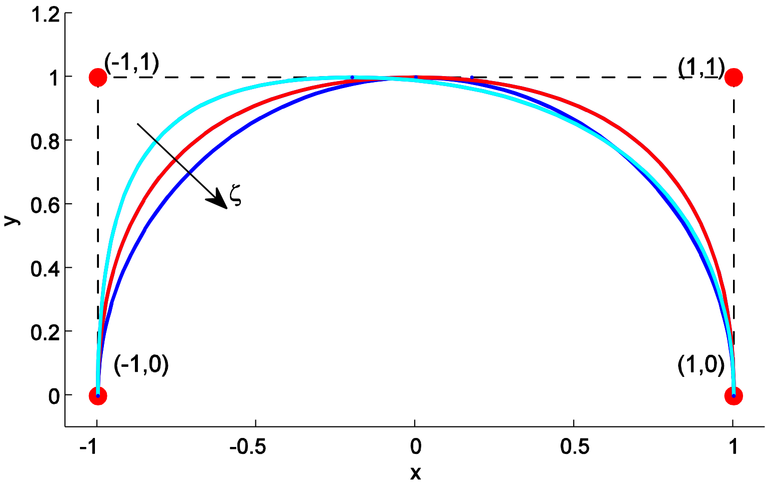

Figure 3.6 Model of a half circle by NURBS. The blue curve – the exact geometry, the red one – the B-spline curve and the cyan one are produced from linear combination between four control points (in red circle) and sets of NURBS basic functions from Figure 3.5a, b and c, respectively.

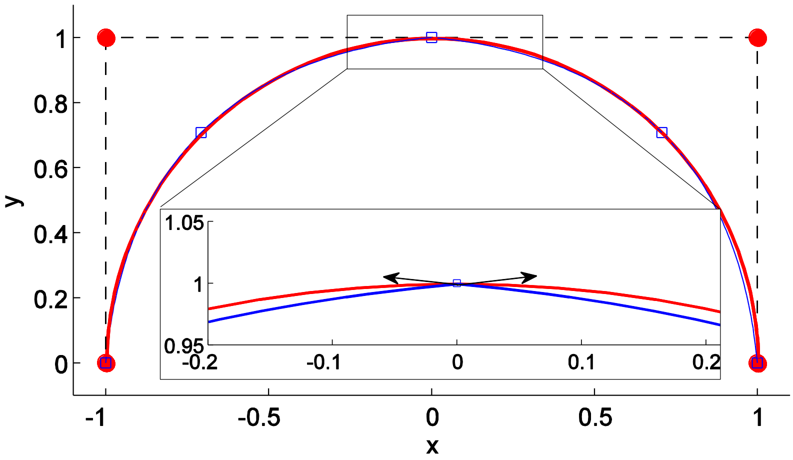

Figure 3.7 Model of a half circle with two elements by quadratic NURBS basis (in red curve) and Lagrange quadratic function (in blue curve).

3.2.3 Refinement technique

In computational analysis, numerical methods usually use refinement technique to reach the desired results. Besides two common refinement techniques in FEM based on control over the element size and the order of the basis, namely *h*- and *p*- refinement, IGA supports *k*-refinement, which is an interesting feature to control the continuity of the basis functions. Herein, we briefly introduce the three refinement algorithms. For more details, readers can find in the textbook [94].

h-refinement is called knot insertion, in which knots can be inserted without changing a domain geometrically and parametrically. As a result, the domain is divided into more elements with smaller size. Let us consider the example shown in Figure 3.8 to illustrate this technique. The knot vector of the original curve is $\Xi=\{0, 0, 0, 1, 1, 1\}$. Then, a knot is inserted at $\bar{\xi}=0.5$. The new curve is geometrically and parametrically identical to the original curve with one more control point, one more element, and one more basis function as well.

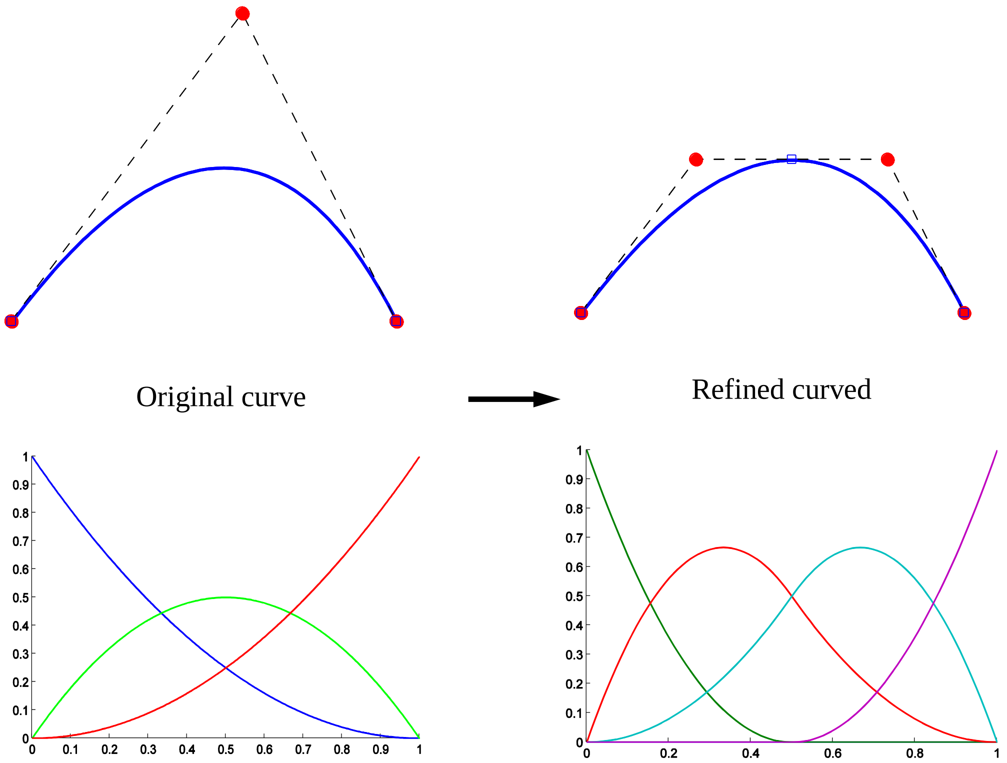

Figure 3.8 Knot insertion on a quadratic curve: upper is geometry while lower is the set of basis fucntions. The curve is subdivided into two elements without changing geometry. Control points are denoted by filled red circles, while element nodes are denoted by blue square.

p-refinement, called order elevation (or degree elevation), makes an increment of the order of the basis functions. During this process, the multiplicity of the knots is increased by one, and no new knot values are added. As a result, the size of knot vector is larger, but no new element is created. Let us consider an example of order elevation. From the initial curve shown in Figure 3.8a, we raise the order to cubic and quartic as shown in Figure 3.9 and the size of knot vector is increased accordingly to $\Xi = \{0, 0, 0, 0, 1, 1, 1, 1\}$ and $\Xi = \{0, 0, 0, 0, 0, 1, 1, 1, 1, 1\}$, respectively. The new curve is still described exactly with more control points, as well as, the basis functions and is geometrically and parametrically identical to the original one. A feature of p–refinement is that it raises the order and keeps the continuity of the basis constant. A major difference as compared with common C^0 continuity p–refinement in FEM is that order elevation in IGA helps the current basis functions to achieve $C^{p\text{-}k}$ continuity depending on the continuities of initial basis functions.

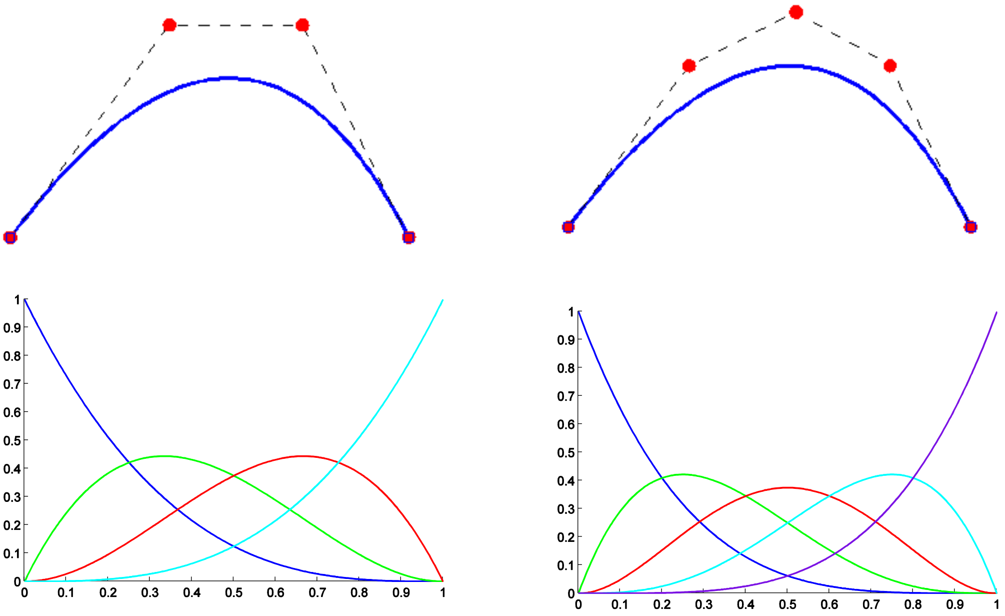

a) Cubic functions

b) Quartic functionsp

Figure 3.9 Order elevation. The number of the control points and the basis function as well are increased, whilst the geometry and the number of elements are kept identically to the original ones.

k–refinement refers to the process, in which the order elevation is followed by knot insertion which results in a higher-order and higher continuity of the basis functions. In this approach as shown in Figure 3.10, the order elevation is performed firstly on the coarsest discretization. Then, subsequent knot insertion will be implemented to make sure that $C^{p\text{-}1}$ continuity is achieved across the newly created element boundaries. Through these examples, we can propose the relation between the number of control points (n_{cp}) and the number of elements (n_{el}) in IGA description as follows:

$$\begin{aligned} n_{el} &= \text{unique(knot vector)} - (p+1) \\ n_{cp} &= (n_{el} - 1) \times (p - k) + (p+1) \end{aligned} \tag{3.8}$$

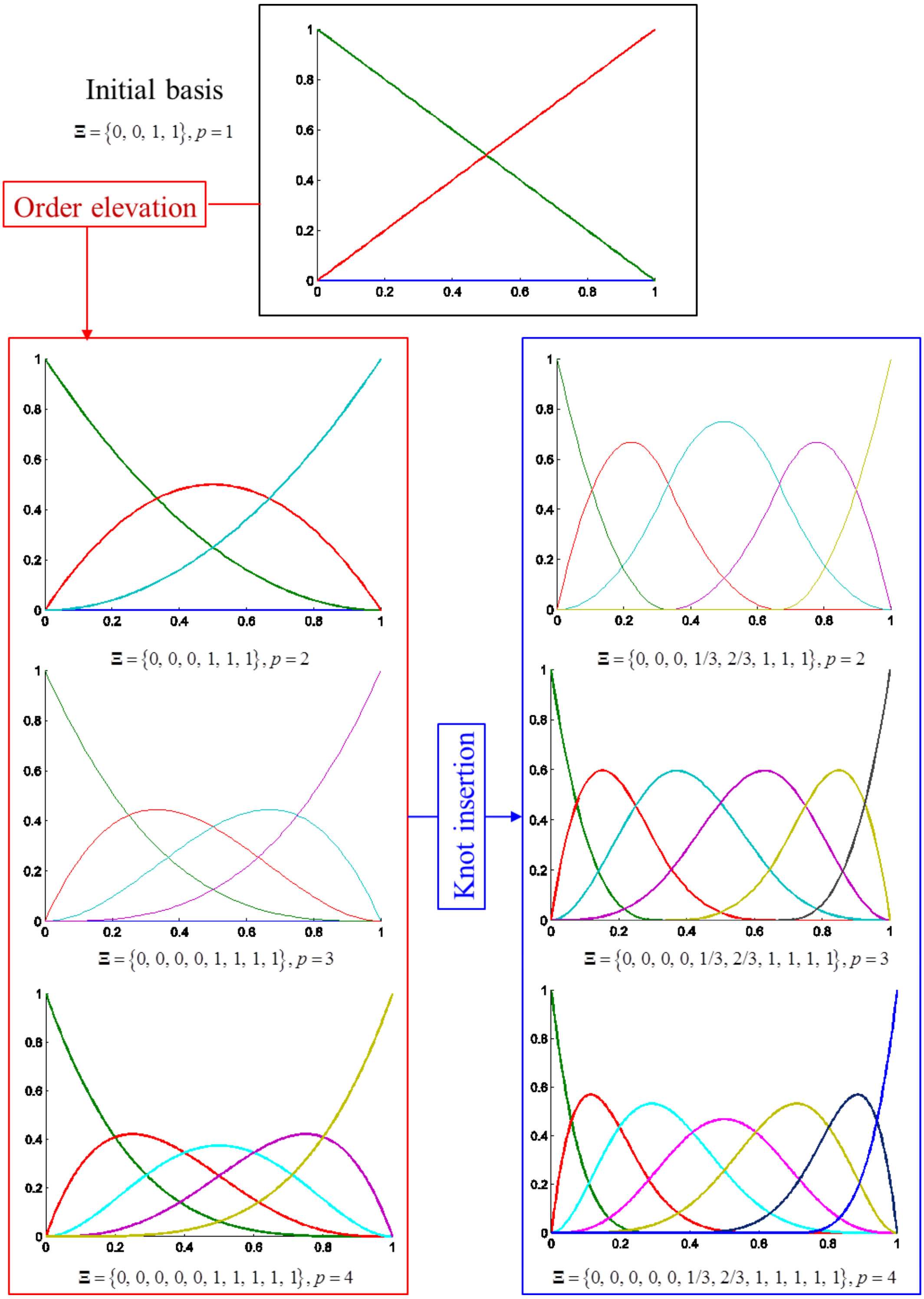

Figure 3.10 k-refinement approach.

Application of refinement technique in 2D [172]: In this thesis, we focus on the study of plate structures, which are constructed in two-dimensional space. Thus, we try to illustrate an application of NURBS with the three refinement techniques for 2D geometry, e.g., a circular plate as revealed in Figure 3.11. To exactly describe this geometry, the coarsest mesh with one quadratic element constructed from a linear combination as Eq. (3.6) between the tensor product of two knot vectors $\mathbf{\Xi} = \{0,0,0,1,1,1\}$ and $\mathbf{H} = \{0,0,0,1,1,1\}$ and nine control points, which coordinates are given in Table 3.1.

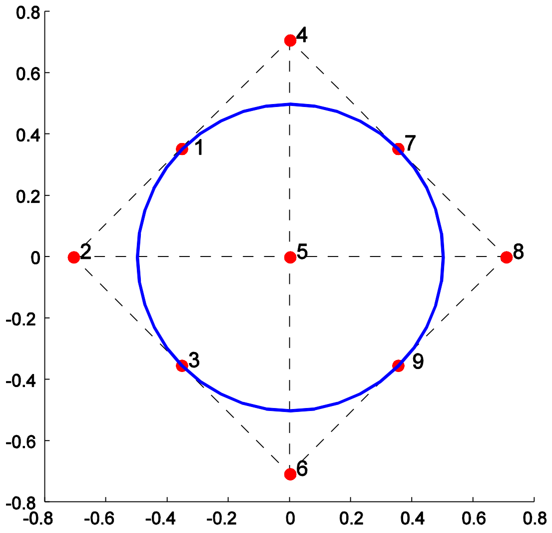

Figure 3.11 Circular geometry is described in the coarsest mesh with 9 control points denoted in red circular marker.

Table 3.1 The coordinates and the weights of control points of a circular plate with radius R = 0.5.

P_i	1	2	3	4	5	6	7	8	9
x_i	$-\sqrt{2}/4$	$-\sqrt{2}/2$	$-\sqrt{2}/4$	0	0	0	$\sqrt{2}/4$	$\sqrt{2}/2$	$\sqrt{2}/4$
y_i	$\sqrt{2}/4$	0	$-\sqrt{2}/4$	$\sqrt{2}/2$	0	$-\sqrt{2}/2$	$\sqrt{2}/4$	0	$-\sqrt{2}/4$
ζ_i	1	$\sqrt{2}/2$	1	$\sqrt{2}/2$	1	$\sqrt{2}/2$	1	$\sqrt{2}/2$	1

Figure 3.12, Figure 3.13 and Figure 3.14 illustrate sequentially three types of refinement schemes in IGA as *h*-,*p*-,*k*- refinement for description of the circular geometry. By inserting the knot value in the range of (0, 1), the length of knot vectors increases and the number of NURBS elements increases accordingly. As it can be seen in Figure 3.12, we can insert different knots in the knot vectors in order to discretise the domain with different numbers of element in each direction. Let us consider a discretization of 2×2 elements as plotted in Figure 3.13, by multiplying every distinct knot one by one, the order of approximated function increases from p = 2 to p = 3, 4. The numbers of knots increases but the number of elements is still constant. For this example, each element

belongs to those knots lying inside element and also on its boundaries. And the C^0-continuity is kept on the element boundaries. Those points are the same as those of quadrilateral elements Q9, Q16, Q25 of Lagrange family in finite element method [173]. Another way, by just repeating the first and the last knots as shown in Figure 3.14, the basis increases the order p as well as its continuity to $C^{p\text{-}1}$. That is, the basis still has p-1 continuous derivatives at an inside knot. As it can be seen, in k-refinement, with the same number elements, it requires less control points than p-refinement. Thus, it is concluded that k-refinement is a potentially superior approach in higher precision than p-refinement [95]. One important issue is that the plate theories in this thesis require C^1-continuity in approximate formulations. Therefore, using k-refinement for NURBS basis with order $p \geq 2$ will naturally satisfy this requirement.

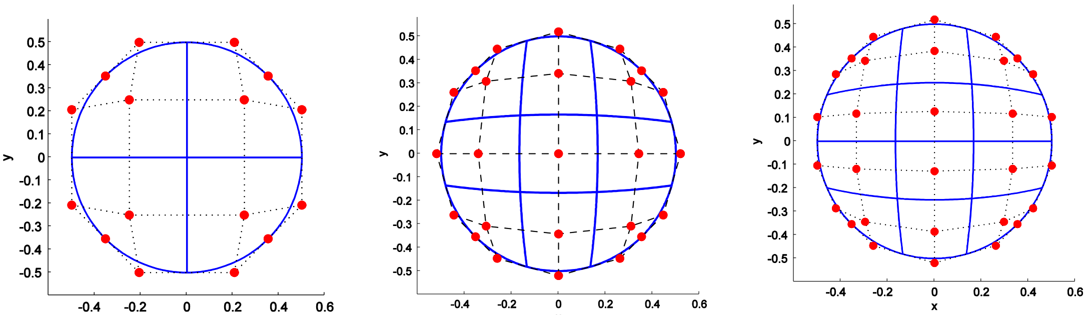

$\Xi, \mathbf{H} = \{0, 0, 0, 0.5, 1, 1, 1\}$

$\Xi, \mathbf{H} = \{0, 0, 0, \tfrac{1}{3}, \tfrac{2}{3}, 1, 1, 1\}$

$\Xi = \{0, 0, 0, \tfrac{1}{3}, \tfrac{2}{3}, 1, 1, 1\}$

$\mathbf{H} = \{0, 0, 0, \tfrac{1}{4}, \tfrac{1}{2}, \tfrac{3}{4}, 1, 1, 1\}$

Figure 3.12 Knot insertion in circle modeling.

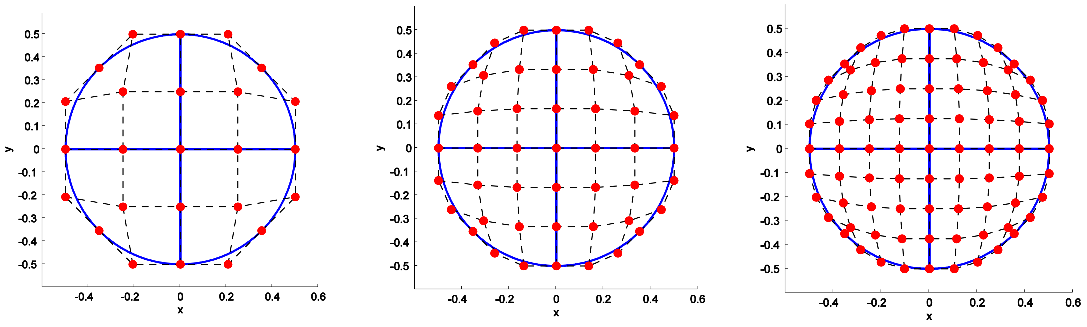

$\Xi, \mathbf{H} = \left\{\begin{matrix} 0, 0, 0, 0.5, ... \\ 0.5, 1, 1, 1 \end{matrix}\right\}$

$\Xi, \mathbf{H} = \left\{\begin{matrix} 0, 0, 0, 0, \tfrac{1}{3}, ... \\ \tfrac{1}{3}, \tfrac{2}{3}, \tfrac{2}{3}, 1, 1, 1, 1 \end{matrix}\right\}$

$\Xi, \mathbf{H} = \left\{\begin{matrix} 0, 0, 0, 0, 0, \tfrac{1}{3}, \tfrac{1}{3}, \tfrac{1}{3}, ... \\ \tfrac{2}{3}, \tfrac{2}{3}, \tfrac{2}{3}, 1, 1, 1, 1, 1 \end{matrix}\right\}$

Figure 3.13 Order elevation: the order of basis functions rises from p = 2 to p = 3, 4, respectively and also keeps the C^0 continuity on the element boundaries.

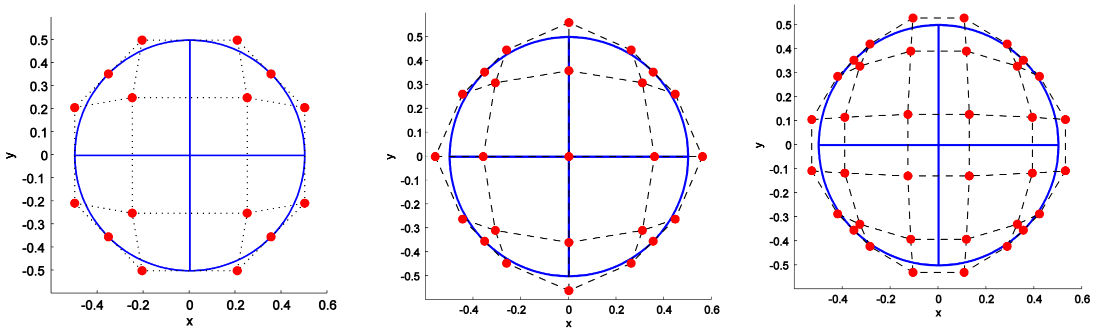

$\Xi,\mathbf{H}=\{0, 0, 0, 0.5, 1, 1, 1\}$ $\Xi,\mathbf{H}=\{0,0,0,0,\tfrac{1}{3},\tfrac{2}{3},1,1,1,1\}$ $\Xi,\mathbf{H}=\left\{\begin{matrix}0,0,0,0,0,\tfrac{1}{3},\ldots\\ \tfrac{2}{3},1,1,1,1,1\end{matrix}\right\}$

Figure 3.14 k-refinement: the basis functions increase and their order also achieves $C^{p\text{-}1}$ *continuity.*

3.2.4 Summary of IGA

The salient features of IGA can be summarized as follows:

- Geometry can be described exactly by a single patch or multi-patch. In which, a mesh of a NURBS patch is defined by the tensor product of knot vectors, for instant, $\Xi\times\mathbf{H}$, $\Xi\times\mathbf{H}\times\mathbf{Z}$ for two- and three-dimension, respectively.
- A linear combination between the control points and the basis functions defines the geometry.
- The unknown variables are the degrees of freedom (control variables) are located at the control points which are not necessary to stay on the actual geometry.
- There are three different mesh refinement strategies: *h*-refinement, *p*-refinement and *k*-refinement which increases both of smoothness and order of the basis functions.

3.3 Discrete system equations

Similar to the traditional finite element method, isogeometric analysis also invokes the isoparametric concept, in which the geometric description and finite analysis share the same basis functions. However, there is a major difference between FEM and IGA regarding the type of basis functions. In classical FEM, the basis functions chosen to approximate the unknown fields are also used to approximate the known geometry, whilst IGA employs the basis functions, which are capable to exactly describe the known geometry such as B-spline or NURBS as shown in Eq. (3.7), to construct finite approximation of the displacements:

$$\mathbf{u}^h(\boldsymbol{\xi}) = \sum_A R_A(\boldsymbol{\xi})\mathbf{q}_A \tag{3.9}$$

where $\mathbf{q}_A$ denotes the vector of nodal degrees of freedom associated with the control point $\mathbf{P}_A$, which has 5 degrees of freedom (DOFs) $\mathbf{q}_A = \left[u_{0A}\ v_{0A}\ \beta_{xA}\ \beta_{yA}\ \ w_{0A}\right]^T$ for TSDT and GSDT and 4 DOFs $\mathbf{q}_A = \left[u_{0A}\ v_{0A}\ \ w_{bA}\ \ w_{sA}\right]^T$ for RPT.

Substituting Eq. (3.9) into Eq. (2.46), the generalized strains can be rewritten in matrix form as:

$$\hat{\boldsymbol{\varepsilon}} = \left(\mathbf{B}^L + \frac{1}{2}\mathbf{B}^{NL}\right)\mathbf{q} \tag{3.10}$$

where

$$\mathbf{B}^L = \left[\left(\mathbf{B}^m\right)^T\ \left(\mathbf{B}^{b1}\right)^T\ \left(\mathbf{B}^{b2}\right)^T\ \left(\mathbf{B}^s\right)^T\right]^T \tag{3.11}$$

in which these strain matrices are defined differently depending on the approximated displacement field of each plate theory given in Section 2.3. The strain matrices **B** are defined as:

Third-order shear deformation theory [73]

$$\mathbf{B}_A^m = \begin{bmatrix} R_{A,x} & 0 & 0 & 0 & 0 \\ 0 & R_{A,y} & 0 & 0 & 0 \\ R_{A,y} & R_{A,x} & 0 & 0 & 0 \end{bmatrix}, \quad \mathbf{B}_A^{b1} = \begin{bmatrix} 0 & 0 & 0 & R_{A,x} & 0 \\ 0 & 0 & 0 & 0 & R_{A,y} \\ 0 & 0 & 0 & R_{A,y} & R_{A,x} \end{bmatrix},$$
$$\mathbf{B}_A^{b2} = -\frac{4}{3h^2}\begin{bmatrix} 0 & 0 & R_{A,xx} & R_{A,x} & 0 \\ 0 & 0 & R_{A,yy} & 0 & R_{A,y} \\ 0 & 0 & 2R_{A,xy} & R_{A,y} & R_{A,x} \end{bmatrix}, \quad \mathbf{B}_A^s = \begin{bmatrix} 0 & 0 & R_{A,x} & R_A & 0 \\ 0 & 0 & R_{A,y} & 0 & R_A \end{bmatrix} \tag{3.12}$$

Refined plate theory [136, 159]

$$\mathbf{B}_A^m = \begin{bmatrix} R_{A,x} & 0 & 0 & 0 \\ 0 & R_{A,y} & 0 & 0 \\ R_{A,y} & R_{A,x} & 0 & 0 \end{bmatrix}, \quad \mathbf{B}_A^{b1} = -\begin{bmatrix} 0 & 0 & R_{A,xx} & 0 \\ 0 & 0 & R_{A,yy} & 0 \\ 0 & 0 & 2R_{A,xy} & 0 \end{bmatrix}, \tag{3.13}$$

$$\mathbf{B}_A^{b2} = \begin{bmatrix} 0 & 0 & 0 & R_{A,xx} \\ 0 & 0 & 0 & R_{A,yy} \\ 0 & 0 & 0 & 2R_{A,xy} \end{bmatrix}, \qquad \mathbf{B}_A^{s} = \begin{bmatrix} 0 & 0 & 0 & R_{A,x} \\ 0 & 0 & 0 & R_{A,y} \end{bmatrix}$$

Generalized shear deformation theory [62]

$$\begin{gathered} \mathbf{B}_A^{m} = \begin{bmatrix} R_{A,x} & 0 & 0 & 0 & 0 \\ 0 & R_{A,y} & 0 & 0 & 0 \\ R_{A,y} & R_{A,x} & 0 & 0 & 0 \end{bmatrix}, \quad \mathbf{B}_A^{b1} = -\begin{bmatrix} 0 & 0 & R_{A,xx} & 0 & 0 \\ 0 & 0 & R_{A,yy} & 0 & 0 \\ 0 & 0 & 2R_{A,xy} & 0 & 0 \end{bmatrix}, \\ \mathbf{B}_A^{b2} = \begin{bmatrix} 0 & 0 & 0 & R_{A,x} & 0 \\ 0 & 0 & 0 & 0 & R_{A,y} \\ 0 & 0 & 0 & R_{A,y} & R_{A,x} \end{bmatrix}, \quad \mathbf{B}_A^{s} = \begin{bmatrix} 0 & 0 & 0 & R_A & 0 \\ 0 & 0 & 0 & 0 & R_A \end{bmatrix} \end{gathered} \tag{3.14}$$

Meanwhile, strain matrix $\mathbf{B}^{NL}$, derived from Eq. (2.34), is still dependent upon displacement gradient

$$\mathbf{B}_A^{NL}(\mathbf{q}) = \begin{bmatrix} \mathbf{A}_\theta \\ \mathbf{0} \end{bmatrix} \mathbf{B}_A^{g} \quad \text{where} \quad \mathbf{B}_A^{g} = \begin{bmatrix} 0 & 0 & R_{A,x} & 0 & 0 \\ 0 & 0 & R_{A,y} & 0 & 0 \end{bmatrix} \tag{3.15}$$

As observed from Eq. (3.12) to (3.14), the SCF is no longer required in the shear strain matrix, as well as, in the global stiffness matrix as shown latter in Eq. (3.18). Furthermore, the bending strain matrices contain the second-order derivative of the shape functions. Hence, it requires C^1-continuity element in approximate formulations. However, the enforcement of even C^1-continuity across inter-element boundaries in standard finite element method is not a trivial task. In an effort to address this difficulty, the Hermite interpolation function was added to satisfy specific approximation of transverse displacement. It may produce extra unknown variables including derivatives of deflection, which lead to an increase in the computational cost, i.e. a C^1-continuity four-node quadrilateral plate element with 10 DOFs/node [174], a conforming element with 8 DOFs or a non-conforming element with 7 DOFs [57, 175] requiring the Lagrange interpolation of u_0, v_0, β_x, β_y and the Hermit interpolation of w_0. It is now interesting to note that our present formulation based on IGA naturally satisfies C^1-continuity from the theoretical/mechanical viewpoint of FGM plates [73]. In our work, the basis functions are C^{p-1} continuous. Therefore, as $p \geq 2$ the present approach always satisfies C^1- continuity requirement in approximate formulations based on the proposed HSDT.

Variation of the generalized strain in Eq. (2.49) can be rewritten in matrix form as:

$$\delta\hat{\boldsymbol{\varepsilon}} = \left(\mathbf{B}^{L} + \mathbf{B}^{NL}\right)\delta\mathbf{q} \tag{3.16}$$

Substituting Eqs. (3.10) and (3.16) into Eq. (2.57), and eliminating the virtual displacement vector $\delta\mathbf{q}$, the equation of motion is written in the following matrix form:

$$\mathbf{K}\mathbf{q} + \mathbf{M}\ddot{\mathbf{q}} = \mathbf{F}^{ext} \tag{3.17}$$

where the global stiffness matrix **K** is expressed as:

$$\begin{aligned}\mathbf{K} &= \int_{\Omega}\left(\mathbf{B}^{L} + \mathbf{B}^{NL}\right)^{T}\hat{\mathbf{D}}\left(\mathbf{B}^{L} + 0.5\mathbf{B}^{NL}\right)\mathrm{d}\Omega - \int_{\Omega}\left(\mathbf{B}^{NL}\right)^{T}\hat{\boldsymbol{\sigma}}_{th}\mathrm{d}\Omega \\ &= \mathbf{K}_{L} + \mathbf{K}_{NL} - \mathbf{K}_{th}\end{aligned} \tag{3.18}$$

in which $\mathbf{K}_{L}$ and $\mathbf{K}_{NL}$ are the linear and non-linear stiffness matrices, respectively, whilst $\mathbf{K}_{th}$ is the initial stress stiffness matrix due to the in-plane compressions by temperature change:

$$\begin{aligned}\mathbf{K}_{L} &= \int_{\Omega}\left(\mathbf{B}^{L}\right)^{T}\hat{\mathbf{D}}\mathbf{B}^{L}\mathrm{d}\Omega \\ \mathbf{K}_{NL} &= \int_{\Omega}\frac{1}{2}\left(\mathbf{B}^{L}\right)^{T}\hat{\mathbf{D}}\mathbf{B}^{NL} + \left(\mathbf{B}^{NL}\right)^{T}\hat{\mathbf{D}}\mathbf{B}^{L} + \frac{1}{2}\left(\mathbf{B}^{NL}\right)^{T}\hat{\mathbf{D}}\mathbf{B}^{NL}\mathrm{d}\Omega\end{aligned} \tag{3.19}$$

$$\mathbf{K}_{th} = \int_{\Omega}\left(\mathbf{B}^{g}\right)^{T}\begin{bmatrix} N_{x}^{th} & N_{xy}^{th} \\ N_{xy}^{th} & N_{y}^{th}\end{bmatrix}\mathbf{B}^{g}\mathrm{d}\Omega \tag{3.20}$$

and **M** is the mass matrix:

$$\mathbf{M} = \int_{\Omega}\tilde{\mathbf{N}}^{T}\mathbf{m}\tilde{\mathbf{N}}\mathrm{d}\Omega \tag{3.21}$$

in which

$$\tilde{\mathbf{N}}_{A} = \begin{bmatrix}\mathbf{N}_{A}^{1} & \mathbf{N}_{A}^{2} & \mathbf{N}_{A}^{3}\end{bmatrix} \tag{3.22}$$

where the inside matrices are in size of 3×5 or 3×4 depending on TSDT, GSDT or four unknown variable RPT.

TSDT, GSDT: $$\mathbf{N}_{A}^{1} = \begin{bmatrix} R_{A} & 0 & 0 & 0 & 0 \\ 0 & R_{A} & 0 & 0 & 0 \\ 0 & 0 & R_{A} & 0 & 0\end{bmatrix}, \tag{3.23}$$

$$\mathbf{N}_A^2 = -\begin{bmatrix} 0 & 0 & R_{A,x} & 0 & 0 \\ 0 & 0 & R_{A,y} & 0 & 0 \\ 0 & 0 & 0 & 0 & 0 \end{bmatrix}, \quad \mathbf{N}_A^3 = \begin{bmatrix} 0 & 0 & 0 & R_A & 0 \\ 0 & 0 & 0 & 0 & R_A \\ 0 & 0 & 0 & 0 & 0 \end{bmatrix}$$

RPT:

$$\mathbf{N}_A^1 = \begin{bmatrix} R_A & 0 & 0 & 0 \\ 0 & 0 & -R_{A,x} & 0 \\ 0 & 0 & 0 & R_{A,x} \end{bmatrix},$$

$$\mathbf{N}_A^2 = \begin{bmatrix} 0 & R_A & 0 & 0 \\ 0 & 0 & -R_{A,y} & 0 \\ 0 & 0 & 0 & R_{A,y} \end{bmatrix}, \quad \mathbf{N}_A^3 = \begin{bmatrix} 0 & 0 & R_A & R_A \\ 0 & 0 & 0 & 0 \\ 0 & 0 & 0 & 0 \end{bmatrix} \tag{3.24}$$

The last term denotes the external force vector, which is the superimposition of the transverse mechanical load and thermal loading

$$\mathbf{F}_A^{ext} = \underbrace{\int_\Omega R_A \bar{\mathbf{f}} \mathrm{d}\Omega + \int_\Gamma R_A \bar{\mathbf{t}} \mathrm{d}\Gamma}_{\mathbf{F}_{me}} + \underbrace{\int_\Omega \left(\mathbf{B}_A^L\right)^T \hat{\boldsymbol{\sigma}}_0 \mathrm{d}\Omega}_{\mathbf{F}_{th}} \tag{3.25}$$

3.4 Numerical integration

In order to calculate the stiffness matrices, mass matrix and force vector in Eqs. (3.19), (3.21) and (3.25) in isogeometric finite element method, a numerical integration following to the Gauss-Legendre quadrature is employed. As it can be seen, these parameters are related to the shape functions and their first and second spatial derivatives in physical coordinate system denoted by $\mathbf{x}$. However, according to Section 3.2 the shape functions are constructed in natural coordinate system denoted by ξ. Thus, a transformation between the two coordinate systems should be established. We define the mapping $\mathbf{x} : \hat{\Omega} \to \Omega$ from the parameter space to the physical space as shown in Figure 3.15.

$$\mathbf{x} = \begin{Bmatrix} x(\xi) \\ y(\xi) \end{Bmatrix} = \sum_i R_i(\xi) \begin{Bmatrix} x_i \\ y_i \end{Bmatrix} \tag{3.26}$$

where (x_i, y_i) are the physical coordinate of the control points utilized defining the two dimensional geometry Ω.

The first spatial derivatives of the shape functions are computed as:

$$\begin{Bmatrix} R_{,x} \\ R_{,y} \end{Bmatrix} = \mathbf{J}^{-1} \begin{Bmatrix} R_{,\xi} \\ R_{,\eta} \end{Bmatrix} \tag{3.27}$$

where **J** is the Jacobian matrix

$$\mathbf{J} = \begin{bmatrix} x_{,\xi} & x_{,\eta} \\ y_{,\xi} & x_{,\eta} \end{bmatrix} \tag{3.28}$$

and their second derivatives are also computed as follows:

$$\begin{Bmatrix} R_{,xx} \\ R_{,yy} \\ R_{,xy} \end{Bmatrix} = \mathbf{J}_3^{-1} \left(\begin{Bmatrix} R_{,\xi\xi} \\ R_{,\eta\eta} \\ R_{,\xi\eta} \end{Bmatrix} - \mathbf{J}_2 \begin{Bmatrix} R_{,\xi} \\ R_{,\eta} \end{Bmatrix} \right) \tag{3.29}$$

where

$$\mathbf{J}_2 = \begin{bmatrix} x_{,\xi\xi} & y_{,\xi\xi} \\ x_{,\eta\eta} & y_{,\eta\eta} \\ x_{,\xi\eta} & y_{,\xi\eta} \end{bmatrix} \quad \text{and} \quad \mathbf{J}_3 = \begin{bmatrix} x_{,\xi}^2 & y_{,\xi}^2 & 2x_{,\xi}y_{,\xi} \\ x_{,\eta}^2 & y_{,\eta}^2 & 2x_{,\eta}y_{,\eta} \\ x_{,\xi}x_{,\eta} & y_{,\xi}y_{,\eta} & x_{,\xi}y_{,\eta} + x_{,\eta}y_{,\xi} \end{bmatrix} \tag{3.30}$$

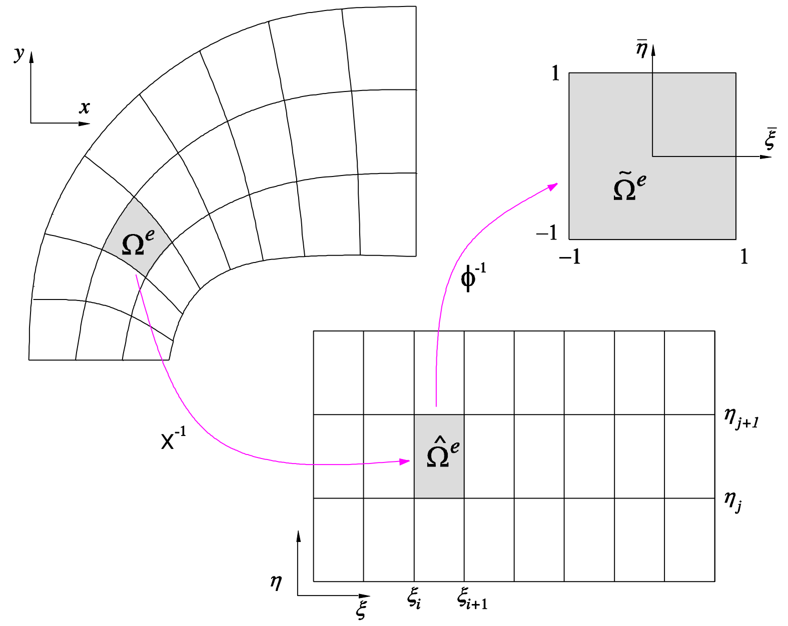

Figure 3.15 Numerical integration in isogeometric analysis.

The fact is that the numerical integration in IGA is the same as in FEM, which is performed by the Gauss-Legendre quadrature. However, there is a more complex implementation in IGA. Integral over the entire geometry (in physical system) is split into integrals over each physical element, Ω^e. The integral is pulled back to the parametric element $\hat{\Omega}^e$ via the geometry mapping $\mathbf{x}^{-1}$. Then, the integral over the parametric element are continued to pull back to the parent domain, $\tilde{\Omega}^e$, where existing integration rules are usually defined. The mapping $\boldsymbol{\phi} : \tilde{\Omega}^e \rightarrow \hat{\Omega}^e$ from the parent domain $[-1, 1]\times[-1, 1]$ to the parametric domain $[\xi_i, \xi_{i+1}]\times[\eta_i, \eta_{i+1}]$ is given by:

$$\xi = \frac{1}{2}\left[\left(\xi_{i+1} - \xi_i\right)\bar{\xi} + \left(\xi_{i+1} + \xi_i\right)\right] \tag{3.31}$$

$$\eta = \frac{1}{2}\left[\left(\eta_{j+1} - \eta_j\right)\bar{\eta} + \left(\eta_{j+1} + \eta_j\right)\right] \tag{3.32}$$

Therefore, the Jacobian of this transformation is defined as:

$$\left|\bar{\mathbf{J}}\right| = \frac{1}{4}\left(\xi_{i+1} - \xi_i\right)\left(\eta_{j+1} - \eta_j\right) \tag{3.33}$$

At the last domain, the integrals can be implemented following the Gauss-Legendre numerical integration as a sum of the value defined at sampling points, known as the Gaussian points. To illustrate this process, we try to integrate mathematically a function $f(x, y)$ over the entire physical domain Ω.

$$\begin{aligned} \int_{\Omega} f\left(x, y\right)\mathrm{d}\Omega &= \sum_{e=1}^{n}\int_{\Omega_e} f\left(x, y\right)\mathrm{d}\Omega_e \\ &= \sum_{e=1}^{n}\int_{\hat{\Omega}_e} f\left(x\left(\xi\right), y\left(\eta\right)\right)\left|\mathbf{J}\right|\mathrm{d}\hat{\Omega}_e \\ &= \sum_{e=1}^{n}\int_{\tilde{\Omega}_e} f\left(\xi, \eta\right)\left|\mathbf{J}\right|\left|\bar{\mathbf{J}}_e\right|\mathrm{d}\tilde{\Omega}_e \\ &= \sum_{e=1}^{n}\sum_{i}^{n_{GP}}\sum_{j}^{m_{GP}} f\left(\xi_i, \eta_j\right)\left|\mathbf{J}\right|\left|\bar{\mathbf{J}}_e\right| W_i W_j \end{aligned} \tag{3.34}$$

where (ξ_i, η_i) are the Gaussian points and W_i, W_j are the weighting coefficients, which are introduced in Table 3.2 following Ref. [52]. Specially, a number of (p +1) × (q +1) Gaussian points are adopted for two-dimensional element by using p^{th} and q^{th} orders NURBS.

Table 3.2 Gauss points and weights in the Gauss-Legendre numerical integration.

n_{GP}	Integration point ξ_i	Weight W_i
1	0.000000000000000	2.000000000000000
2	±0.577350269189625	1.000000000000000
3	0.000000000000000	0.888888888888888
	±0.774596669241483	0.555555555555555
4	±0.339981043584856	0.652145154862546
	±0.861136311594052	0.347854845137453
5	0.000000000000000	0.568888888888888
	±0.538469310105683	0.478628670499366
	±0.906179845938664	0.236926885056189
6	±0.238619186083196	0.467913934572691
	±0.661209386466264	0.360761573048138
	±0.932469514203152	0.171324492379170
7	0.000000000000000	0.417959183673469
	±0.405845151377397	0.381830050505118
	±0.741531185599394	0.279705391489276
	±0.949107912342758	0.129484966168869

3.5 Boundary conditions

In solid mechanics, boundary conditions can be divided into groups of homogeneous and inhomogeneous Direchlet boundary conditions (BCs). In this section, we address a general procedure to treat those boundary conditions in NURBS approximation.

3.5.1 Homogeneous boundary conditions

The homogeneous Dirichlet BCs can be enforced easily by setting the corresponding control point value as zero. For example, let us consider the simply support condition in Figure 3.16, the BCs are treated in the same way as the standard FEM by assigning their zero-values for all control points in cyan square around the boundary:

$$\begin{aligned} u_0 = w_0 = \beta_x = 0 \quad & \text{at lower and upper edges} \\ v_0 = w_0 = \beta_y = 0 \quad & \text{at left and right edges} \end{aligned} \tag{3.35}$$

For the clamped boundary as shown in Figure 3.17, the BCs are:

$$u = v = w = 0 \;\; \Rightarrow \begin{cases} u_0 = v_0 = w_0 = \beta_x = \beta_y = 0 \\ w_{0,n} = 0 \end{cases} \tag{3.36}$$

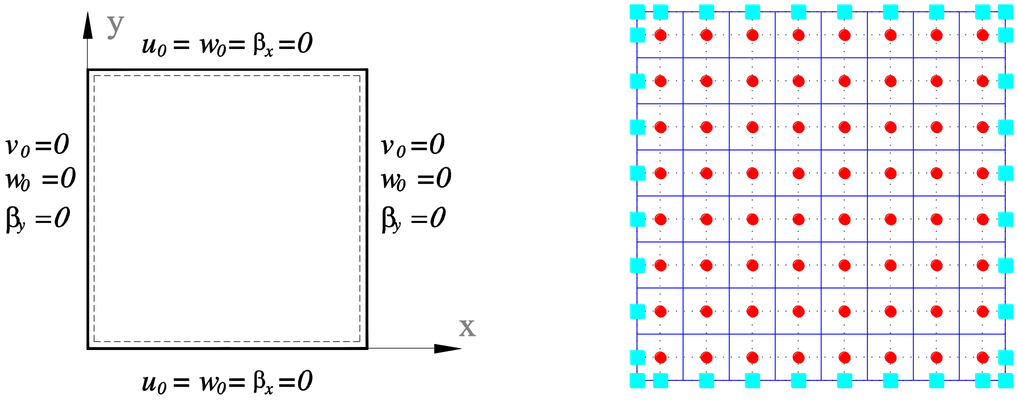

Figure 3.16 Simply support boundary condition: assign zero-displacements for those control points in cyan square around the boundary.

Herein, the Dirichlet boundary conditions on u_0, v_0, w_0 and β_x, β_y is easily treated as in the case of simply supported condition. However, for the derivatives $w_{0,n}$ the enforcement of BCs can be solved in a simple and effective way [176], such as rotation-free [93, 124]. The derivatives can be included in a compact form of the normal slope at the boundary:

$$\frac{\partial w_0}{\partial n} = \lim_{\Delta n \to 0} \frac{w_0(n(\mathbf{x}_C) + \Delta n) - w_0(n(\mathbf{x}_C))}{\Delta n} = 0 \tag{3.37}$$

As $w_0(n(\mathbf{x}_C)) = 0$ according to Eq. (3.36), Eq. (3.37) leads to impose the zero value on the deflection variable at control points $\mathbf{x}_\mathrm{A}$, which is adjacent to the boundary control points $\mathbf{x}_\mathrm{C}$. It can be observed that implementing the essential boundary condition using this method is very simple in IGA.

Symmetry boundary conditions are given by:

$$\begin{cases} u_0 = \beta_x = 0 \\ w_{,x} = 0 \end{cases} \quad \text{at} \quad x = 0 \tag{3.38}$$

Based on Eq. (3.37), the zero-rotation condition along the symmetry line is enforced by assigning equal deflection of two rows of control points. This constraint can be implemented using a simple penalty technique [177] to ensure an equal deflection of the two adjacent control nets as revealed in Figure 3.17.

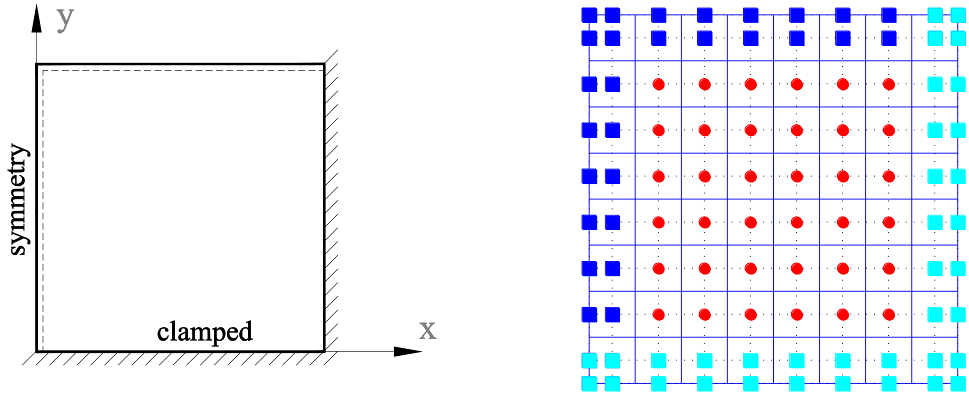

Figure 3.17 Clamped and symmetric boundary conditions: to constrain zero-deflection of two rows of control points in cyan square while it is assigned the equal deflection of two rows of control points in blue square to make sure the zero-rotation condition along these boundaries.

3.5.2 Inhomogeneous boundary condition

Being different from the homogeneous BCs, the displacement gets non-zero value in the inhomogeneous Dirichlet boundary conditions. Let us consider an example of one edge of the plate with a given displacement $u_x = \bar{u}$ as plotted in Figure 3.18. Inhomogeneous Dirichlet BCs are applied directly at the two end nodes of the edge by simply setting the control variables equal to the prescribed values. For the case of interior control points such as points 2 and 3, which is stood outside the geometry because NURBS shape functions do not satisfy the Kronecker delta property at these points, there is no available displacement constraints for them. Thus, some special treatment [135] e.g. the Lagrange multiplier method, the penalty method, the augmented Lagrange method, etc. were proposed to estimate the prescribed displacements. Herein, we prefer to treat inhomogeneous using a least square minimization, which is described in [112]. The basic idea of this treatment is to find the parameters of the boundary control points that minimize the following quantity:

$$J = \frac{1}{2}\sum\left[u(x_C) - \bar{u}(x_C)\right]^2 \tag{3.39}$$

where x_C denotes a set of collocation points distributed on the essential boundary. $u(x_C)$ is the displacement at point x_C and is approximated using the partition of unity property of the NURBS basis functions:

$$u(x_C) = \sum R_i(x_C)u_i \tag{3.40}$$

where u_i is the unknown displacement, which we want to impose at the control points. For the sake of simplicity, let us consider the case where there is only one collocation point and a quadratic basis (there are 3 non-zero functions R_i at x_C). Thus, we have:

$$J = \frac{1}{2}\left[R_1(x_C)u_1 + R_2(x_C)u_2 + R_3(x_C)u_3 - \bar{u}(x_C)\right]^2 \tag{3.41}$$

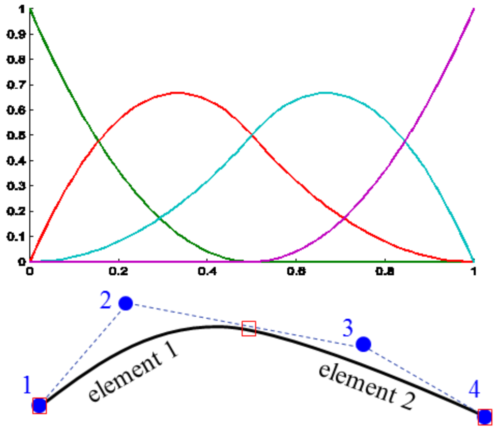

Figure 3.18 Illustration of imposing inhomogeneous BC: blue circle points denote the control points while red square point denotes the element node.

The partial derivatives of J with respect to u_i are given by:

$$\frac{\partial J}{\partial u_i} = [R_1(x_C)u_1 + R_2(x_C)u_2 + R_3(x_C)u_3 - \bar{u}(x_C)]R_i(x_C) \tag{3.42}$$

The condition $\partial J/\partial \mathbf{u} = 0$ gives the following linear system of equations:

$$\begin{bmatrix} R_1R_1 & R_2R_1 & R_3R_1 \\ & R_2R_2 & R_3R_2 \\ sym & & R_3R_3 \end{bmatrix}_{x_C} \begin{Bmatrix} u_1 \\ u_2 \\ u_3 \end{Bmatrix} = \bar{u}(x_C) \begin{Bmatrix} R_1 \\ R_2 \\ R_3 \end{Bmatrix} \tag{3.43}$$

Repeating the same analysis for other collocation points and other elements on the boundary, one obtains the linear system of equations in the form $\mathbf{Ku} = \mathbf{f}$. After solving it, these boundary displacements are enforced on the control points.

Chapter 4 Static Analysis

4.1 Introduction

In this chapter, stress analyses of FGM plates based on the HSDT models with arbitrary boundary conditions under a thermo-mechanical loading is studied by using the NURBS-based isogeometric approach. By using higher-order of NURBS basis functions, as $p \geq 2$, the present method enables to produce the C^1-continuity, which is naturally fulfils the stringent continuity required by the HSDT models with no additional variables like C^0-continuity elements [63, 75, 76] or some works of Thai [174]. Moreover, beside linear analysis geometrically nonlinear analysis based on using the von Kármán assumptions, which deal with small strains and moderate rotations, is employed to fully investigate the plate behaviour in the large deformation regime.

This chapter is outlined as follows. The general governing equations for both linear and nonlinear bending problems are introduced in Section 4.2. Herein, the flowchart for solving the nonlinear equation is represented by employing the Newton-Raphson method. Several numerical examples given in Section 4.3, show the excellent performance of the present method. To close this chapter, some concluding remarks are given in Section 4.4.

4.2 Governing equation

The static solutions can be obtained by solving the algebraic equation Eq. (3.17) without the rotational inertia:

$$\mathbf{Kq} = \mathbf{F}^{ext} \tag{4.1}$$

From Eqs. (3.18) and (3.19), it can be seen that the stiffness matrix, $\mathbf{K}$, has a nonlinear relation with the unknown variable $\mathbf{q}$ because $\mathbf{B}^{NL}$ is a function of displacement field. Thus, the nonlinear equilibrium equation, Eq. (4.1), must be solved iteratively. Firstly, the governing equation can be rewritten in the form of residual force:

$$\boldsymbol{\varphi}(\mathbf{q}) = \mathbf{K}\mathbf{q} - \mathbf{F}^{ext} \to 0 \tag{4.2}$$

The residual force presents the error in this approximation and tends to zero during iteration. If ${}^{i}\mathbf{q}$, an approximate trial solution at the *i*th iteration, makes unbalance residual force an improved solution ${}^{i+1}\mathbf{q}$ is then proposed as:

$${}^{i+1}\mathbf{q} = {}^{i}\mathbf{q} + \Delta\mathbf{q} \tag{4.3}$$

where the incremental displacement $\Delta\mathbf{q}$ is calculated by equating curtailed Taylor's series expansion of $\boldsymbol{\varphi}({}^{i+1}\mathbf{q})$ in the adjacency of ${}^{i}\mathbf{q}$ to zero:

$$\boldsymbol{\varphi}({}^{i+1}\mathbf{q}) \simeq \boldsymbol{\varphi}({}^{i}\mathbf{q}) + \mathbf{K}_T \Delta\mathbf{q} = 0 \tag{4.4}$$

in which $\mathbf{K}_T$ is called the tangent stiffness matrix evaluated at the *i*th iteration as follows:

$$\mathbf{K}_T = \frac{\partial \boldsymbol{\varphi}({}^{i}\mathbf{q})}{\partial\, {}^{i}\mathbf{q}} = \tilde{\mathbf{K}}_{NL} + \mathbf{K}_g \tag{4.5}$$

where the stiffness matrix $\tilde{\mathbf{K}}_{NL}$ strongly depends on displacement

$$\tilde{\mathbf{K}}_{NL} = \int_{\Omega} \left(\mathbf{B}^{L} + \mathbf{B}^{NL}\right)^{T} \hat{\mathbf{D}} \left(\mathbf{B}^{L} + \mathbf{B}^{NL}\right) \mathrm{d}\Omega \tag{4.6}$$

and the geometric stiffness matrix is given by:

$$\mathbf{K}_g = \int_{\Omega} \left(\mathbf{B}^{g}\right)^{T} \begin{bmatrix} N_x & N_{xy} \\ N_{xy} & N_y \end{bmatrix} \left(\mathbf{B}^{g}\right) \mathrm{d}\Omega \tag{4.7}$$

It is noted that being different from the initial stress stiffness matrix, $\mathbf{K}_0$, the geometric stiffness matrix is calculated using the internal forces according to Eq. (2.42).

Equation (4.3) is repeated until the displacement error between two adjacent iterations is reduced to the desired error with tolerance $\varepsilon = 0.01$. The Newton-Raphson procedure is summarized according to the flowchart in Figure 4.1.

$$\frac{\left\| {}^{i+1}\mathbf{q} - {}^{i}\mathbf{q} \right\|}{\left\| {}^{i}\mathbf{q} \right\|} < 0.01 \tag{4.8}$$

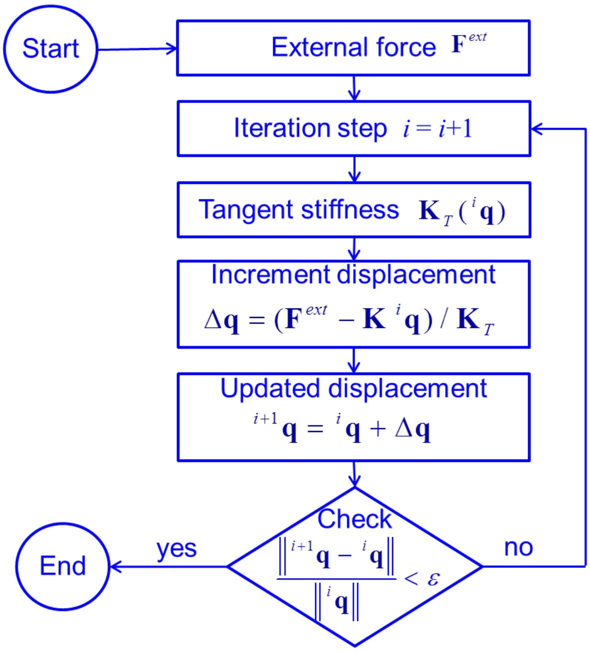

Figure 4.1 Flowchart for geometrically nonlinear bending analysis of plate.

4.3 Numerical results

For convenience, the following normalized transverse displacement, in-plane stresses and shear stresses are expressed as:

$$\hat{w} = \frac{w}{h}, \quad \bar{w} = \frac{10^2 w E_m h^3}{f_z L^4}, \quad \bar{\sigma} = \frac{\sigma h^2}{f_z L^2}, \quad \bar{\tau} = \frac{\tau h}{f_z L}, \quad \bar{P} = \frac{f_z L^4}{E_m h^4} \tag{4.9}$$

4.3.1 Linear analysis

In the linear problems, the nonlinear stiffness matrices are set to zero. The finite element model for static analysis becomes a linear system of equations as follows:

$$\mathbf{K}_L \mathbf{q} = \mathbf{F}^{ext} \tag{4.10}$$

4.3.1.1 Convergence study

Let us consider a simply supported Al/SiC square FGM plate, for which properties are given in Table 2.1. The plate is subjected to a sinusoidal pressure defined as $f_z \sin(\pi x / L) \sin(\pi y / W)$ at the top surface as shown in Figure 4.2. A convergence study of transverse displacement by quadratic ($p = 2$), cubic ($p = 3$) and quartic ($p = 4$) elements is tabulated in Table 4.1 and also depicted in Figure 4.3 according to power index, $n = 1$ and 6, respectively. It is observed that as the number of element increases, the obtained results converge to the exact solutions from 3D deformation model by Vel and Batra [23]. IGA, moreover, gains the super-convergence with the discrepancy between meshing of 5×5 and 25×25 around 0.05% as $p \geq 3$. Herein, IGA just using 11×11 cubic NURBS elements as shown in Figure 4.2c produces an ultra-accurate solution that is very close to the exact solution with very small error around 0.02%. Therefore, in next investigations, the meshing of 11×11 cubic NURBS elements is used.

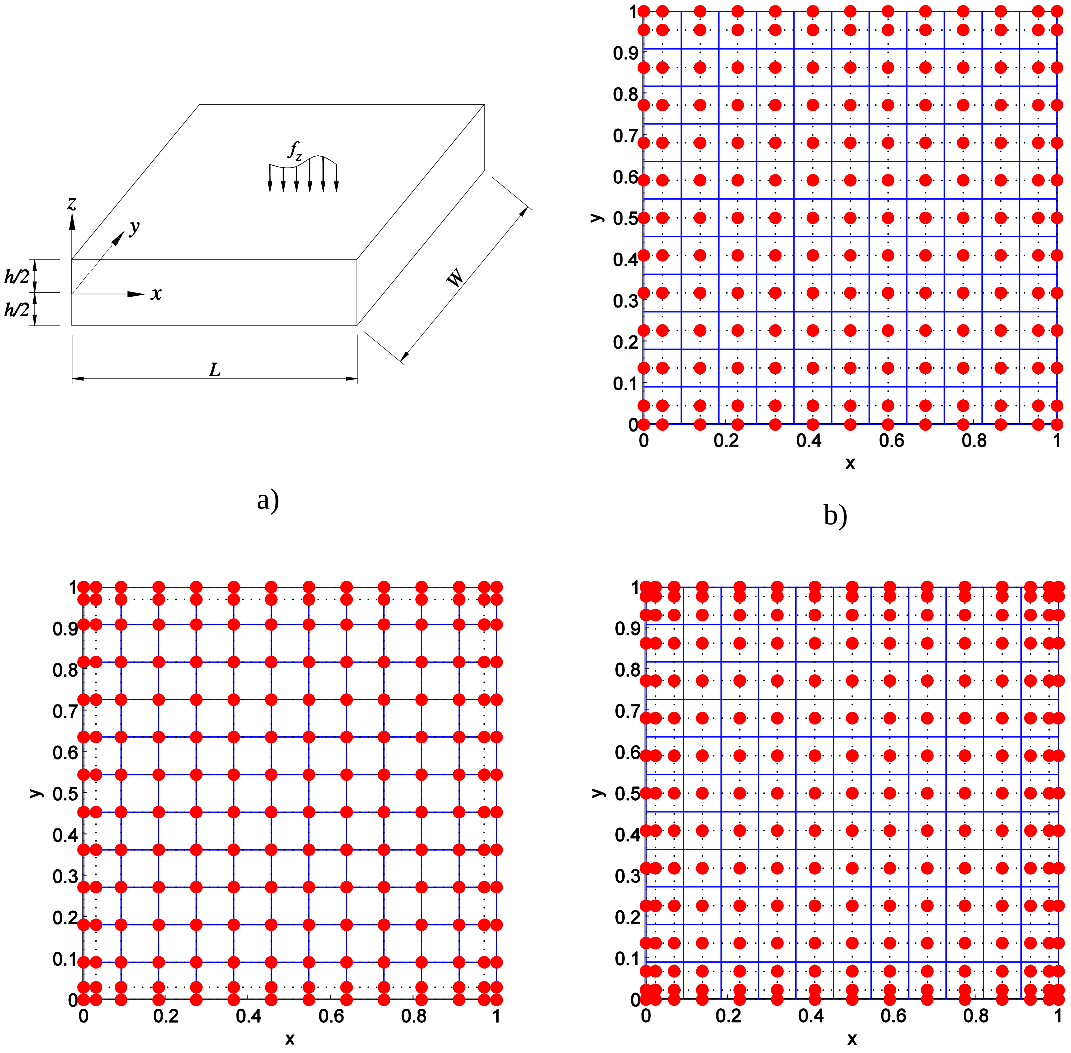

a)

b)

c)

d)

Figure 4.2 Square plate: a) geometry; b), c), d): meshing of 11×11 quadratic, cubic and quartic elements, respectively. Noted that control points are in red circle, whitls elements are borderd by blue lines.

Table 4.1 Convergence study of deflection of square Al/SiC FGM plate.

	p	5×5	7×7	11×11	15×15	19×19	25×25	3D sol. [23]
n = 1	Quadratic	1.5032	1.5150	1.5226	1.5250	1.5261	1.5269	1.5281
	Cubic	1.5271	1.5277	1.5279	1.5279	1.5279	1.5279	
	Quartic	1.5275	1.5279	1.5279	1.5279	1.5279	1.5279	
n = 6	Quadratic	2.2906	2.3052	2.3147	2.3178	2.3192	2.3202	2.3218
	Cubic	2.3203	2.3212	2.3214	2.3215	2.3215	2.3215	
	Quartic	2.3207	2.3215	2.3215	2.3215	2.3215	2.3215	

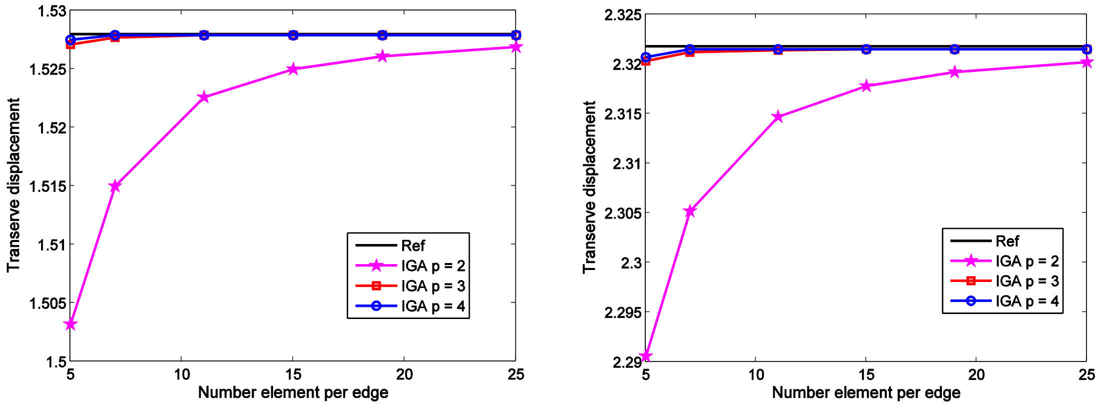

a) n =1 b) n = 6

Figure 4.3 Comparison of present result with analytical solution of Vel and Batra according to power indices.

4.3.1.2 Shear locking test

This phenomenon is investigated for an isotropic plate subjected to a uniform transverse load. Figure 4.4 reveals the relation between the central deflection and the length-to-thickness ratio under full simply supported and full clamped boundary conditions. For fair comparison between the plate theories: FSDT, TSDT, GSDT and RPT, the same mesh of 11×11 cubic NURBS elements is utilized to model the plates for both cases of boundary conditions. Some concluding remarks are drawn as:

- The CPT [158] based on Kirchhoff assumption gives constant results which are independent of the length-to-thickness ratio (L/h).
- For thick and moderate plate (L/h < 100), these HSDT models including TSDT, GSDT, RPT gain nearly the same deflections and slightly higher than FSDT one.

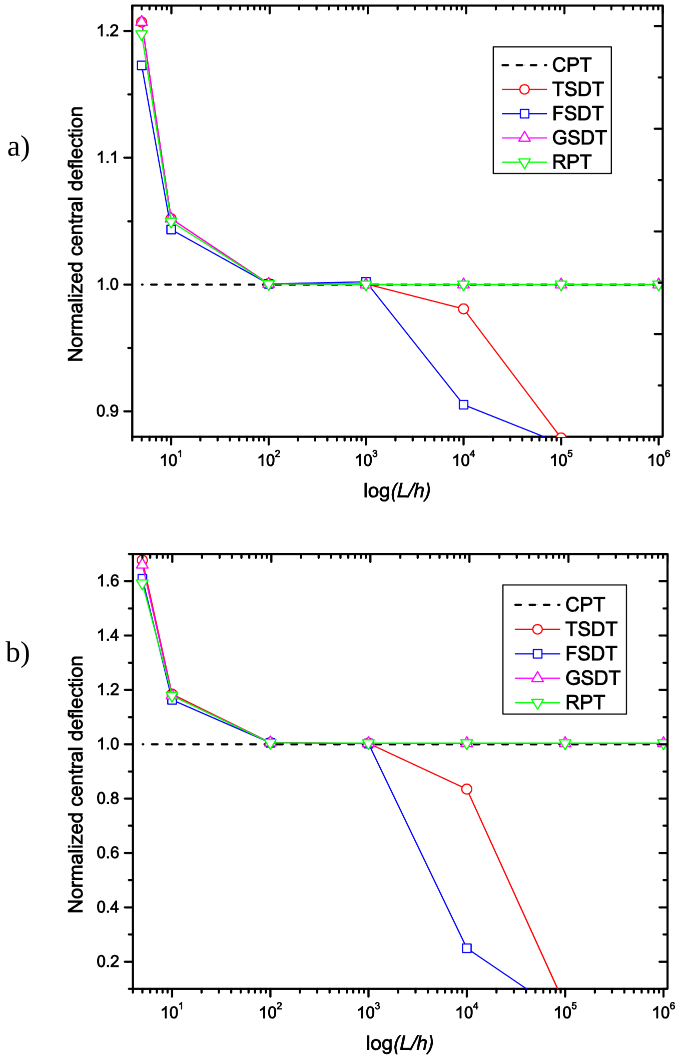

Figure 4.4 The central deflection via length to thickness ratios and boundary conditions: a) Simply supported and b) Clamped.

- As the plates become thin ($L/h > 100$), all models give the same results, which match well with CPT [158]. However, for very thin plate ($L/h > 1000$), being different from GSDT and RPT, both TSDT and FSDT give the divergent transverse displacements as compared to CPT. This is called shear-locking phenomenon. According to Kirchhoff theory, as thickness, h, approaches to zero, the rotations ($\boldsymbol{\beta}$ in Eq. (2.32)) as well as the shear component (w_S in Eq. (2.26)) are very small and can be eliminated. That causes zero shear strains/stresses. Therefore, GSDT and RPT are naturally free of shear locking. In case of FSDT and TSDT, shear strains are related to parameter $\beta_{\mathrm{x}} + w_{0,\mathrm{x}}$, as noted in Eq. (2.22). As Kirchhoff constraint is imposed, this parameter must identically vanish, $\beta_{\mathrm{x}} + w_{0,\mathrm{x}} = 0$. However, in numerical method, with the same approximated function for both of rotations and transverse displacement, the linear combination of this function and its derivatives mathematically results in non-zero value. Consequently, the shear energy remains, which dominate the bending energy and causes shear-locking.

4.3.1.3 Comparison of plate theories

Next, a simply supported Aluminium/Alumina (Al/Al$_2$O$_3$) FGM plate subjected to a sinusoidal pressure defined as $f_z = \sin(\pi x / L)\sin(\pi y / W)$ is considered. It is noted that the material properties are computed by the rule of mixture in Eq. (2.3). Using different distributed functions *f(z)* in the form of third-order polynomials (f_1) by Reddy [57], inverse trigonometric function (f_2) by Thai [165] and our proposed function in inverse tangent form, the results based on RPT and GSDT including deflection $\bar{w} = 10wE_c h^3 / (f_z L^4)$ and axial stress $\bar{\sigma}_x = \sigma_x h / (f_z L^2)$ at the centre of the plate are summarized in Table 4.2. The solutions are in good agreement with that of Zenkour's generalized shear deformation theory [64], and those from Carrera et al. [178, 179] using Carrera's unified formulation and Neves et al. [180, 181] using sinusoidal shear deformation theory (SSDT) and HSDT models. It is concluded that the quasi-3D models accounting for the thickness stretching effect $\varepsilon_z \neq 0$ gain the lower transverse displacement and higher axial stress than the 2D plate models, which eliminate the stretching effect. However, the discrepancy between the two models reduces as the plate becomes thinner. An interesting point is that HSDT using present function gains the lowest deflections being closest to the quasi-3D models. In addition, there is no different in results obtained by GSDT and RPT. Thus, without other notification, GSDT is preferred to be employed in these numerical results.

Figure 4.5 plots the stress distribution through the thickness of thick plate with *L*/*h*=4 and *n* = 1. Using HSDT, the axial stress is plotted in a coincident path, while there is a slight difference observed for shear stress distribution. And all of them satisfy the traction-free boundary conditions at the plate surfaces. Figure 4.6 presents the curved distribution of the axial and shear stresses through the plate thickness according to power index n = 1, 4, 10, respectively. It can be concluded that the present model based on NURBS approximation yields very promising results compared to those by Neves et al. [180].

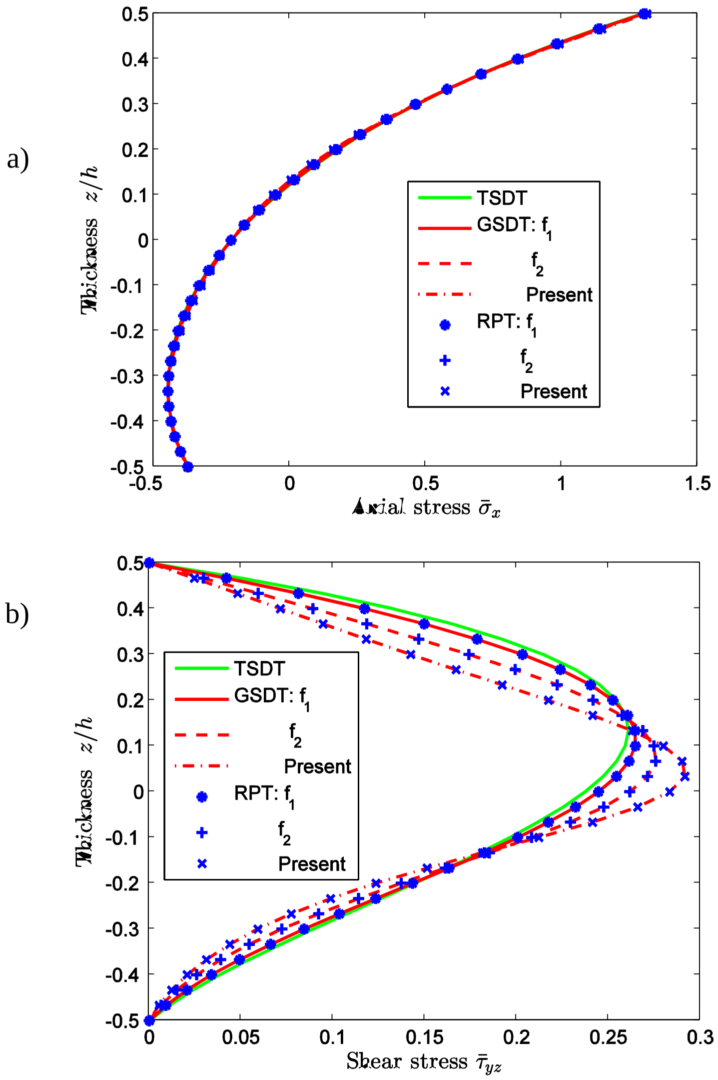

Figure 4.5 The stresses through thickness of SSSS Al/Al$_2$O$_3$ FGM plate under sinusoidal load with L/h=4, n=1, via different plate models: a) $\bar{\sigma}_x(\frac{L}{2},\frac{W}{2},z)$ and b) $\bar{\tau}_{yz}(\frac{L}{2},0,z)$.

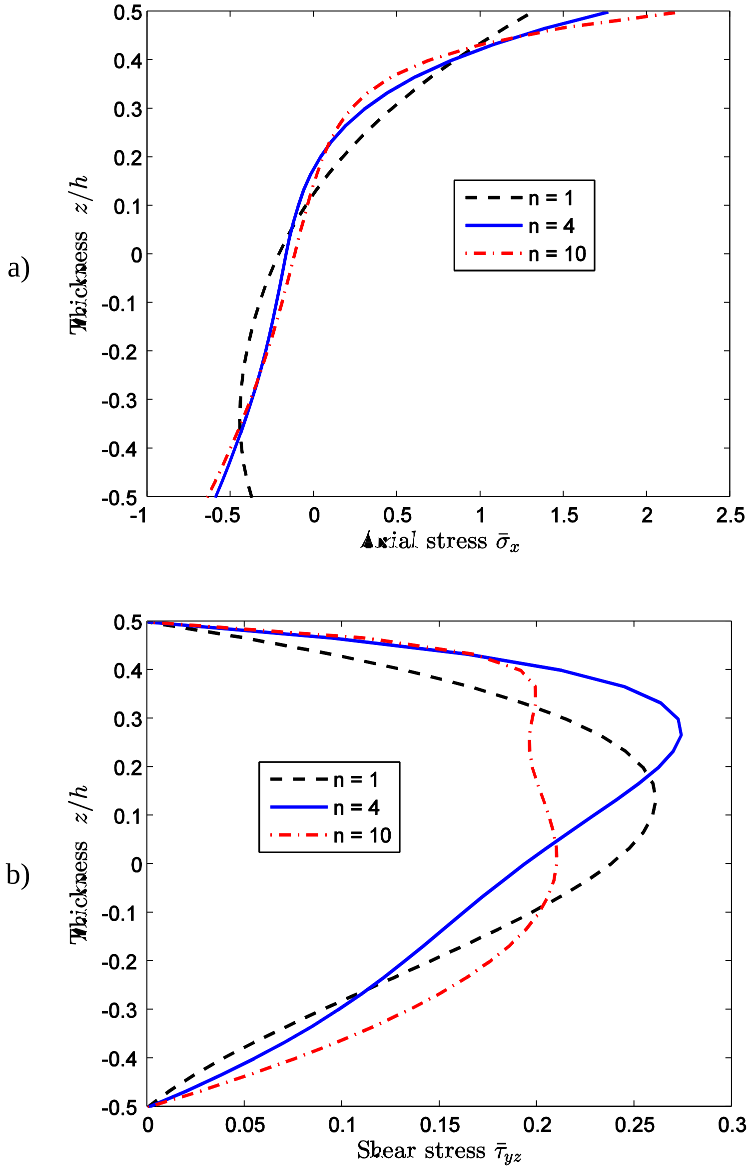

Figure 4.6 The stresses through thickness of SSSS Al/Al$_2$O$_3$ FGM plate under sinusoidal load with L/h=4, n=1 via various power indices n: a) axial stress $\bar{\sigma}_x(\frac{L}{2},\frac{W}{2},z)$ *and b) shear stress* $\bar{\tau}_{yz}(\frac{L}{2},0,z)$.

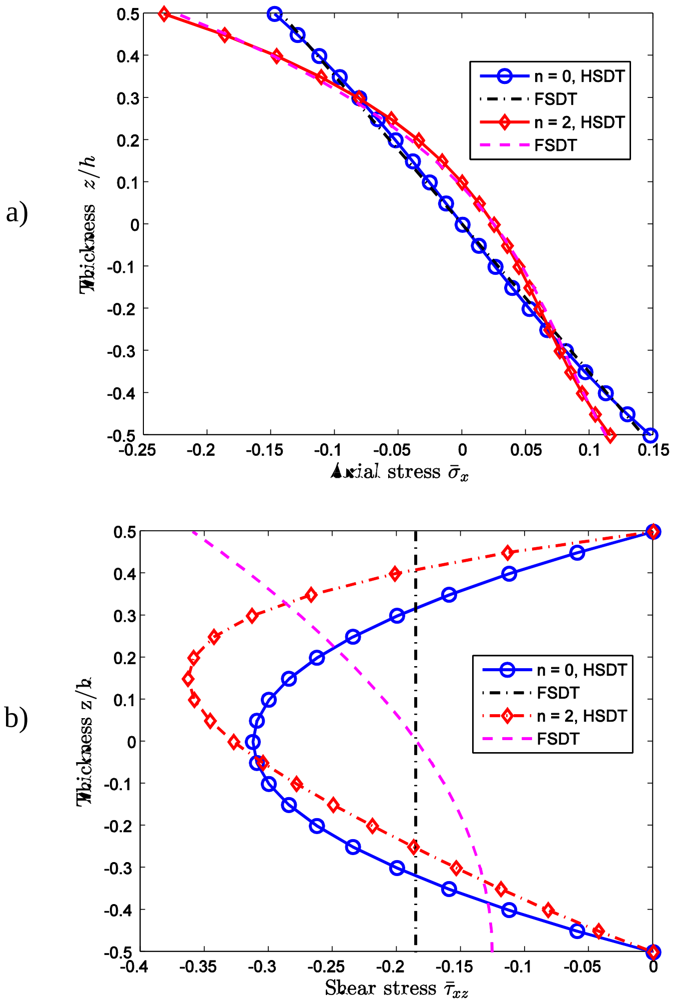

Figure 4.7 The stresses through thickness of Al/ZrO$_2$-1 FGM plate under uniform loads L/h=5 and clamped edges based on HSDT & FSDT: a) $\bar{\sigma}_x(\frac{L}{2},\frac{W}{2},z)$ *and b)* $\bar{\tau}_{xz}(0,\frac{W}{2},z)$.

Figure 4.7a plots the axial stress at the central point of the clamped plate according to *n* = 0, 2, respectively under FSDT and HSDT formulations. It is revealed that with homogeneous material, axial stress is symmetric through the middle plan. In inhomogeneous case, the stress is distributed in tendency that the magnitude of compressive stress at the top is greater than the tensile one at the bottom. Furthermore, we can see that there is an overlap in results between FSDT and HSDT models. Nevertheless, this observation is no longer true in case of shear stress $\bar{\tau}_{xz}(0, W/2, z)$ as plotted in Figure 4.7b. Employing FSDT, the shear stress is wrongly distributed with constant (*n*=0) and has negative values at the two free surfaces. While HSDT yields parabolic curves of shear stress with traction free boundary at top and bottom surfaces of the plate.

Table 4.2 The non-dimensional deflection and, axial stress of SSSS Al/Al_2O_3 square plate under sinusoidal load.

n	Model		ε_z	L/h = 4		10		100	
				$\bar{w}$	$\bar{\sigma}_x(z=\frac{h}{3})$	$\bar{w}$	$\bar{\sigma}_x(z=\frac{h}{3})$	$\bar{w}$	$\bar{\sigma}_x(z=\frac{h}{3})$
1	Ref. [179]		≠0	0.7171	0.6221	0.5875	1.5064	0.5625	14.969
	FSDT		0	0.7291	0.806	0.5889	2.015	0.5625	20.15
	GSDT [64]		0	-	-	0.5889	1.4894	-	-
	Ref. [178]		0	0.7289	0.7856	0.589	2.0068	0.5625	20.149
			≠0	0.7171	0.6221	0.5875	1.5064	0.5625	14.969
	SSDT [181]		≠0	0.6997	0.5925	0.5845	1.4945	0.5624	14.969
	HSDT [180]		0	0.7308	0.5806	0.5913	1.4874	0.5648	14.944
			≠0	0.702	0.5911	0.5868	1.4917	0.5647	14.945
	TSDT			0.7284	0.5806	0.5889	1.4886	0.5625	14.9553
	RPT	f_1		0.7284	0.5796	0.5889	1.4856	0.5625	14.9255
		f_2		0.7254	0.5779	0.5885	1.4849	0.5625	14.9255
		Present		0.7204	0.5793	0.5878	1.4854	0.5625	14.9255
	GSDT	f_1		0.7284	0.5783	0.5889	1.4816	0.5625	14.889
		f_2		0.7254	0.5755	0.5885	1.4809	0.5625	14.889
		Present		0.7203	0.5769	0.5878	1.4814	0.5625	14.889
4	Ref. [179]		≠0	1.1585	0.4877	0.8821	1.1971	0.8286	11.923
	FSDT		0	1.1125	0.642	0.8736	1.6049	0.828	16.049
	GSDT [64]		0	-	-	0.8651	1.1783	-	-
	Ref. [178]		0	1.1673	0.5986	0.8828	1.5874	0.8286	16.047
			≠0	1.1585	0.4877	0.8821	1.1971	0.8286	11.923
	SSDT [181]		≠0	1.1178	0.4404	0.875	1.1783	0.8286	11.932
	HSDT [180]		0	1.1553	0.4338	0.877	1.1592	0.8241	11.737
			≠0	1.1108	0.433	0.87	1.1588	0.824	11.737
	TSDT			1.1598	0.4443	0.8815	1.1782	0.8286	11.9092
	RPT	f_1		1.1599	0.4433	0.8815	1.1753	0.8287	11.8796
		f_2		1.162	0.4371	0.882	1.1727	0.8287	11.8793
		Present		1.1562	0.4369	0.8812	1.1726	0.8287	11.8793
	GSDT	f_1		1.1598	0.4406	0.8815	1.1711	0.8287	11.8436
		f_2		1.162	0.4344	0.882	1.1686	0.8287	11.8434
		Present		1.1562	0.4342	0.8812	1.1684	0.8287	11.8433
10	Ref. [179]		≠0	1.3745	0.3695	1.0072	0.8965	0.9361	8.9077
	FSDT		0	1.3178	0.4796	0.9966	1.199	0.936	11.99
	GSDT [64]		0	-	-	1.0089	0.8775	-	-
	Ref. [178]		0	1.3925	0.4345	1.009	1.1807	0.9361	11.989
			≠0	1.3745	0.1478	1.0072	0.8965	0.9361	8.9077
	SSDT [181]		≠0	1.349	0.3227	0.875	1.1783	0.8286	11.932
	HSDT [180]		0	1.376	0.3112	0.9952	0.8468	0.9228	8.6011
			≠0	1.3334	0.3097	0.9888	0.8462	0.9227	8.601
	TSDT			1.3908	0.3255	1.0087	0.8777	0.9362	8.8988
	RPT	f_1		1.3908	0.3249	1.0087	0.876	0.9362	8.8804
		f_2		1.3871	0.3189	1.0084	0.8735	0.9362	8.8802
		Present		1.3738	0.3183	1.0064	0.8732	0.9362	8.8802
	GSDT	f_1		1.3908	0.323	1.0087	0.8733	0.9362	8.8582
		f_2		1.387	0.317	1.0084	0.8709	0.9362	8.8580
		Present		1.3738	0.3165	1.0064	0.8706	0.9362	8.8579

4.3.1.4 Effect of boundary conditions

In this subsection, the effect of boundary conditions on the normalized central deflection $\tilde{w} = 100 w E_m h^3 / \{12(1-\nu^2) f_z L^4\}$ of Al/ZrO$_2$-1 plate subjected to uniform load is investigated. In this problem the Mori-Tanaka scheme is used for homogenizing the Al/ZrO$_2$-1 FGM plate. Table 4.3 shows the comparisons between present results (TSDT and GSDT using 5 DOFs/point and RPT using 4 DOFs/point) and those of Gilhooley [60] based on higher-order shear and normal deformable plate theory (HOSNDPT) using 18 DOFs/node. Figure 4.8 shows that using NURBS-based isogeometric finite element method produces solutions very close to Ref. [60] for all boundary conditions. Moreover, when the boundary conditions change from CCCC to SSSS and SFSF, the structural stiffness reduces and the magnitudes of deflection increase. The shapes of transverse displacement according to the various boundary conditions are illustrated in Figure 4.9.

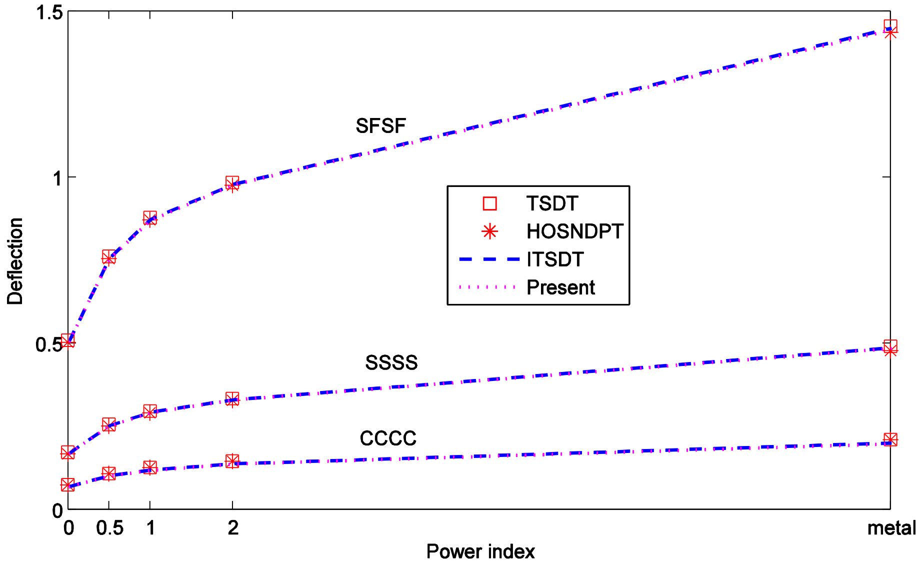

Figure 4.8 The normalized deflection of Al/ZrO$_2$-1 FGM plate (L/h = 5) via power indexes and boundary conditions.

Table 4.3 The non-dimension deflection of Al/ZrO$_2$-1 plate under uniform load with *L/h* = 5 via different boundary conditions.

BC	*n*	HOSNDPT [60]	TSDT	GSDT	RPT
SFSF	0	0.5019	0.5088	0.5054	0.506
	0.5	0.7543	0.7607	0.7559	0.7568
	1	0.8708	0.8776	0.8721	0.8732
	2	0.9744	0.9830	0.9767	0.9784
	4	-	1.0701	1.0626	1.0648
	8	-	1.1577	1.1486	1.1504
	Metal	1.4345	1.4537	1.444	1.4458
SSSS	0	0.1671	0.1716	0.1711	0.1703
	0.5	0.2505	0.2554	0.2547	0.2536
	1	0.2905	0.2955	0.2948	0.2934
	2	0.328	0.3334	0.3328	0.3312
	4	-	0.3655	0.3648	0.363
	8	-	0.3958	0.3945	0.3922
	Metal	0.4775	0.4903	0.4888	0.4865
CCCC	0	0.0731	0.0734	0.0725	0.0701
	0.5	0.1073	0.1077	0.1064	0.1029
	1	0.1253	0.1256	0.1241	0.1201
	2	0.1444	0.1447	0.143	0.1384
	4	-	0.1622	0.1598	0.1546
	8	-	0.1760	0.1729	0.1669
	Metal	0.2088	0.2098	0.207	0.2001

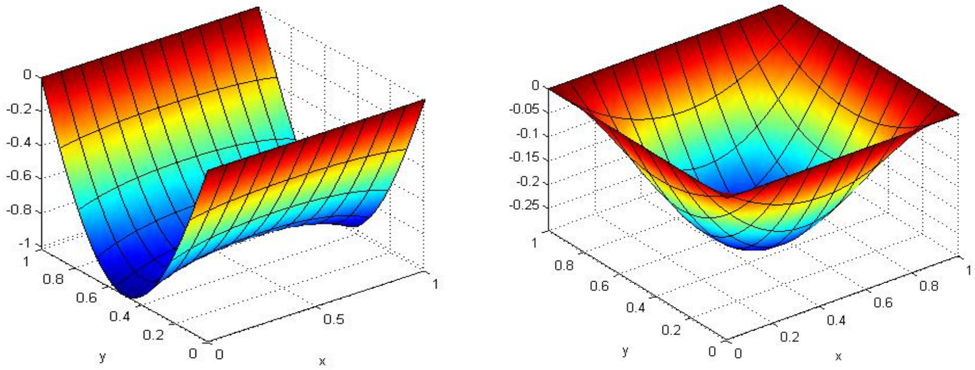

a) SFSF

b) SSSS

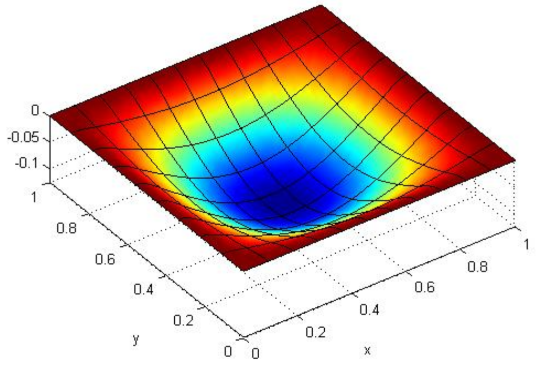

c) CCCC

Figure 4.9 Deflection profile of Al/ZrO$_2$-1 FGM plates under various boundary conditions.

4.3.1.5 Effect of the types of homogenization scheme

Table 4.4 summarizes the IGA results in comparison with those of mesh-less method [70] and MLPG [142] using the same HSDT for thick and moderate Al/ZrO$_2$-2 plates. The plate is simply supported and subjected to uniform load f_z. In this example, both homogenization schemes: the Mori-Tanaka method and the rule of mixture are employed. From the obtained non-dimensional deflections, some remarks are withdrawn. (1) There is a good agreement between NURBS-based approximation using quadratic, cubic and quartic elements. (2) The present results are in excellent agreement with those obtained by mesh-less method [70] using 19×19 number of colocation points for both homogeneous schemes. And (3) Figure 2.4 shows that the rule of mixtures procedures larger effective Young modulus through the plate thickness than that produced by the Mori-Tanaka scheme. Thus, the transverse displacement by former model is slightly smaller than that of the latter because of stiffer stiffness matrix.

Table 4.4 Non-dimensional centre deflection $\bar{w}_c = 100 w_c / h$ of simply supported square Al/ZrO$_2$-2 plate subjected to a uniform load.

L/h	Method	*n*				
		0	0.5	1	2	∞
20	Mesh-less method [70]	2.08 (2.08)*	2.79 2.65	3.09 2.97	3.33 3.24	4.48 (4.48)
	MLPG [142]	2.118	-	3.150	3.395	4.580
	IGA (*p* = 2)	2.0827 (2.0827)	2.7919 (2.6611)	3.0916 (2.9778)	3.3392 (3.2512)	4.4928 (4.4928)
	IGA (*p* = 3)	2.0831 (2.0831)	2.7924 (2.6616)	3.0922 (2.9783)	3.3398 (3.2518)	4.4935 (4.4935)
	IGA (*p* = 4)	2.0831 (2.0831)	2.7924 (2.6616)	3.0922 (2.9783)	3.3398 (3.2518)	4.4935 (4.4935)
5	Mesh-less method [70]	2.477 (2.477)	3.2930 (3.135)	3.6660 (3.515)	4.0090 (3.883)	5.343 (5.343)
	MLPG [142]	2.436	-	3.634	3.976	5.253
	IGA (*p* = 2)	2.4818 (2.4818)	3.3008 (3.1424)	3.6739 (3.5231)	4.0160 (3.8903)	5.3536 (5.3536)
	IGA (*p* = 3)	2.4819 (2.4819)	3.3009 (3.1425)	3.6741 (3.5233)	4.0162 (3.8905)	5.3538 (5.3538)
	IGA (*p* = 4)	2.4819 (2.4819)	3.3009 (3.1425)	3.6741 (3.5233)	4.0162 (3.8905)	5.3538 (5.3538)

*Results according to the rule of mixture are in parentheses

4.3.1.6 Skew plate subjected to a uniform mechanical load

Skew plate is one of the widely used structures in civil, mechanical, marine and aeronautical engineering applications. In this subsection, we apply the present method to analyse a simply supported Al/ZrO_2-1 skew plate considering the change of the skew angle. The plate with geometry shown in Figure 4.10 is constrained by soft simply supported condition (just $w_0 = 0$ on all edges), has the length to thickness ratio $L/h = 100$, and is subjected to a uniform mechanical load $f_z = -10^4$ N/m^2. Figure 4.11 plots the axial stress distribution at the plate centre versus the change of gradient index from 0.5 to 1 and 2. It is observed that the axial stress increases when the skew angle increases. This conclusion was also observed in Ref. [45] by Lee et al. using the *kp*-Ritz method.

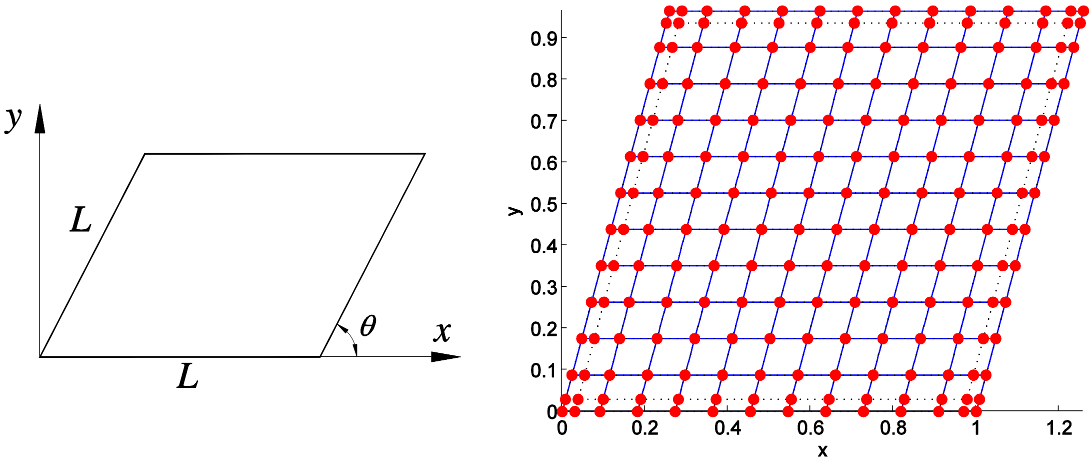

a) b)

Figure 4.10 The skew plate: a) Geometry and b) Meshing of 11×11 cubic elemements.

4.3.1.7 Behaviour of plate under thermo-mechanical loading

It is well known that FGM structure is commonly used in high temperature environments. In this problem, we simulate a simply supported Al/ZrO_2-2 FGM plate under both mechanical and thermal loadings. The plate is made of Aluminium at the bottom surface and Zirconia at the top surface, and has dimensions as: length $L = 0.2$ m and thickness $h = 0.01$ m. Material properties vary through the thickness of the plate following the rule of mixture. It is assumed that temperature at the bottom surface is held at $T_m = 20$°C (room temperature) and the temperature at the top surface varies from 0°C to 500°C.

a) $n = 0.5$

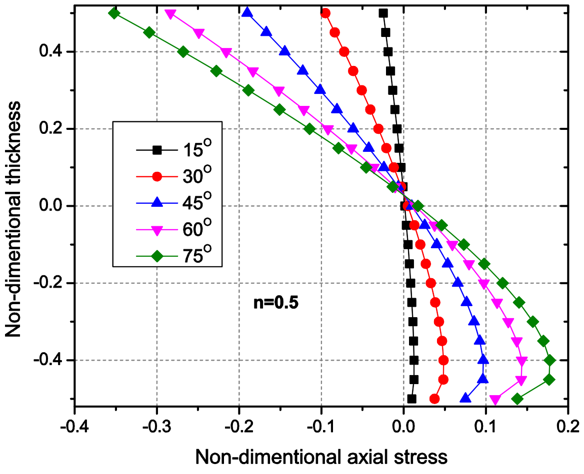

b) $n = 1$

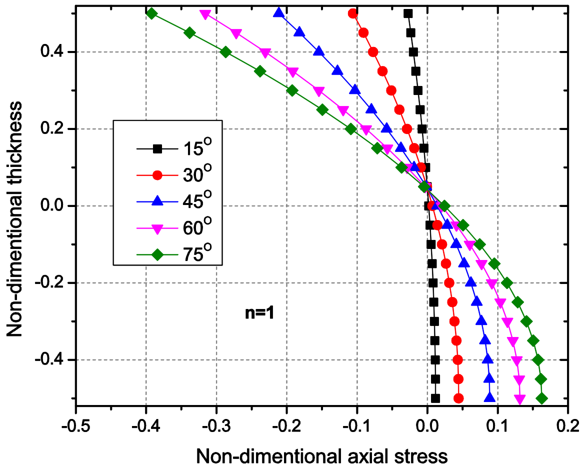

c) $n = 2$

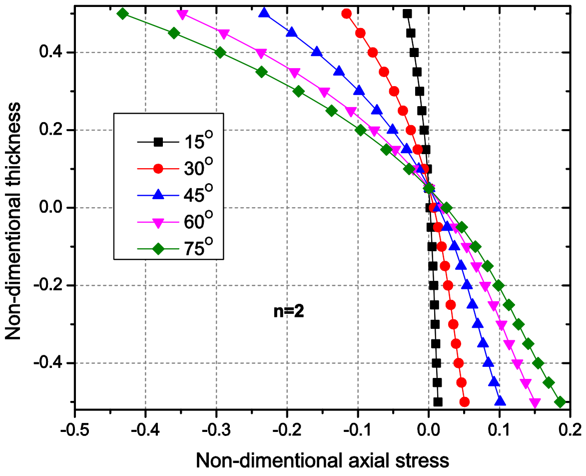

Figure 4.11 The axial stress distribution at the centre of Al/ZrO_2-1 skew plate via various gradient indices.

Figure 4.12 shows the non-dimensional central deflection of Al/ZrO_2 plate under thermal load. Because of the high temperature at the top surface, the plate is deflected upward. The metal plate undergoes the maximum deflection due to its high sensitivity to temperature. The FGM plate with respect to the volume fraction (n =1) can produce the minimum deflection. As observed, the FGM plates experience less deflection than the isotropic ones, i.e. fully ceramic and fully metal plates. This is due to the fact that temperature distribution through the thickness of FGM plates is always lower than that of the counterparts, as shown in Figure 2.5. This leads to produce less thermal resultants (according to Eq. (2.45)), which directly cause bending of the plate. Hence, it is concluded that the FGM plates can well resist high temperature conditions.

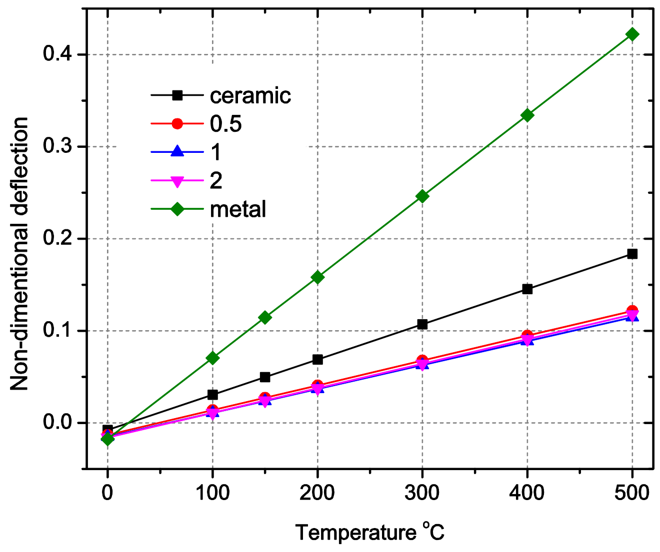

Figure 4.12 Non-dimension central deflection of simply supported Al/ZrO$_2$ plate under thermal load.

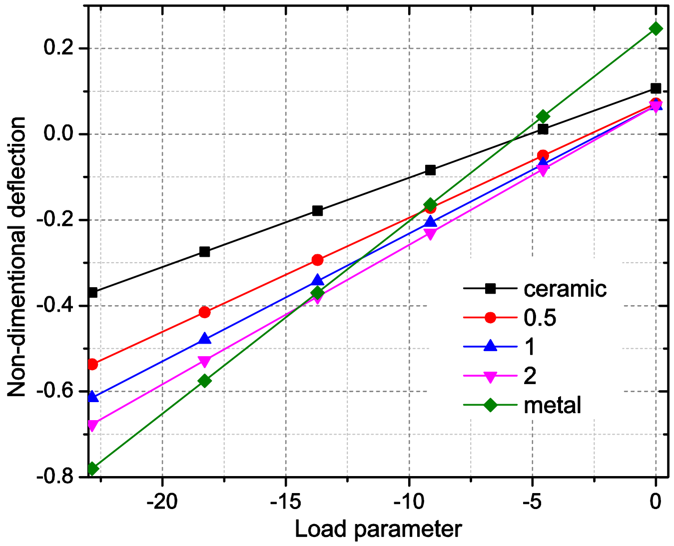

Figure 4.13 Non-dimensional central deflection $\hat{w} = w/h$ of Al/ZrO$_2$ FGM plate subjected to thermo-mechanical load.

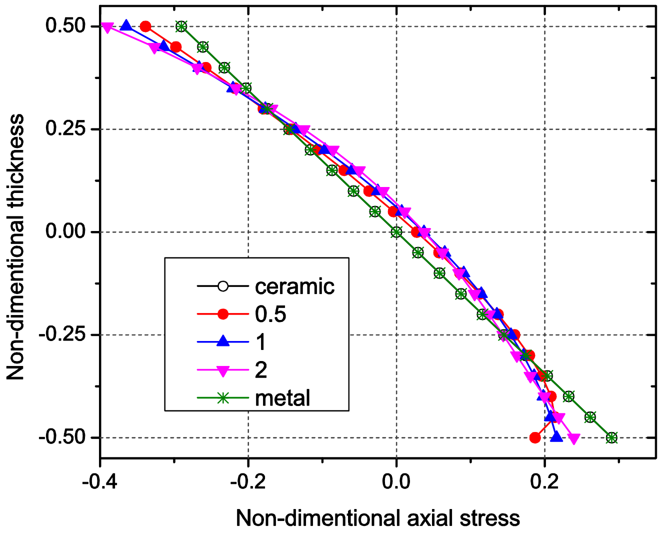

a) Mechanical loading

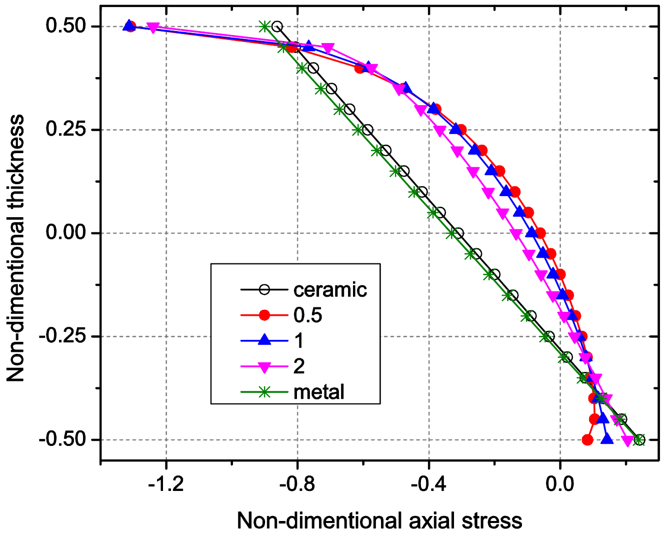

b) Thermo-mechancial loading

Figure 4.14 Central axial stress $\bar{\sigma}_x = \sigma_x h^2 / (f_z L^2)$ *at points on the vertical line passing through the centroid of Al/ZrO₂ FGM plate subjected to a thermo-mechanical load.*

At last but not least, we investigate the behaviour of FGM plates under the thermal-mechanical effect. The temperature is now constantly held T_m = 20°C at the bottom surface and T_c = 300°C at the top surface. By applying uniform pressure changing from 0 to 10^7 N/m^2, the central deflection is plotted in Figure 4.13. It is seen that the behaviour of deflection under thermo-mechanical load is quite different from the pure mechanical load. Because the high temperature at the top surface causes the thermal expansion, the plates result in upward deflections. The deflection of the plates then varies from positive side to negative side when the mechanical load increases. As a result, the behaviour is similar to that in the case of purely mechanical load. However, the intermediate response of graded plates is not as similar as that in the case of purely mechanical load. The metallic plate is also found to be highly sensitive to the temperature when deflection varies largely. The ceramic plate gives the deflection that is smaller than that of the intermediate plates, when the mechanical load increases. Figure 4.14 shows the axial stress distribution through the thickness of plates with a uniform mechanical distributed load of $f_z = -10^6$ N/m^2. With the presence of the temperature field given above, compression occurs at the top surface, while tension occurs at the bottom surface. Except for fully ceramic or fully metal plates, the stress distribution of FGM plates has a similar trend.

4.3.2 Geometrically nonlinear bending analysis

4.3.2.1 Validation study

Let us first consider a thin (L/h =100) clamped square plate (E = 206.84 GPa, ν = 0.316) under a uniformly distributed load. This problem is often studied by many authors [171, 182, 183] for the geometrically nonlinear validation of thin plate models. Figure 4.15 shows the central deflection $\hat{w}$ and axial stress $\bar{\sigma}_x(0,0,h/2)$, which have nonlinear curves as function of the load parameter $\bar{P}$ because of geometrically nonlinearity effect. The present results are in good agreement with those of analytical solution using a double Fourier series by Levy [182], nine-node finite element (FEM Q9) [183] and mixed finite element model (MIXFEM) [171]. Especially, using 5DOFs/point, the present method produces more accurate stress solutions than MIXFEM using eight DOFs.

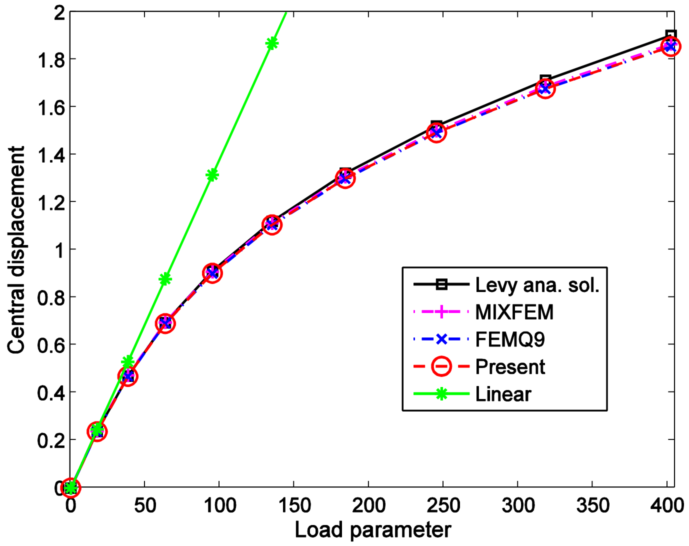

a) Transverse displacement

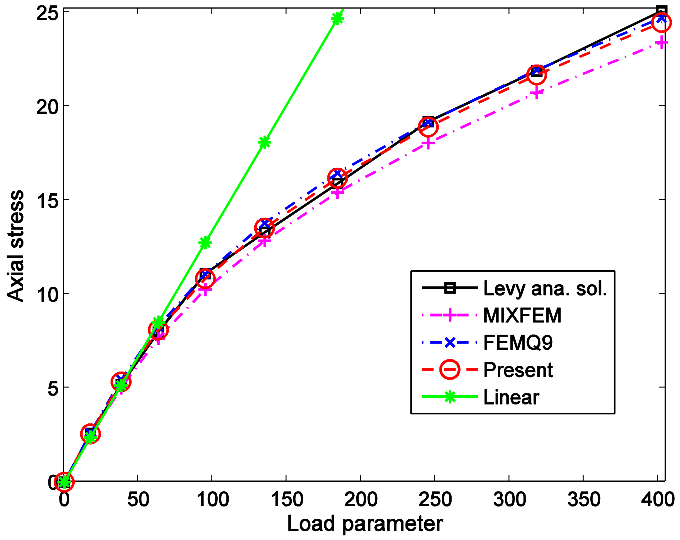

b) Axial stress

Figure 4.15 Comparison of (a) the non-dimensional central deflection and (b) normal stress of thin clamped square plate.

Next, the geometrically nonlinear behaviour of a circular isotropic plate under a uniform pressure is investigated. We consider the plate with radius-to-thickness ratio, $R/h=50$ and material properties: Young's modulus $E=10^7$ psi (68.95 GPa) and Poisson's ratio $\nu = 0.3$. The present transverse central displacements listed in Table 4.5 are compared with the analytical Kirchhoff solution [184], that of Kirchhoff-based elements, such as discrete Kirchhoff theory (DKT) [185], refined non-conforming element method (RNEM) [186] and that of Mindlin-based elements: nine-node Lagrangian quadrilateral element (QL) [183], mixed interpolation smoothing quadrilateral element (MISQ20) [187]. It is noted that the error as compared with analytical solution [184] are shown in parenthesis. As it can be seen, the present method produces the most accurate solution.

Table 4.5 Normalized central deflection of a clamped circular plate under uniform load

Load $\bar{P}$	Normalized central deflection $\hat{w}$					
	MISQ20 [187]	QL [183]	DKT [185]	RNEM [186]	Present	Anal. Sol. [184]
1	0.170 (0.59)*	0.1682 (0.47)	0.172 (1.78)	0.1664 (1.54)	0.1669 (1.24)	0.169
2	0.327 (1.24)	0.3231 (0.03)	0.330 (2.17)	0.3179 (1.58)	0.3208 (0.68)	0.323
3	0.465 (1.75)	0.4591 (0.46)	0.470 (2.84)	0.4514 (1.23)	0.4562 (0.18)	0.457
6	0.780 (2.50)	0.7702 (1.21)	0.791 (3.94)	0.7637 (0.35)	0.7671 (0.80)	0.761
10	1.067 (3.09)	1.0514 (1.58)	1.082 (4.54)	1.0544 (1.87)	1.0487 (1.32)	1.035
15	1.320 (3.21)	1.3007 (1.70)	1.342 (4.93)	1.3164 (2.92)	1.2989 (1.56)	1.279

*The relative error is listed in parenthesis.

At last, the benchmark problems with the experimental results of Zaghloul and Kenedy [139] are studied. The comparisons between the obtained results based on the HSDT model and others according to CPT [139], FSDT [171] and the experimental results [139] are revealed in Figure 4.16 for a simply supported orthotropic plate having material properties E_1 = 20.684 GPa, E_2 = 8.825 GPa, $G_{12} = G_{23} = G_{31}$ =2.551 GPa, ν = 0.32 and a clamped 4 cross-ply [0/90/90/0] plate which set material of E_1 = 12.604 GPa, E_2 = 12.627 GPa, $G_{12} = G_{23} = G_{31}$ =2.155 GPa, ν = 0.2395 [139], respectively. It is clearly observed that the present results with just 5 DOFs per each control point match well with those of FSDT [171] using MIXFEM with 8 DOFs/node. Considering the shear deformation effect, both HSDT and FSDT models achieve more accurate solutions than CPT. However, in case of the clamped plate in Figure 4.16b, there is a small discrepancy between them. This may due to the effect of the boundary conditions and material properties used in the experiment [171].

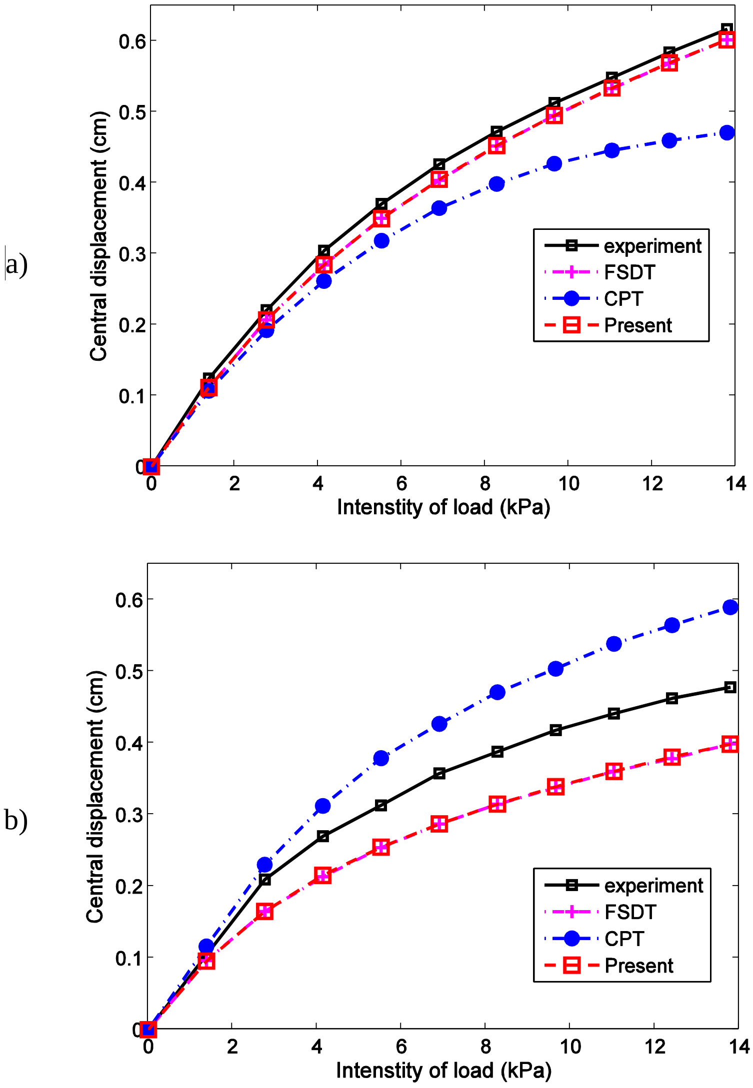

Figure 4.16 The load-deflection curves of: (a) the simply supported orthotropic plate (L = 304.8 mm, h = 3.51 mm) and (b) the clamped [0/90/90/0] crossply plate (L = 304.8 mm, h = 2.44 mm).

4.3.2.2 FGM plate

Let us investigate the Al/ZrO2-2 plate with data given in sub-section 4.3.1.7. The plate is subjected to uniformly distributed load, which is increased sequential to $f_z = -10^7$ N/m^2 after five steps. Figure 4.17 shows the variation of the central deflection $\hat{w} = w/h$ versus load parameter $\bar{P}$ and power index n. It should be noted that index n = 0 corresponds to the ceramic plate, whilst $n = \infty$ indicates the metal plate. As expected, the deflection response of FGM plates is moderate for both linear and nonlinear cases, compared to that of ceramic (stiffer) and metal (softer) plates. One more interesting point may be noted that the nonlinear deflections are smaller than the linear ones, and their discrepancy increases by increasing load. This is due to the stiffer stiffness matrix with additional nonlinear stiffness matrix, $\mathbf{K}_{NL}$, which strongly depends on the deflection. Figure 4.18 plots the stress distributions through the plate thickness of the FGM plate (n=1) via the change of load intensity. It can be seen that the effect of nonlinearity reduces the amplitude of the normalized stresses.

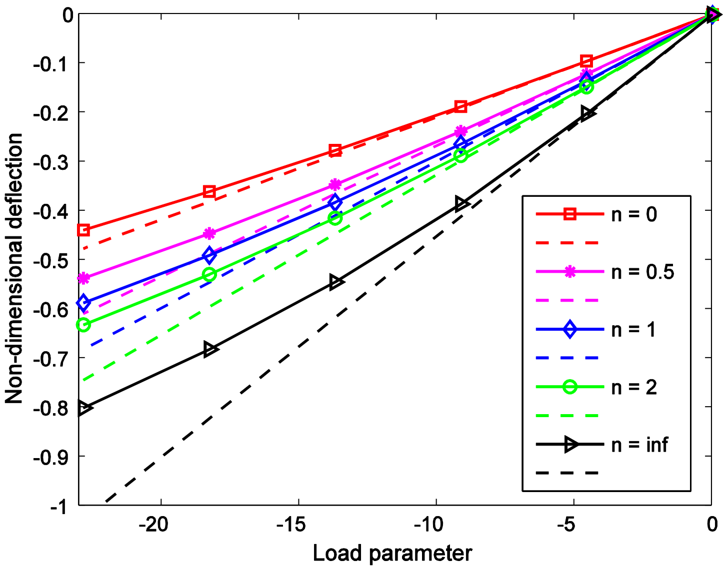

Figure 4.17 Non-dimensional center deflection via load parameter and power index: non-linear results (in solid line) and linear results (in dash line).

By enforcing the temperature field to this plate as T_m = 20°C and T_c = 300°C at the bottom and top surfaces, respectively, the mechanical load versus transverse displacement curves via gradient index are plotted in Figure 4.19. The tendency is observed for nonlinear analysis similar to linear analysis as shown in Figure 4.13 except that the nonlinear deflections are larger than the linear ones under purely thermal load. Because the initial stress stiffness matrix $\mathbf{K}_{\text{th}}$, which is generated by thermal membranes, makes reduction in the overall plate stiffness. Another difference from linear solution is that the nonlinear results cannot be superimposed. For instant, as n = 0 the total deflection $\hat{w} = -0.3963$ is different from a sum of $\hat{w} = -0.4385$ and $\hat{w} = 0.124$ in case of purely transverse and thermal load.

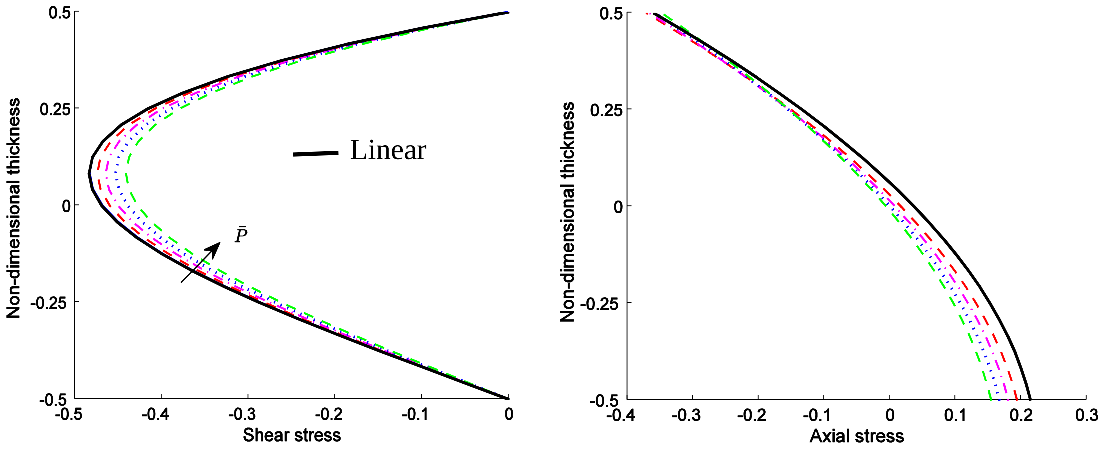

a) The shear stress $\bar{\tau}_{yz}(\frac{L}{2},0,z)$ b) The axial stress $\bar{\sigma}_x(\frac{L}{2},\frac{W}{2},z)$.

Figure 4.18 Effect of the load parameter $\bar{P}$ on the stresses distributions. Increase in load reduces the magnitude of the normalized stresses. Noted that the arrow denotes increase in magnitude of the load parameter.

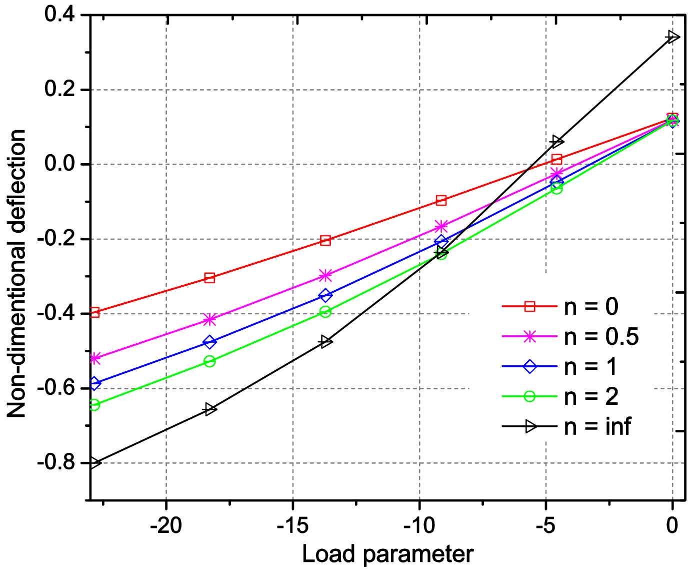

Figure 4.19 Non-dimensional central deflection $\hat{w}$ of FGM plate under thermo-mechanical load.

4.4 Concluding remarks

In this chapter, the plate formulations, based on a combination between NURBS-based isogeometric approach and HSDT models including TSDT, RPT and GSDT, have been applied to stress analysis of FGM plates under thermo-mechanical loadings. The

FGM plates made of a mixture of two distinct material phases varying through the plate thickness is homogenized by two homogenization techniques: the rule of mixture or the Mori-Tanaka scheme. Thanks to higher-order continuity of NURBS functions, the present method allows us to achieve easily the smoothness with arbitrary continuity order compared with the traditional FEM. As a result, the present NURBS formulation naturally fulfils the C^1-continuity of HSDT models. Furthermore, based on using the von Kármán assumptions, the effect of geometric nonlinearity on static analysis is studied. Through various numerical results, some concluding remarks can be drawn:

- By including higher-order terms in the displacement fields, HSDTs can describe more exactly the shear energy part without SCF requirement. They provide better results and more accurate shear stresses than FSDT with the curved shapes through the plate thickness and traction free at the plate surfaces.
- Being different from GSDT and RPT, which naturally and absolutely overcome shear-locking phenomenon, FSDT and TSDT just attain reliable results with limitation of span-to-thickness ratio, $L/h \leq 1000$.
- All HSDT models including TSDT, GSDT and RPT gain very similar results for the FGM plates, which are in excellent agreement with the available solutions in literature. By using four unknown variables, one reduced DOF per each control point, RPT is known as an effective model in analysis the FGM plates because of the reduction in computational cost.
- There is a reduction of thermal deflection in the FGM plates as compared to homogeneous plates. Under thermo-mechanical load, axial stress in FGM plate is also distributed taking advantage of material characteristic with increase of compression at the top (ceramic surface) and decrease of tension at the bottom (metal surface), respectively.
- There is a quite difference between linear and nonlinear solutions. Under transverse load, nonlinear analysis achieves lower displacements because of additional nonlinear stiffness matrix. In case of purely thermal load, due to thermal membrane effect, the overall plate stiffness is reduced. As a result, the nonlinear deflections are larger than the linear ones.

In this thesis, we present GSDT and RPT in general forms based on the distributed function $f(z)$, which is chosen to satisfy the tangential zero value on the top and bottom faces, i.e., $f'(\pm h/2)=0$. Following to this condition, we try to propose a novel function as an inverse tangent form. By using it, the HSDT models gain the best deflection, which is the closest to the quasi-3D models.

Chapter 5 Elastic Instability

5.1 Introduction

In the preceding chapter, we assumed that the plates were bent by transverse loading and the stretching of the middle plane is too small and can be neglected. However, when a slender structure is loaded by in-plane compressions, the plate can be deformed and failed by stretching effect. Under small compressive loading, the plate hardly deforms with any noticeable change in geometry. As load increases to a predetermined magnitude, the structure suddenly experiences a large deformation and may lose its load carrying capacity. This is called buckling phenomenon and also known as structural instability. The load, at which the structure is unstable, is called the critical buckling load or simply critical load.

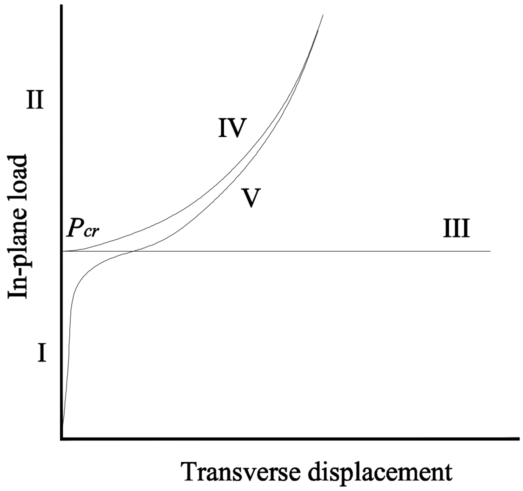

Figure 5.1 The relation between in-plane loading force and deflection at a representative point in a plate.

Plate buckling may be represented by a deflection path plotting in-plane loading force (P) versus the deflection (w) at a representative point on the plate [188] as shown in Figure 5.1. In classical buckling theory, the curve follows the paths I, II and III. That is, with increase in loading P, the curve follows the vertical path (I) upwards known as the primary path, showing no displacement until a critical load P_{cr} (the bifurcation point) is reached. Then, by continuously increasing the in-plane force to overcome the bifurcation point, the curve theoretically may continue up the vertical path (II), or may follow a buckling path, which is horizontal path (III) for the linear idealization or increasing slope (IV) for a nonlinear one considering large displacement assumptions. The latter curve (IV) is also called the secondary or post buckling path that depicts the behaviour of the plate after bifurcation. This behaviour is an important consideration in structural design, especially for slender and lightweight structures. Finally, as the plate has initial deflection (commonly called a geometric imperfection or imperfection), the P-w curve will follow a curved path V because of bending effect. For this type of analysis, no bifurcation phenomenon is observed.

The buckling and post-buckling phenomena are one of the major design criteria of the plate/panel structures for their optimal usage. Thus, study of stability of the plates has been receiving considerable attentions, especially for FGM plates. For examples, Birman [11] was the first person, who studied the buckling of FGM hybrid composite plates under uniaxial compressive loadings. Javaheri and Eslami utilized Kirchhoff's thin plate theory to study the mechanical and thermal buckling of FGM plates [35, 189] and also obtained the closed-form solutions of the critical buckling temperature for FGM plates using Reddy's TSDT [68]. It is concluded that TSDT underestimates the buckling load in comparison with CPT. Najafizadeh and Heydari [69] investigated the thermal stability of circular FGM plates based on HSDT whereas Liew et al. [141] and Lee et al. [190] spent their attention on post-buckling analysis under thermo-mechanical loads. Shen [140] has examined thermal post buckling of FGM plates considering the effect of temperature-dependent thermo-elastic properties of the constituent materials.

In this chapter, we present a simple and efficient formulation relied on the framework of NURBS-based IGA for buckling and post-buckling analyses of FGM plates under thermal and mechanical loads. It is assumed that the plates are flat with no initial imperfection in geometry. The von Kármán nonlinear strain-displacement relation is adopted to study the secondary path (IV). Herein, three types of temperature rise are investigated including: uniform temperature rise, linear and nonlinear temperature change across the plate thickness. Furthermore, the effect of temperature-dependent material properties is considered to lead the nonlinear governing equation to depend on not only unknown displacement but also temperature. Thus, an incremental/iterative approach presented in Section 5.2 is utilized to obtain the temperature-deflection curves. Various numerical examples are given in Section 5.3 to investigate the effect of various parameters, such as length to thickness ratios, plate aspect ratios, gradient index, types of loads and material properties on thermo-mechanical critical load. This chapter is closed by some concluding remarks in Section 5.4.

5.2 Governing equations

5.2.1 Pre-buckling state

By neglecting the inertia and the non-linear terms in the transverse displacement component, the pre-buckling response is obtained by solving a linear set of algebraic equations from Eq. (4.10):

$$\mathbf{K}_L \mathbf{q} = \mathbf{F}^{ext} \tag{5.1}$$

where the external load vector is calculated from the applied in-plane force or temperature rise. Obtained unknown displacements are used to calculate the pre-buckling force $\mathbf{N} = \left[N_x \;\; N_y \;\; N_{xy} \right]^T$ according to Eq. (2.43), which is valid just before the plate buckles

$$\mathbf{N} = \mathbf{A}\boldsymbol{\varepsilon}_L + \mathbf{B}\boldsymbol{\kappa}_1 + \mathbf{E}\boldsymbol{\kappa}_2 - \mathbf{N}^{th} \tag{5.2}$$

Note that in mechanical buckling, we eliminate thermal load, i.e. $\mathbf{N}^{\text{th}} = 0$.

5.2.2 Buckling state

At buckling state, the initial flat plate is buckled with an additional deflection, i.e.,

$$w = w_b \tag{5.3}$$

Let us consider the equilibrium of a small element cut out from the plate by two pairs of planes parallel to *yz* and *xz* planes with the in-plane forces as shown in Figure 5.2.

Projecting these forces into *x* and *y* axes sequentially, we obtain the following equation of equilibrium:

$$\begin{cases} \dfrac{\partial N_x}{\partial x} + \dfrac{\partial N_{yx}}{\partial y} = 0 \\ \dfrac{\partial N_y}{\partial y} + \dfrac{\partial N_{xy}}{\partial x} = 0 \end{cases} \tag{5.4}$$

Then, projecting in-plane force N_x on the z-axis as depicted in Figure 5.2a gives:

$$F_z^1 = -\left(N_x \frac{\partial^2 w_b}{\partial x^2} + \frac{\partial N_x}{\partial x}\frac{\partial w_b}{\partial x} \right) dxdy \tag{5.5}$$

In the same way, projection of N_y on the z-axis is given as:

$$F_z^2 = -\left(N_y \frac{\partial^2 w_b}{\partial y^2} + \frac{\partial N_y}{\partial y}\frac{\partial w_b}{\partial y} \right) dxdy \tag{5.6}$$

And, that of the shear forces N_{xy} and N_{yx} is:

$$F_z^3 = -\left(2N_{xy} \frac{\partial^2 w_b}{\partial x \partial y} + \frac{\partial N_{xy}}{\partial x}\frac{\partial w_b}{\partial y} + \frac{\partial N_{xy}}{\partial y}\frac{\partial w_b}{\partial x} \right) dxdy \tag{5.7}$$

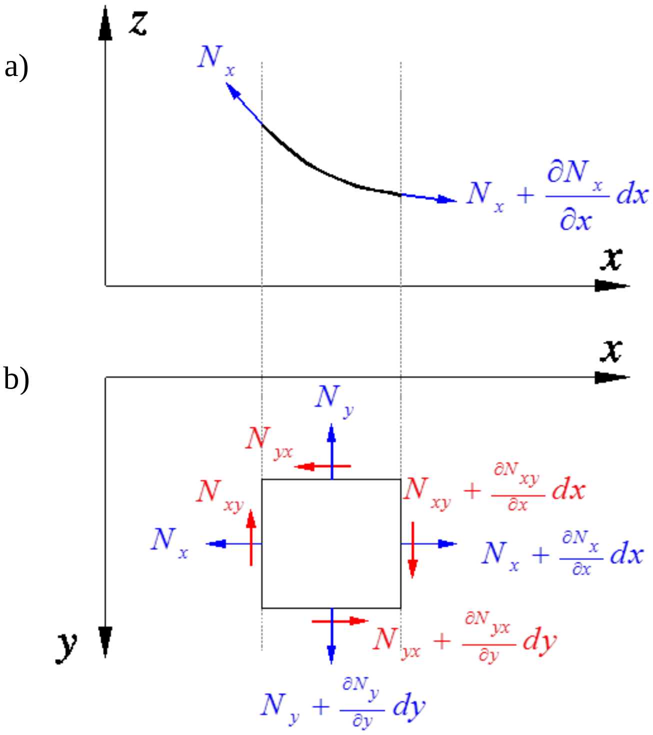

Figure 5.2 In-plane forces in a plate element [191].

Summation of (5.5), (5.6) and (5.7) acting on the element and combining with condition in Eq. (5.4), we obtain the bending energy due to the initial in-plane forces [191] as follows:

$$\delta V = -\int_{\Omega} \delta w_b \left(N_x \frac{\partial^2 w_b}{\partial x^2} + N_y \frac{\partial^2 w_b}{\partial y^2} + 2N_{xy} \frac{\partial^2 w_b}{\partial x \partial y} \right) \mathrm{d}\Omega = \int_{\Omega} \nabla^T (\delta w_b) \hat{\mathbf{N}}_0 \nabla w_b \mathrm{d}\Omega \tag{5.8}$$

where $\hat{\mathbf{N}}_0 = \begin{bmatrix} N_x & N_{xy} \ ; & N_{xy} & N_y \end{bmatrix}$.

Substituting Eq. (5.8) into Eq. (2.47), the governing equation is written as

$$\int_{\Omega} \hat{\boldsymbol{\varepsilon}}_L^T \hat{\mathbf{D}} \delta \hat{\boldsymbol{\varepsilon}}_L \mathrm{d}\Omega - \int_{\Omega} \nabla w_b \hat{\mathbf{N}}_0 \nabla^T (\delta w_b) \mathrm{d}\Omega = 0 \tag{5.9}$$

Equation (5.9) is the plate buckling equation in fundamental form. It should be understood that it is the equation of equilibrium of the plate in a condition of neutral stability. After eliminating the virtual displacement vector $\delta \mathbf{q}$, the linear eigenvalue equation is given by:

$$\left(\mathbf{K}_L - \lambda \mathbf{K}_g \right) \mathbf{q} = 0 \tag{5.10}$$

in which $\mathbf{K}_\mathrm{L}$ and $\mathbf{K}_\mathrm{g}$ are linear and geometric stiffness matrices, calculated according to Eqs. (3.18) and (4.7), respectively and parameter $\lambda \in \mathbb{R}^+$ is the load factor and is multiplied with membrane forces to define the critical buckling load, i.e. $P_{cr} = \lambda N$.

Depending on type of loading, herein, we classify buckling in two classes: mechanical loading and thermal loading. In the former, it is assumed that the pre-buckling force resultants are equal to in-plane compression loads, i.e., $N_x = -N_x^0$, $N_y = -N_y^0$ $N_{xy} = -N_{xy}^0$, whilst in the latter, the pre-buckling thermal force resultants, $\mathbf{N}^{th}$, is estimated according to Eq. (2.45) as follows:

$$\begin{Bmatrix} N_x^{th} \\ N_y^{th} \\ N_{xy}^{th} \end{Bmatrix} = \left(\int_{-h/2}^{h/2} \frac{E_e(z)}{1+\nu_e(z)} \alpha_e(z) \Delta T(z) \mathrm{d}z \right) \begin{Bmatrix} 1 \\ 1 \\ 0 \end{Bmatrix} \tag{5.11}$$

Herein, temperature change is given by:

$$\Delta T = T(z) - T_i \tag{5.12}$$

where T_i is the initial temperature and $T(z)$ is the current temperature, which can be assumed to have various distribution variously through the plate thickness.

Uniform temperature rise: It is assumed that the temperature can be uniformly raised to a constant value $T(z) = T_f \quad \forall z$. Therefore, the critical buckling temperature difference $\Delta T_{cr} = T_f - T_i$ is constant through the plate thickness. Substituting it into Eq. (5.11) leads to:

$$\Delta T_{cr} = N_{cr}^{th} / \tilde{X}$$

where
$$\tilde{X} = \int_{-h/2}^{h/2} \frac{E_e(z)}{1+\nu_e(z)} \alpha_e(z) \mathrm{dz} \tag{5.13}$$

Linear temperature change across the plate thickness: It is assumed that a linear temperature variation across the thickness is given by:

$$T(z) = \left(T_c - T_m\right)\left(\frac{z}{h} + \frac{1}{2}\right) + T_m \tag{5.14}$$

Similar to the previous case, after finding the pre-buckling thermal stress, the critical buckling temperature difference between the ceramic-rich and metal-rich surfaces of the plate, $\Delta T_{cr} = T(h/2) - T(-h/2)$ is computed as:

$$\Delta T_{cr} = \frac{N_{cr}^{th} - \tilde{X}\left(T_m - T_i\right)}{\tilde{Y}}$$

where
$$\tilde{Y} = \int_{-h/2}^{h/2} \frac{E_e(z)\alpha_e(z)}{1+\nu_e(z)} \left(\frac{z}{h} + \frac{1}{2}\right) \mathrm{dz} \tag{5.15}$$

Non-linear temperature change across the plate thickness: For the FGM plate, according to Eq. (2.10), it is seen that the temperature nonlinearly varies through the plate thickness as follows:

$$T(z) = \left(T_c - T_m\right)\eta(z) + T_m \tag{5.16}$$

Substituting Eq. (5.16) into Eq. (5.11), the critical buckling temperature difference between two opposite plate surfaces is found as:

$$\Delta T_{cr} = \frac{N_{cr}^{th} - \tilde{X}\left(T_m - T_i\right)}{\tilde{Z}}$$

where
$$\tilde{Z} = \int_{-h/2}^{h/2} \frac{E_e(z)\alpha_e(z)}{1+\nu_e(z)} \eta(z) \mathrm{dz} \tag{5.17}$$

5.2.3 Post-buckling state

As discussed above (see Figure 5.1), a linear buckling analysis can get the critical load for a particular plate. However, plates are typically capable of carrying considerable additional load before collapse. In some case, this is even several times as much as the critical load [188]. For the post-buckling analysis, the effect of geometrical nonlinearity must be considered by using the von Kármán nonlinear strain-displacement formulation.

In this present work, only thermal post-buckling is studied. By eliminating the mechanical load and the inertia terms, the governing equation (2.57), reduces to (considering $\delta\hat{\boldsymbol{\varepsilon}} = \delta\hat{\boldsymbol{\varepsilon}}_L + \delta\hat{\boldsymbol{\varepsilon}}_{NL}$):

$$\int_\Omega \delta\hat{\boldsymbol{\varepsilon}}^T \hat{\mathbf{D}}\hat{\boldsymbol{\varepsilon}}\mathrm{d}\Omega - \int_\Omega \delta\hat{\boldsymbol{\varepsilon}}_{NL}^T \hat{\boldsymbol{\sigma}}_{th}\mathrm{d}\Omega - \int_\Omega \delta\hat{\boldsymbol{\varepsilon}}_L^T \hat{\boldsymbol{\sigma}}_{th}\mathrm{d}\Omega = 0 \tag{5.18}$$

Substituting Eq. (3.10) into Eq. (5.18), one can obtain the non-linear system of algebraic equation as:

$$\left(\mathbf{K}_L + \mathbf{K}_{NL} - \mathbf{K}_{th}\right)\mathbf{q} = \mathbf{F}_{th} \tag{5.19}$$

where $\mathbf{F}_{th}$ is defined in Eq. (3.25) and $\mathbf{K}_{th}$ is established due to work by pre-stress $\hat{\boldsymbol{\sigma}}_{th}$ as:

$$\int_\Omega \delta\hat{\boldsymbol{\varepsilon}}_{NL}^T \hat{\boldsymbol{\sigma}}_{th}\mathrm{d}\Omega = \int_\Omega \delta\boldsymbol{\varepsilon}_{NL}^T \mathbf{N}^{th}\mathrm{d}\Omega \tag{5.20}$$

Substituting Eq. (2.50) into Eq. (5.20) leads to:

$$\begin{aligned}\int_\Omega \delta\boldsymbol{\varepsilon}_{NL}^T \mathbf{N}^{th}\mathrm{d}\Omega &= \int_\Omega \begin{Bmatrix}\delta w_{,x}\\ \delta w_{,y}\end{Bmatrix}^T \begin{bmatrix} w_{,x} & 0 & w_{,y}\\ 0 & w_{,y} & w_{,x}\end{bmatrix} \begin{Bmatrix} N_x^{th}\\ N_y^{th}\\ N_{xy}^{th}\end{Bmatrix}\mathrm{d}\Omega \\ &= \int_\Omega \begin{bmatrix}\delta w_{,x} & \delta w_{,y}\end{bmatrix} \begin{bmatrix} N_x^{th} & N_{xy}^{th}\\ N_{xy}^{th} & N_y^{th}\end{bmatrix} \begin{Bmatrix} w_{,x}\\ w_{,y}\end{Bmatrix}\mathrm{d}\Omega = \delta\mathbf{q}^T\left(\mathbf{K}_{th}\right)\mathbf{q}\end{aligned} \tag{5.21}$$

For the case of the isotropic plates under uniform temperature rise, the force vector is zero because only membrane forces are generated. And, they are accounted for in the geometric stiffness matrix and have no effect on bending energy. Therefore, the critical buckling parameter is found by solving nonlinear eigenvalue problem:

$$\left(\mathbf{K}_L + \mathbf{K}_{NL} - \lambda\mathbf{K}_{th}\right)\mathbf{q} = 0 \tag{5.22}$$

In the case of FGM plate, because of non-symmetric-through-thickness, temperature rise produces bending moments along with membrane forces, which enforce the FGM plate to deflect. Hence, the bifurcation buckling cannot occur. In such case, the nonlinear equation (5.19) is solved by Newton-Raphson technique as mentioned in Section 4.2. However, for some special case, that is clamped edges, the supports are capable to handle the produced thermal moments. The plate remains un-deformed in pre-buckling state. Therefore, buckling bifurcation phenomenon can occur. The properties of FGM are also a function of temperature as shown in Eq. (2.12). Thus, Eq. (5.22), which is a function of both the nodal variables **q** and temperature $T(z)$, should be solved by the incremental iterative methodology.

Firstly, using thermo-elastic properties at T_m (the final temperature at the plate bottom), the smallest eigenvalue (load factor) and its corresponding eigenvector are obtained from the linear eigenvalue equation, Eq. (5.10). The buckling load, computed from multiplying the initial load with the load factor, is utilized to calculate the critical buckling temperature difference following Eq. (5.13), (5.15) or (5.17) and according to the type of temperature rise. Next, the thermo-elastic properties at $T = T_m + \Delta T_{cr}$ is updated. Besides, the eigenvector is normalized and scaled up to desired amplitude, such as $w_\mathrm{c}/h = 0.1$ (where w_c is the maximum deflection) and then it is used as the displacement vector for evaluation of the nonlinear stiffness. Eq. (5.22) is solved to obtain the load factor and the associated eigenvector. Subsequently, updated temperature T is implemented. Convergence is verified by using a desired tolerance, i.e. $\varepsilon = 0.01$. If this is not satisfied, all the matrices are updated at the updated temperature by current load factor and displacement vector according to current buckling mode shape. Eq. (5.22) is solved again to obtain the load factor and buckling mode shape. This iterative procedure keeps going until the convergence of the thermal buckling temperature is achieved. A brief summary of this procedure is shown in Figure 5.3 with three steps of the stability analysis. It is noted that in each displacement incremental step, the desired amplitude (w_c/h) is kept constant.

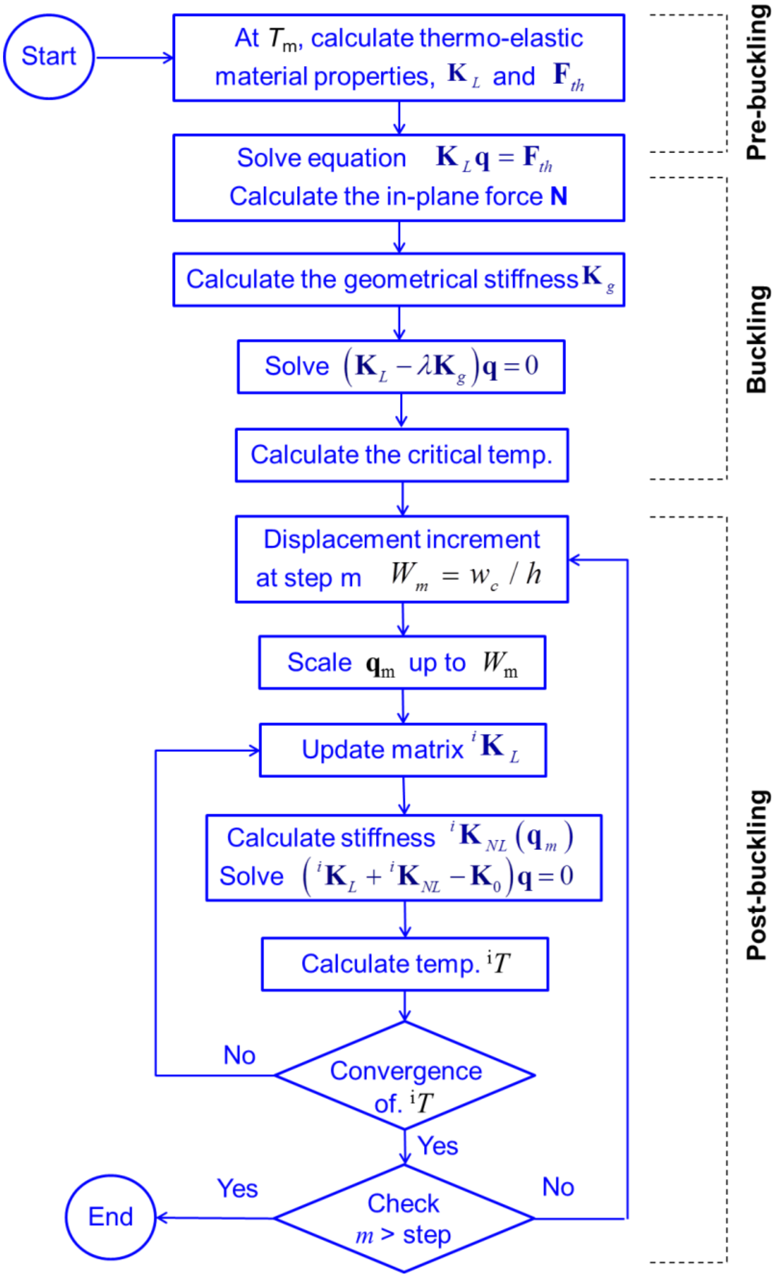

Figure 5.3 Flow chart for thermal post-buckling analysis of plate.

5.3 Numerical results

5.3.1 Mechanical buckling

Let us consider a clamped circular plate of radius R and thickness h subjected to a uniform radial pressure p_0 as illustrated in Figure 5.4. By using knot insertion and order elevation, the domain is discretized into a sequence of refined meshes with 11×11 cubic elements as shown in Figure 5.5. It is observed that, the geometry is described exactly.

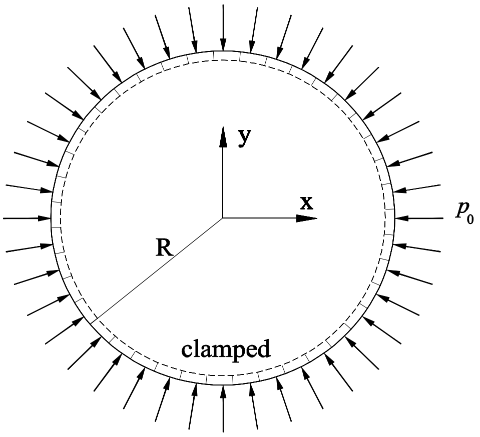

Figure 5.4 *Clamped circular plate under radial compression.*

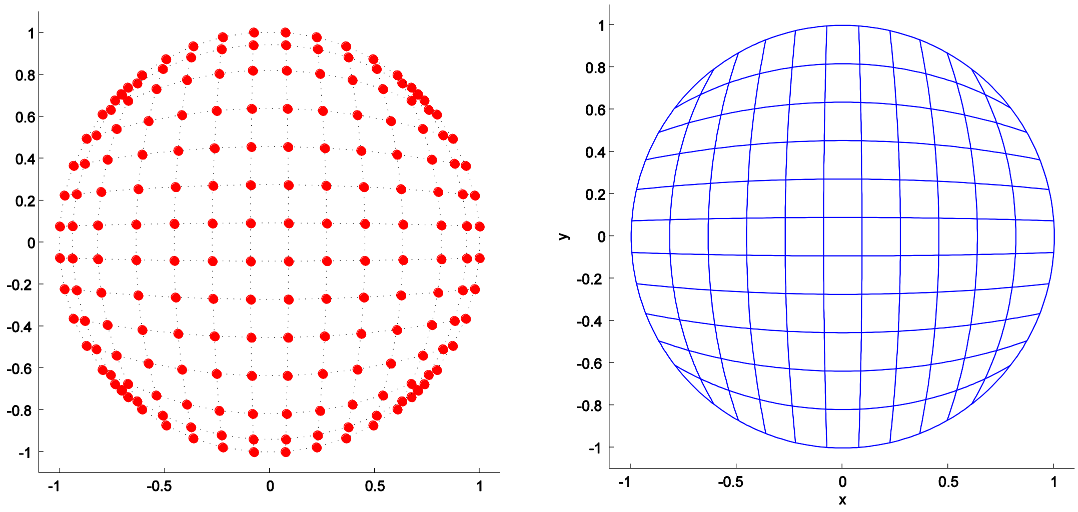

a) Control net (b) Discretization

Figure 5.5 *The meshing of 11×11 cubic elements.*

The plate made from Al/ZrO2-2 is homogenized using the rule of mixture, in which the effective Young's modulus E_e and Poison's ratio ν_e are calculated according to [192]:

$$P_e = P_c V_c + P_m V_m \tag{5.23}$$

where $$V_m = \left(\frac{1}{2} - \frac{z}{h}\right)^n, \ V_c = 1 - V_m$$

Table 5.1 shows the comparison between the present results numerically obtained from IGA using TSDT, RPT and GSDT with closed form solutions published in the literature [192, 193]. It is seen that the results from the three HSDT models are nearly similar and in good agreement with those of unconstrained third-order shear deformation plate theory (UTSDT) [193] with differences of 0.5% and 1.8%. And, the discrepancy between them reduces as plate becomes thinner. Next, the variation of the critical load parameter $\bar{p}_{cr} = p_{cr}R^2 / D_m$ with $D_m = E_m h^3 / \{12(1-\nu^2)\}$ versus the gradient index and the thickness to radius ratio is illustrated in Figure 5.6. It is observed that the critical buckling load increases due to the decrease in the *h/R* ratios and the increase in the value of *n*. As $n > 10$, the gradient index seems to have no effect on the buckling load. In addition, among plate models, TSDT achieves slightly smaller critical buckling load than the counterparts do. In the next examples TSDT, thus, is the preferred model to employ. Figure 5.7 presents the first four buckling mode shapes of the clamped circular Al/ZrO$_2$-2 plate with *h/R* = 0.1 and *n* = 2.

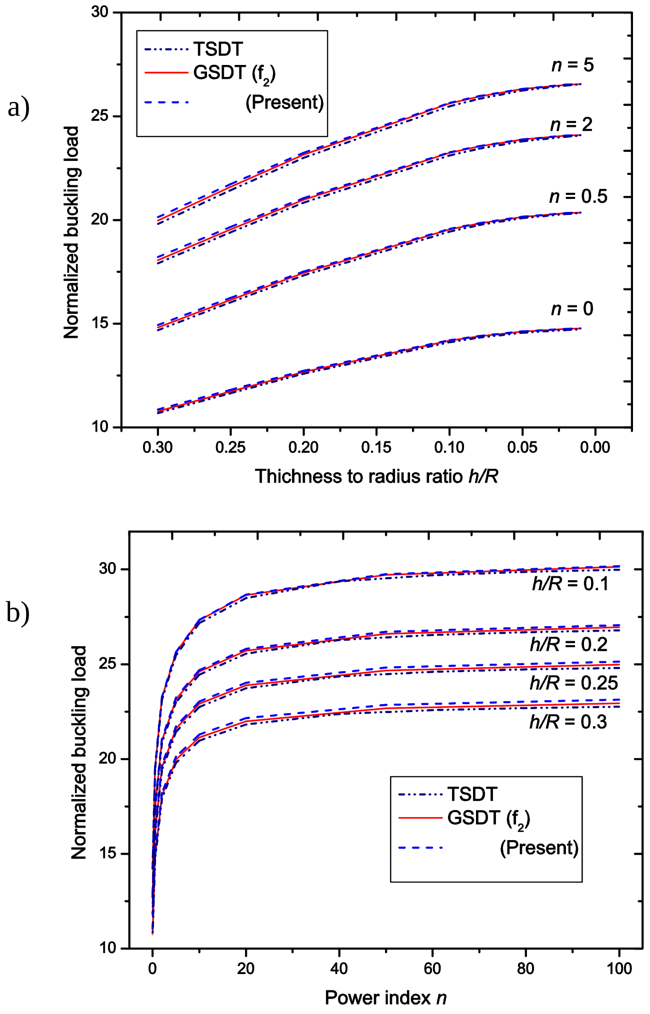

Figure 5.6 The effect of ratio R/h and power index n on the buckling load $\bar{p}_{cr}$.

Table 5.1 Comparison of the buckling load parameter of clamped thick circular Al/ZrO$_2$-2 plate.

Power index n	Plate theory		h/R			
			0.1	0.2	0.25	0.3
0.5	FST [193]		19.423	17.34	16.048	14.711
	TST [192]		19.411	17.311	16.013	14.672
	UTSDT [193]		19.413	17.31	16.012	14.672
	TSDT		19.4391	17.3327	16.0334	14.691
	RPT	f_1	19.4391	17.3327	16.0334	14.6910
		f_2	19.5439	17.4441	16.1492	14.8118
		Present	19.5663	17.518	16.2506	14.9381
	GSDT	f_1	19.532	17.4088	16.1012	14.7511
		f_2	19.5436	17.4493	16.1585	14.825
		Present	19.5662	17.5239	16.2609	14.9526
2	FST [193]		23.057	20.742	19.29	17.77
	TST [192]		23.074	20.803	19.377	17.882
	UTSDT [193]		23.075	20.805	19.378	17.881
	TSDT		23.1062	20.8319	19.4033	17.906
	RPT	f_1	23.1062	20.8319	19.4033	17.9060
		f_2	23.2342	20.9728	19.552	18.0628
		Present	23.2592	21.0569	19.6687	18.2099
	GSDT	f_1	23.2186	20.9256	19.4873	17.9811
		f_2	23.2336	20.978	19.5616	18.077
		Present	23.2589	21.0629	19.6794	18.2255
10	FST [193]		27.111	24.353	22.627	20.823
	TST [192]		27.133	24.423	22.725	20.948
	UTSDT [193]		27.131	24.422	22.725	20.949
	TSDT		27.1684	24.4542	22.7536	20.975
	PRT	f_1	27.1684	24.4542	22.7536	20.9750
		f_2	27.3155	24.6077	22.9117	21.1383
		Present	27.3429	24.6994	23.0389	21.2986
	GSDT	f_1	27.3008	24.5641	22.852	21.0627
		f_2	27.3148	24.6136	22.9228	21.1548
		Present	27.3425	24.7065	23.0515	21.3169

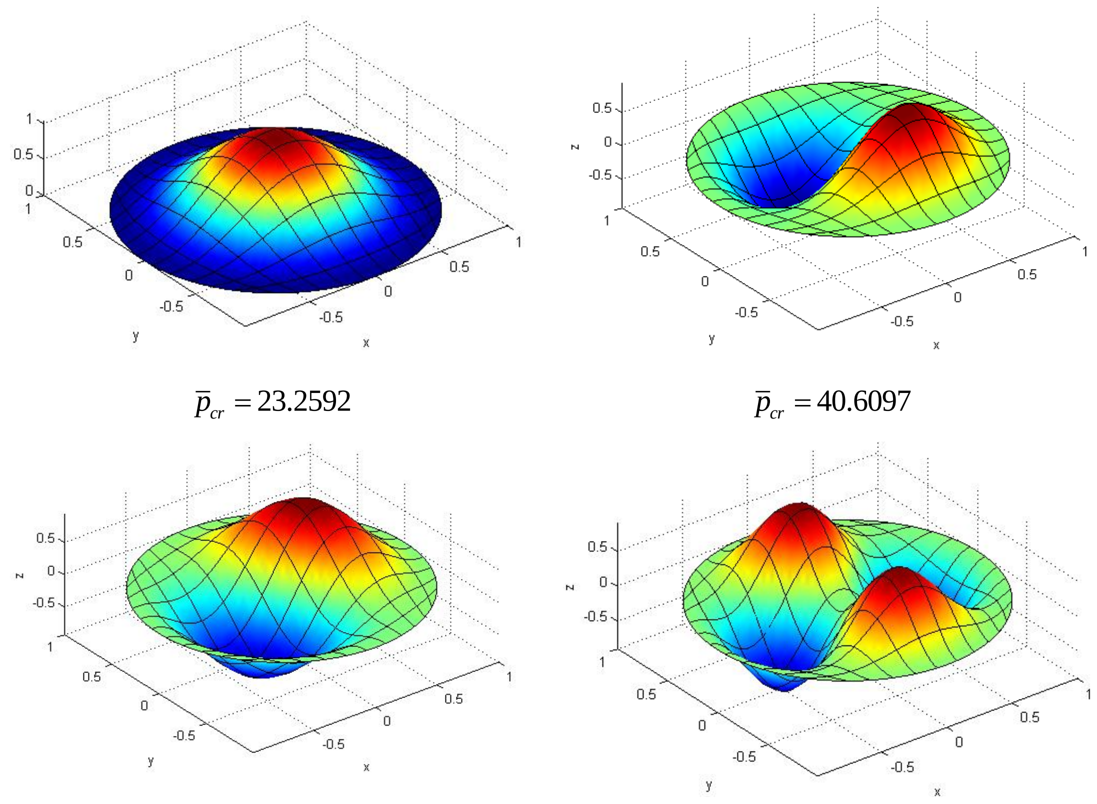

$\bar{p}_{cr} = 23.2592$ $\bar{p}_{cr} = 40.6097$

$\bar{p}_{cr} = 40.6097$ $\bar{p}_{cr} = 60.5599$

Figure 5.7 The first four buckling modes of Al/ZrO$_2$-2 plate with h/R = 0.1 and n = 2.

5.3.2 Thermal buckling

5.3.2.1 Convergence study

Table 5.2 shows the convergence of critical temperature of the circular plate. Here we use quadratic, cubic and quartic elements according to order of NURBS function p = 2, 3, 4, respectively. The convergence of the present elements is shown in Figure 5.8. It is observed that the present results converge well to the closed form solution reported in [194]. Also, the NURBS approximation with the highest order (p = 4) produce the most exact solution.

Table 5.2 Convergence of thermal buckling of the Al/Al$_2$O$_3$ FGM plate (R/h = 100).

Mesh	n = 0				n = 1			
	quadratic (p = 2)	cubic (p = 3)	quartic (p = 4)	Ref. [194]	quadratic (p = 2)	cubic (p = 3)	quartic (p = 4)	Ref. [194]
4×4	274.803	17.5081	13.4059	12.712	150.561	8.4393	6.2543	5.906
8×8	24.5348	12.9758	12.7292		12.419	6.0461	5.9151	
16×16	13.3846	12.7247	12.7173		6.2761	5.9128	5.9093	
20×20	12.9895	12.7201	12.7154		6.0586	5.9106	5.9086	
24×24	12.8496	12.7180	12.7137		5.9816	5.9097	5.9082	

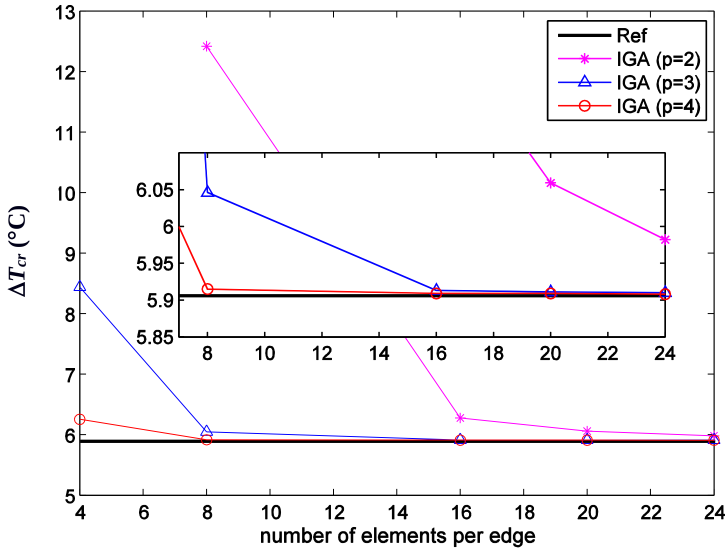

Figure 5.8 The convergence of critical buckling temperature of FGM circular plate.

5.3.2.2 Circular functionally graded plates

In this sub-section, let us consider the clamped FGM plate with meshing as shown in Figure 5.5b and subjected to temperature rise.

Table 5.3 Critical buckling temperature of the clamped circular FGM plate under uniform temperature rise.

n	Method	*h/R*				
		0.01	0.02	0.03	0.04	0.05
0	quadratic	13.3846	51.4591	114.5560	202.2010	313.7709
	cubic	12.7247	50.7470	113.6986	201.0238	312.0007
	quartic	12.7173	50.7029	113.5274	200.5534	310.9643
	FSDT [194]	12.712	50.795	114.090	202.333	315.160
	CPT [194]	12.716	50.866	114.449	203.456	317.914
0.5	quadratic	7.6414	29.2259	65.0216	114.7970	178.2466
	cubic	7.2107	28.7673	64.4906	114.1103	177.2762
	quartic	7.2065	28.7454	64.4077	113.8854	176.7840
	FSDT [194]	7.202	28.783	64.662	114.706	178.731
	CPT [194]	7.204	28.819	64.843	115.237	180.121
1	quadratic	6.2761	23.9771	53.3350	94.1640	146.2188
	Cubic	5.9128	23.5899	52.8871	93.5859	145.4027
	quartic	5.9093	23.5719	52.8191	93.4005	144.9953
	FSDT [194]	5.906	23.603	53.029	94.081	146.815
	CPT [194]	5.907	23.630	53.169	94.520	147.694

Table 5.3 and Table 5.4 exhibit critical buckling temperatures according to uniform and non-uniform temperature distribution, respectively. The obtained results are compared with those of the closed form solutions [194] and the FEM [195] using a three-

node shear flexible plate element based on the field-consistency principle. It is again observed that with the moderate thin plates the present results based on HSDT are lower than those obtained by using FSDT and CPT models. As the plates become thinner, the buckling temperature parameter decreases rapidly and converges to that of the FSDT model [194, 195].

Table 5.4 Critical buckling temperature of the clamped circular FGM plate under nonlinear temperature rise.

n	Method	*h/R*				
		0.01	0.02	0.03	0.04	0.05
0	quadratic	26.7693	102.9183	229.1120	404.4020	627.5418
	Cubic	25.4494	101.4939	227.3972	402.0476	624.0014
	quartic	25.4347	101.4059	227.0547	401.1068	621.9286
	FSDT [195]	25.426	101.576	-	404.258	629.279
	FSDT [194]	25.924	101.455	228.180	404.666	630.320
	CPT [194]	25.433	101.59	228.898	405.821	635.828
0.5	quadratic	20.1554	77.0880	171.5049	302.7956	470.1542
	Cubic	19.0193	75.8784	170.1043	300.9842	467.5945
	quartic	19.0083	75.8205	169.8857	300.3910	466.2963
	FSDT [195]	18.996	75.913	-	302.29	470.746
	FSDT [194]	18.996	75.915	170.594	302.532	471.393
	CPT [194]	19.002	76.009	171.021	304.039	475.061
1	quadratic	16.3386	62.4200	138.8481	245.1389	380.6544
	Cubic	15.3929	61.4121	137.6820	243.6341	378.5297
	quartic	15.3839	61.3652	137.5049	243.1514	377.4691
	FSDT [195]	15.377	61.441	-	244.721	381.164
	FSDT [194]	15.373	61.440	138.037	244.897	381.646
	CPT [194]	15.378	61.512	138.433	246.05	384.453

Figure 5.9 and Figure 5.10 describe the change of buckling temperature using the cubic NURBS element with respect to the thickness-to-radius ratios *h/R* and power indices *n*, respectively. It can be seen that increase in *h/R* ratio enables the plate to resist higher temperature. With increase in the gradient power *n*, the critical temperature values reduce because of the stiffness degradation by the enrichment of the metal material proportion. The change is rapid as $n \leq 2$ and becomes slightly independent with power index $n > 2$, especially in case of uniform temperature distribution. Furthermore, it is also revealed that under non-uniform distribution assumption, FGM plates gain higher buckling temperature than that using uniform temperature rise across the thickness. Figure 5.11 depicted the ratio of critical temperature due to non-uniform and uniform temperature rise via the power index. The ratio depending on material properties due to the value of *n* is always larger than 2 and gains the maximum at 2.638 with $n = 0.5$.

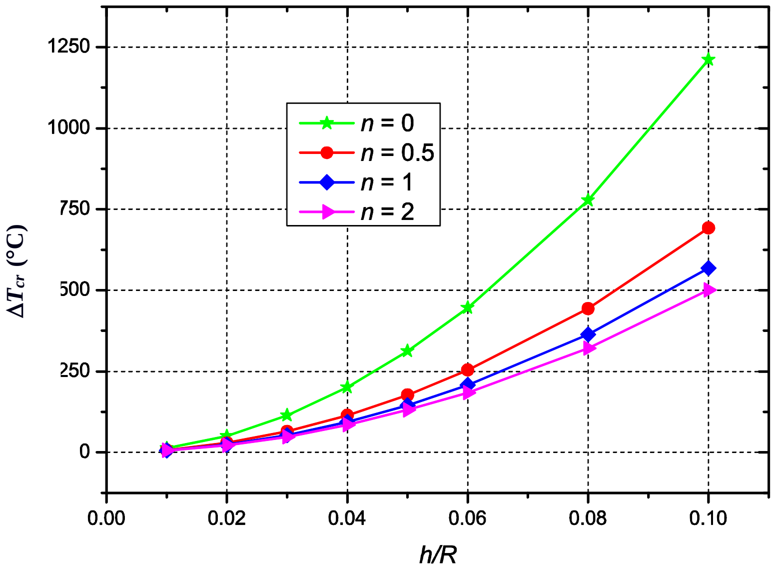

Figure 5.9 The buckling temperature of clamped FGM circular plate under uniform temperature distribution.

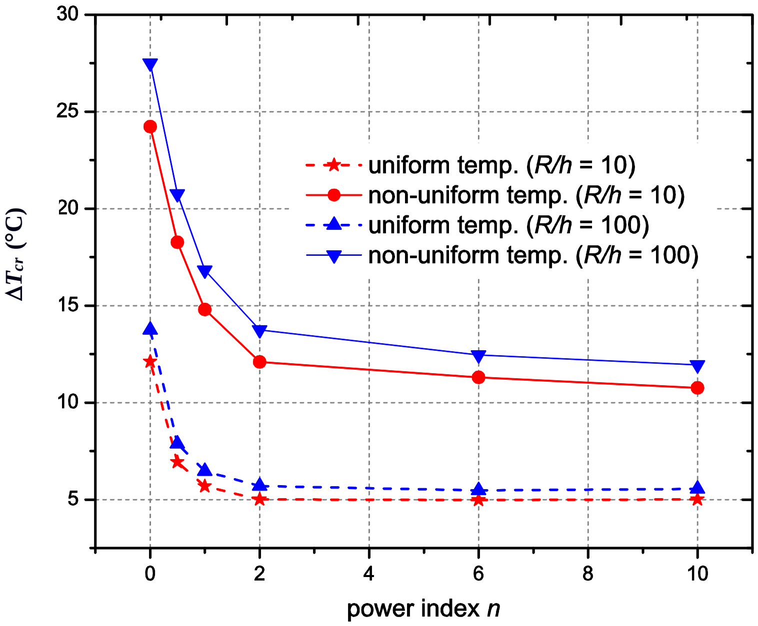

Figure 5.10 Critical buckling temperature of FGM circular plates via power index n. Note that in case of R/h = 10, plotted results are in the form of $\Delta T_{cr}/100$

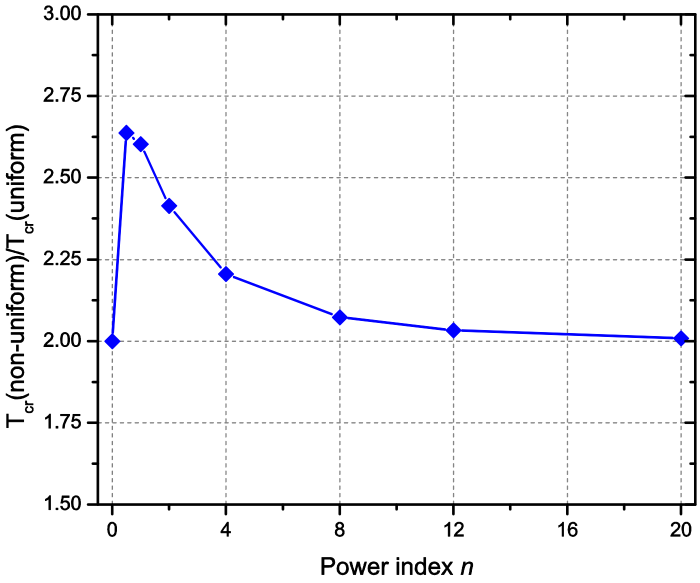

Figure 5.11 The effect of volume fraction exponent on the buckling temperature ratio of FGM circular plate.

5.3.2.3 Rectangular functionally graded plates

Consider the thermal buckling of the Al/Al203 rectangular plate with its dimension: length *L*, width *W* and thickness *h*. The plate is discretized into uniform mesh of quadratic, cubic and quartic elements, respectively. It is assumed that the FGM plate having initial stress free state at T_0 = 0°C is subjected to the temperature T_c at the top surface and T_m = 5°C at the bottom surface. First, the behaviour of the simply supported FGM plates under uniform temperature rise is studied. For comparison purposes, the problems are solved using the eigenvalue approach according to Eq. (5.10) by neglecting the bending moment effect. The critical thermal parameter ΔT_{cr} corresponding to various exponent values, *n*, for both thin and thick plates is summarized in Table 5.5. The obtained solution matches very well with that of the analytical approach reported by Javaheri [68] and the semi-analytical method based on the HSDT proposed by Matsunaga [196].

Table 5.5 Critical buckling temperature of the clamped circular FGM plate under nonlinear temperature rise.

L/h	Method	Power index n					
		0	0.5	1	4	5	10
10	HSDT [196]	1599.294	914.1890	749.26	660.5410	669.402	683.211
	CPT [68]	1709.911	-	794.377	-	726.571	746.927
	TSDT [68]	1617.484	-	757.891	-	678.926	692.519
	Quadratic	1618.9900	923.3422	758.5504	670.5738	679.4528	692.8362
	Cubic	1618.7752	923.2171	758.4422	670.4712	679.3494	692.7331
	Quartic	1618.7468	923.1991	758.4267	670.4594	679.3379	692.7225
100	HSDT [196]	17.087	9.7068	7.939	7.1297	7.259	7.462
	CPT [68]	17.099	-	7.943	-	7.265	7.469
	TSDT [68]	17.088	-	7.939	-	7.26	7.462
	Quadratic	17.1152	9.6995	7.9538	7.1409	7.2697	7.4719
	Cubic	17.0967	9.6876	7.9437	7.1342	7.2633	7.4659
	Quartic	17.0913	9.6842	7.9409	7.1322	7.2614	7.4641

The FGM plates, however, under simply supported boundary conditions exhibits no bifurcation type of instability except for the homogeneous plates [197] because of the structural asymmetry through thickness. The governing equation (5.10), therefore, must be solved with the existence of the load vector $\mathbf{F}^{\text{ext}}$, which is defined in Eq. (3.25). Note that the equilibrium equation is solved linearly based on the classical buckling theory without the nonlinear effect. Figure 5.12 reveals the influence of the temperature field on the central displacement w/h of the simply supported FGM plates. Considering the effect of the geometric stiffness, the total structure stiffness reduces according to temperature increment. This makes the plate weaker and more flexible. As the gradient temperature ΔT_{cr} is large enough, the deflection increases rapidly without depending on the rise of thermal load. This is unreal because as deflection is large enough, i.e. $w/h > 1$, the von Kármán strain needs to be considered in the strain tensor. Thus, full equilibrium equation, as Eq. (5.19), will be established in order to exactly describe this situation. This problem will be re-investigated in the post-buckling section. Under this temperature field which is higher at the top surface than at the bottom one, the plate has an upward deflection as shown in Figure 5.13.

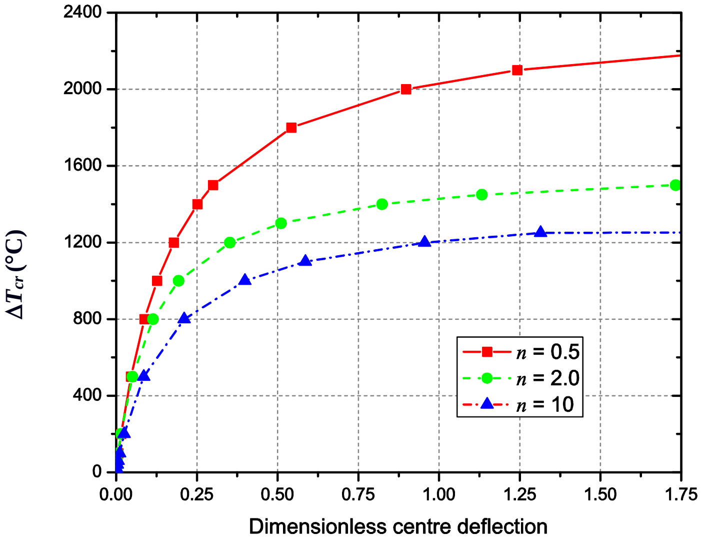

a) *L/h* =10

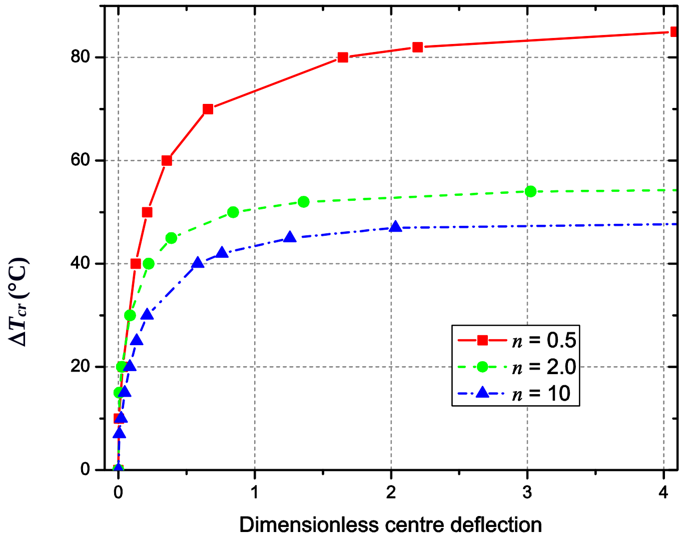

b) *L/h* = 50

Figure 5.12 The central deflection of the simply supported FGM plates via the power indices n and the length-to-thickness ratio L/h.

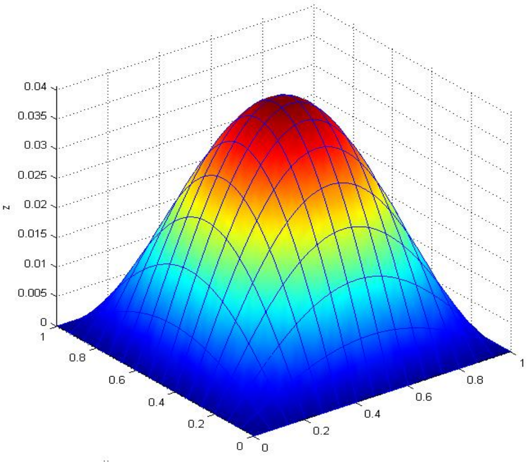

Figure 5.13 The deflection of the simply supported plate (L/h = 10) under temperature rise.

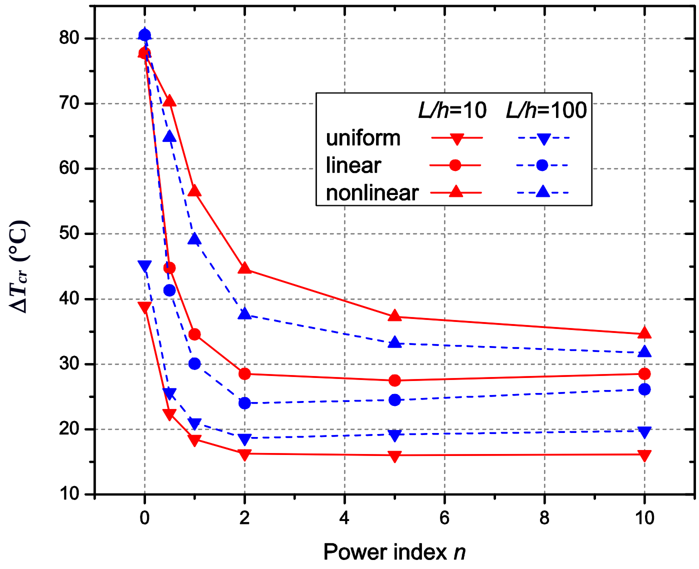

Figure 5.14 Critical buckling temperature of clamped FGM plates versus n: solid line: L/h=10 (ΔT_{cr} /100); dash line: L/h=100.

Next, the relation between critical buckling temperature ΔT_{cr} and power index n under three types of thermal distribution for the clamped FGM plates is investigated. Note that, in case of thick plate ($L/h = 10$), the critical temperature, ΔT_{cr}, is divided by 100. The clamped edge support neutralizes the extension-bending coupling [197]. This helps the plate to prevent the occurrence of the initial transverse deformation under temperature field [198]. Hence, the buckling bifurcation type is exhibited. In Figure 5.14, it can be seen that for homogeneous plates, the non-uniform thermal distribution becomes in the linear form. The results obtained for the two cases are therefore identical. Moreover, the same conclusions for the circular plates in the previous sub-section are obtained for the rectangular plates such as: ΔT_{cr} reduces according to increase in power index *n* or length to thickness ratio *L/h* and the critical gradient ΔT_{cr} using nonlinear distribution is higher than that of linear or uniform distribution.

5.3.3 Thermal post-buckling

In this sub-section, we focus on a study of the nonlinear behaviour of the plates under uniform, linear and non-linear temperature distribution through the plate thickness. The plates are constrained on all edges by clamped or simply supported conditions, which are divided in two cases: movable and immovable in the in-plane directions:

$$\text{Movable edge (SSSS1)}: \quad \begin{cases} v_0 = w_0 = \beta_y = 0 & \text{on } \ x = 0,\ L \\ u_0 = w_0 = \beta_x = 0 & \text{on } \ y = 0,\ W \end{cases} \tag{5.24}$$

$$\text{Immovable edge (SSSS2)}: \quad \begin{cases} u_0 = v_0 = w_0 = \beta_y = 0 & \text{on } \ x = 0,\ L \\ u_0 = v_0 = w_0 = \beta_x = 0 & \text{on } \ y = 0,\ W \end{cases} \tag{5.25}$$

5.3.3.1 Isotropic plates

In this section, two examples, for which solutions are available in the literature, are considered in order to validate the efficiency of the present method for the thermal instability. Firstly, the thermal post-buckling temperature – deflection curve of a simply supported square plate (*L/h* = 10, $\nu = 0.3$, $\alpha = 10^{-6}$/°C) under uniform temperature rise is plotted in Figure 5.15. The obtained results are compared with those of Bhimaraddi and Chandashekhara [199] using the single mode approach and the parabolic shear deformation theory and the closed-form solutions by Shen [140] based on higher-order shear deformation plate theory. Herein, it is evident that identical results are obtained in comparison with Shen's solutions for both perfect and imperfect plates (initial deflection $w^* / h = 0.1$) even in the dimensionless critical temperature $\Delta T_{cr}^* = \alpha \Delta T_{cr} \times 10^4$, which has a value of 119.783°C [140].

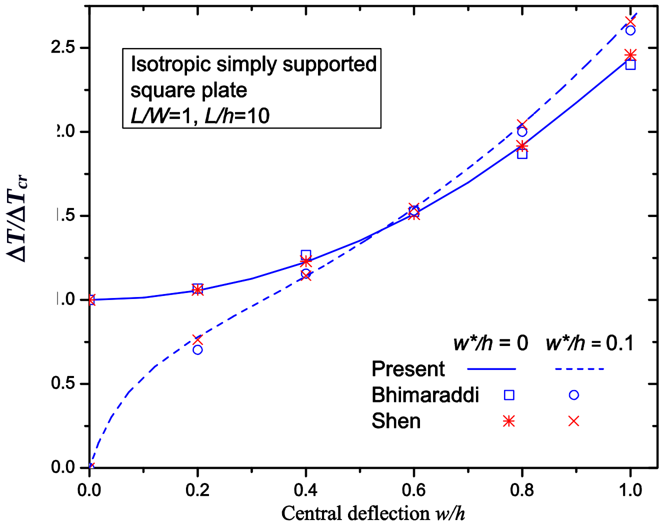

Figure 5.15 Temperature-deflection curve of an isotropic square plate.

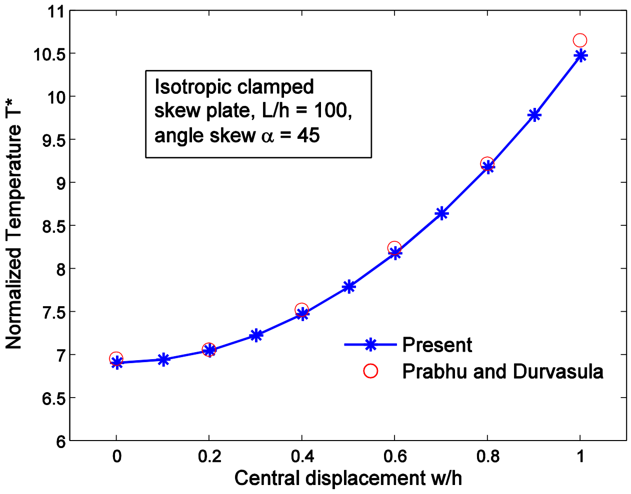

Figure 5.16 Temperature-deflection curve of a clamped isotropic skew plate.

Secondly, the comparison of the post-buckling path of a clamped skew plate (skew angle = 45°, E = 1GPa, $\nu = 0.3$, α = 10^{-6}/°C) with that of Prabhu and Durvasula [200] is depicted in Figure 5.16. In this example, the temperature is normalized as $T^* = T_{cr} E\alpha L^2 h / (\pi^2 D)$ with the flexural rigidity $D = Eh^3 / 12(1-\nu^2)$. A good agreement is observed again in the comparison study.

5.3.3.2 Temperature-independent material Al/Al$_2$O$_3$ plate

Let us continue studying the problem in section 5.3.2.2 with the thermal post-buckling analysis. Herein, the plate is made from Al/Al$_2$O$_3$, for which material properties are assumed to be independent of temperature. Figure 5.17 shows the effect of power index *n* on the thermal post-buckling paths of the FGM plates subjected to the uniform and non-linear temperature rise. Noted that in case of nonlinear temperature rise, it is assumed that no temperature change in the bottom of the plate, $\Delta T_m = 0$. Some remarks are concluded:

- The thermal resistance of the FGM plates reduces due to increase in the material gradient index, *n*, because of the stiffness degradation by the higher metal inclusion, i.e., the buckling strength is highest if the plate is fully-ceramic ($n = 0$) and lowest if the homogeneous metal plate is retrieved (*n* = infinitive).
- If we can keep the temperature varies non-uniformly through the thickness, FGM plates can resist higher buckling temperature.
- The clamped plates exhibit a bifurcation-type of instability, which is vertically symmetric.
- It is also observed that after getting the bifurcation temperature, the post-buckling temperature increases monotonically with the increase in the transverse displacement and suddenly drops to the secondary instability path. The transition from primary post-buckling path to the secondary one is caused by redistribution of post-buckling displacement mode shape. The maximum transverse displacement shifts from the plate centre towards one plate corner. This phenomenon is similar to what reported for angle-ply composite plate by Singha et al [201] and for FGM plate by Prakash et al. [197, 202]. After the secondary instability, the post-buckling temperature slightly increases due to increase in deflection. This point is clearly illustrated in Figure 5.18.

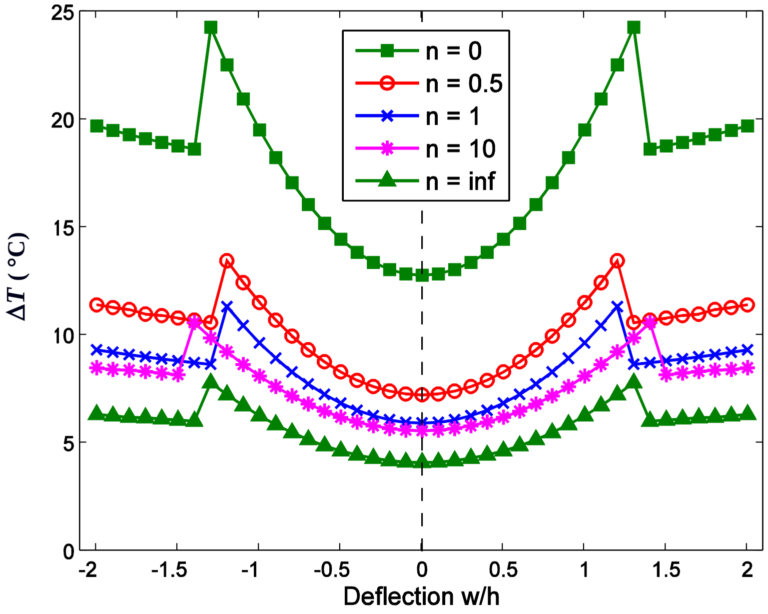

a) Uniform temperature rise

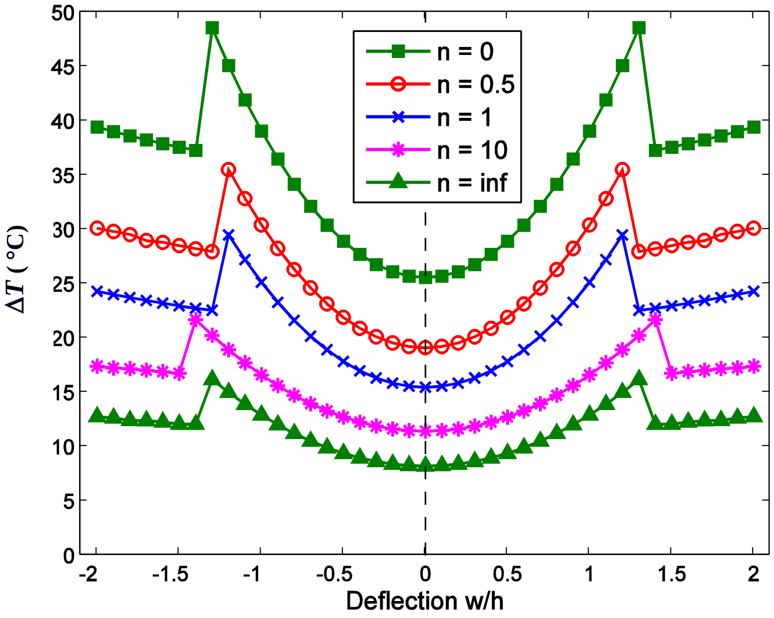

b) Nonlinear temperature rise

Figure 5.17 Bifurcation buckling paths of the clamped circular Al/Al_2O_3 plate (R/h=100) under uniform and nonlinear temperature rise.

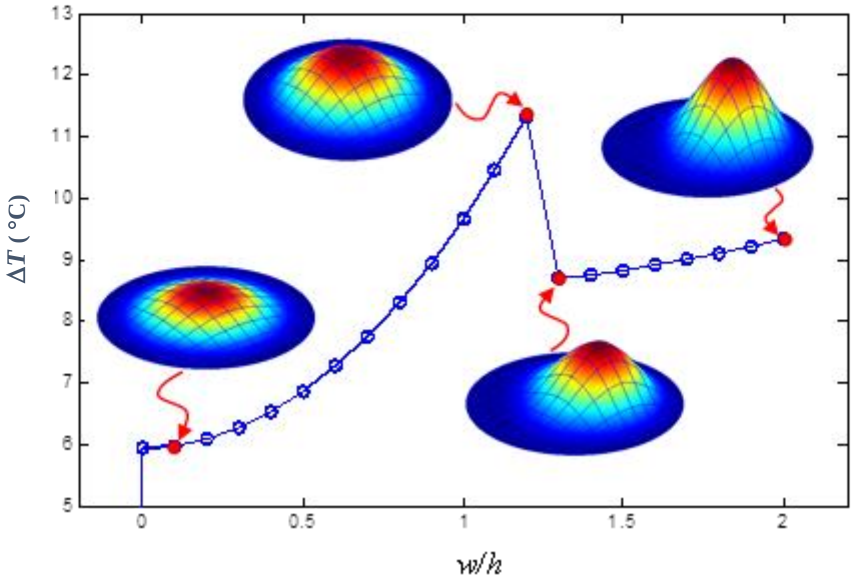

Figure 5.18 Buckling modes of the clamped circular Al/Al$_2$O$_3$ plate (n =1, R/h = 100) under uniform temperature rise.

Next, the nonlinear behaviour of simply supported thin square Al/Al$_2$O$_3$ plate under nonlinear temperature distribution is investigated. The temperature-maximum deflection curves using various values of gradient index are shown in Figure 5.19. It is noted that, being different from homogeneous plates, which have bifurcation buckling paths, FGM plates bend as soon as the thermal load is applied. Because the presence of extension-bending coupling effect produces the bending moment ($\mathbf{M}_{th}$ and $\mathbf{P}_{th}$), the plates bend toward to the upper side. In Figure 5.20, for comparison purpose, the nonlinear bending behaviour of Al/Al$_2$O$_3$ plate (n = 1) under uniform, linear and nonlinear temperature rise is studied. Herein, the plate boundaries are constrained by two simply supported conditions: movable edges (SSSS1) and immovable edges (SSSS2). It is found that at an enough high temperature level, the uniform temperature distribution produces more transverse displacement in the plates than linear and nonlinear temperature distributions. In addition, the plate with SSSS1 boundary condition undergoes smaller deformation than that having SSSS2. Because of movability of in-plane displacements around its edges (except four corners), the thermal effect is reduced as shown in Figure 5.21. It should be noted that, for clear vision, the in-plane displacements are scale by 1000.

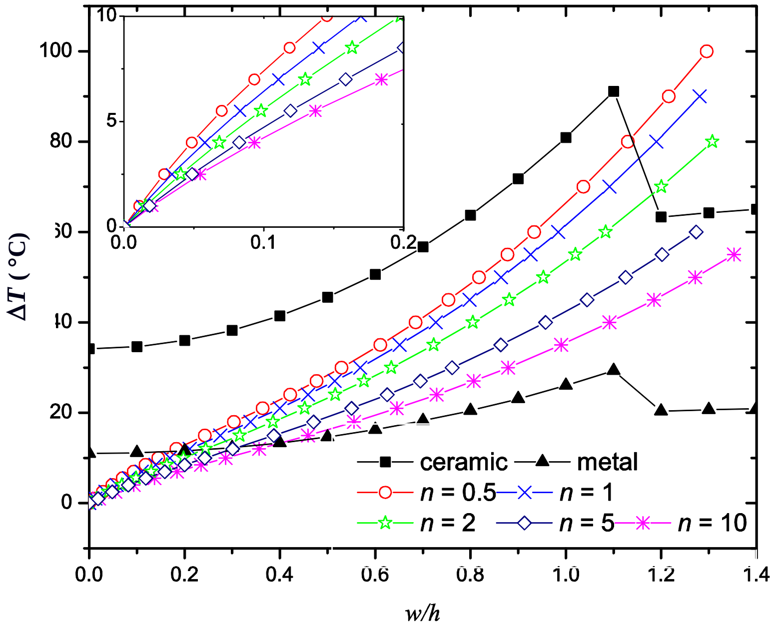

Figure 5.19 Thermal post-buckling paths of SSSS2 square Al/Al$_2$O$_3$ plate (L/h = 100) under nonlinear temperature rise.

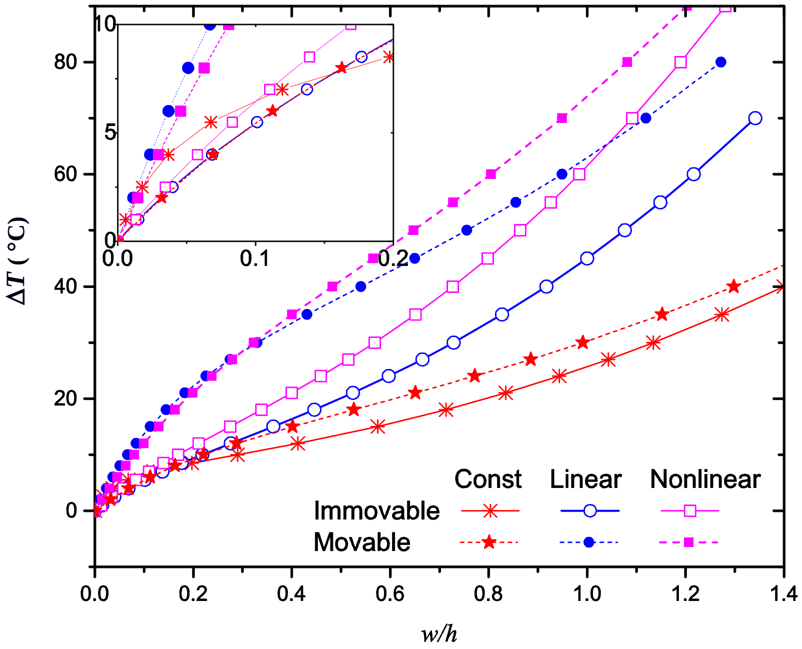

Figure 5.20 Thermal post-buckling paths of the Al/Al$_2$O$_3$ plate (n = 1, L/h = 100).

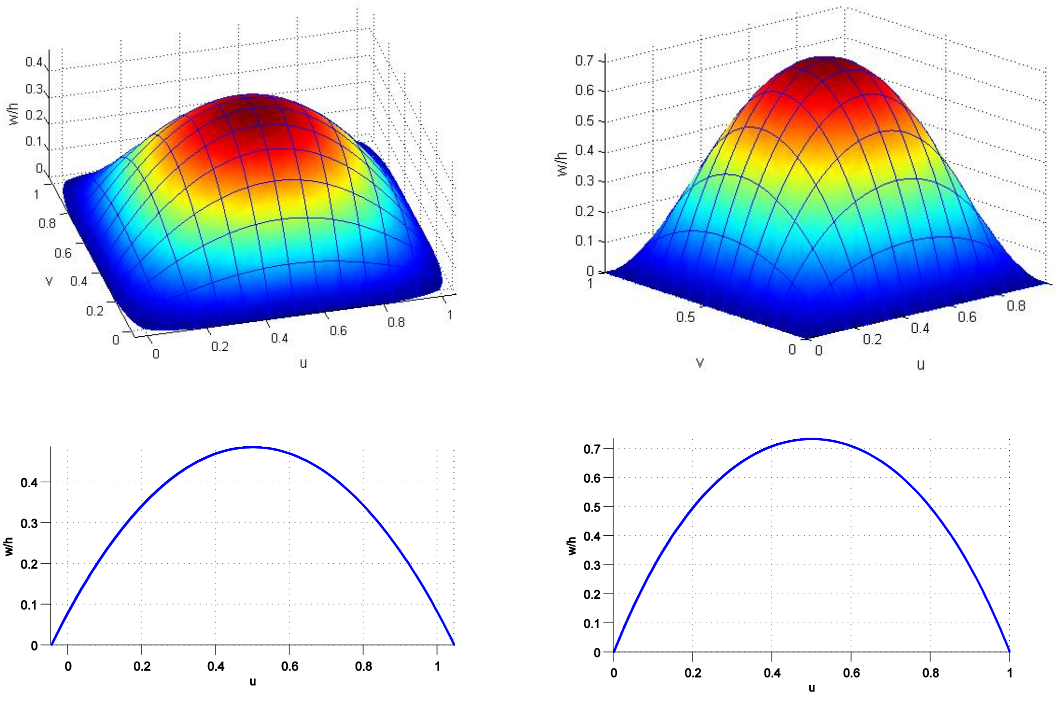

a) Movable edges (SSSS1) b) Immovable edges (SSSS2).

Figure 5.21 Displacement of Al/Al_2O_3 plate ($n = 1$) at $\Delta T = 40$℃ under types of boundary condition: Whole plate profile (upper) and thermal deflection at cross section $y = W/2$ (lower).

5.3.3.3 Temperature-dependent material Si_3N_4/SUS304 plate

In this section, the thermal post-buckling behaviour of temperature-dependent material square plate, made of Silicon nitride (Si3N4) and Stainless steel (SUS304), is investigated. Their material properties are functions of temperature following Eq. (2.12) with the coefficients listed in Table 5.6 [157].

Table 5.6 Temperature dependent coefficients of Si_3N_4 and SUS304

Material	Property	P_{-1}	P_0	P_1	P_2	P_3
Silicon nitride Si_3N_4	E (Pa)	0	3.4843e11	-3.0700e-4	2.1600e-7	-8.946e-11
	ν	0	0.24	0	0	0
	α (1/K)	0	5.8723e-6	9.0950e-4	0	0
	k (W/mK)	0	13.723	-1.0320e-3	5.47e-7	-7.88e-11
Stainless steel SUS304	E (Pa)	0	2.0104e11	3.0790e-4	-6.534e-7	0
	ν	0	0.3262	-2.00e-4	3.80e-7	0
	α (1/K)	0	1.2330e-5	8.0860e-4	0	0
	k (W/mK)	0	15.379	-1.26Ee-3	2.09e-6	-7.22e-10

An example of the effect of temperature change on material properties of Si_3N_4/SUS304 FGM plate, i.e. Young modulus is illustrated in Figure 5.22. It is observed that increase in temperature reduces Young modulus magnitude for both isotropic (n = 0) and FGM plates (n = 1, 10).

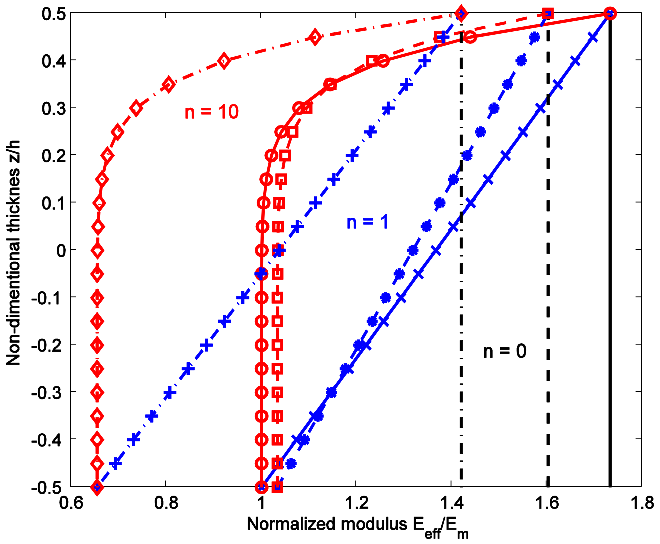

Figure 5.22 The effective Young modulus of Si_3N_4/SUS304 plate at sepcified temperature: T=0 K (solid line), T=300 K (dashed line), T=1000 K (dash dot line).

Figure 5.23 reveals the thermal post-buckling behaviours for Si_3N_4/SUS304 FGM plate with various power indices n =0, 1, 10. The post-buckling paths for temperature-dependent and temperature-independent are presented in solid and dashed curves, respectively. Herein, the results considering temperature-independent material property (values are estimated at T_0 = 300K) are also presented for comparison purpose. It is observed that the thermal post-buckling curve becomes lower when considering the thermal dependent properties and increase in value of n. Furthermore, with thin plate (L/h=100), the discrepancy between temperature-independent solutions and temperature-dependent solutions is insignificant due to the very small buckling temperature. As expected, with an increase in the length-to-thickness ratio, the critical buckling temperature increases accordingly.

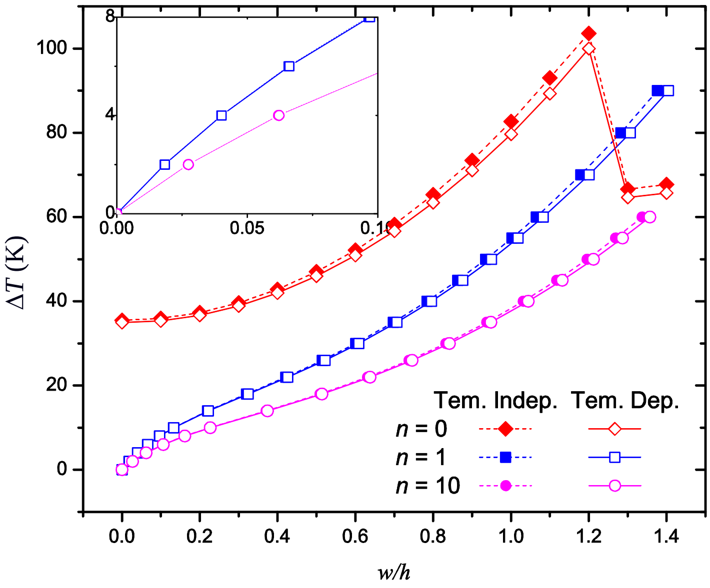

a) *L/h* =100

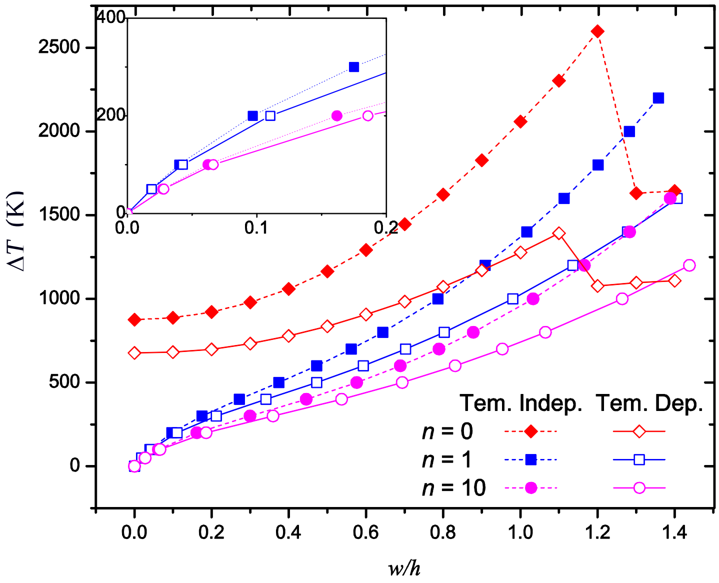

b) *L/h* =20

Figure 5.23 Thermal post-buckling paths of Si_3N_4*/SUS304 FGM plate via various power indices and length-to-thickness ratios L/h.*

5.4 Concluding remarks

This chapter presents a simple and efficient formulation relied on the framework of NURBS-based IGA for elastic instability analysis of the FGM plates under thermal and mechanical loads. The problem can be classified into two categories: buckling and post-buckling analyses. The former with assumption that the plates are flat with no initial imperfection in geometry, is solved by eigenvalue analysis, whilst the latter, which considers the von Kármán assumptions, is solved by an incremental/iterative approach. Through various numerical results, some concluding remarks can be drawn:

- In the FGM plates, there are non-symmetric material properties and temperature field through the plate thickness. Therefore, no bifurcation type of instability occurs for simply supported conditions. Under this boundary condition, the plate exhibits bending behaviour because of extra extension-bending coupling or thermal moment. The clamped boundary condition is capable to neutralize the extra bending. Thus, the buckling bifurcation type can be exhibited.
- The critical buckling value of FGM plates increases due to increase in plate thickness and also decrease in the gradient index n because of the material degradation by enrichment of ceramic constituent – higher Young modulus.
- The critical thermal gradient ΔT_{cr} of the FGM plates under nonlinear temperature distribution is greater than that under uniform or linear ones.
- The difference in thermal resistance in the FGM plates with and without considering temperature-dependent material property is substantially higher in the thick plate as compared to the thin one.

Chapter 6 Dynamic Analysis

6.1 Introduction

The dynamic analysis of FGM structures plays an important role in various branches of engineering applications, particularly aerospace and other area of transportation. Thus, there are many researchers paying their attention to this problem that can be classified into two main groups: 1) free vibration analysis, which studies the fundamental natural frequencies and corresponding distributions of model displacements and 2) forced vibration analysis related to the transient response of the plate structures under dynamic loading. Various methods have been employed so far for the vibration analysis of FGM plates. Vel and Batra [24] have presented an exact solution using a 3D elastic theory for the free and forced vibration of simply-supported rectangular FGM plates. Reddy and Chen [25] studied the harmonic vibration problem of FGM plates with 3D asymptotic approach. Matsunaga [58] predicted closed form analytical natural frequencies of simply supported FGM plates using the method of power series expansion of displacement components. Ref. [12] concluded that solution of eigenvalue problems using 3D elasticity theories is hard to obtain particularly, when the material properties are graded according to power law. Moreover, the analytical solutions for practical applications are highly mathematical complexity. Due to these limitations, the numerical methods have become the most widely used computational tools for plate structures [39, 44, 46, 48, 72].

In this chapter, we develop the NURBS-based isogeometric finite element method to study free and forced vibrations of FGM plates. In the former, without the force vector, the fundamental natural frequencies are obtained by solving the eigenvalue analysis, whilst the latter considers the applied forces and the von Kármán strain. Thus, the geometrically nonlinear equation of dynamic system, which is dependent upon both time domain and unknown variables, is solved by the Newmark time-stepping scheme in association with the Picard iteration method.

This chapter is outlines as follows. The general governing equations for free vibration and geometrically nonlinear transient problems are introduced in Section 6.2. Using HSDT models that accounts for the transverse shear strains and rotary inertia, the present method not only overcomes naturally shear-locking phenomenon but also produces excellent results as compared with those available in the literature. Numerical results of the vibration analysis presented in Section 6.3 investigate the effect of the gradient index, boundary conditions, length to thickness ratios as well as the loading on the response of various shapes of FGM plates. Finally, some concluding remarks are reported in Section 6.4.

6.2 Governing equations

For this problem, we investigate separately two categories: free vibration and geometrically nonlinear transient analysis.

6.2.1 Free vibration

For free vibration problem, after eliminating the load vector and the nonlinear effect, the governing equation, Eq. (3.17), reduces to a simple form:

$$\mathbf{K}_L\mathbf{q}+\mathbf{M}\ddot{\mathbf{q}}=0 \tag{6.1}$$

The solution is assumed to be periodic:

$$\mathbf{q}(\mathbf{x},t)=\mathbf{Q}_0(\mathbf{x})e^{i\omega t} \tag{6.2}$$

where $\omega\in\mathbb{R}^+$ is the frequency of natural vibration of the plate. Substituting Eq. (6.2) into Eq. (6.1) yields:

$$\left(\mathbf{K}_L-\omega^2\mathbf{M}\right)\mathbf{q}=0 \tag{6.3}$$

Because of non-zero displacement, the natural frequency is obtained by solving the eigenvalue problem as:

$$\left|\mathbf{K}_L-\omega^2\mathbf{M}\right|=0 \tag{6.4}$$

6.2.2 Geometrically nonlinear transient

In case of geometrically nonlinear transient analysis of the plate, the governing equation is the same as Eq. (3.17):

$$\mathbf{Kq}+\mathbf{M}\ddot{\mathbf{q}}=\mathbf{F}^{ext} \tag{6.5}$$

It is observed that the equation of dynamic system in Eq. (6.5) is dependent on both time domain and unknown displacement vector. To discretize this problem, the Newmark's integration scheme in association with the Picard methods is employed. The dynamic problem is solved in step-by-step for a number of equal time intervals, Δt. Once the displacement at time $t=(m+1)\Delta t$ is known, its first and second derivatives, i.e. velocity and acceleration, are sought implicitly as follows:

$$\ddot{\mathbf{q}}_{m+1}=\frac{1}{\beta\Delta t^2}(\mathbf{q}_{m+1}-\mathbf{q}_m)-\frac{1}{\beta\Delta t}\dot{\mathbf{q}}_m-\left(\frac{1}{2\beta}-1\right)\ddot{\mathbf{q}}_m \tag{6.6}$$

$$\dot{\mathbf{q}}_{m+1}=\dot{\mathbf{q}}_m+\Delta t(1-\gamma)\ddot{\mathbf{q}}_m+\gamma\Delta t\ddot{\mathbf{q}}_{m+1} \tag{6.7}$$

Herein, we choose two variables β = 0.25 and γ = 0.5 following the average acceleration method, an unconditional stable method in the Newmark family method [203]. As it can be seen, the information at current is calculated based on the converged solutions at the previous time step $t = m\Delta t$. Hence, to start this process, the initial conditions are assumed to be known. In this study, the initial conditions are zero displacement, velocity and acceleration at time $t = 0$ [203]. Substituting Eq. (6.6) into Eq. (6.5), a quasi-static equation is obtained as:

$$\hat{\mathbf{K}}_{m+1}\mathbf{q}_{m+1}=\hat{\mathbf{F}}_{m+1} \tag{6.8}$$

where $\hat{\mathbf{K}}_{m+1}$ and $\hat{\mathbf{F}}_{m+1}$ are the effective stiffness matrix and force vector at time $(m+1)\Delta t$

$$\begin{gathered}\hat{\mathbf{K}}_{m+1}=\mathbf{K}_{m+1}+\frac{1}{\beta\Delta t^2}\mathbf{M}\ , \\ \hat{\mathbf{F}}_{m+1}=\mathbf{F}^{ext}_{m+1}+\mathbf{M}\left[\frac{1}{\beta\Delta t^2}\mathbf{q}_m+\frac{1}{\beta\Delta t}\dot{\mathbf{q}}_m+\left(\frac{1}{2\beta}-1\right)\ddot{\mathbf{q}}_m\right]\end{gathered} \tag{6.9}$$

Referring to Eq. (6.9), all parameters are known from the converged solutions at previous time step, i.e. $t = m\Delta t$ except the stiffness matrix $\mathbf{K}_{m+1}$, which nonlinearly depends on the displacements at the present time $\mathbf{q}_{m+1}$. Therefore, the Picard algorithm is used to re-approximate Eq. (6.8) as follows:

$$\hat{\mathbf{K}}({}^{i}\mathbf{q}_{m+1})\,{}^{i+1}\mathbf{q}_{m+1}=\hat{\mathbf{F}}_{m+1} \tag{6.10}$$

where the superscript is the iteration number, while the subscript denotes the load step.

Eq. (6.10) is iteratively solved until the difference between ${}^{i}\mathbf{q}_{m+1}$ and ${}^{i+1}\mathbf{q}_{m+1}$ reduces to a pre-selected error tolerance, i.e.

$$\frac{\left\| {}^{i+1}\mathbf{q}_{m+1} - {}^{i}\mathbf{q}_{m+1} \right\|}{\left\| {}^{i}\mathbf{q}_{m+1} \right\|} < 0.01 \tag{6.11}$$

The procedure is summarized by a flow chart as shown in Figure 6.1.

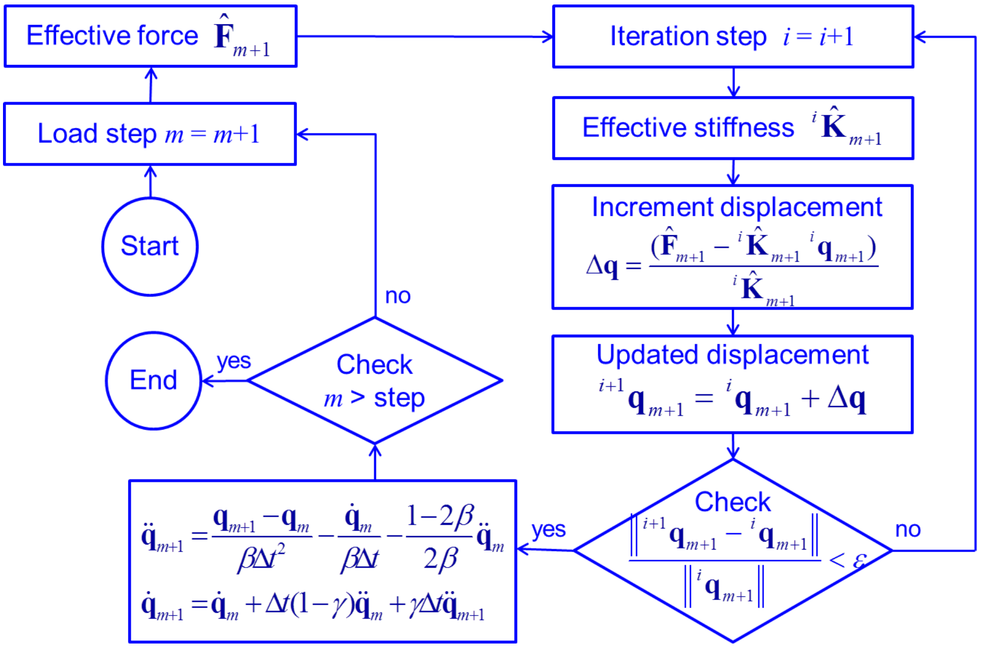

Figure 6.1 Flow chart for geometrically nonlinear transient analysis of plate.

6.3 Numerical results

In this section, we investigate two problems: free vibration and geometrically nonlinear transient analysis.

For convenience, the obtained results are normalized as:

$$\bar{\omega} = \omega L^2 / h\sqrt{\rho_m / E_m} \tag{6.12}$$

6.3.1 Free vibration

6.3.1.1 Shear locking test

Let us consider an isotropic plate with dimension $L \times W \times h$ having fully simply supported edges. Figure 6.2 reveals the relation between the first five natural frequencies and the length-to-thickness ratio *L/h*. Herein, increase in *L/h* ratio leads to increase in the obtained natural frequencies from the thick plate theories such as: FSDT and GSDT, which converge to CPT results by Leissa [204]. While GSDT produces the well-matched results with thin plate frequencies, a significant decrease in accuracy is observed from the FSDT for extremely thin plate (L/h > 1000). The phenomenon maybe attributed to the shear locking of the plate model.

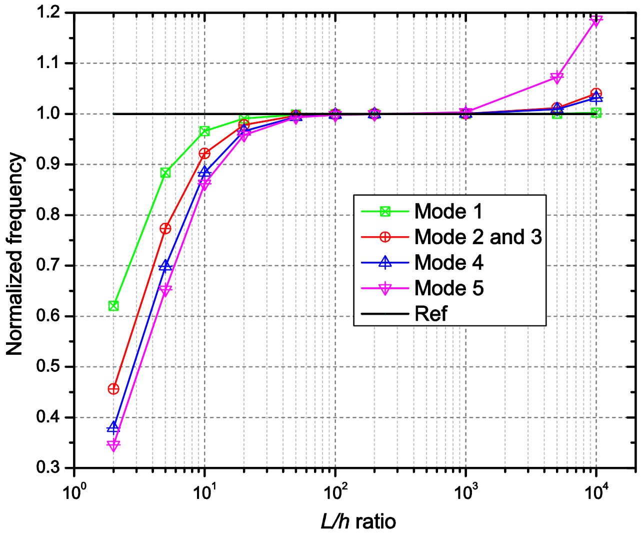

a) FSDT

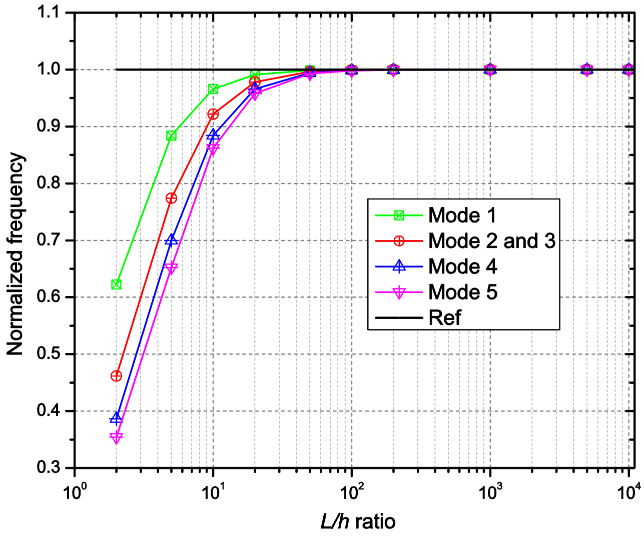

b) GSDT

Figure 6.2 The first five natural frequencies of an isotropic plate via length to thickness ratio using: a)FSDT and b)GSDT

6.3.1.2 Free vibration of square Al/ZrO$_2$-1 plate

Let us consider a simply supported Al/ZrO$_2$-1 plate, which is homogenized by the Mori-Tanaka scheme. In Table 6.1, we put the numerical results based on the HSDTs with various functions $f(z)$: f_1 by Reddy [57], f_2 by Thai [165] and the proposed function in inverse tangent form, in comparison with the exact solution [24], that of HOSNDPT [142] and quasi-3D solution using SSDT and HSDT [180, 181]. The excellent correlation between these models is achieved with very small error which is less than 0.4% for all values of exponent n. In addition, it is revealed that the proposed distributed function gives the best natural frequency with the least error as compared to the exact solution [24] by Vel and Batra. The first ten natural frequencies of the thick and moderate plate with a/h = 5, 10, 20 are listed in Table 6.2. The computed values agree well with the literature [142] for various L/h ratios and mode number. For n = 1, the first six mode shapes are plotted in Figure 6.3.

Table 6.1 The natural frequency $\bar{\omega}$ of SSSS Al/ZrO$_2$-1 plate with L/h = 5.

Model		ε_z	Power index n						
			0	0.5	1	2	3	5	10
Exact [24]			-	-	0.2192	0.2197	0.2211	0.2225	-
HOSNDPT [142]			-	-	0.2152 (-1.82)*	0.2153 (-2.00)	0.2172 (-1.76)	0.2194 (-1.39)	-
SSDT [181]		0	-	-	0.2184 (-0.36)	0.2189 (-0.36)	0.2202 (-0.41)	0.2215 (-0.45)	-
		≠0	-	-	0.2193 (0.05)	0.2198 (0.05)	0.2212 (0.05)	0.2225 (0.00)	-
HSDT [180]		0	0.2459	0.2219	0.2184 (-0.36)	0.2191 (-0.27)	0.2206 (-0.23)	0.222 (-0.22)	0.2219
		≠0	0.2469	0.2228	0.2193 (0.05)	0.22 (0.14)	0.2215 90.18)	0.223 (0.22)	0.2229
TSDT			0.2461	0.2222	0.2185 (-0.32)	0.2190 (-0.32)	0.2204 (-0.32)	0.2216 (-0.40)	0.2211
RPT	f_1		0.2459	0.2221	0.2184 (-0.36)	0.2189 (-0.36)	0.2203 (-0.36)	0.2216 (-0.40)	0.2211
	f_2		0.2462	0.2224	0.2186 (-0.27)	0.2191 (-0.27)	0.2205 (-0.27)	0.2218 (-0.31)	0.2215
	Present		0.2468	0.2229	0.2192 (0.00)	0.2196 (-0.05)	0.221 (-0.05)	0.2224 (-0.04)	0.2222
GSDT	f_1		0.2461	0.2222	0.2185 (-0.32)	0.219 (-0.32)	0.2204 (-0.32)	0.2216 (-0.40)	0.2211
	f_2		0.2464	0.2225	0.2188 (-0.18)	0.2192 (-0.23)	0.2205 (-0.27)	0.2218 (-0.31)	0.2215
	Present		0.247	0.223	0.2193 (0.05)	0.2197 (0.00)	0.2211 (0.00)	0.2224 (-0.04)	0.2222

(*) The error in parentheses

Table 6.2 The natural frequency $\bar{\varpi}$ of Al/ZrO2-1 plate with various ratios *L/h*.

L/h	Model		Mode number						
			1	(2,3)	4	5	6	7	8
5	Exact [24]		0.2192	-	-	-	-	-	-
	HOSNDPT [142]		0.2152	0.4114	0.4761	0.4761	0.582	0.6914	0.8192
	TSDT		0.2185	0.4118	0.4794	0.4794	0.5823	0.6948	0.8219
	RPT	f_1	0.2187	0.4116	0.4806	0.4806	0.5821	0.6976	0.8233
		f_2	0.2186	0.4116	0.4804	0.4804	0.5821	0.6972	0.8233
		Present	0.2192	0.4116	0.4827	0.4827	0.5821	0.7018	0.8233
	GSDT	f_1	0.2185	0.4118	0.4794	0.4794	0.5823	0.6948	0.8226
		f_2	0.2188	0.4118	0.4808	0.4808	0.5823	0.6977	0.8233
		Present	0.2193	0.4118	0.4831	0.4831	0.5823	0.7023	0.8233
10	Exact [24]		0.0596	-	-	-	-	-	-
	HOSNDPT [142]		0.0584	0.141	0.2058	0.2058	0.2164	0.2646	0.2677
	Quasi 3D	SSDT[181]	0.0596	0.1426	0.2058	0.2058	0.2193	0.2676	0.2676
		HSDT[180]	0.0596	0.1426	0.2059	0.2059	0.2193	0.2676	0.2676
	TSDT		0.0596	0.1423	0.2059	0.2059	0.2185	0.2666	0.2666
	RPT	f_1	0.0595	0.1423	0.2058	0.2058	0.2187	0.2668	0.2668
		f_2	0.0595	0.1423	0.2058	0.2058	0.2187	0.2667	0.2667
		Present	0.0596	0.1425	0.2058	0.2058	0.2192	0.2675	0.2675
	GSDT	f_1	0.0596	0.1423	0.2059	0.2059	0.2185	0.2666	0.2666
		f_2	0.0596	0.1424	0.2059	0.2059	0.2188	0.2669	0.2669
		Present	0.0596	0.1426	0.2059	0.2059	0.2193	0.2677	0.2677
20	Exact [24]		0.0153	-	-	-	-	-	-
	HOSNDPT [142]		0.0149	0.0377	0.0593	0.0747	0.0747	0.0769	0.0912
	Quasi 3D	SSDT[181]	0.0153	0.0377	0.0596	0.0739	0.0739	0.095	0.095
		HSDT[180]	0.0153	0.0377	0.0596	0.0739	0.0739	0.095	0.095
	TSDT		0.0153	0.0377	0.0596	0.0739	0.0739	0.0949	0.0949
	RPT	f_1	0.0153	0.0377	0.0595	0.0739	0.0739	0.0949	0.0949
		f_2	0.0153	0.0377	0.0595	0.0739	0.0739	0.0949	0.0949
		Present	0.0153	0.0377	0.0596	0.0739	0.0739	0.095	0.095
	GSDT	f_1	0.0153	0.0377	0.0596	0.0739	0.0739	0.0949	0.0949
		f_2	0.0153	0.0377	0.0596	0.0739	0.0739	0.095	0.095
		Present	0.0153	0.0377	0.0596	0.074	0.074	0.0951	0.0951

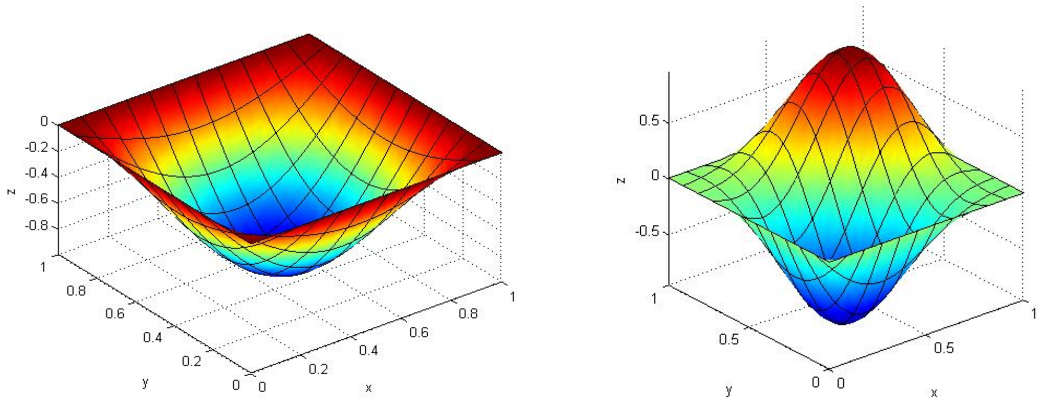

Mode 1 Mode 2

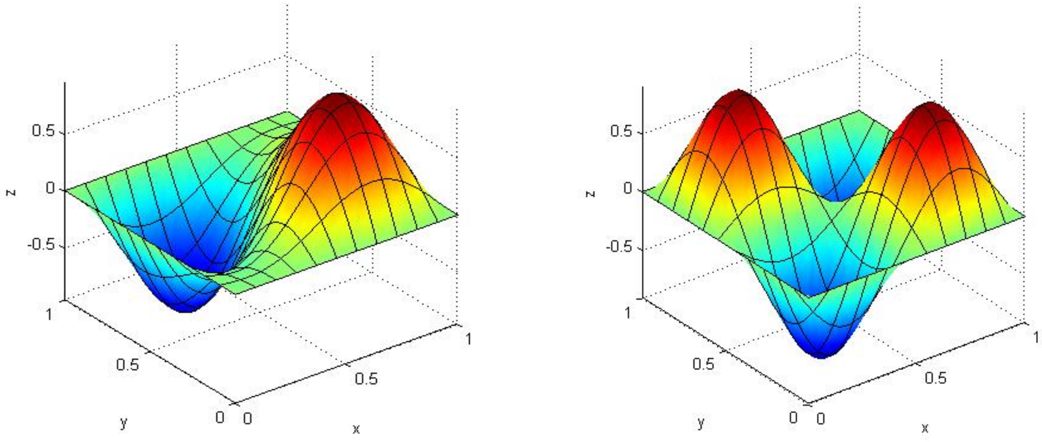

Mode 3 Mode 4

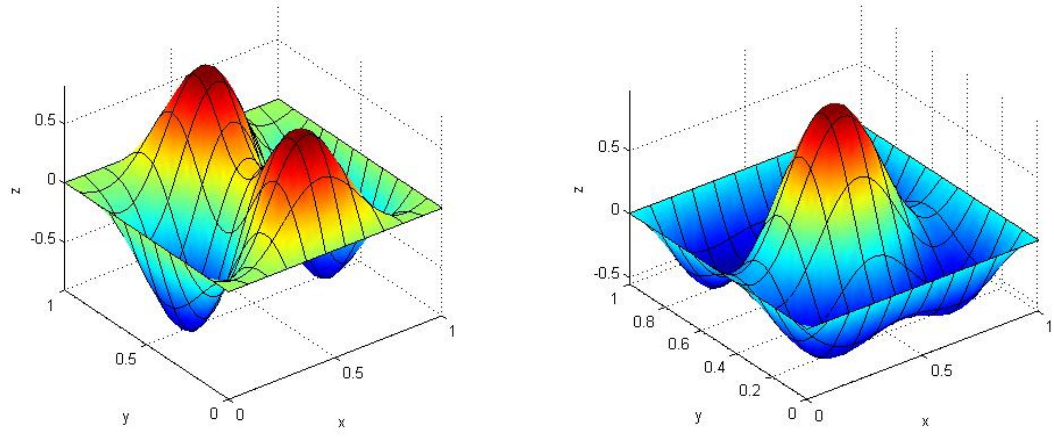

Mode 5 Mode 6

Figure 6.3 The first six mode shapes of Al/ZrO2-1 with n =1, L/h=5.

6.3.1.3 Free vibration of circle Al/Al$_2$O$_3$ plate

In this section, the normalized frequency $\hat{\omega} = 100\omega h\sqrt{\rho_c / E_c}$ of the clamped circular Al/Al$_2$O$_3$ plate with radius R = 0.5 are investigated. The effective Young's modulus E_e

and density ρ_e of FGM plate are calculated according to the rule of mixture following Ref. [205] by Reddy et al.

$$E_e = (E_m - E_c)\left(\frac{1}{2} - \frac{z}{h}\right)^n + E_c \, , \tag{6.13}$$

Eq. (6.13) shows that as $n = 0$, the plate is fully metal and as $n \rightarrow \infty$, the homogeneous ceramic plate is retrieved. Herein, the effects of the power index and radius to thickness ratio *R/h* are investigated. The obtained results as shown in Table 6.3 agree well with those obtained by three methods: semi-analytical solution [206], a FEM from ABAQUS software package and a method named the uncoupled model (UM), formerly proposed by Ebrahimi et al. [207]. To close this section, the first six mode shapes of circular plate are plotted in Figure 6.4.

Table 6.3 The first eight frequencies $\hat{\omega}$ of clamped circular Al/Al_2O_3 FGM plate.

h/R	Method	Mode number							
		1	2	3	4	5	6	7	8
0.01	Semi-anal.	0.0236	0.0491	0.0805	0.0918	0.1178	0.1404	0.1607	0.1951
	FEM	0.0234	0.0486	0.0798	0.0909	0.1167	0.1391	0.1592	0.1933
	UM	0.0257	0.0535	0.0877	0.1000	0.1283	0.1529	0.1751	0.2126
	IGA	0.0236	0.0492	0.0807	0.0924	0.1191	0.1431	0.1643	0.1991
0.1	Semi-anal.	2.3053	4.6934	7.5146	8.5181	10.7128	12.6197	14.2324	16.9838
	FEM	2.2888	4.6661	7.4808	8.4829	10.6776	12.5877	14.2025	16.9583
	UM	2.5038	5.0831	8.1156	9.1931	11.5376	13.5743	15.2879	18.2114
	IGA	2.3076	4.7005	7.5318	8.5380	10.7483	12.6636	14.2925	17.0520
0.2	Semi-anal.	8.6535	16.7666	25.6486	28.7574	34.0756	35.0981	39.4394	40.5889
	FEM	8.6403	16.7890	25.7661	28.9152	34.1893	35.3618	39.4169	40.9538
	UM	9.3162	17.9164	27.2480	30.4998	-	37.1197	-	42.8001
	IGA	8.6787	16.8595	25.8479	29.0092	34.0581	35.4875	39.4177	41.0759

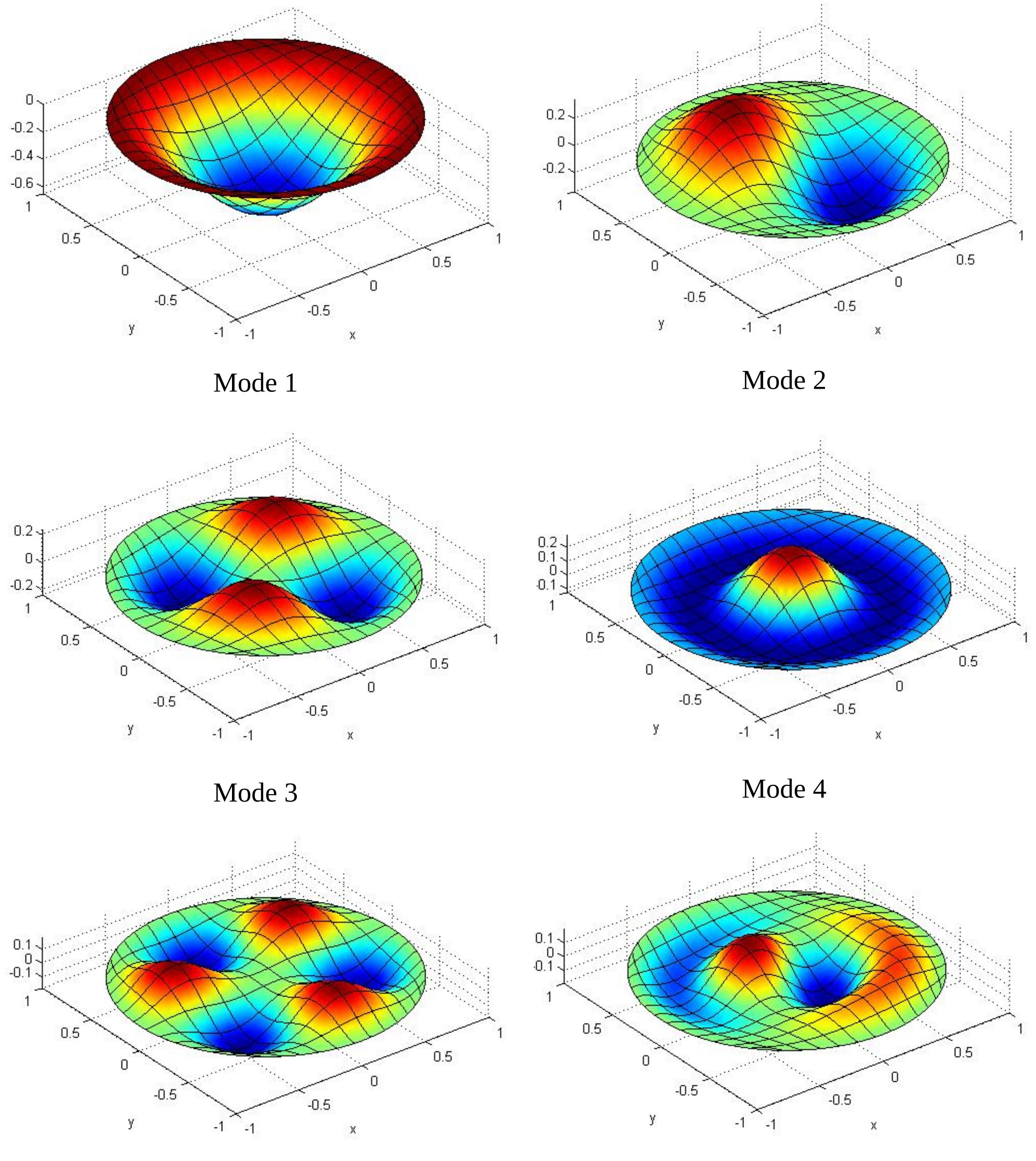

Mode 1 Mode 2

Mode 3 Mode 4

Mode 5 Mode 6

Figure 6.4 The first six mode shapes of Al/Al$_2$O$_3$ plate with h/R=0.1.

6.3.1.4 Free vibration of skew Al/ZrO$_2$-2 plate

Let us consider a skew Al/ZrO$_2$-2 plate with geometry and meshing as illustrated in Figure 4.10. Figure 6.5 plots the first four non-dimensional frequencies $\tilde{\omega}=\omega L^2/h\sqrt{\rho_c/E_c}$ of clamped Al/ZrO$_2$-2 plate corresponding to the skew angle ranging from 30° to 90°. The present method gives slightly higher results than the element-free *kp*-Ritz method [46] and also ES-DSG [48]. All results are in good agreement except case of skew angle fixed at $\theta = 30°$, the difference between ES-DSG and IGA is approximately around 3.5%.

It is believed that very small skew angle leads to distortion mesh, which affects the accuracy of the finite element method. It can be also seen that the natural frequencies decrease due to increase in the power index *n* and angle skew. According to Eq. (2.1), an increase in *n* leads to reduction of ceramic proportion in FGM plate, which causes the stiffness degradation of the plate. Figure 6.6 depicts the first eight mode shapes of the Al/ZrO_2-2 skew plate.

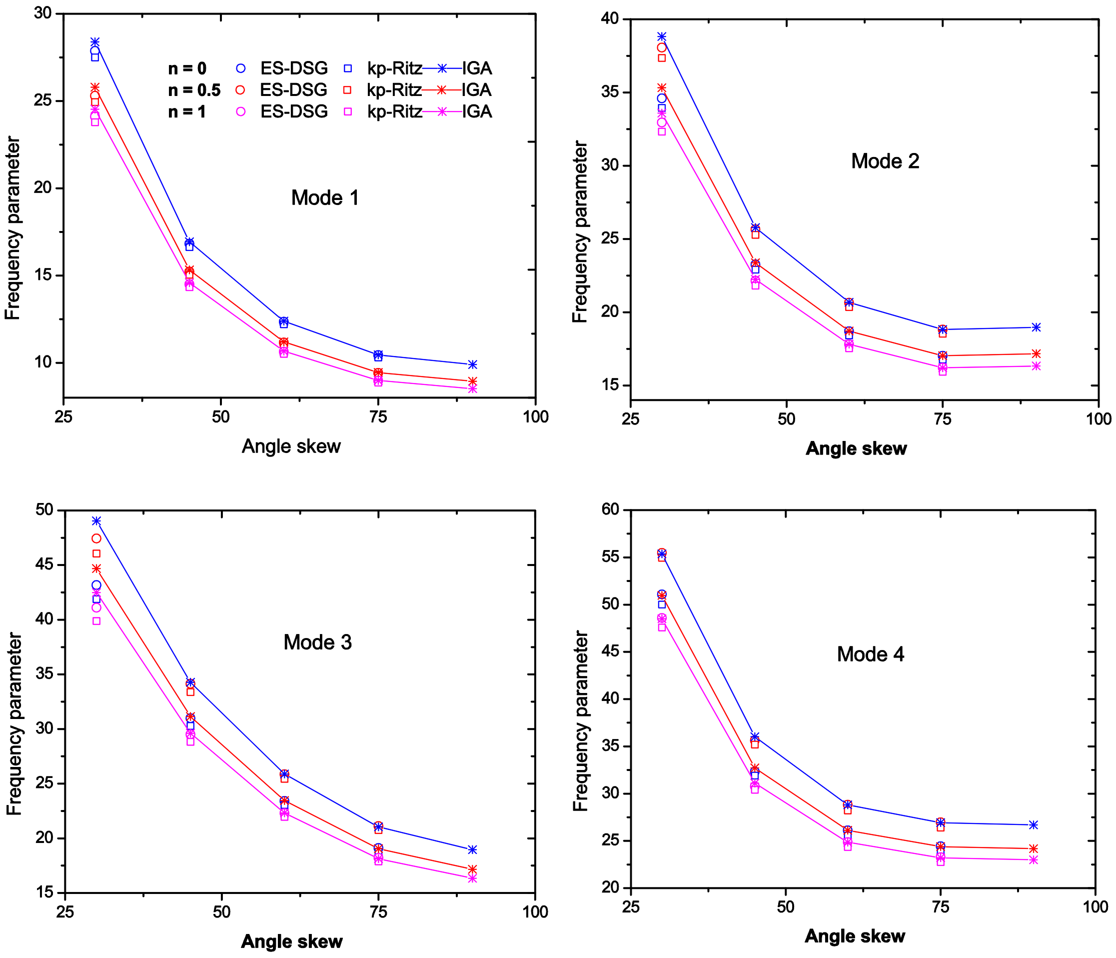

Figure 6.5 Comparison of the first four frequencies $\bar{\omega}$ of the clamped skew Al/ZrO_2-2 plate with L/h=10.

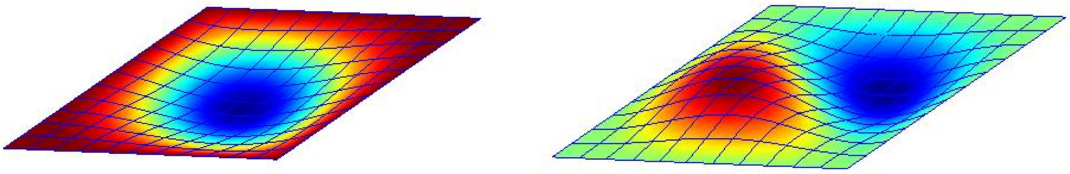

Mode 1 Mode 2

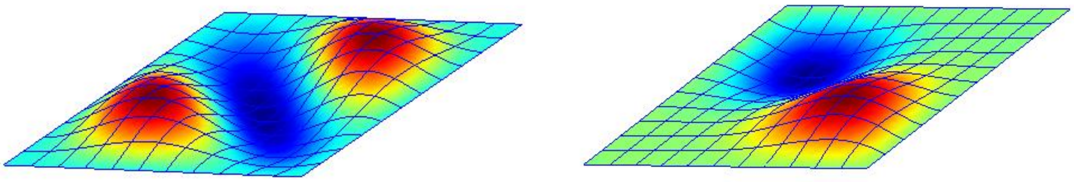

Mode 3 Mode 4

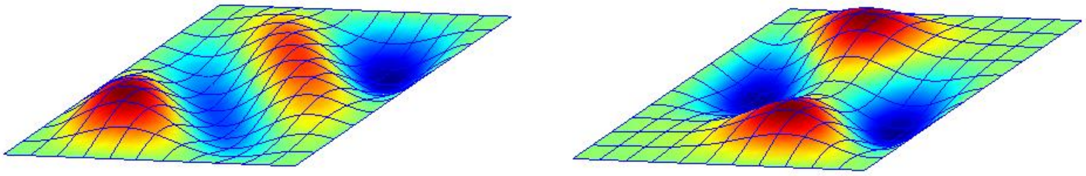

Mode 5 Mode 6

Figure 6.6 The first six mode shapes of the clamped skew Al/ZrO$_2$-2 with n =1, L/h=10 and angle skew = 45°.

6.3.2 Nonlinear dynamic analysis

6.3.2.1 Verification of IGA for dynamic responses

An orthotropic plate with material properties [208] E_1 = 525 GPa, E_2 = 21 GPa, G_{12} = G_{23} = G_{31} =10.5 GPa, ν = 0.25, ρ = 800 Ns^2/m^4 (80kg/m^3) and dimensions: length L = 250 mm, thickness h = 5 mm, is firstly studied for validation. For this problem, the fully simply supported plate is subjected to a uniform step loading of 1 MPa. Its transient response according to the normalized central deflection $\hat{w} = w/h$ under both linear and nonlinear analyses is shown in Figure 6.7. It is observed that present method predicts very close deflection response as compared with finite strip method (FSM) by Chen et al. [208]. It also clearly exhibits that the magnitude and wavelength of the non-linear response are lower than that of linear case with the same loading intensity.

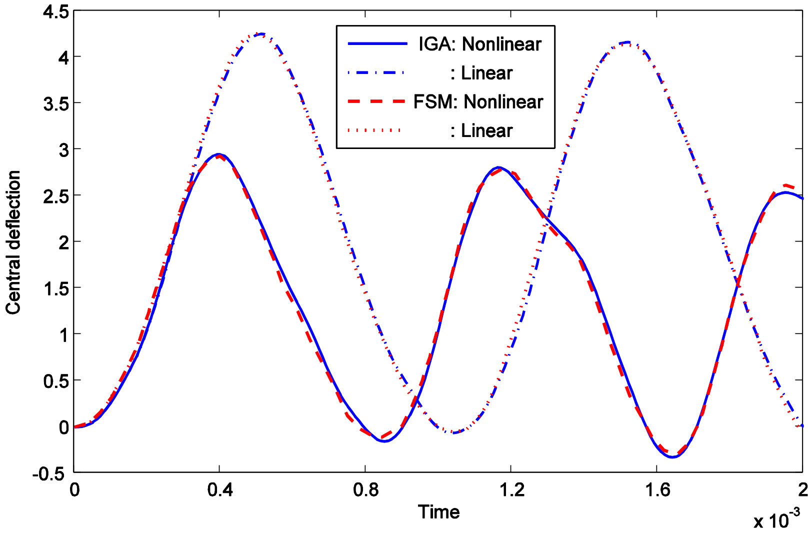

Figure 6.7 Time history of the transverse displacement of an orthotropic plate under step uniform load with intensity 1MPa[1].

6.3.2.2 Dynamic respond of Al/Al$_2$O$_3$ FGM plates

Next, the dynamic response of Al/Al$_2$O$_3$ FGM plate (L = 0.2 m, h = 0.01 m) is investigated. The transverse load is distributed sinusoidally in duration of t_1 = 3 ms as follows:

$$f_z(x,y,t) = q_0 \sin(\frac{\pi x}{a})\sin(\frac{\pi y}{b})F_0(t) \tag{6.14}$$

in which $q_0 = 15\ \text{MPa}$ and value of force $F_0(t)$ depicted in Figure 6.8 depends on loading types: step, triangular, sinusoidal and explosive blast, respectively.

$$F_0(t) = \begin{cases} \begin{cases} 1 & 0 \le t \le t_1 \\ 0 & t > t_1 \end{cases} & \text{Step loading} \\ \begin{cases} 1 - t/t_1 & 0 \le t \le t_1 \\ 0 & t > t_1 \end{cases} & \text{Triangular loading} \\ \begin{cases} \sin(\pi t/t_1) & 0 \le t \le t_1 \\ 0 & t > t_1 \end{cases} & \text{Sine loading} \\ e^{-\gamma t} & \text{Explosive blast loading} \end{cases} \tag{6.15}$$

where γ = 330 s^{-1}.

---

[1] The results of FSM by Chen et al.

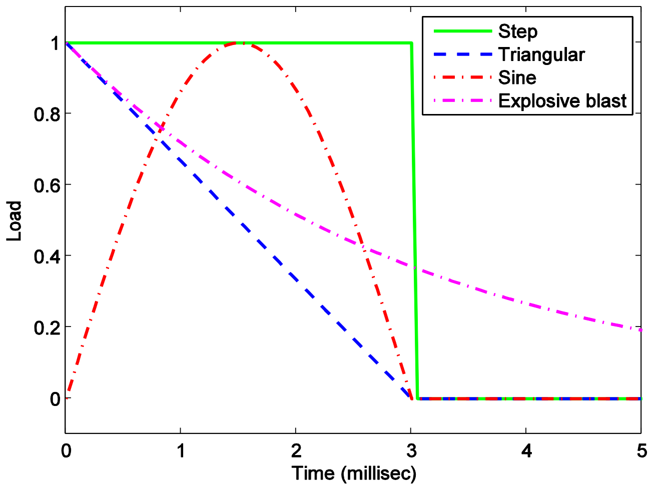

Figure 6.8 Time history of applied load $F_0(t)$.

Figure 6.9 presents the time history of the central displacement of FGM plate ($n = 1$) under four types of loading in short time $t = 5$ millisecond. As it can be seen, except for sin loading, all types of loading give nearly same period of the central deflection. And after removing the applied load, the plate still deflects and vibrates harmonically. The response of the plate under sine loading with two load levels q_0 and $2q_0$, as predicted by linear and nonlinear analysis, is shown in Figure 6.10. As it can be seen, at the lower loading level, there is less difference between the two models. However, at loading level $2q_0$, Figure 6.10b shows that linear IGA predicts higher magnitudes of deflection and period of the motion as compared to nonlinear case. Under the step loading, the time history of the deflection and normalized axial stress at the central point of the FGM plates using various value of power index, i.e. $n = 0.5, 1, 2$ are given in Figure 6.11. It is observed that increase in power index n reduces the plate stiffness, making the plate to be more sensitive to vibration with higher magnitude and period in the deflection and the axial stress.

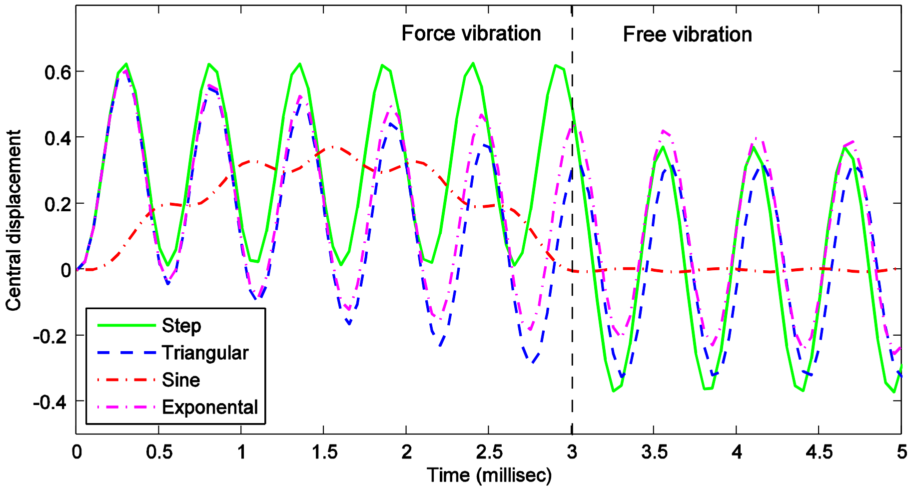

Figure 6.9 The deflection response of the FGM plate (n=1) under various loading types.

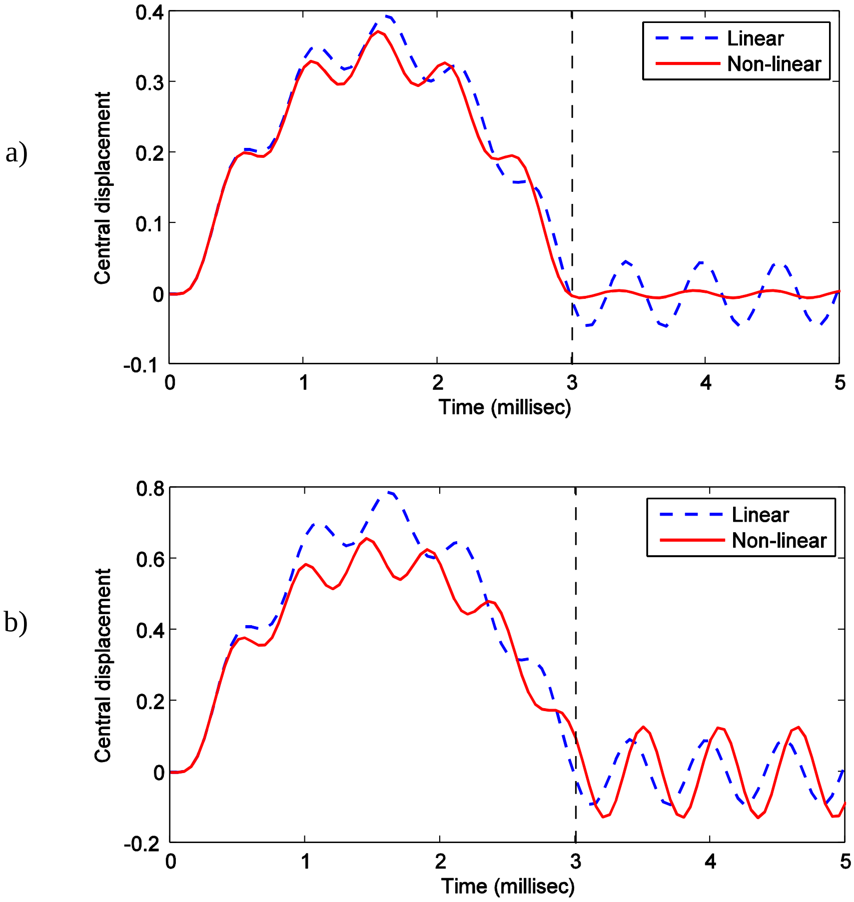

Figure 6.10 Comparsion of linear and nonlinear delfection response of FGM plate (n=1) under sine loading due to the level of load: a) q_0 and b) $2q_0$.

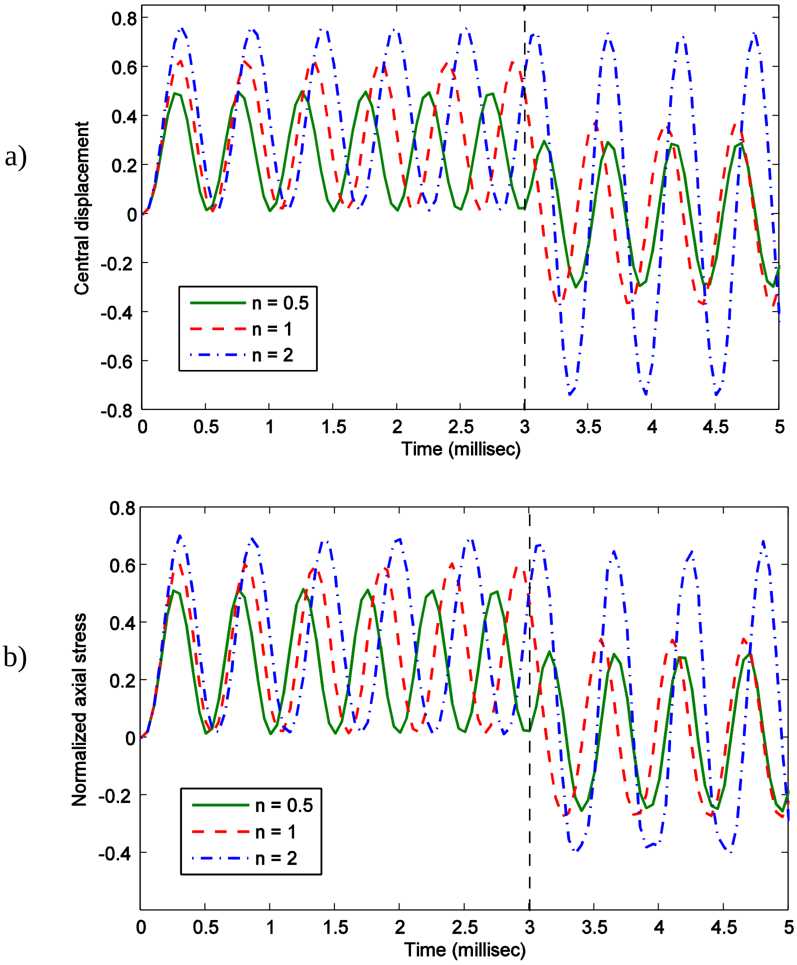

Figure 6.11 Response of the FGM plates to a step loading: a)central deflection versus time, b) central axial stress versus time.

6.4 Concluding remarks

The free vibration and forced vibration analyses of FGM plates were performed using a combination of isogeometric finite element method and HSDT models. The former without the force vector is solved by eigenvalue analysis to study the fundamental natural frequencies, while the latter is solved by the Newmark time-stepping scheme in association with the iteration method to study the response of the plate structures as a function of time. Several types of plate with many shapes: rectangle, circle, skew are investigated and the obtained results are in good agreement with the analytical and other available solutions in literature. Similar to static analysis in Chapter 4, HSDT shows more advantage than FSDT in overcoming the shear-locking phenomenon naturally. Moreover, employing our proposed distributed function helps HSDT models to gain the most accurate natural frequencies with the least error as compared to 3D exact results. The proposed method not only describes exactly the plate geometry, but also satisfies the stringent continuity required by the HSDT models. It is, therefore, believed that the present approach can be very promising to provide the reliable reference sources for analysing the FGM plates.

Chapter 7 Analysis of Cracked Plates

7.1 Introduction

In the previous chapters, this research was carried out for designing FGM plate structures without the presences of cracks or flaws. However, during manufacturing, FGM or general plate structures may have some flaws or defects. In service, the cracks can be generated and grown from defects under a cyclic loading. It is known that the cracks affect the dynamic response and stability characteristics of the plate structures and cause a reduction of their load carrying capacity. Therefore, various researches on dynamic behaviour of cracked plates become attractive to engineers and designers. Vibration of cracked plates was early studied in 1967 by Lynn and Kumbasar [209] using Green's function for approximating the transverse displacements. Stahl and Keer [210] used the Levy-Nadai approach and the homogeneous Fredholm integral equations of the second kind to deal with the free vibration analysis of the cracked rectangular plates. Hirano and Okazaki [211] utilized the Levy solution to investigate eigenvalue problems of the cracked rectangular plates with two opposite edges simply supported. Qian [212] applied a finite element method to the free vibration analysis of the square thin plates. Krawczuk [213] presented a finite element model to evaluate the influence of the crack location and its length on the amplitude of the natural frequencies. Su et al. [214] further extended FEM to the free vibration analysis of thin plates with arbitrary boundary conditions. Yuan and Dickinson [215] introduced the artificial springs at the interconnecting boundaries in the Reyleigh-Ritz method to analyse the flexural vibration of rectangular plates. Lee and Lim [216] studied the natural frequencies of rectangular plates with central crack by considering transverse shear deformation and rotary inertia. Also, Liew et al. [217] used domain decomposition method to devise the plate domain into the numerous subdomains around the crack location. Recently, Huang and Leissa [218] utilized the famous Ritz method with special displacement functions to take into account the stress singularity near the crack tips.

Almost all researches focused on considering thin homogenous plates based on the CPT. However, to produce accurately the natural frequency of moderate and thick anisotropic plates the transverse shear deformation needs to be taken into account. To author's knowledge, there are a few publications in the free vibration analysis of cracked plates considering the transverse shear deformation. Bachene et al. [219] utilized the extended finite element method (XFEM) to analyse the free vibration of cracked rectangular plates based on the FSDT. However, they only used Heaviside function for discontinuous enrichment and ignored the asymptotic functions to approximate the singular field near the crack tips. Natarajan et al. [220] extended XFEM to the dynamic analysis of FGM plates. Huang et al. [221] used the Ritz method and the Reddy's theory to obtain the free vibration solution of FGM thick plates with side cracks. Yang et al. [67] studied the nonlinear dynamic response of the cracked FGM plates based on TSDT using the Galerkin method. Recently, Huang et al. [222] employed three-dimensional elasticity theory to study the free vibration of cracked rectangular FGM plates.

In this chapter, we present the GSDT for modelling cracked FGM plates. It is worth mentioning that this model requires C^1-continuity of the generalized displacements leading to the second-order derivative of the stiffness formulation, which causes some obstacles in standard C^0-continuity finite element formulations. Fortunately, it is shown that such a C^1-GSDT formulation can be easily achieved using a NURBS-based isogeometric approach. In addition, to capture the discontinuous phenomenon in the cracked FGM plates, the enrichment functions through the partition of unity method (PUM) originated by Belytschko and Black [223] are incorporated with NURBS basic functions to create a novel method, so-called eXtended Isogeometric Analysis (XIGA), which is presented in Section 7.2. XIGA has been applied to stationary and propagating cracks in 2D [113], plastic collapse load analysis of cracked plane structures [224] and cracked plate/shell structures [225]. Herein, we investigate the vibration of the cracked FGM plates with an initial crack emanating from an edge or centrally located. Several numerical examples are provided in Section 7.3. Finally, the chapter is closed with some concluding remarks in Section 7.4.

7.2 An extended isogeometric (XIGA) cracked plate formulation

The basic idea is that enriched functions to capture the local discontinuous and singular fields are enhanced in the standard approximation as follows [223]:

$$\mathbf{u}^h(\mathbf{x}) = \sum_{I \in S} N_I(\mathbf{x})\mathbf{q}_I^{std} + \text{enrichment fields} \tag{7.1}$$

where $N_I(\mathbf{x})$ and $\mathbf{q}_I^{std}$ are the standard finite element shape function and nodal degrees of freedom associated with node *I*, respectively. To enhance the capability of IGA in analysing the cracked structures, a new numerical procedure, XIGA, was firstly proposed by Luycker et al. [112] and developed by Ghorashi et al. [113] and Nguyen et al. [177] as a combination of IGA and PUM. Being different from XFEM, which uses the Lagrange polynomials in approximation, XIGA utilizes the NURBS basis functions:

$$\mathbf{u}^h(\mathbf{x}) = \sum_{I \in S} R_I(\xi)\mathbf{q}_I^{std} + \sum_{J \in S^{enr}} R_J^{enr}(\xi)\mathbf{q}_J^{enr} \tag{7.2}$$

in which R_J^{enr} are the enrichment functions associated with node *J* located in the enriched domain S^{enr}, which is split up into two parts including: a set S^c for Heaviside enriched control points and a set S^f for crack tip enriched control points as shown in Figure 7.1. Furthermore, the enrichment functions are determined for each domain.

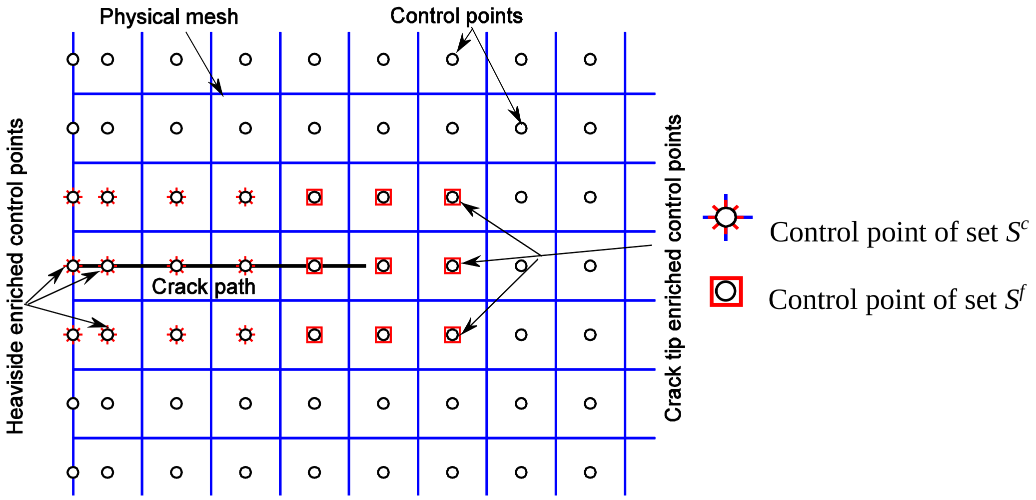

Figure 7.1 Illustration of the nodal sets S^c and S^f for a quadratic NURBS mesh.

To describe the discontinuous displacement field, the enrichment function is defined as:

$$R_J^{enr}(\xi) = R_J(\xi)\big(H(\mathbf{x}) - H(\mathbf{x}_J)\big), \quad J \in S^c \tag{7.3}$$

where the Heaviside function is given by:

$$H(\mathbf{x})=\begin{cases}+1 & \text{if } (\mathbf{x}-\mathbf{x}^*)\mathbf{n}>0\\ -1 & \text{orthewise}\end{cases}\tag{7.4}$$

in which **x*** is the projection of point **x** on the crack path, and **n** is the normal vector of crack at point **x***. Because the Heaviside function is a step function, its derivative equals to zero [113, 219, 225] except at the crack point, where there is no derivative. Thus, the first derivative of enrichment basis function by Heaviside function can be written in the following form:

$$(R_J^{enr})'=\left[R_J\left(H(\mathbf{x})-H(\mathbf{x}_J)\right)\right]'=R_J'\left(H(\mathbf{x})-H(\mathbf{x}_J)\right)\quad,\quad \mathbf{x}\neq\mathbf{x}^*\tag{7.5}$$

Similarly, the second derivative of Heaviside enrichment function is expressed as:

$$(R_J^{enr})''=\left[R_J'\left(H(\mathbf{x})-H(\mathbf{x}_J)\right)\right]'=R_J''\left(H(\mathbf{x})-H(\mathbf{x}_J)\right)\quad,\quad \mathbf{x}\neq\mathbf{x}^*\tag{7.6}$$

Let us consider the one-dimensional domain discretized into three elements as illustrated in Figure 7.2. For an open uniform knot vector $\boldsymbol{\Xi}=\left[0\;0\;0\;0\;\tfrac{1}{3}\;\tfrac{2}{3}\;1\,1\,1\,1\right]$, the cubic B-spline basic functions and their first derivatives are revealed from Figure 7.2b and c, respectively. It is clearly observed that the C^2 and C^1 continuities are gained at all interior knots for the basis functions and their derivatives, respectively. The discontinuous point locates at position $\xi=0.45$ belonging to the second element, which is described by four basis functions, i.e. $R_i^3\;\;(i:=3-6)$, By multiplying the Heaviside functions in Eq. (7.3), they attain the opposite values through the crack point. That enables us to model the discontinuity. As it can be seen in Figure 7.2d and e, the Heaviside enrichment functions and their first derivatives also keep the original continuities except at the crack position. On the other hand, the crack tip enrichment function can be written in the following form [226]:

$$R_J^{enr}(\xi)=R_J(\xi)\left(\sum_{L=1}^{4}\left(G_L(r,\theta)-G_L(r_J,\theta_J)\right)\right),\quad J\in S^f\tag{7.7}$$

where

$$G_L(r,\theta)=\begin{cases}r^{3/2}\left[\sin\dfrac{\theta}{2}\quad\cos\dfrac{\theta}{2}\quad\sin\dfrac{3\theta}{2}\quad\cos\dfrac{3\theta}{2}\right] & \text{for } \mathbf{u}_1 \text{ variable}\\ r^{1/2}\left[\sin\dfrac{\theta}{2}\quad\cos\dfrac{\theta}{2}\quad\sin\dfrac{\theta}{2}\sin\theta\quad\cos\dfrac{\theta}{2}\sin\theta\right] & \text{for } \boldsymbol{\beta} \text{ variable}\end{cases}\tag{7.8}$$

in which r and θ are polar coordinates in the local crack tip coordinate system.

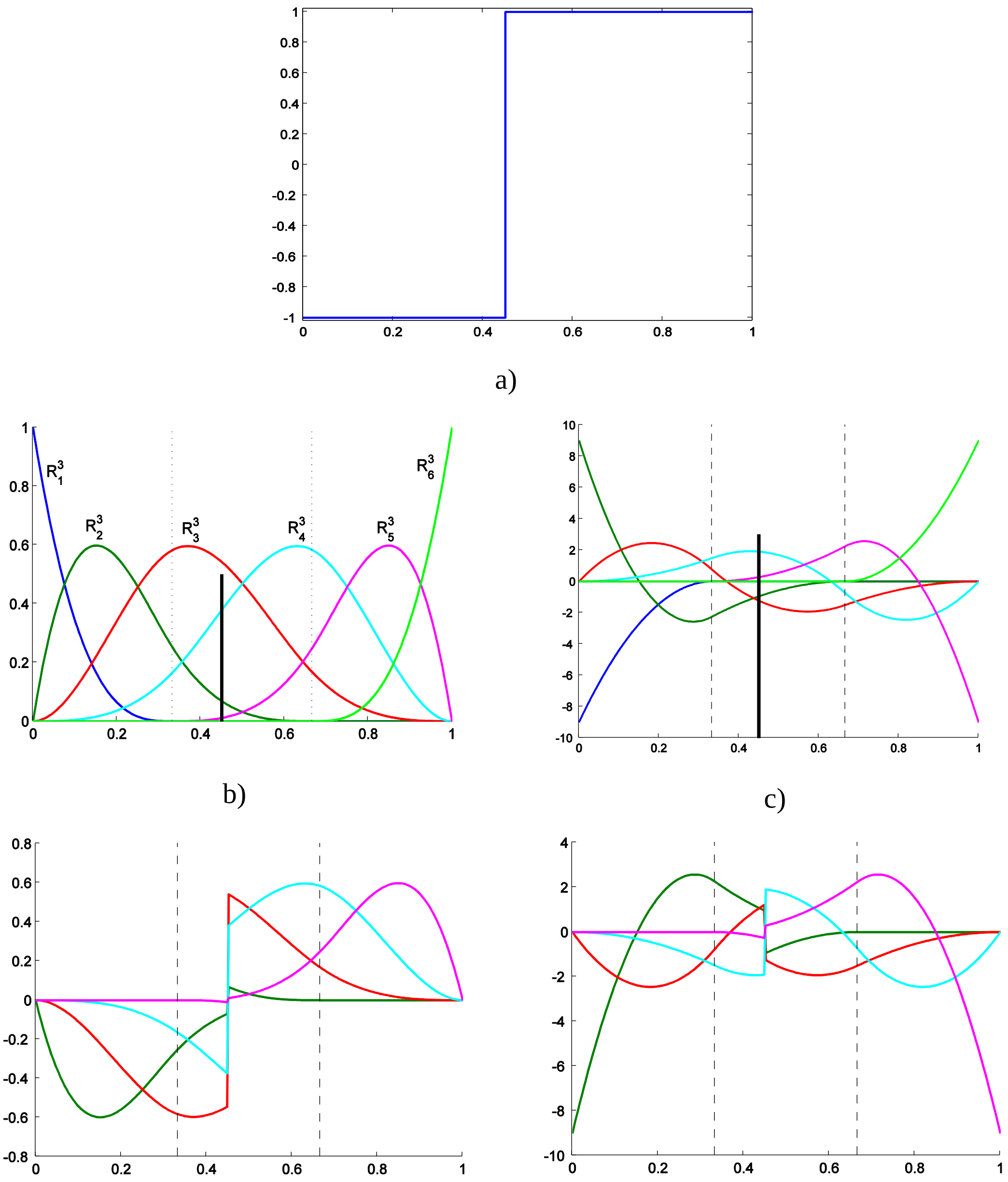

a)

b)

c)

d)

e)

Figure 7.2 An 1D example of the enrichment basis functions by Heaviside function for the split element cut by the crack located at $\xi = 0.45$*: a) The Heaviside function; b) the B-spline basis functions and c) their first derivative; d) the enrichment basis functions and e) their first derivative.*

Now, substituting the displacement field approximated in Eq. (7.2) into Eq. (3.9) and considering the enriched displacement field, the strain matrices can be rewritten in general form as:

$$\mathbf{B} = \left[\mathbf{B}^{std} \middle| \mathbf{B}^{enr} \right] \tag{7.9}$$

where $\mathbf{B}^{std}$ and $\mathbf{B}^{enr}$ are the standard and enriched strain matrices of **B** defined in the forms similar to Eq. (3.14):

$$\mathbf{B}^{m} = \begin{bmatrix} \bar{R}_{,x} & 0 & 0 & 0 & 0 \\ 0 & \bar{R}_{,y} & 0 & 0 & 0 \\ \bar{R}_{,y} & \bar{R}_{,x} & 0 & 0 & 0 \end{bmatrix}, \quad \mathbf{B}^{b1} = -\begin{bmatrix} 0 & 0 & \bar{R}_{,xx} & 0 & 0 \\ 0 & 0 & \bar{R}_{,yy} & 0 & 0 \\ 0 & 0 & 2\bar{R}_{,xy} & 0 & 0 \end{bmatrix},$$
$$\mathbf{B}^{b2} = \begin{bmatrix} 0 & 0 & 0 & \bar{R}_{,x} & 0 \\ 0 & 0 & 0 & 0 & \bar{R}_{,y} \\ 0 & 0 & 0 & \bar{R}_{,y} & \bar{R}_{,x} \end{bmatrix}, \quad \mathbf{B}^{s} = \begin{bmatrix} 0 & 0 & 0 & \bar{R} & 0 \\ 0 & 0 & 0 & 0 & \bar{R} \end{bmatrix} \tag{7.10}$$

in which $\bar{R}$ can be either the NURBS basic functions $R(\boldsymbol{\xi})$ or enriched functions R^{enr}. While, the global mass matrix **M** is estimated similarly to Eq. (3.21), i.e.:

$$\tilde{\mathbf{N}} = \begin{Bmatrix} \mathbf{N}_1 \\ \mathbf{N}_2 \\ \mathbf{N}_3 \end{Bmatrix}, \quad \mathbf{N}_1 = \begin{bmatrix} \bar{R} & 0 & 0 & 0 & 0 \\ 0 & \bar{R} & 0 & 0 & 0 \\ 0 & 0 & \bar{R} & 0 & 0 \end{bmatrix};$$
$$\mathbf{N}_2 = -\begin{bmatrix} 0 & 0 & \bar{R}_{,x} & 0 & 0 \\ 0 & 0 & \bar{R}_{,y} & 0 & 0 \\ 0 & 0 & 0 & 0 & 0 \end{bmatrix}; \quad \mathbf{N}_3 = \begin{bmatrix} 0 & 0 & 0 & \bar{R} & 0 \\ 0 & 0 & 0 & 0 & \bar{R} \\ 0 & 0 & 0 & 0 & 0 \end{bmatrix} \tag{7.11}$$

Resolve the linear eigenvalue equation Eq. (6.3), the natural frequency $\omega \in \mathbb{R}^{+}$ of the cracked plates is obtained.

7.3 Numerical results

7.3.1 Verification of XIGA

In order to validate the efficiency of the present method for the crack problems, two examples are studied, for which solutions are available in the literature. Let us firstly consider an isotropic infinite plate with material parameters of E = 10^7 kPa, ν = 0.3 containing a centre crack of length 2a subjected to a remote uniform stress σ = 10^2 kPa. The plane strain state is assumed. The closed form displacement field in term of polar coordinates in a reference frame (r, θ) centred at the crack tip is [227]:

$$u_x = \frac{2(1+\nu)}{\sqrt{2\pi}} \frac{K_I}{E} \sqrt{r} \cos\frac{\theta}{2}\left(2 - 2\nu - \cos^2\frac{\theta}{2}\right)$$
$$u_y = \frac{2(1+\nu)}{\sqrt{2\pi}} \frac{K_I}{E} \sqrt{r} \sin\frac{\theta}{2}\left(2 - 2\nu - \cos^2\frac{\theta}{2}\right) \tag{7.12}$$

While the stress field is given by:

$$\sigma_x = \frac{K_I}{\sqrt{2\pi r}} \cos\frac{\theta}{2}\left(1 - \sin\frac{\theta}{2}\sin\frac{3\theta}{2}\right)$$
$$\sigma_y = \frac{K_I}{\sqrt{2\pi r}} \cos\frac{\theta}{2}\left(1 + \sin\frac{\theta}{2}\sin\frac{3\theta}{2}\right) \tag{7.13}$$
$$\sigma_{xy} = \frac{K_I}{\sqrt{2\pi r}} \sin\frac{\theta}{2}\cos\frac{\theta}{2}\cos\frac{3\theta}{2}$$

where $K_I = \sigma\sqrt{\pi a}$ is the mode I stress intensity factor. A unit shaded domain with crack length of 0.5 mm is modelled (as shown in Figure 7.3) with the prescribed displacements on the bottom, right and top edges prescribed by Eq. (7.12) and traction along the left edge defined by Eq. (7.13). Herein, the inhomogeneous Dirichlet BCs in IGA is treated according to the instruction in Section 3.5.2.

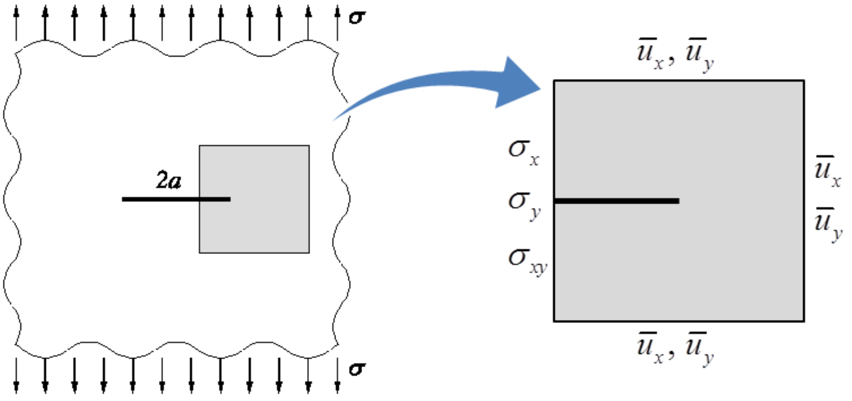

Figure 7.3 Infinite crack plate in tension.

To evaluate the present method, Figure 7.4 reveals a comparison between XFEM and XIGA (p = 3) using the relative error norms of displacement and energy, which are given by [169]:

$$\|\mathbf{u}\| = \left[\frac{\int_\Omega \left(\mathbf{u}-\mathbf{u}^h\right)^T \left(\mathbf{u}-\mathbf{u}^h\right) d\Omega}{\int_\Omega \mathbf{u}^T \mathbf{u}\, d\Omega}\right]^{1/2} \tag{7.14}$$

$$\|\mathbf{e}\| = \left[\frac{\int_{\Omega} \left(\boldsymbol{\varepsilon} - \boldsymbol{\varepsilon}^h\right)^T \left(\boldsymbol{\sigma} - \boldsymbol{\sigma}^h\right) d\Omega}{\int_{\Omega} \boldsymbol{\varepsilon}^T \boldsymbol{\sigma} d\Omega} \right]^{1/2} \tag{7.15}$$

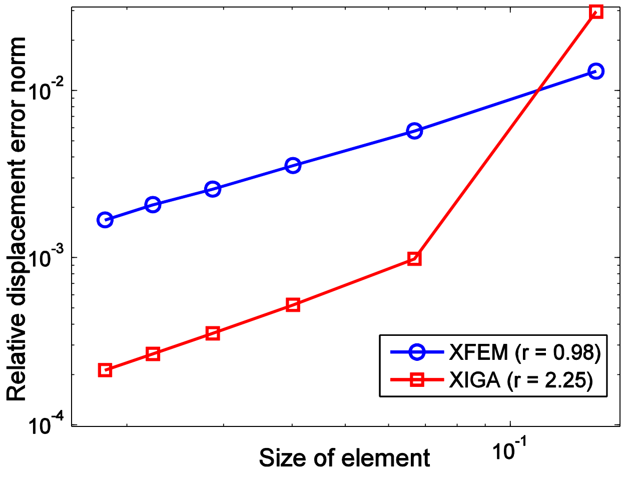

a) Displacement error norm

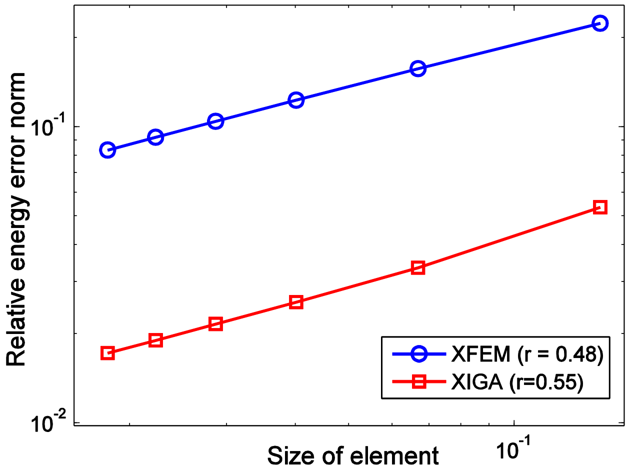

b) Enegy error norm

Figure 7.4 Comparison of relative error norms between XIGA and XFEM.

To estimate the convergence rate, we choose horizontal parameter to be the size of element, which is defined as the maximum distance of element edge. As compared with XFEM, it is observed that XIGA using higher-order basis function (cubic function) achieves better accuracy and higher convergence rate in displacement error norm as well as energy error norm. Figure 7.5 shows the contour plots of displacements and stress distributions in x and y directions, respectively.

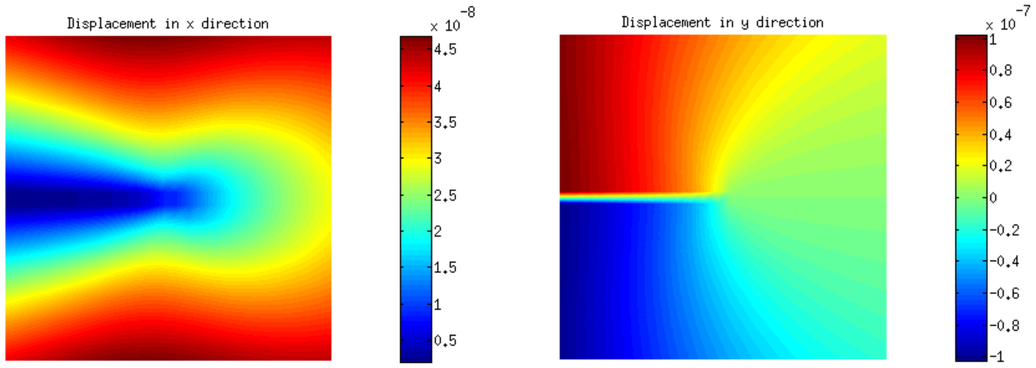

a) Displacement in *x*-direction b) Displacement in *y*-direction

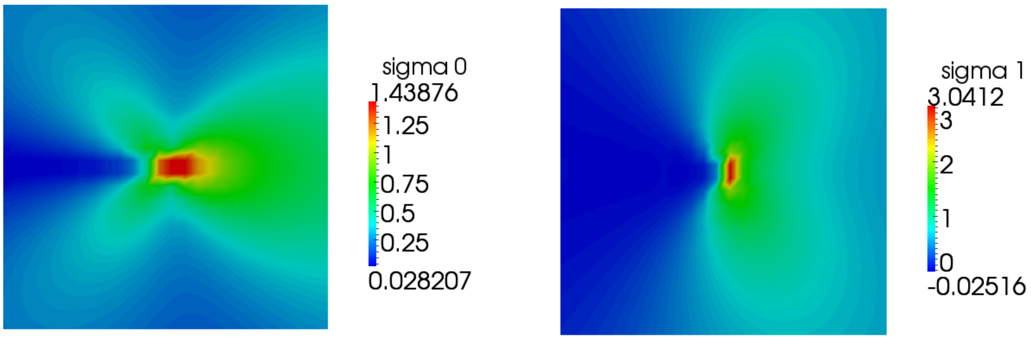

c) Axial stress σ_x d) Axial stress σ_y

Figure 7.5 Contour plot of the displacements and stresses distribution.

In the next example, we investigate a rectangular plate of length L = 16 mm, width W = 7 mm, thickness h = 1 mm and crack length of $a = W/2$ with material parameters of $E = 3\times10^7$kPa, $\nu = 0.25$. The planar plate is enforced at the top edge by a shear loading τ = 1kPa and also clamped at the bottom edge as shown in Figure 7.6a. Herein, we use cubic element (p = 3) with an example of meshing as shown in Figure 7.6b. The analytical stress intensity factor (SIF) for this problem is K_I = 34.0 as reported by Yau et al. [228]. Figure 7.7a and b show the relations between the relative error of SIF via the number of degrees of freedom (DOFs) and CPU time, respectively. Herein, the computations are performed on a laptop computer with CPU Intel® core (TM) 2 Duo T6400, 2.00 GHz processor. The present method has been coded in the Matlab language. It is again seen that the present method achieves more accurate results than XFEM. Indeed, to get the accuracy of SIF K_I with error lower than 0.1%, XIGA needs approximately 4300 DOFs, while XFEM uses more than 25000 DOFs with nearly two times the required computational cost. Figure 7.8 plots the distribution of axial stress, shear stress and displacement along *y* direction.

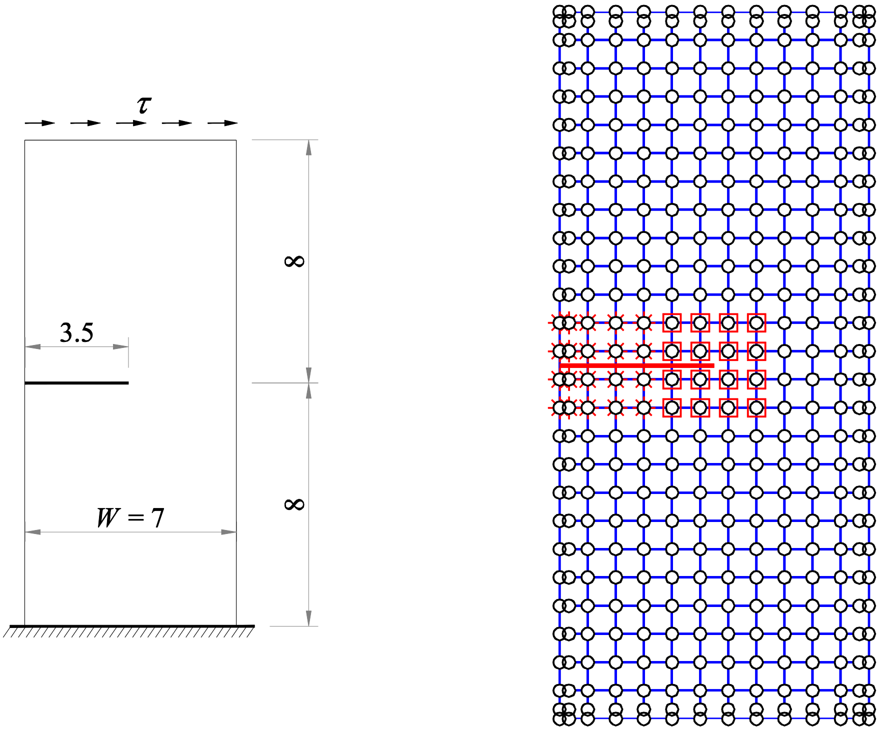

Figure 7.6 An edge crack plate under shear stress: a)model and b) meshing of 11×25 cubic elements.

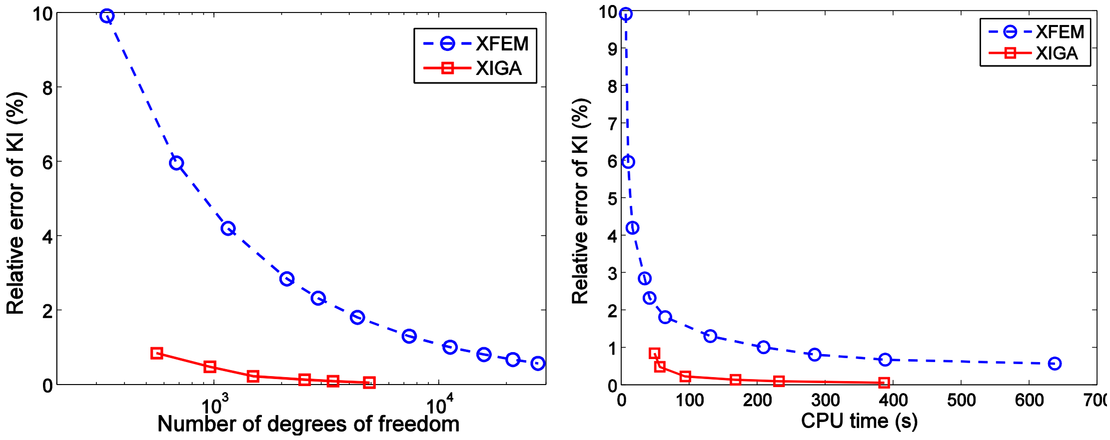

Figure 7.7 Comparison between XIGA and XFEM.

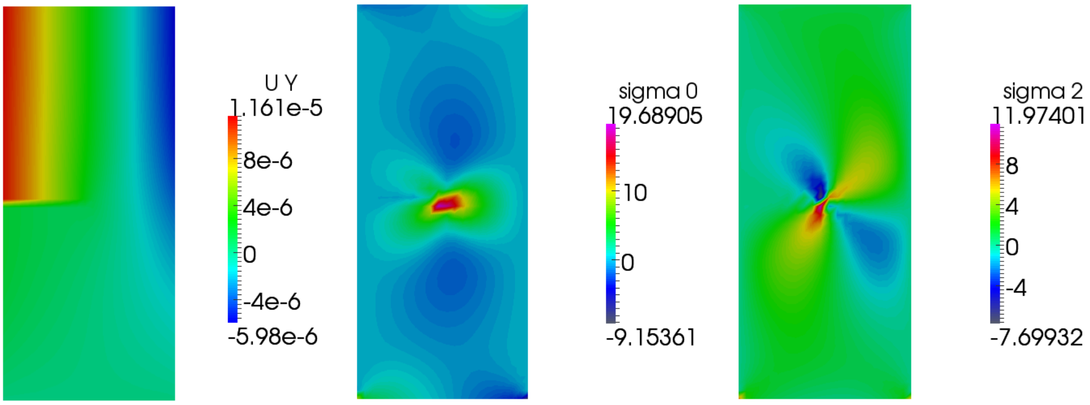

a) Displacement U_y b) Axial stress σ_x c) Axial stress σ_{xy}

Figure 7.8 Contour plot of the displacement and stresses distribution.

7.3.2 Central crack plate

Let us consider an isotropic plate with dimension $L \times W \times h$ having a central crack length a as shown in Figure 7.9a. The plate having fully simply supported edges is discretizing in 21×21 cubic elements as plotted in Figure 7.9b.

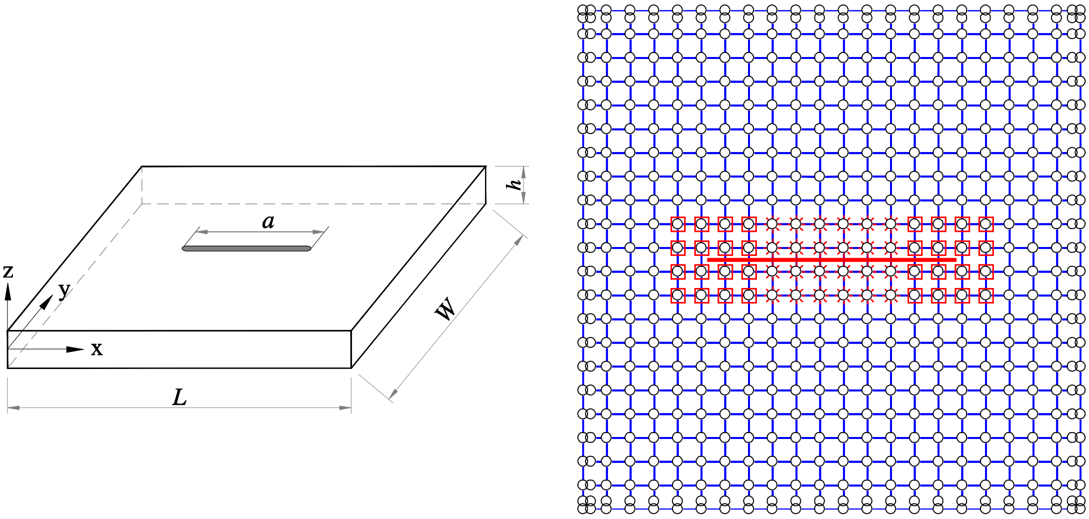

a) Plate model b) mesh of 21x21 cubic elements

Figure 7.9 The plate with a center crack

Table 7.1 reveals the effect of L/h ratio on the first five natural frequencies $\hat{\omega} = \omega L^2 \sqrt{\rho h / D}$ of a central crack plate (a/L=0.5), where $D = Eh^3 / \left(12(1-\nu^2)\right)$ is the flexural rigidity of the plate. As expected, the obtained results match well with 3D solutions using Ritz method by Huang [222]. Herein, increase in the length-to-thickness ratio makes the plates thinner and the results reach CPT solutions by Stahl and Keer [210] and Liew [217]. In case of thin plate (*L/h* = 100), the present model using thick plate theory also yields highly consistent results with lower than 1% error. Thus, for comparison with thin plate results, the length-to-thickness ratio *L/h* = 100 is used for further analysis.

Table 7.1 Effect of *L/h* ratio on the non-dimension frequency $\hat{\omega}$ of the centre cracked plate (*a/L*=0.5).

L/h	Source	Mode 1	Mode 2	Mode 3	Mode 4	Mode 5
5	3D elasticity [222]	15.3099	28.9610	37.7709	52.7735	55.8137
	XIGA (GSDT)	15.2563	29.8746	37.3251	52.4719	55.3396
	XIGA (FSDT)	15.2478	28.9675	37.4698	52.3002	55.3078
10	3D elasticity	16.7507	36.6804	44.7765	67.2474	70.8494
	XIGA (GSDT)	16.7205	37.2500	44.4276	66.8942	70.3951
	XIGA (FSDT)	16.7155	36.8069	44.6413	67.0764	70.5312
20	3D elasticity [222]	17.3092	40.5798	47.4863	74.1539	77.9872
	XIGA (GSDT)	17.2894	40.9878	47.2903	73.9589	77.6872
	XIGA (FSDT)	17.2810	40.7329	47.4410	74.1472	77.8016
100	3D elasticity [222]	17.6892	42.8930	48.6429	77.5246	81.9196
	XIGA (GSDT)	17.6638	43.3424	48.5695	77.4614	81.7008
	XIGA (FSDT)	17.6595	43.6574	48.6100	77.5809	81.7446
CPT	Stahl [210]	17.706	43.031	48.697	77.733	82.155
	Liew [217]	17.85	42.82	48.72	77.44	83.01

Next, Table 7.2 tabulates a convergence study of the first five natural frequencies $\hat{\omega}$ of the thin plate. It is observed that within thick plate theories such as FSDT and HSDT, the present method gains good accuracy with slightly lower results as compared to that of CPT [210, 217] with very small errors of less than 0.18% and 0.96% for the intact and cracked plate, respectively. Using a mesh of 21×21 cubic elements, the relation between non-dimensional frequencies $\hat{\omega}$ and crack length ratio is listed in Table 7.3. The results obtained from XIGA are in good agreement with those obtained from CPT solution by Stahl [210] using Levy-Nadia approach, Liew et al. [217] using the domain decomposition method, 3D elasticity [222] and Mindlin plate theory [229] using Ritz method. In addition, the comparison of first five frequencies with CPT results is depicted in Figure 7.10. It reveals that the frequencies decrease due to an increase in crack length ratio. For example, the values of frequency, according to change mode shape from 1 to 5, reduce up to 18.4%, 67.3%, 5.4%, 40.8% and 23.8% of its initial values for intact plate, respectively. It is concluded that the magnitude of the frequency for anti-symmetric modes through the *y*-axis, which is perpendicular to the cracked path (e.g. mode 2, mode 4, as shown in Figure 7.11), is much more affected by the crack length. The discontinuous displacement is shown clearly along the crack path.

Table 7.2 Convergence study of natural frequencies for the thin plate.

a/L	Mode	GSDT					FSDT	Stahl
		9×9	13×13	17×17	21×21	25×25	25×25	[210]
0.5	1	17.5193	17.6820	17.6744	17.6638	17.6555	17.6473	17.706
	2	40.7297	43.4868	43.4441	43.3424	43.2637	43.4461	43.031
	3	45.3888	48.2668	48.5149	48.5695	48.5857	48.6015	48.697
	4	66.4784	76.5502	77.3085	77.4614	77.5011	77.5584	77.733
	5	69.5361	81.7570	81.7221	81.7008	81.6812	81.6758	82.155

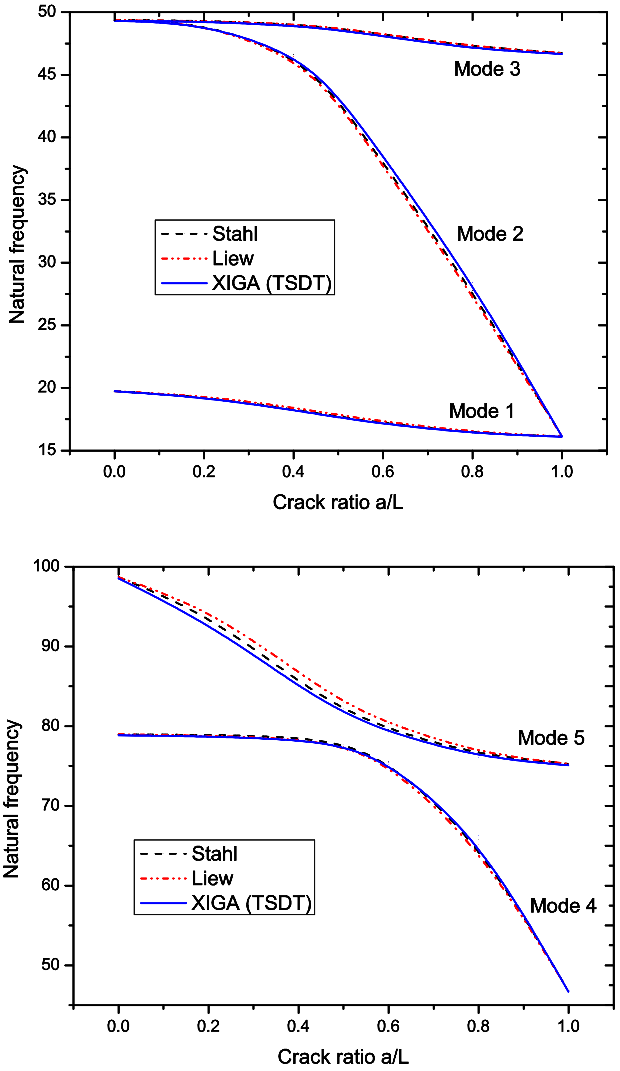

Figure 7.10 Variation of the first five natural frequencies versus crack length ratios.

Table 7.3 Non dimensional natural frequencies of the isotropic square plate (*L/h*=100) for different crack length ratios

Mode	Source	Crack length ratio *a/L*						
		0	0.2	0.4	0.5	0.6	0.8	1
1	Stahl	19.739	19.305	18.279	17.706	17.193	16.403	16.127
	Liew	19.74	19.38	18.44	17.85	17.33	16.47	16.13
	Huang	-	-	-	17.69$^{(*)}$	17.13$^{(**)}$	-	-
	XIGA (GSDT)	19.732 (0.04)	19.2638 (0.21)	18.2349 (0.24)	17.6638 (0.24)	17.1305 (0.36)	16.3587 (0.27)	16.1096 (0.11)
	XIGA (FSDT)	19.732 (0.04)	19.2711 (0.18)	18.2324 (0.25)	17.6595 (0.26)	17.1204 (0.42)	16.3544 (0.30)	16.1092 (0.11)
2	Stahl	49.348	49.170	46.624	43.031	37.978	27.773	16.127
	Liew	49.35	49.16	46.44	42.82	37.75	27.43	16.13
	Huang	-	-	-	42.89	37.69	-	-
	XIGA (GSDT)	49.3033 (0.09)	49.098 (0.15)	46.7232 (0.21)	43.3424 (0.72)	38.1929 (0.57)	27.9035 (0.47)	16.1096 (0.11)
	XIGA (FSDT)	49.3034 (0.09)	49.1147 (0.11)	46.8296 (0.44)	43.6574 (1.46)	38.3476 (0.97)	28.0654 (1.05)	16.1092 (0.11)
3	Stahl	49.348	49.328	49.032	48.697	48.223	47.256	46.742
	Liew	49.35	49.31	49.04	48.72	48.26	47.27	46.74
	Huang	-	-	-	48.64	48.13	-	-
	XIGA (GSDT)	49.3033 (0.09)	49.2557 (0.15)	48.9313 (0.21)	48.5695 (0.26)	48.1013 (0.25)	47.0781 (0.38)	46.6618 (0.17)
	XIGA (FSDT)	49.3034 (0.09)	49.2761 (0.11)	48.9668 (0.13)	48.6100 (0.18)	48.1154 (0.22)	47.088 (0.36)	46.6611 (0.17)
4	Stahl	78.957	78.957	78.602	77.733	75.581	65.732	46.742
	Liew	78.96	78.81	78.39	77.44	75.23	65.19	46.74
	Huang	-	-	-	77.52	75.28		
	XIGA (GSDT)	78.8423 (0.15)	78.7275 (0.29)	78.3262 (0.35)	77.4614 (0.35)	75.4169 (0.22)	65.7993 (0.10)	46.6618 (0.17)
	XIGA (FSDT)	78.8424 (0.15)	78.7689 (0.24)	78.4028 (0.25)	77.5809 (0.20)	75.4895 (0.12)	65.9949 (0.40)	46.6611 (0.17)
5	Stahl	98.696	93.959	85.510	82.155	79.588	76.371	75.285
	Liew	98.70	94.69	86.71	83.01	80.32	76.60	75.28
	Huang	-	-	-	81.92	79.22	-	-
	XIGA (GSDT)	98.5193 (0.18)	92.9166 (1.11)	84.9408 (0.67)	81.7008 (0.55)	79.2038 (0.48)	76.0646 (0.40)	75.1033 (0.24)
	XIGA (FSDT)	98.5206 (0.18)	93.4560 (0.54)	85.0508 (0.54)	81.7446 (0.50)	79.1787 (0.51)	76.0581 (0.41)	75.1019 (0.24)

$^{(*)}$3D-elasticity theory [222], and $^{(**)}$Mindlin plate theory [229]

In parenthesis, there are the relative errors as compared with CPT's solution [210]

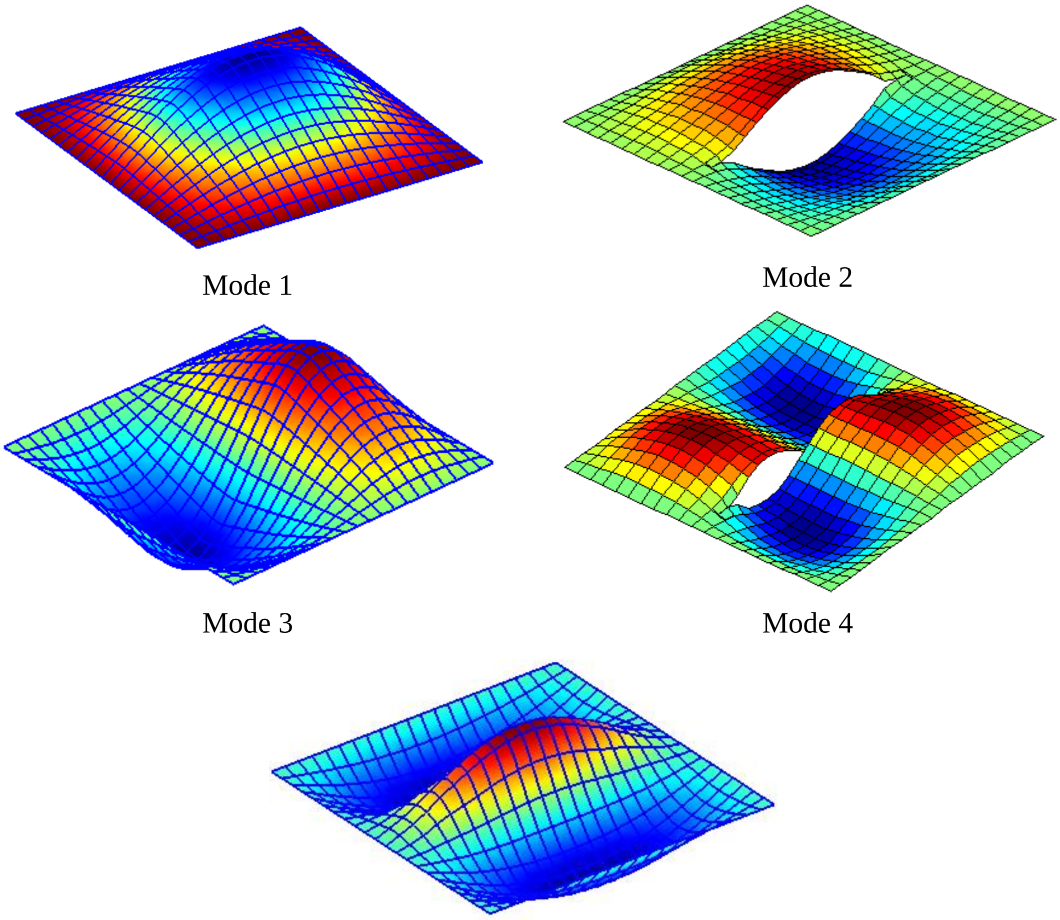

Mode 1

Mode 2

Mode 3

Mode 4

Mode 5

Figure 7.11 The first five mode shapes of the simply supported plate with the center crack with a/L =0.8

Finally, the effect of length to thickness ratio *L/h* on the frequencies of Al/Al_2O_3 FGM plate is shown in Figure 7.12. In this example, the material properties are calculated by two homogenization schemes including the rule of mixture and the Mori-Tanaka scheme with the power index $n = 1$. For inhomogeneous materials, the effective property through the thickness of the former is higher than the latter. The results from the Mori-Tanaka scheme, hence, are lower than that of the counterpart because of lower stiffness. Moreover, the value of natural frequency changes rapidly between thick plate (L/h =2) and moderate thin plate (L/h =50) with discrepancy up to 57.2% and 71.3% via the rule of mixture and the Mori-Tanaka scheme, respectively. However, for thin plates ($L/h \geq 100$), it is independent of the length to thickness ratio with approximated difference up to 1% due to naturally shear-locking free by the present plate theory.

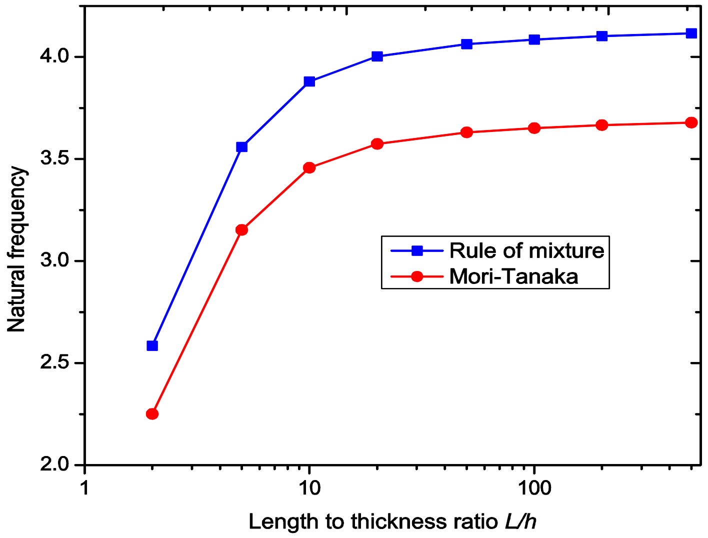

Figure 7.12 The first frequency of the central cracked Al/Al$_2$O$_3$ plate obtained for both mixture and Mori-Tanaka schemes.

7.3.3 Edge cracked plate

Let us consider a simply supported square plate with uniform thickness *h* and length *L*, respectively. The FGM plates containing a crack side from the left edge with length *a*, is discretized into 21×21 cubic NURBS elements as shown in Figure 7.13.

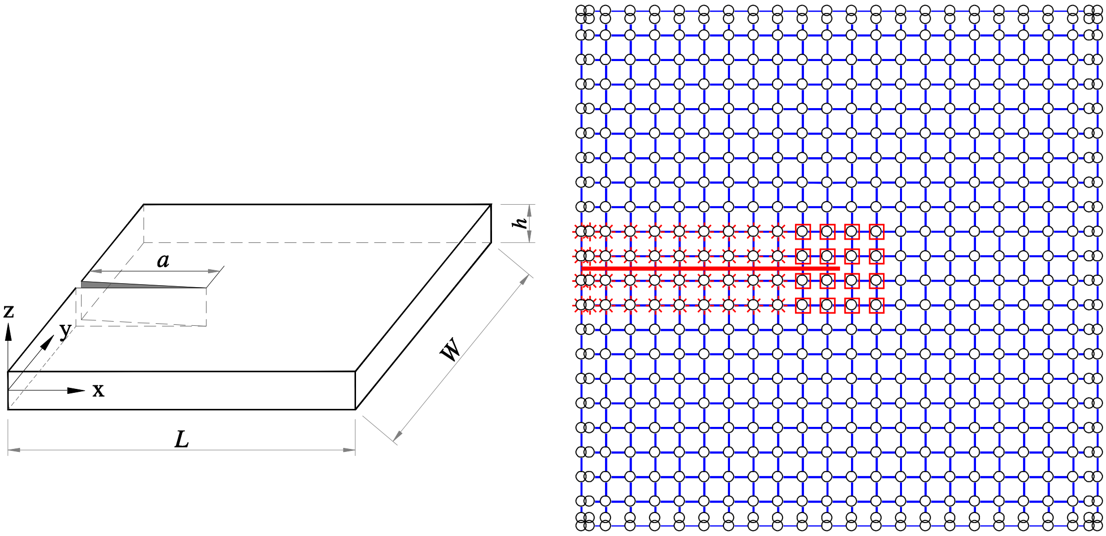

a) Plate model b) Mesh of 21x21 cubic elements

Figure 7.13 The plate with an edge crack.

Herein, the variation of material properties through the plate thickness is evaluated using the rule of mixture. Table 7.4 depicts the effect of the power index *n* on the first five natural frequencies of a simply supported Al/Al$_2$O$_3$ plate with length to thickness ratio *L/h*=10 and crack length ratio *a/L*=0.5. The present method gives good agreement compared to both the Ritz method and XFEM. It can be seen that the present results are slightly lower than that of Huang et al. [221] based on TSDT or even Natarajan et al. [220] based on FSDT. Compared to 3D elasticity solution calculated by ABAQUS finite element package (using 130791 nodes) [221], the proposed approach based on TSDT model obtains the most accurate first natural frequency. As shown in Figure 2.4, increasing volume fraction exponent *n* reduces the effective property of the material through the plate thickness. Thus, frequency parameter $\bar{\omega} = \omega L^2 / h\sqrt{\rho_c / E_c}$ decreases because of reduction in the stiffness of FGM plate. The same conclusions are drawn for cantilever Al/ZrO2 cracked plate with results listed in Table 7.5. The first four mode shapes of the edge cracked FGM plate under fully simply supported and clamped edge right conditions are shown in Figure 7.14 and Figure 7.15, respectively. It can be again seen that the magnitude of deflection based on anti-symmetric mode through the *y*-axis changes drastically around the crack path (for example, modes 2 and 4).

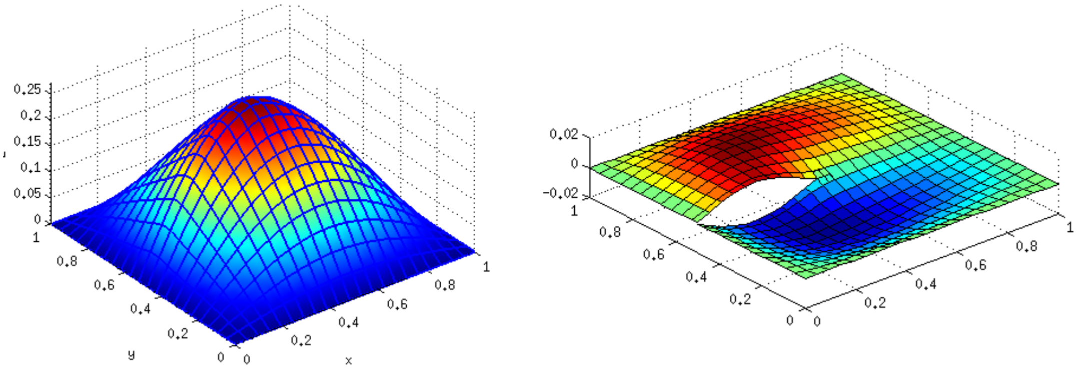

Mode 1 Mode 2

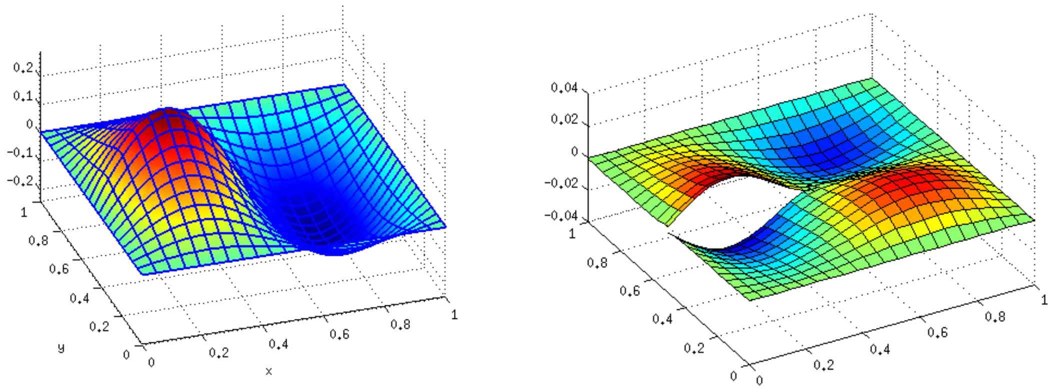

Mode 3 Mode 4

Figure 7.14 First four mode shapes of the edge crack Al/Al$_2$O$_3$ plate.

Table 7.4 The first five natural frequencies of the simply supported Al/Al_2O_3 plate (*a/ L*= 0.5)

n	Method	Mode number				
		1	2	3	4	5
0	Ritz [221]	5.379	11.450	13.320	16.180	17.320
	XFEM [220]	5.387	11.419	13.359	-	-
	XIGA (GSDT)	5.3643	11.4734	13.2801	16.2062	17.2927
	XIGA (FSDT)	5.3657	11.3901	13.2818	16.2062	17.2433
0.2	Ritz [221]	5.001	10.680	12.410	15.420	16.150
	XFEM [220]	5.028	10.659	12.437	-	-
	XIGA (GSDT)	4.9879	10.7069	12.3702	15.4377	16.1267
	XIGA (FSDT)	4.9877	10.6208	12.3641	15.4376	16.0678
1	3D elasticity [221]	4.115	8.836	10.240	13.330	13.520
	Ritz [221]	4.122	8.856	10.250	13.310	13.490
	XFEM [220]	4.1220	8.5260	10.2850	-	-
	XIGA (GSDT)	4.1119	8.8791	10.2131	13.3103	13.4946
	XIGA (FSDT)	4.1123	8.8129	10.2139	13.2728	13.4911
5	Ritz [221]	3.511	7.379	8.621	10.490	11.170
	XFEM [220]	3.626	7.415	8.566	-	-
	XIGA (GSDT)	3.5018	7.3980	8.5912	10.4928	11.1511
	XIGA (FSDT)	3.5218	7.4559	8.6873	10.4956	11.2728
10	Ritz [221]	3.388	7.062	8.289	9.569	10.710
	XFEM [220]	3.409	7.059	8.221	-	-
	XIGA (GSDT)	3.3773	7.0792	8.2582	9.5750	10.6887
	XIGA (FSDT)	3.3986	7.1420	8.3594	9.5757	10.8206

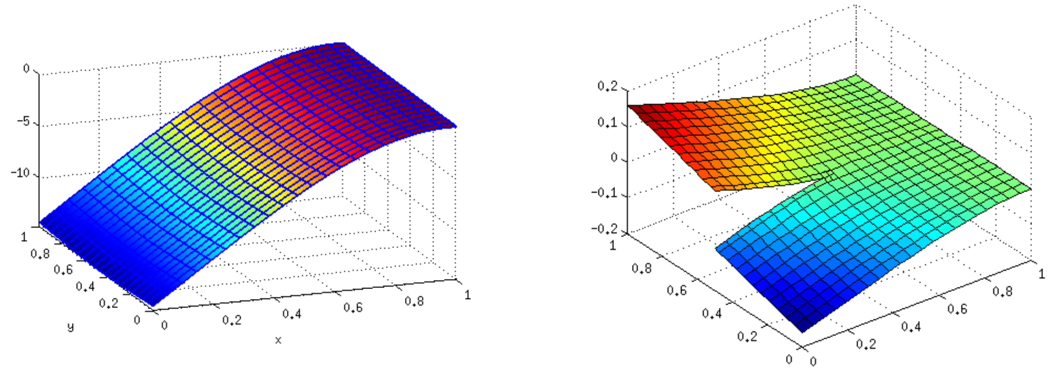

Mode 1 Mode 2

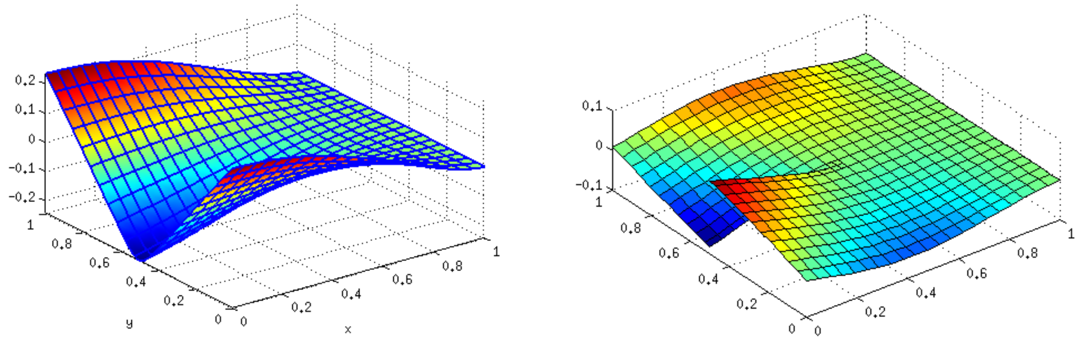

Mode 3 Mode 4

Figure 7.15 First four mode shapes of the cantilever Al/ZrO$_2$ plate with the edge crack.

Table 7.5 The first five natural frequencies of the cantilever Al/ZrO$_2$ plate (a/L = 0.5)

Mode	Method	*n*				
		0	0.2	1	5	10
1	Ritz [221]	1.0380	1.0080	0.9549	0.9743	0.9722
	XFEM [220]	1.0380	1.0075	0.9546	0.9748	0.9722
	XIGA (GSDT)	1.0381	1.0076	0.9547	0.9738	0.9716
	XIGA (FSDT)	1.0380	1.0074	0.9546	0.9744	0.9721
2	Ritz [221]	1.7330	1.6840	1.5970	1.6210	1.6170
	XFEM [220]	1.7329	1.6834	1.5964	1.6242	1.6194
	XIGA (GSDT)	1.7363	1.6871	1.6006	1.6238	1.6189
	XIGA (FSDT)	1.7271	1.6778	1.5919	1.6191	1.6135
3	Ritz [221]	4.8100	4.6790	4.4410	4.4760	4.4620
	XFEM [220]	4.8231	4.6890	4.4410	4.4955	4.4845
	XIGA (GSDT)	4.8084	4.6782	4.4407	4.4743	4.4586
	XIGA (FSDT)	4.8015	4.6695	4.4340	4.4883	4.4693
4	Ritz [221]	5.2180	5.0780	4.8200	4.8500	4.8340
	XIGA (GSDT)	5.2332	5.0923	4.8336	4.8626	4.8457
	XIGA (FSDT)	5.2067	5.0644	4.8089	4.8618	4.8409
5	Ritz [221]	6.1850	6.0250	5.7160	5.5900	5.4780
	XIGA (GSDT)	6.1959	6.0246	5.7148	5.5986	5.4866
	XIGA (FSDT)	6.1950	6.0216	5.7139	5.5987	5.4866

7.3.4 Circular and annular plates with a central crack

We study circular and annular plates with uniform thickness h, outer radius R and inner one r as shown in Figure 7.16. The Al/Al_2O_3 FGM plate is clamped at the outer boundary and has a central crack with length $a=(R-r)/2$. Herein, the Mori-Tanaka homogenization scheme is used.

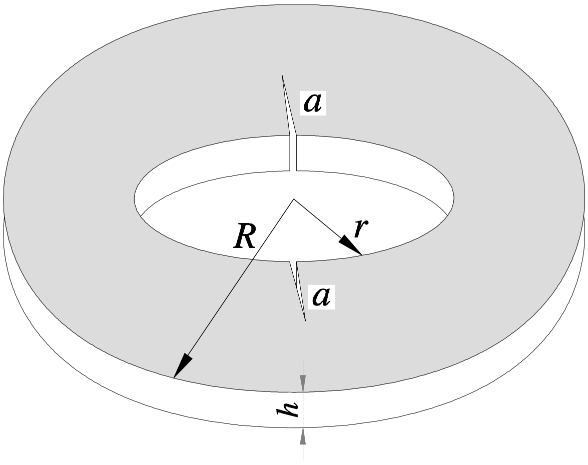

Figure 7.16 The model of an annular plate.

First, the cracked circular plate with the central crack length 2a is investigated by setting the inner radius r = 0. Because the reference solution of this problem is not available, the present method is compared with the XFEM [226]. Note that XFEM incorporated with the FSDT employs the selective integration technique in order to enhance the results [230]. The computed frequency parameters $\left(\hat{\omega}=\omega R^2/h\sqrt{\rho_c/E_c}\right)$ are illustrated in Figure 7.17. It is clear that XIGA provides lower frequencies and higher convergence rate than XFEM. Table 7.6 shows the effect of the power index n on the first five natural frequencies. Observation is again that the frequency parameter decreases due to increase in gradient index, n from 0 to 10. It is also seen that there is a bit difference between the two methods. This may be caused by the following reasons: (1) geometric error due to curved geometry is exact description by XIGA based on NURBS instead of the approximation in XFEM and (2) approximated order: XIGA utilizes NURBS with higher-order functions than XFEM using bilinear Lagrange functions. Furthermore, in XIGA, cubic basis functions (p = 3) gains less results than quadratic basic functions (p = 2). It is believed that with higher-order approximated function, cubic elements produce better results. This conclusion has been previously confirmed in [116]. Figure 7.18 plots the fundamental mode shapes of the circular plate. Using NURBS functions, the curved boundary of the circular plate is still described exactly.

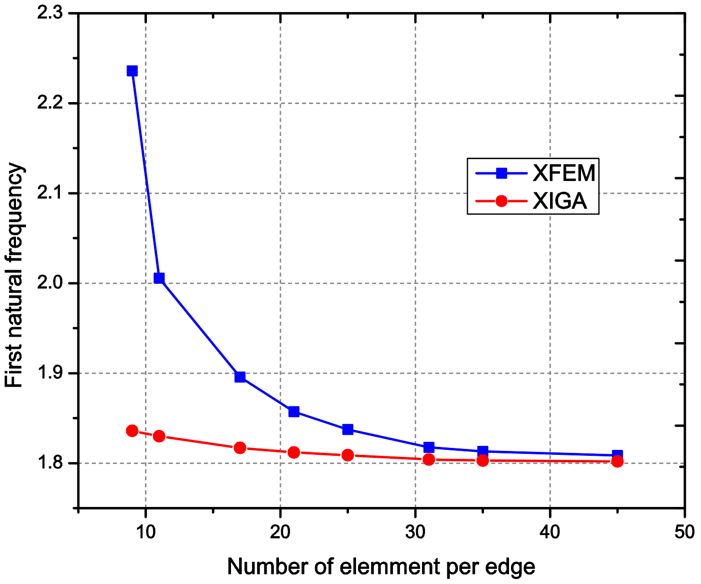

Figure 7.17 Convergence of the first frequency of a cracked FGM circular plate with a/R = 0.5, h/R = 0.1, n = 1.

Table 7.6 The first five natural frequencies $\bar{\omega}$ of a clamped circular Al/Al_2O_3 plate with the central crack (a/R = 0.5)

n	Method	Mode number				
		1	2	3	4	5
0	XFEM$^{(*)}$	2.6436	4.4598	5.9206	8.6034	9.0733
	XIGA$^{(**)}$ (p=2)	2.6406	4.4929	5.9177	8.6315	9.1287
	XIGA$^{(**)}$ (p=3)	2.6309	4.3435	5.8750	8.5429	8.9441
0.2	XFEM	2.2080	3.7396	4.9485	7.1937	7.5976
	XIGA (p=2)	2.2055	3.7674	4.9467	7.2188	7.6452
	XIGA (p=3)	2.1972	3.6414	4.9111	7.1434	7.4922
1	XFEM	1.8086	3.0674	4.0536	5.8914	6.2259
	XIGA (p=2)	1.8044	3.0869	4.0442	5.8989	6.2474
	XIGA (p=3)	1.7969	2.9762	4.0127	5.8306	6.1146
5	XFEM	1.6364	2.7475	3.6526	5.2942	5.5742
	XIGA (p=2)	1.6288	2.7536	3.629	5.2732	5.5584
	XIGA (p=3)	1.6223	2.6538	3.5999	5.211	5.4347
10	XFEM	1.5678	2.6276	3.4977	5.0687	5.3326
	XIGA (p=2)	1.5624	2.6391	3.4821	5.0609	5.3338
	XIGA (p=3)	1.5564	2.5462	3.4550	5.0036	5.2181

$^{(*)}$XFEM uses a fine mesh of 45×45 4-node quadrilateral elements;
$^{(**)}$XIGA uses a mesh of 31×31quadratic (or cubic) NURBS elements.

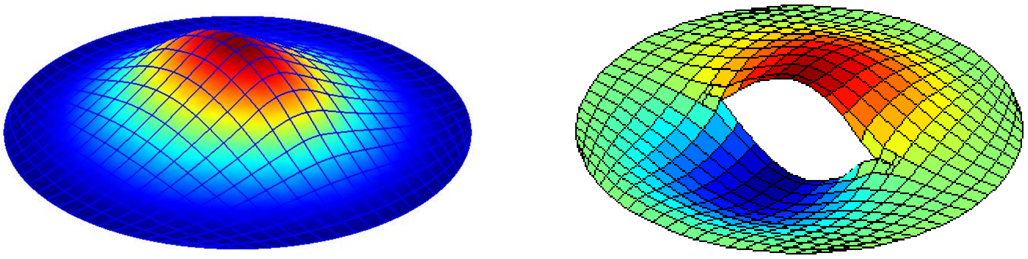

Mode 1

Mode 2

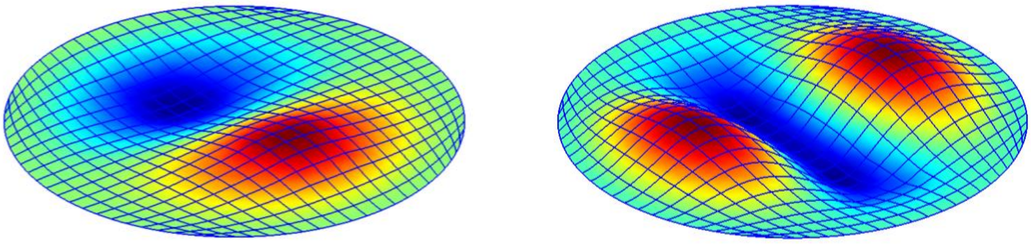

Mode 3

Mode 4

Figure 7.18 First four mode shapes of the edge crack Al/Al_2O_3 plate.

Finally, as the inner radius $r \neq 0$, we have the full annular plate shown in Figure 7.16. Because of symmetry, an upper haft of plate has been modelled, as shown in Figure 7.19, with the symmetric constraint along the line y = 0. Herein, the treatment of symmetric BCs is implemented according to Section 3.5.1.

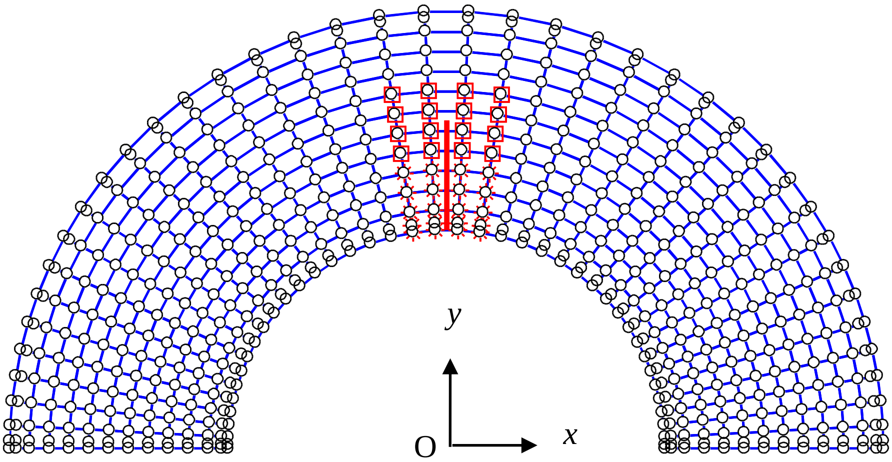

Figure 7.19 Mesh of an upper half of an annular plate.

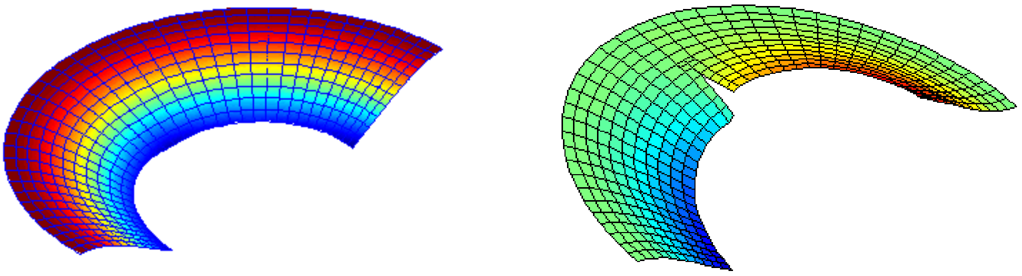

Mode 1 Mode 2

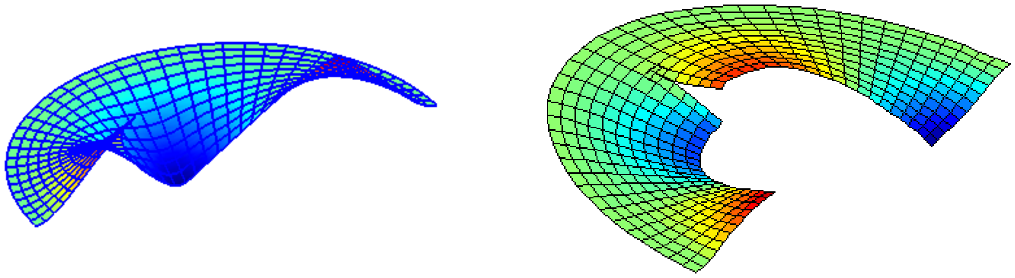

Mode 3 Mode 4

Figure 7.20 First four mode shapes of the annular plate with R/r=2, R/h=10.

Table 7.7 shows the frequency parameter $\tilde{\omega}=\omega(R-r)^2/h\sqrt{\rho_c/E_c}$ of the annular Al/Al_2O_3 plates for different outer radius to inner radius ratios, *R/r* and radius to thickness ratios, *R/h* according to *n* = 1. It is concluded that the frequency parameters decrease sequentially by increasing inner radius to outer radius ratio *r/R*. To close this section, the first four mode shapes of annular FGM plate are depicted in Figure 7.20.

7.4 Concluding remarks

A novel and effective formulation based on combining XIGA and GSDT has been applied to dynamic analysis of cracked FGM plates. In this method, the Heaviside function is enriched to capture the discontinuous phenomenon at the crack faces while, the tip enrichment functions from analytical solution are incorporated with NURBS to perform the singular displacement field at the crack tips. The obtained results, which are in excellent agreement with that of analytical and numerical methods in the literature, demonstrate that XIGA is an effectively computational tool for vibration analysis of the cracked plates.

It is also concluded that magnitudes of the natural frequencies decrease due to an increase in crack length ratio. They change dramatically according to anti-symmetric mode through the *y*-axis, which is perpendicular to crack path.

Herein, two homogenous models based on exponent function have been used to estimate the effective property of the FGM plates including the rule of mixture and the Mori-Tanaka technique. It can be seen that, increasing power index *n* leads to a reduction of frequency parameter of the FGM plates. In addition, to consider the interactions among the constituents, the Mori-Tanaka homogenization scheme gains lower frequency value than the rule of mixture.

Beside the study of some benchmarks in rectangular geometry for purpose of comparison, extensive studies were conducted to concentrate in circular and annular FGM plates. It is believed that XIGA with non-geometric approximation can be very promising to provide good reference results for vibration analysis of these plates with curved boundaries.

Table 7.7 The frequency parameter $\tilde{\omega}$ of the annular pate for different inner radius to outer radius ratios, *r/R* and radius to thickness ratios, *R/h* according to *n* = 1.

R/h	*r/R*	Mode number				
		1	2	3	4	5
2	0	1.2786	1.7682	2.3336	2.7352	2.8058
	0.2	0.8438	1.0109	1.7316	1.8588	1.9021
	0.5	0.5516	0.5896	0.7308	0.8458	0.9817
	0.8	0.2760	0.2771	0.2800	0.2896	0.2905
5	0	1.6804	2.6230	3.5290	4.9598	5.0683
	0.2	1.0877	1.3898	2.7728	3.4371	4.0295
	0.5	0.7845	0.8556	1.1536	1.3664	1.9105
	0.8	0.4923	0.4965	0.5066	0.5225	0.5537
10	0	1.8480	3.5185	4.0473	5.9916	6.3512
	0.2	1.1563	1.5352	3.1932	4.1404	4.8849
	0.5	0.8621	0.9560	1.3533	1.6388	2.3101
	0.8	0.6470	0.6540	0.6730	0.6975	0.7545
20	0	1.8379	3.1941	4.1533	6.1526	6.4956
	0.2	1.1793	1.598	3.3309	4.4139	5.2045
	0.5	0.8877	0.9954	1.4507	1.7937	2.5902
	0.8	0.7279	0.7371	0.7655	0.7999	0.8775
100	0	1.8649	3.3264	4.2398	6.3270	6.7435
	0.2	1.1922	1.6442	3.4202	4.6187	5.3415
	0.5	0.8973	1.0154	1.5007	1.8656	2.6187
	0.8	0.7646	0.7753	0.8124	0.8567	0.9362

Chapter 8 Conclusions and Future Work

8.1 Summary and conclusion

This thesis has successfully addressed the plate formulation based on higher-order plate theories for modelling and analysing functionally graded material plates by using NURBS-based isogeometric analysis. The FGM plates, made of a mixture of two distinct material phases varying through the plate thickness, are homogenized by two homogenization techniques: the rule of mixture or the Mori-Tanaka scheme. The two models produce the same parameters for homogeneous material. As material is inhomogeneous, the former produces higher effective properties than the latter. Thus, the two homogenization techniques give quite different results for FGM plates.

By including higher-order terms in the displacement fields, a family of HSDT models including Reddy's TSDT, RPT and GSDT is constructed to describe more accurately the shear energy part without SCF requirement. They provide better results and more accurate shear stresses than FSDT with the curved shapes through the plate thickness and traction free at top and bottom surfaces. RPT and GSDT produce the shear strains/stresses, which are independent of the transverse displacement. As a result, they naturally overcome the shear-locking phenomenon.

An isogeometric approach based on B-spline and non-uniform rational B-spline achieves easily the smoothness with C^{p-1}continuity by using p^{th} order NURBS. The main advantage of this method is that it naturally fulfils the C^1-continuity requirement of the HSDT models by using higher-order NURBS basis, a non-trivial task in traditional FEM. By embedding the well-known framework of isogeometric finite element, the exact geometry is represented in the first coarsest mesh and is preserved throughout the refinement process. It enables us to eliminate the geometric error. Consequently, the present method produces more accurate and cost-effective results for the plate problems. Furthermore, using the higher-order NURBS basis functions enables us to reduce the shear locking effect in TSDT and FSDT for very thin plate (L/h >1000).

In this thesis, the GSDT and RPT models are presented in the general forms, which are strongly dependent on the function *f*(*z*). Beside, some other available functions [57, 118, 160, 162, 164, 165], a new inverse tangent function is proposed. Through numerous examples for static, free vibration and buckling analyses of the FGM plates, it is observed that the proposed function enhances the solutions, which are more accurate than those of IGA based on other functions or that of quasi-3D models as compared to the 3D elasticity solutions.

By adopting large deflection assumptions, the von Kármán strain-displacement relation is considered in the plate formulations for geometrically nonlinear bending, transient and post-buckling analyses. The nonlinear governing equations are originally established in the Lagrangian system (initial configuration) and then solved by the incremental/iterative approaches. With the additional nonlinear stiffness in the global stiffness, the nonlinear deflections are always lower than the linear ones.

Because of the non-symmetric material properties and temperature field through the plate thickness in the FGM plates, there is no bifurcation-type of instability occurs for simply supported conditions. Under these boundary conditions, the plate exhibits bending behaviour due to the existence of extra extension-bending coupling or thermal moment. In special case, the clamped boundary condition is capable to neutralize the extra moments. Thus, the primary path and the secondary path (post buckling path) can be exhibited for the clamped FGM plates.

In the last chapter, an extended isogeometric analysis (XIGA) is successfully developed for the cracked 2D structures and FGM plates. In this method, the Heaviside function is enriched to capture the discontinuous phenomenon at the crack faces, whilst the tip enrichment functions from analytical solution are incorporated with NURBS to approximate the singular field at the crack tips. The obtained results from some benchmark problems show that proposal method achieves better accuracy and super-convergence as compared to traditional XFEM.

8.2 Future research

This thesis is restricted to study FGM plate problems related to static and vibration analyses, elastic stability based on a framework of isogeometric approach. Many aspects have been not yet studied here. They can be suggested as possible future extension of the present work:

- With many wonderful features, FGMs have been applied in the nano/micro structures such as nano-electro-mechanical systems (NEMS) and micro-electro-mechanical systems (MEMS). Beside some experimental results, the present method can be combined with the nonlocal continuum mechanics to model the nano and micro material mechanical behaviours.
- The results in this thesis are given for one layer FGM, for which properties vary according to one dimension through plate thickness. In some realistic structures, volume fractions of the constituents can be distributed variously through two-directions
- Under high temperature, the constituents can react with oxygen and become oxidized. It is obvious that their material nonlinear behaviour will dominate. Therefore, nonlinear material models need to be developed and incorporated in the present formulation to capture more realistic structural behaviours.
- All the presented examples are either square or circle/ellipse, which are the simplest geometries that can be modelled straightforward with only a single patch. To describe some complex geometries, the new techniques based on IGA: multi-patch or finite cell method have been developed. It is believed that they are very useful for analysis of real structures.
- Another research direction is to extend the present 2D theories to full-3D or quasi-3D theories.
- Currently, uniform mesh is utilized at discontinuous points. To enhance results, local refinement strategies can be developed for the present approach. We suggest to use T-spline basis functions instead of NURBS basis functions.
- A possible interesting topic is to apply XIGA for vibration based damage assessment.
- In chapter 7, the crack was assumed to develop through the whole thickness of the plate. An interesting direction, in particular for fracture mechanics, related to the part-through surface crack in an elastic plate is suggested. A special treatment could be developed in the vicinity of damage position while standard homogenized plate model is used elsewhere.

References

[1] D. Jha, T. Kant, R. Singh, A critical review of recent research on functionally graded plates, Composite Structures, 96 (2013) 833-849.

[2] M. Koizumi, FGM activities in Japan, Composites Part B: Engineering, 28 (1997) 1-4.

[3] E.C.N. Silva, M.C. Walters, G.H. Paulino, Modeling bamboo as a functionally graded material: lessons for the analysis of affordable materials, Journal of Materials Science, 41 (2006) 6991-7004.

[4] M. Bever, P. Duwez, Gradients in composite materials, Materials Science and Engineering, 10 (1972) 1-8.

[5] M. Shen, M. Bever, Gradients in polymeric materials, Journal of Materials science, 7 (1972) 741-746.

[6] M. Niino, K. A, R. Watanabe, Fabrication of a high pressure thrust chamber by the CIP forming method, AIAA Journal, (1986).

[7] N. Noda, T. Tsuji, Steady thermal stresses in a plate of functionally gradient material, Trans. Jpn. Soc. Mech. Eng. A, 57 (1991) 98-103.

[8] K. Tanaka, Y. Tanaka, K. Enomoto, V. Poterasu, Y. Sugano, Design of thermoelastic materials using direct sensitivity and optimization methods. Reduction of thermal stresses in functionally gradient materials, Computer Methods in Applied Mechanics and Engineering, 106 (1993) 271-284.

[9] K. Tanaka, Y. Tanaka, H. Watanabe, V. Poterasu, Y. Sugano, An improved solution to thermoelastic material design in functionally gradient materials: scheme to reduce thermal stresses, Computer Methods in Applied Mechanics and Engineering, 109 (1993) 377-389.

[10] J. Zhi-He, N. Naotake, Transient thermal stress intensity factors for a crack in a semi-infinite plate of a functionally gradient material, International journal of solids and structures, 31 (1994) 203-218.

[11] V. Birman, L.W. Byrd, Modeling and analysis of functionally graded materials and structures, Applied Mechanics Reviews, 60 (2007) 195-216.

[12] K. Swaminathan, D. Naveenkumar, A. Zenkour, E. Carrera, Stress, vibration and buckling analyses of FGM plates—A state-of-the-art review, Composite Structures, 120 (2015) 10-31.

[13] K. Khor, Y. Gu, Z. Dong, Mechanical behavior of plasma sprayed functionally graded YSZ/NiCoCrAlY composite coatings, Surface and Coatings Technology, 139 (2001) 200-206.

[14] Y. Miyamoto, W. Kaysser, B. Rabin, A. Kawasaki, R. Ford, Functionally graded materials: design, processing and applications, Springer Science & Business Media, 2013.

[15] T. Krell, U. Schulz, M. Peters, W.A. Kaysser, Graded EB-PVD alumina-zirconia thermal barrier coatings-an experimental approach, in: Materials science forum, Trans Tech Publ, 1999, pp. 396-401.

[16] M.M. Gasik, Functionally graded materials: bulk processing techniques, International Journal of Materials and Product Technology, 39 (2010) 20-29.

[17] F. Watari, A. Yokoyama, M. Omori, T. Hirai, H. Kondo, M. Uo, T. Kawasaki, Biocompatibility of materials and development to functionally graded implant for bio-medical application, Composites Science and Technology, 64 (2004) 893-908.

[18] M. Tobioka, ACE COAT AC 15 aluminum oxide coated cutting tool for highly efficient machining, in, Technical Report" Sumitomodenki", 135, 190-196, 1989.

[19] N. Pagano, Exact solutions for rectangular bidirectional composites and sandwich plates, Journal of composite materials, 4 (1970) 20-34.

[20] A.K. Noor, Free vibrations of multilayered composite plates, AIAA journal, 11 (1973) 1038-1039.

[21] A.K. Noor, Stability of multilayered composite plates, Fibre Science and Technology, 8 (1975) 81-89.

[22] E. Pan, Exact solution for functionally graded anisotropic elastic composite laminates, Journal of Composite materials, 37 (2003) 1903-1920.

[23] S.S. Vel, R. Batra, Exact solution for thermoelastic deformations of functionally graded thick rectangular plates, AIAA journal, 40 (2002) 1421-1433.

[24] S.S. Vel, R. Batra, Three-dimensional exact solution for the vibration of functionally graded rectangular plates, Journal of Sound and Vibration, 272 (2004) 703-730.

[25] J. Reddy, Z.-Q. Cheng, Frequency of functionally graded plates with three-dimensional asymptotic approach, Journal of Engineering Mechanics, 129 (2003) 896-900.

[26] P. Malekzadeh, S. Shahpari, H. Ziaee, Three-dimensional free vibration of thick functionally graded annular plates in thermal environment, Journal of Sound and Vibration, 329 (2010) 425-442.

[27] A.R. Mojdehi, A. Darvizeh, A. Basti, H. Rajabi, Three dimensional static and dynamic analysis of thick functionally graded plates by the meshless local Petrov–Galerkin (MLPG) method, Engineering Analysis with Boundary Elements, 35 (2011) 1168-1180.

[28] C. Dong, Three-dimensional free vibration analysis of functionally graded annular plates using the Chebyshev–Ritz method, Materials & Design, 29 (2008) 1518-1525.

[29] J.N. Reddy, Mechanics of laminated composite plates-theory and analysis, CRC Press 2nd Edit, New York, 2004.

[30] E. Carrera, Evaluation of layerwise mixed theories for laminated plates analysis, AIAA journal, 36 (1998) 830-839.

[31] E. Carrera, Historical review of zig-zag theories for multilayered plates and shells, Applied mechanics reviews, 56 (2003) 287-308.

[32] G.R. Kirchhoff, Uber das Gleichgewicht und die Bewegung einer elastischen Scheibe, (1850).

[33] A.E.H. Love, The small free vibrations and deformation of a thin elastic shell, Philosophical Transactions of the Royal Society of London. A, (1888) 491-546.

[34] E. Feldman, J. Aboudi, Buckling analysis of functionally graded plates subjected to uniaxial loading, Composite Structures, 38 (1997) 29-36.

[35] R. Javaheri, M. Eslami, Thermal buckling of functionally graded plates, AIAA journal, 40 (2002) 162-169.

[36] S.-H. Chi, Y.-L. Chung, Mechanical behavior of functionally graded material plates under transverse load—Part I: Analysis, International Journal of Solids and Structures, 43 (2006) 3657-3674.

[37] J. Yang, H.-S. Shen, Dynamic response of initially stressed functionally graded rectangular thin plates, Composite Structures, 54 (2001) 497-508.

[38] J. Yanga, H.-S. Shen, Non-linear analysis of functionally graded plates under transverse and in-plane loads, International Journal of Non-Linear Mechanics, 38 (2003) 467-482.

[39] C.-S. Chen, A.-H. Tan, Imperfection sensitivity in the nonlinear vibration of initially stresses functionally graded plates, Composite Structures, 78 (2007) 529-536.

[40] E. Reissner, The effect of transverse shear deformation on the bending of elastic plates, (1945).

[41] E. Reissner, On bending of elastic plates, Quart. Appl. Math, 5 (1947) 55-68.

[42] R.D. Mindlin, Influence of rotary inertia and shear on flexural motions of isotropic elastic plates, (1951).

[43] G. Praveen, J. Reddy, Nonlinear transient thermoelastic analysis of functionally graded ceramic-metal plates, International Journal of Solids and Structures, 35 (1998) 4457-4476.

[44] N. Sundararajan, T. Prakash, M. Ganapathi, Nonlinear free flexural vibrations of functionally graded rectangular and skew plates under thermal environments, Finite Elements in Analysis and Design, 42 (2005) 152-168.

[45] Y. Lee, X. Zhao, K.M. Liew, Thermoelastic analysis of functionally graded plates using the element-free kp-Ritz method, Smart Materials and Structures, 18 (2009) 035007.

[46] X. Zhao, Y. Lee, K.M. Liew, Free vibration analysis of functionally graded plates using the element-free kp-Ritz method, Journal of sound and Vibration, 319 (2009) 918-939.

[47] X. Zhao, K.M. Liew, Geometrically nonlinear analysis of functionally graded plates using the element-free kp-Ritz method, Computer Methods in Applied Mechanics and Engineering, 198 (2009) 2796-2811.

[48] H. Nguyen-Xuan, L.V. Tran, T. Nguyen-Thoi, H. Vu-Do, Analysis of functionally graded plates using an edge-based smoothed finite element method, Composite Structures, 93 (2011) 3019-3039.

[49] H. Nguyen-Xuan, L.V. Tran, C.H. Thai, T. Nguyen-Thoi, Analysis of functionally graded plates by an efficient finite element method with node-based strain smoothing, Thin-Walled Structures, 54 (2012) 1-18.

[50] N. Valizadeh, S. Natarajan, O.A. Gonzalez-Estrada, T. Rabczuk, T.Q. Bui, S.P. Bordas, NURBS-based finite element analysis of functionally graded plates: static bending, vibration, buckling and flutter, Composite Structures, 99 (2013) 309-326.

[51] S. Yin, T. Yu, T.Q. Bui, M.N. Nguyen, Geometrically nonlinear analysis of functionally graded plates using isogeometric analysis, Engineering Computations, 32 (2015) 519-558.

[52] Y.W. Kwon, H. Bang, The finite element method using MATLAB, CRC press, 2000.

[53] K.J. Bathe, E.N. Dvorkin, A four-node plate bending element based on Mindlin/Reissner plate theory and a mixed interpolation, International Journal for Numerical Methods in Engineering, 21 (1985) 367-383.

[54] A. Tessler, T.J. Hughes, A three-node Mindlin plate element with improved transverse shear, Computer Methods in Applied Mechanics and Engineering, 50 (1985) 71-101.

[55] K.-U. Bletzinger, M. Bischoff, E. Ramm, A unified approach for shear-locking-free triangular and rectangular shell finite elements, Computers & Structures, 75 (2000) 321-334.

[56] A. Ferreira, L.M. Castro, S. Bertoluzza, A high order collocation method for the static and vibration analysis of composite plates using a first-order theory, Composite Structures, 89 (2009) 424-432.

[57] J.N. Reddy, A Simple Higher-Order Theory for Laminated Composite Plates, Journal of Applied Mechanics, 51 (1984) 745-752.

[58] H. Matsunaga, Free vibration and stability of functionally graded plates according to a 2-D higher-order deformation theory, Composite structures, 82 (2008) 499-512.

[59] N. Senthilnathan, S. Lim, K. Lee, S. Chow, Buckling of shear-deformable plates, AIAA journal, 25 (1987) 1268-1271.

[60] D. Gilhooley, R. Batra, J. Xiao, M. McCarthy, J. Gillespie, Analysis of thick functionally graded plates by using higher-order shear and normal deformable plate theory and MLPG method with radial basis functions, Composite Structures, 80 (2007) 539-552.

[61] W. Zhen, C. Wanji, A higher-order theory and refined three-node triangular element for functionally graded plates, European Journal of Mechanics-A/Solids, 25 (2006) 447-463.

[62] C.H. Thai, S. Kulasegaram, L.V. Tran, H. Nguyen-Xuan, Generalized shear deformation theory for functionally graded isotropic and sandwich plates based on isogeometric approach, Computers & Structures, 141 (2014) 94-112.

[63] T. Kant, K. Swaminathan, Analytical solutions for the static analysis of laminated composite and sandwich plates based on a higher order refined theory, Composite Structures, 56 (2002) 329-344.

[64] A.M. Zenkour, Generalized shear deformation theory for bending analysis of functionally graded plates, Applied Mathematical Modelling, 30 (2006) 67-84.

[65] S. Xiang, Y.-x. Jin, Z.-y. Bi, S.-x. Jiang, M.-s. Yang, A n-order shear deformation theory for free vibration of functionally graded and composite sandwich plates, Composite Structures, 93 (2011) 2826-2832.

[66] J. Reddy, Analysis of functionally graded plates, International Journal for Numerical Methods in Engineering, 47 (2000) 663-684.

[67] J. Yang, Y. Hao, W. Zhang, S. Kitipornchai, Nonlinear dynamic response of a functionally graded plate with a through-width surface crack, Nonlinear Dynamics, 59 (2010) 207-219.

[68] R. Javaheri, M. Eslami, Thermal buckling of functionally graded plates based on higher order theory, Journal of Thermal Stresses, 25 (2002) 603-625.

[69] M. Najafizadeh, H. Heydari, Thermal buckling of functionally graded circular plates based on higher order shear deformation plate theory, European Journal of Mechanics-A/Solids, 23 (2004) 1085-1100.

[70] A. Ferreira, R. Batra, C. Roque, L. Qian, P. Martins, Static analysis of functionally graded plates using third-order shear deformation theory and a meshless method, Composite Structures, 69 (2005) 449-457.

[71] A.J. Ferreira, C. Roque, R. Jorge, G. Fasshauer, R. Batra, Analysis of functionally graded plates by a robust meshless method, Mechanics of Advanced Materials and Structures, 14 (2007) 577-587.

[72] A. Ferreira, R. Batra, C. Roque, L. Qian, R. Jorge, Natural frequencies of functionally graded plates by a meshless method, Composite Structures, 75 (2006) 593-600.

[73] L.V. Tran, A.J.M. Ferreira, H. Nguyen-Xuan, Isogeometric analysis of functionally graded plates using higher-order shear deformation theory, Composites Part B: Engineering, 51 (2013) 368-383.

[74] L.V. Tran, C.H. Thai, H. Nguyen-Xuan, An isogeometric finite element formulation for thermal buckling analysis of functionally graded plates, Finite Elements in Analysis and Design, 73 (2013) 65-76.

[75] C. Shankara, N. Iyengar, A C0 element for the free vibration analysis of laminated composite plates, Journal of Sound and Vibration, 191 (1996) 721-738.

[76] C.H. Thai, L.V. Tran, D.T. Tran, T. Nguyen-Thoi, H. Nguyen-Xuan, Analysis of laminated composite plates using higher-order shear deformation plate theory and node-based smoothed discrete shear gap method, Applied Mathematical Modelling, 36 (2012) 5657-5677.

[77] M.G. Taj, A. Chakrabarti, A.H. Sheikh, Analysis of functionally graded plates using higher order shear deformation theory, Applied Mathematical Modelling, 37 (2013) 8484-8494.

[78] P. Phung-Van, T. Nguyen-Thoi, L.V. Tran, H. Nguyen-Xuan, A cell-based smoothed discrete shear gap method (CS-DSG3) based on the C 0-type higher-order shear deformation theory for static and free vibration analyses of functionally graded plates, Computational Materials Science, 79 (2013) 857-872.

[79] P. Phung-Van, T. Nguyen-Thoi, H. Luong-Van, Q. Lieu-Xuan, Geometrically nonlinear analysis of functionally graded plates using a cell-based smoothed three-node plate element (CS-MIN3) based on the C 0-HSDT, Computer Methods in Applied Mechanics and Engineering, 270 (2014) 15-36.

[80] R.C. Beach, An Introduction to the Curves and Surfaces of Computer-Aided Design, Van Nostrand Reinhold Co., 1991.

[81] I.J. Schönberg, Contributions to the problem of approximation of equidistant data by analytic functions, Quart. Appl. Math, 4 (1946) 45-99.

[82] R.F. Riesenfeld, Applications of B-spline approximation to geometric problems of computer-aided design, (1973).

[83] K.J. Versprille, Computer-aided design applications of the rational B-spline approximation form, (1975).

[84] M.G. Cox, The numerical evaluation of B-splines, IMA Journal of Applied Mathematics, 10 (1972) 134-149.

[85] C. De Boor, On calculating with B-splines, Journal of Approximation Theory, 6 (1972) 50-62.

[86] C. De Boor, A practical guide to splines, Mathematics of Computation, (1978).

[87] E. Cohen, T. Lyche, R. Riesenfeld, Discrete B-splines and subdivision techniques in computer-aided geometric design and computer graphics, Computer graphics and image processing, 14 (1980) 87-111.

[88] L. Ramshaw, Blossoms are polar forms, Computer Aided Geometric Design, 6 (1989) 323-358.

[89] T.W. Sederberg, J. Zheng, A. Bakenov, A. Nasri, T-splines and T-NURCCs, in: ACM transactions on graphics (TOG), ACM, 2003, pp. 477-484.

[90] T.W. Sederberg, D.L. Cardon, G.T. Finnigan, N.S. North, J. Zheng, T. Lyche, T-spline simplification and local refinement, in: ACM Transactions on Graphics (TOG), ACM, 2004, pp. 276-283.

[91] J. Deng, F. Chen, X. Li, C. Hu, W. Tong, Z. Yang, Y. Feng, Polynomial splines over hierarchical T-meshes, Graphical models, 70 (2008) 76-86.

[92] N. Nguyen-Thanh, H. Nguyen-Xuan, S.P.A. Bordas, T. Rabczuk, Isogeometric analysis using polynomial splines over hierarchical T-meshes for two-dimensional elastic solids, Computer Methods in Applied Mechanics and Engineering, 200 (2011) 1892-1908.

[93] N. Nguyen-Thanh, J. Kiendl, H. Nguyen-Xuan, R. Wüchner, K. Bletzinger, Y. Bazilevs, T. Rabczuk, Rotation free isogeometric thin shell analysis using PHT-splines, Computer Methods in Applied Mechanics and Engineering, 200 (2011) 3410-3424.

[94] J.A. Cottrell, T.J. Hughes, Y. Bazilevs, Isogeometric analysis: toward integration of CAD and FEA, John Wiley & Sons, 2009.

[95] T.J.R. Hughes, J.A. Cottrell, Y. Bazilevs, Isogeometric analysis: CAD, finite elements, NURBS, exact geometry and mesh refinement, Computer Methods in Applied Mechanics and Engineering, 194 (2005) 4135-4195.

[96] X. Qian, O. Sigmund, Isogeometric shape optimization of photonic crystals via Coons patches, Computer Methods in Applied Mechanics and Engineering, 200 (2011) 2237-2255.

[97] Y. Bazilevs, T. Hughes, NURBS-based isogeometric analysis for the computation of flows about rotating components, Computational Mechanics, 43 (2008) 143-150.

[98] H. Gomez, T.J. Hughes, X. Nogueira, V.M. Calo, Isogeometric analysis of the isothermal Navier–Stokes–Korteweg equations, Computer Methods in Applied Mechanics and Engineering, 199 (2010) 1828-1840.

[99] P.N. Nielsen, A.R. Gersborg, J. Gravesen, N.L. Pedersen, Discretizations in isogeometric analysis of Navier–Stokes flow, Computer methods in applied mechanics and engineering, 200 (2011) 3242-3253.

[100] Y. Bazilevs, V. Calo, T. Hughes, Y. Zhang, Isogeometric fluid-structure interaction: theory, algorithms, and computations, Computational mechanics, 43 (2008) 3-37.

[101] Y. Bazilevs, V. Calo, Y. Zhang, T.J. Hughes, Isogeometric fluid–structure interaction analysis with applications to arterial blood flow, Computational Mechanics, 38 (2006) 310-322.

[102] Y. Bazilevs, M.-C. Hsu, M. Scott, Isogeometric fluid–structure interaction analysis with emphasis on non-matching discretizations, and with application to wind turbines, Computer Methods in Applied Mechanics and Engineering, 249 (2012) 28-41.

[103] I. Temizer, P. Wriggers, T. Hughes, Contact treatment in isogeometric analysis with NURBS, Computer Methods in Applied Mechanics and Engineering, 200 (2011) 1100-1112.

[104] J. Lu, Isogeometric contact analysis: Geometric basis and formulation for frictionless contact, Computer Methods in Applied Mechanics and Engineering, 200 (2011) 726-741.

[105] L. De Lorenzis, I. Temizer, P. Wriggers, G. Zavarise, A large deformation frictional contact formulation using NURBS-based isogeometric analysis, International Journal for Numerical Methods in Engineering, 87 (2011) 1278-1300.

[106] N.D. Manh, A. Evgrafov, A.R. Gersborg, J. Gravesen, Isogeometric shape optimization of vibrating membranes, Computer Methods in Applied Mechanics and Engineering, 200 (2011) 1343-1353.

[107] H. Gómez, V.M. Calo, Y. Bazilevs, T.J. Hughes, Isogeometric analysis of the Cahn–Hilliard phase-field model, Computer methods in applied mechanics and engineering, 197 (2008) 4333-4352.

[108] C.V. Verhoosel, M.A. Scott, T.J. Hughes, R. De Borst, An isogeometric analysis approach to gradient damage models, International Journal for Numerical Methods in Engineering, 86 (2011) 115-134.

[109] P. Fischer, M. Klassen, J. Mergheim, P. Steinmann, R. Müller, Isogeometric analysis of 2D gradient elasticity, Computational Mechanics, 47 (2011) 325-334.

[110] J. Cottrell, A. Reali, Y. Bazilevs, T. Hughes, Isogeometric analysis of structural vibrations, Computer methods in applied mechanics and engineering, 195 (2006) 5257-5296.

[111] C.V. Verhoosel, M.A. Scott, R. de Borst, T.J. Hughes, An isogeometric approach to cohesive zone modeling, International Journal for Numerical Methods in Engineering, 87 (2011) 336-360.

[112] E. De Luycker, D. Benson, T. Belytschko, Y. Bazilevs, M. Hsu, X-FEM in isogeometric analysis for linear fracture mechanics, International Journal for Numerical Methods in Engineering, 87 (2011) 541-565.

[113] S.S. Ghorashi, N. Valizadeh, S. Mohammadi, Extended isogeometric analysis for simulation of stationary and propagating cracks, International Journal for Numerical Methods in Engineering, 89 (2012) 1069-1101.

[114] A. Cazzani, M. Malagù, E. Turco, Isogeometric analysis of plane-curved beams, Mathematics and Mechanics of Solids, (2014) 1081286514531265.

[115] A.-T. Luu, N.-I. Kim, J. Lee, NURBS-based isogeometric vibration analysis of generally laminated deep curved beams with variable curvature, Composite Structures, 119 (2015) 150-165.

[116] C.H. Thai, H. Nguyen-Xuan, N. Nguyen-Thanh, T.H. Le, T. Nguyen-Thoi, T. Rabczuk, Static, free vibration, and buckling analysis of laminated composite Reissner–Mindlin plates using NURBS-based isogeometric approach, International Journal for Numerical Methods in Engineering, 91 (2012) 571-603.

[117] S. Yin, J.S. Hale, T. Yu, T.Q. Bui, S.P. Bordas, Isogeometric locking-free plate element: a simple first order shear deformation theory for functionally graded plates, Composite Structures, 118 (2014) 121-138.

[118] H. Nguyen-Xuan, C.H. Thai, T. Nguyen-Thoi, Isogeometric finite element analysis of composite sandwich plates using a higher order shear deformation theory, Composites Part B: Engineering, 55 (2013) 558-574.

[119] C.H. Thai, H. Nguyen-Xuan, S. Bordas, N. Nguyen-Thanh, T. Rabczuk, Isogeometric analysis of laminated composite plates using the higher-order shear deformation theory, Mechanics of Advanced Materials and Structures, 22 (2015) 451-469.

[120] P. Phung-Van, M. Abdel-Wahab, K. Liew, S. Bordas, H. Nguyen-Xuan, Isogeometric analysis of functionally graded carbon nanotube-reinforced composite plates using higher-order shear deformation theory, Composite Structures, 123 (2015) 137-149.

[121] Y. Guo, A.P. Nagy, Z. Gürdal, A layerwise theory for laminated composites in the framework of isogeometric analysis, Composite Structures, 107 (2014) 447-457.

[122] C.H. Thai, A.J.M. Ferreira, E. Carrera, H. Nguyen-Xuan, Isogeometric analysis of laminated composite and sandwich plates using a layerwise deformation theory, Composite Structures, 104 (2013) 196-214.

[123] J. Kiendl, Y. Bazilevs, M.-C. Hsu, R. Wüchner, K.-U. Bletzinger, The bending strip method for isogeometric analysis of Kirchhoff–Love shell structures comprised of multiple patches, Computer Methods in Applied Mechanics and Engineering, 199 (2010) 2403-2416.

[124] D. Benson, Y. Bazilevs, M.-C. Hsu, T. Hughes, A large deformation, rotation-free, isogeometric shell, Computer Methods in Applied Mechanics and Engineering, 200 (2011) 1367-1378.

[125] N. Collier, D. Pardo, L. Dalcin, M. Paszynski, V.M. Calo, The cost of continuity: A study of the performance of isogeometric finite elements using direct solvers, Computer Methods in Applied Mechanics and Engineering, 213 (2012) 353-361.

[126] R. Sevilla, S. Fernández-Méndez, A. Huerta, NURBS-enhanced finite element method (NEFEM), International Journal for Numerical Methods in Engineering, 76 (2008) 56-83.

[127] R. Sevilla, S. Fernández-Méndez, A. Huerta, 3D NURBS-enhanced finite element method (NEFEM), International Journal for Numerical Methods in Engineering, 88 (2011) 103-125.

[128] R.N. Simpson, S.P. Bordas, J. Trevelyan, T. Rabczuk, A two-dimensional isogeometric boundary element method for elastostatic analysis, Computer Methods in Applied Mechanics and Engineering, 209 (2012) 87-100.

[129] R.N. Simpson, S.P.A. Bordas, H. Lian, J. Trevelyan, An isogeometric boundary element method for elastostatic analysis: 2D implementation aspects, Computers & Structures, 118 (2013) 2-12.

[130] S. Natarajan, J. Wang, C. Song, C. Birk, Isogeometric analysis enhanced by the scaled boundary finite element method, Computer Methods in Applied Mechanics and Engineering, 283 (2015) 733-762.

[131] K.M. Liew, X. Zhao, A.J. Ferreira, A review of meshless methods for laminated and functionally graded plates and shells, Composite Structures, 93 (2011) 2031-2041.

[132] T. Belytschko, Y. Krongauz, D. Organ, M. Fleming, P. Krysl, Meshless methods: an overview and recent developments, Computer methods in applied mechanics and engineering, 139 (1996) 3-47.

[133] S. Li, W.K. Liu, Meshfree and particle methods and their applications, Applied Mechanics Reviews, 55 (2002) 1-34.

[134] J.-S. Chen, C.-T. Wu, S. Yoon, Y. You, A stabilized conforming nodal integration for Galerkin mesh-free methods, International journal for numerical methods in engineering, 50 (2001) 435-466.

[135] V.P. Nguyen, T. Rabczuk, S. Bordas, M. Duflot, Meshless methods: a review and computer implementation aspects, Mathematics and computers in simulation, 79 (2008) 763-813.

[136] H. Nguyen-Xuan, L.V. Tran, C.H. Thai, S. Kulasegaram, S.P.A. Bordas, Isogeometric analysis of functionally graded plates using a refined plate theory, Composites Part B: Engineering, 64 (2014) 222-234.

[137] L.V. Tran, J. Lee, H. Nguyen-Van, H. Nguyen-Xuan, M.A. Wahab, Geometrically nonlinear isogeometric analysis of laminated composite plates based on higher-order shear deformation theory, International Journal of Non-Linear Mechanics, 72 (2015) 42-52.

[138] J. Aliaga, J. Reddy, Nonlinear thermoelastic analysis of functionally graded plates using the third-order shear deformation theory, International Journal of Computational Engineering Science, 5 (2004) 753-779.

[139] S. Zaghloul, J. Kennedy, Nonlinear behavior of symmetrically laminated plates, Journal of Applied Mechanics, 42 (1975) 234-236.

[140] H.-S. Shen, Thermal postbuckling behavior of shear deformable FGM plates with temperature-dependent properties, International Journal of Mechanical Sciences, 49 (2007) 466-478.

[141] K. Liew, J. Yang, S. Kitipornchai, Postbuckling of piezoelectric FGM plates subject to thermo-electro-mechanical loading, International Journal of Solids and Structures, 40 (2003) 3869-3892.

[142] L. Qian, R. Batra, L. Chen, Static and dynamic deformations of thick functionally graded elastic plates by using higher-order shear and normal deformable plate theory and meshless local Petrov–Galerkin method, Composites Part B: Engineering, 35 (2004) 685-697.

[143] T. Mori, K. Tanaka, Average stress in matrix and average elastic energy of materials with misfitting inclusions, Acta metallurgica, 21 (1973) 571-574.

[144] Y. Benveniste, A new approach to the application of Mori-Tanaka's theory in composite materials, Mechanics of materials, 6 (1987) 147-157.

[145] H. Hatta, M. Taya, Effective thermal conductivity of a misoriented short fiber composite, Journal of Applied Physics, 58 (1985) 2478-2486.

[146] B.W. Rosen, Z. Hashin, Effective thermal expansion coefficients and specific heats of composite materials, International Journal of Engineering Science, 8 (1970) 157-173.

[147] R. Hill, A self-consistent mechanics of composite materials, Journal of the Mechanics and Physics of Solids, 13 (1965) 213-222.

[148] Z. Hashin, The elastic moduli of heterogeneous materials, Journal of Applied Mechanics, 29 (1962) 143-150.

[149] Z. Hashin, B.W. Rosen, The elastic moduli of fiber-reinforced materials, Journal of Applied Mechanics, 31 (1964) 223-232.

[150] C. Chamis, G. Sendeckyj, Critique on theories predicting thermoelastic properties of fibrous composites, Journal of Composite Materials, 2 (1968) 332-358.

[151] J. Aboudi, Mechanics of composite materials: a unified micromechanical approach, Elsevier, 2013.

[152] T. Reiter, G.J. Dvorak, V. Tvergaard, Micromechanical models for graded composite materials, Journal of the Mechanics and Physics of Solids, 45 (1997) 1281-1302.

[153] S. Suresh, A. Mortensen, Fundamentals of functionally graded materials, The Institut of Materials, 1998.

[154] C. Chinosi, L. Della Croce, Approximation of functionally graded plates with non-conforming finite elements, Journal of computational and Applied Mathematics, 210 (2007) 106-115.

[155] B.S. Shariat, M. Eslami, Thermal buckling of imperfect functionally graded plates, International Journal of Solids and Structures, 43 (2006) 4082-4096.

[156] Y.S. Touloukian, Thermophysical Properties of High Temperature Solid Materials. Volume 4. Oxides and Their Solutions and Mixtures. Part I. Simple Oxygen Compounds and Their Mixtures, in, DTIC Document, 1966.

[157] J. Reddy, C. Chin, Thermomechanical analysis of functionally graded cylinders and plates, Journal of Thermal Stresses, 21 (1998) 593-626.

[158] S. Timoshenko, S. Woinowsky-Krieger, S. Woinowsky-Krieger, Theory of plates and shells, McGraw-hill New York, 1959.

[159] L.V. Tran, C.H. Thai, H.T. Le, B.S. Gan, J. Lee, H. Nguyen-Xuan, Isogeometric analysis of laminated composite plates based on a four-variable refined plate theory, Engineering Analysis with Boundary Elements, 47 (2014) 68-81.

[160] R.P. Shimpi, Refined plate theory and its variants, AIAA journal, 40 (2002) 137-146.

[161] R. Shimpi, H. Patel, A two variable refined plate theory for orthotropic plate analysis, International Journal of Solids and Structures, 43 (2006) 6783-6799.

[162] M. Karama, K. Afaq, S. Mistou, Mechanical behaviour of laminated composite beam by the new multi-layered laminated composite structures model with transverse shear stress continuity, International Journal of Solids and Structures, 40 (2003) 1525-1546.

[163] M. Touratier, An efficient standard plate theory, International journal of engineering science, 29 (1991) 901-916.

[164] H. Arya, R. Shimpi, N. Naik, A zigzag model for laminated composite beams, Composite structures, 56 (2002) 21-24.

[165] C.H. Thai, A.J.M. Ferreira, S.P.A. Bordas, T. Rabczuk, H. Nguyen-Xuan, Isogeometric analysis of laminated composite and sandwich plates using a new inverse trigonometric shear deformation theory, European Journal of Mechanics - A/Solids, 43 (2014) 89-108.

[166] J. Reddy, Nonlinear finite element analysis, Oxford University Press, New York, 2004.

[167] J.N. Reddy, An introduction to the finite element method, McGraw-Hill New York, 1993.

[168] T.J. Hughes, The finite element method: linear static and dynamic finite element analysis, Courier Corporation, 2012.

[169] O.C. Zienkiewicz, R.L. Taylor, The finite element method: Solid mechanics, Butterworth-heinemann, 2000.

[170] Les Piegl, Wayne Tiller, The NURBS book, Springer 2nd edition, Germany, 1997.

[171] Y. Urthaler, J.N. Reddy, A Mixed Finite Element for the Nonlinear Bending Analysis of Laminated Composite Plates Based on FSDT, Mechanics of Advanced Materials and Structures, 15 (2008) 335-354.

[172] T.V. Loc, T.H. Chien, N.X. Hung, On two-field nurbs-based isogeometric formulation for incompressible media problems, Vietnam Journal of Mechanics, 35 (2013) pp. 225–237.

[173] O.C. Zienkiewicz, R.L. Taylor, The finite element method, Vol. 1, in, McGraw-Hill, London, 1989.

[174] H.-T. Thai, D.-H. Choi, Finite element formulation of various four unknown shear deformation theories for functionally graded plates, Finite Elements in Analysis and Design, 75 (2013) 50-61.

[175] N. Phan, J. Reddy, Analysis of laminated composite plates using a higher-order shear deformation theory, International Journal for Numerical Methods in Engineering, 21 (1985) 2201-2219.

[176] F. Auricchio, L.B. da Veiga, A. Buffa, C. Lovadina, A. Reali, G. Sangalli, A fully "locking-free" isogeometric approach for plane linear elasticity problems: a stream function formulation, Computer methods in applied mechanics and engineering, 197 (2007) 160-172.

[177] V.P. Nguyen, S. Bordas, T. Rabczuk, Isogeometric analysis: an overview and computer implementation aspects, arXiv preprint arXiv:1205.2129, (2012).

[178] E. Carrera, S. Brischetto, M. Cinefra, M. Soave, Effects of thickness stretching in functionally graded plates and shells, Composites Part B: Engineering, 42 (2011) 123-133.

[179] E. Carrera, S. Brischetto, A. Robaldo, Variable kinematic model for the analysis of functionally graded material plates, AIAA journal, 46 (2008) 194-203.

[180] A. Neves, A. Ferreira, E. Carrera, M. Cinefra, C. Roque, R. Jorge, C. Soares, Static, free vibration and buckling analysis of isotropic and sandwich functionally graded plates using a quasi-3D higher-order shear deformation theory and a meshless technique, Composites Part B: Engineering, 44 (2013) 657-674.

[181] A. Neves, A. Ferreira, E. Carrera, C. Roque, M. Cinefra, R. Jorge, C. Soares, A quasi-3D sinusoidal shear deformation theory for the static and free vibration analysis of functionally graded plates, Composites Part B: Engineering, 43 (2012) 711-725.

[182] L. S., Square plate with clamped edges under normal pressure producing large deflections, Tech. Report, National Advisory committee for Aeronautics, 847 (1942).

[183] A. Pica, R.D. Wood, E. Hinton, Finite element analysis of geometrically nonlinear plate behaviour using a mindlin formulation, Computers & Structures, 11 (1980) 203-215.

[184] N. Weil, N. Newmark, Large deflections of elliptical plates, Journal of Applied Mechanics, 23 (1956) 21-26.

[185] R. Gunderson, W. Haisler, J. Stricklin, P. Tisdale, A rapidly converging triangular plate element, AIAA journal, 7 (1969) 180-181.

[186] Y.X. Zhang, Y.K. Cheung, Geometric nonlinear analysis of thin plates by a refined nonlinear non-conforming triangular plate element, Thin-Walled Structures, 41 (2003) 403-418.

[187] H. Nguyen-Van, N. Nguyen-Hoai, T. Chau-Dinh, T. Nguyen-Thoi, Geometrically nonlinear analysis of composite plates and shells via a quadrilateral element with good coarse-mesh accuracy, Composite Structures, 112 (2014) 327-338.

[188] G.J. Turvey, Buckling and postbuckling of composite plates, Springer Science & Business Media, 1995.

[189] R. Javaheri, M. Eslami, Buckling of Functionally Graded Plates under In-plane Compressive Loading, ZAMM-Journal of Applied Mathematics and Mechanics/Zeitschrift für Angewandte Mathematik und Mechanik, 82 (2002) 277-283.

[190] Y. Lee, X. Zhao, J. Reddy, Postbuckling analysis of functionally graded plates subject to compressive and thermal loads, Computer Methods in Applied Mechanics and Engineering, 199 (2010) 1645-1653.

[191] S. Timoshenko, J. Gere, Theory of Elastic Stability, McGraw-Hill Book Co., Art, 1 (1961) 372.

[192] L. Ma, T. Wang, Relationships between axisymmetric bending and buckling solutions of FGM circular plates based on third-order plate theory and classical plate theory, International Journal of Solids and Structures, 41 (2004) 85-101.

[193] A. Saidi, A. Rasouli, S. Sahraee, Axisymmetric bending and buckling analysis of thick functionally graded circular plates using unconstrained third-order shear deformation plate theory, Composite Structures, 89 (2009) 110-119.

[194] M. Najafizadeh, B. Hedayati, Refined theory for thermoelastic stability of functionally graded circular plates, Journal of thermal stresses, 27 (2004) 857-880.

[195] T. Prakash, M. Ganapathi, Asymmetric flexural vibration and thermoelastic stability of FGM circular plates using finite element method, Composites Part B: Engineering, 37 (2006) 642-649.

[196] H. Matsunaga, Thermal buckling of functionally graded plates according to a 2D higher-order deformation theory, Composite Structures, 90 (2009) 76-86.

[197] T. Prakash, M. Singha, M. Ganapathi, Thermal postbuckling analysis of FGM skew plates, Engineering Structures, 30 (2008) 22-32.

[198] J. Woo, S. Meguid, K. Liew, Thermomechanical postbuckling analysis of functionally graded plates and shallow cylindrical shells, Acta Mechanica, 165 (2003) 99-115.

[199] A. Bhimaraddi, K. Chandrashekhara, Nonlinear vibrations of heated antisymmetric angle-ply laminated plates, International journal of solids and structures, 30 (1993) 1255-1268.

[200] M. Prabhu, S. Durvasula, Elastic stability of thermally stressed clamped-clamped skew plates, Journal of Applied Mechanics, 41 (1974) 820-821.

[201] M.K. Singha, L. Ramachandra, J. Bandyopadhyay, Thermal postbuckling analysis of laminated composite plates, Composite Structures, 54 (2001) 453-458.

[202] T. Prakash, M. Singha, M. Ganapathi, Thermal snapping of functionally graded materials plates, Materials & Design, 30 (2009) 4532-4536.

[203] J.N. Reddy, Geometrically nonlinear transient analysis of laminated composite plates, AIAA Journal, 21 (1983) 621-629.

[204] A.W. Leissa, The free vibration of rectangular plates, Journal of Sound and vibration, 31 (1973) 257-293.

[205] J. Reddy, C. Wang, S. Kitipornchai, Axisymmetric bending of functionally graded circular and annular plates, European Journal of Mechanics-A/Solids, 18 (1999) 185-199.

[206] S. Hosseini-Hashemi, M. Fadaee, M. Es' Haghi, A novel approach for in-plane/out-of-plane frequency analysis of functionally graded circular/annular plates, International Journal of Mechanical Sciences, 52 (2010) 1025-1035.

[207] F. Ebrahimi, A. Rastgoo, A. Atai, A theoretical analysis of smart moderately thick shear deformable annular functionally graded plate, European Journal of Mechanics-A/Solids, 28 (2009) 962-973.

[208] J. Chen, D.J. Dawe, S. Wang, Nonlinear transient analysis of rectangular composite laminated plates, Composite Structures, 49 (2000) 129-139.

[209] P. Lynn, N. Kumbasar, Free vibration of thin rectangular plates having narrow cracks with simply supported edges, Dev. Mech, 4 (1967) 911-928.

[210] B. Stahl, L. Keer, Vibration and stability of cracked rectangular plates, International Journal of Solids and Structures, 8 (1972) 69-91.

[211] Y. Hirano, K. Okazaki, Vibrarfon of Cracked Rectangular Plates, Bulletin of JSME, 23 (1980) 732-740.

[212] Q. Guan-Liang, G. Song-Nian, J. Jie-Sheng, A finite element model of cracked plates and application to vibration problems, Computers & structures, 39 (1991) 483-487.

[213] M. Krawczuk, Natural vibrations of rectangular plates with a through crack, Archive of applied mechanics, 63 (1993) 491-504.

[214] R. Su, A. Leung, S. Wong, Vibration of cracked Kirchhoff's plates, in: Key Engineering Materials, Trans Tech Publ, 1997, pp. 167-172.

[215] J. Yuan, S. Dickinson, The flexural vibration of rectangular plate systems approached by using artificial springs in the Rayleigh-Ritz method, Journal of Sound and Vibration, 159 (1992) 39-55.

[216] H. Lee, S. Lim, Vibration of cracked rectangular plates including transverse shear deformation and rotary inertia, Computers & structures, 49 (1993) 715-718.

[217] K. Liew, K. Hung, M. Lim, A solution method for analysis of cracked plates under vibration, Engineering fracture mechanics, 48 (1994) 393-404.

[218] C. Huang, A. Leissa, Vibration analysis of rectangular plates with side cracks via the Ritz method, Journal of Sound and Vibration, 323 (2009) 974-988.

[219] M. Bachene, R. Tiberkak, S. Rechak, Vibration analysis of cracked plates using the extended finite element method, Archive of Applied Mechanics, 79 (2009) 249-262.

[220] S. Natarajan, P.M. Baiz, S. Bordas, T. Rabczuk, P. Kerfriden, Natural frequencies of cracked functionally graded material plates by the extended finite element method, Composite Structures, 93 (2011) 3082-3092.

[221] C. Huang, O. McGee, M. Chang, Vibrations of cracked rectangular FGM thick plates, Composite Structures, 93 (2011) 1747-1764.

[222] C. Huang, P. Yang, M. Chang, Three-dimensional vibration analyses of functionally graded material rectangular plates with through internal cracks, Composite Structures, 94 (2012) 2764-2776.

[223] T. Belytschko, T. Black, Elastic crack growth in finite elements with minimal remeshing, International journal for numerical methods in engineering, 45 (1999) 601-620.

[224] H. Nguyen-Xuan, L.V. Tran, C.H. Thai, C.V. Le, Plastic collapse analysis of cracked structures using extended isogeometric elements and second-order cone programming, Theoretical and Applied Fracture Mechanics, 72 (2014) 13-27.

[225] N. Nguyen-Thanh, N. Valizadeh, M. Nguyen, H. Nguyen-Xuan, X. Zhuang, P. Areias, G. Zi, Y. Bazilevs, L. De Lorenzis, T. Rabczuk, An extended isogeometric thin shell analysis based on Kirchhoff–Love theory, Computer Methods in Applied Mechanics and Engineering, 284 (2015) 265-291.

[226] J. Dolbow, N. Moës, T. Belytschko, Modeling fracture in Mindlin–Reissner plates with the extended finite element method, International Journal of Solids and Structures, 37 (2000) 7161-7183.

[227] T.L. Anderson, Fracture mechanics: fundamentals and applications, CRC press, 2005.

[228] J.F. Yau, S.S. Wang, H.T. Corten, A Mixed-Mode Crack Analysis of Isotropic Solids Using Conservation Laws of Elasticity, Journal of Applied Mechanics, 47 (1980) 335-341.

[229] C. Huang, A. Leissa, R. Li, Accurate vibration analysis of thick, cracked rectangular plates, Journal of Sound and Vibration, 330 (2011) 2079-2093.

[230] N.S. Putcha, J.N. Reddy, A refined mixed shear flexible finite element for the nonlinear analysis of laminated plates, Computers & Structures, 22 (1986) 529-538.

Publication

A. Journal Articles

Articles related to the present thesis

1. **Loc V. Tran**, Phuc Phung-Van, J. Lee, M. Abdel Wahab and H. Nguyen-Xuan, Isogeometric analysis for nonlinear thermomechanical stability of functionally graded plates, Composite Structure, 140 (2016) 655–667 (IF = 3.318).
2. **Loc V. Tran**, J. Lee, H. A. Ly, M. Abdel Wahab, H. Nguyen-Xuan, Vibration analysis of cracked FGM plates using higher-order shear deformation theory and extended isogeometric approach, International Journal of Mechanical Sciences, 96 (2015) 65-78, (IF=2.061).
3. **Loc V. Tran**, J. Lee, H. Nguyen-Van, H. Nguyen-Xuan, M. Abdel Wahab, Geometrically nonlinear isogeometric analysis of laminated composite plates based on higher-order shear deformation theory. International Journal of Non-Linear Mechanics, 72 (2015) 42-52 (IF=1.977).
4. H. Nguyen-Xuan, **Loc V. Tran**, C.H. Thai, S. Kulasegaram, S.P.A. Bordas, Isogeometric analysis of functionally graded plates using a refined plate theory, Composites Part B: Engineering, 64 (2014) 222-234 (IF = 2.143).

Other articles

1. **Loc V. Tran**, T. Nguyen-Thoi, C. H. Thai, H. Nguyen-Xuan, An edge-based smoothed discrete shear gap method (ES-DSG) using the C^0-type higher-order shear deformation theory for analysis of laminated composite plates, Mechanics of Advanced Materials and Structures, 22 (2015) 248-268 (IF=0.773).

2. Phuc Phung-Van, Lieu B. Nguyen, **Loc V. Tran**, Tien Dung Dinh, Chien H. Thai, S.P.A. Bordas, M. Abdel-Wahab, H. Nguyen-Xuan, An efficient computational approach for control of nonlinear transient responses of smart piezoelectric composite plates, International Journal of Non-Linear Mechanics, 76 (2015) 190-202 (IF=1.977).
3. H. Nguyen-Xuan, **Loc V. Tran**, C.H. Thai, C.V. Le, Plastic collapse analysis of cracked structures using extended isogeometric elements and second-order cone programming, Theoretical and Applied Fracture Mechanics, 72 (2014) 13-27 (IF = 1.138).
4. **Loc V. Tran**, C.H. Thai, H.T. Le, B.S. Gan, J. Lee, H. Nguyen-Xuan, Isogeometric analysis of laminated composite plates based on a four-variable refined plate theory, Engineering Analysis with Boundary Elements, 47 (2014) 68-81 (IF = 1.596).
5. C.H. Thai, S. Kulasegaram, **Loc V. Tran**, H. Nguyen-Xuan, Generalized shear deformation theory for functionally graded isotropic and sandwich plates based on isogeometric approach, Computers & Structures, 141 (2014) 94-112 (IF = 1.509).
6. **Loc V. Tran**, A.J.M. Ferreira, H. Nguyen-Xuan, Isogeometric analysis of functionally graded plates using higher-order shear deformation theory, Composites Part B: Engineering, 51 (2013) 368-383 (IF = 2.143).
7. P. Phung-Van, T. Nguyen-Thoi, **Loc V. Tran**, H. Nguyen-Xuan, A cell-based smoothed discrete shear gap method (CS-DSG3) based on the C^0-type higher-order shear deformation theory for static and free vibration analyses of functionally graded plates, Computational Materials Science, 79 (2013) 857-872 (IF = 1.878).
8. **Loc V. Tran**, C.H. Thai, H. Nguyen-Xuan, An isogeometric finite element formulation for thermal buckling analysis of functionally graded plates, Finite Elements in Analysis and Design, 73 (2013) 65-76 (IF = 1.389).
9. **Tran Vinh Loc**, Thai Hoang Chien, Nguyen Xuan Hung, On two-field nurbs-based isogeometric formulation for incompressible media problems, Vietnam Journal of Mechanics, Vol.35(3), p.1–13, 2013 (national journal).

10. H. Nguyen-Xuan, **Loc V. Tran**, C.H. Thai, T. Nguyen-Thoi, Analysis of functionally graded plates by an efficient finite element method with node-based strain smoothing, Thin-Walled Structures, 54 (2012) 1-18 (IF = 1.231).
11. C.H. Thai, **Loc V. Tran**, D. T. Tran, T. Nguyen-Thoi, H. Nguyen-Xuan, Analysis of laminated composite plates using higher-order shear deformation theory and node-based smoothed discrete shear gap method, Applied Mathematical Modelling, 36(2012) 5657–5677 (IF = 1.706)
12. H. Nguyen-Xuan, **Loc V. Tran**, T. Nguyen-Thoi, H. Vu-Do, Analysis of functionally graded plates using an edge-based smoothed finite element method, Composite Structures, 93 (2011) 3019-3039 (IF = 2.24).
13. **Tran Vinh Loc**, Thai Hoang Chien, Nguyen Xuan Hung, Static analysis of composite plate using edge-based smoothed finite element method based on a C^0-type higher-order shear deformation theory, Journal of Science and Technology, Vol. 49(4A), p. 327-337, 2011 (national journal).
14. Phuc Phung-Van, **Loc V. Tran**, AJM. Ferreira, M. Abdel-Wahab, H. Nguyen-Xuan, Nonlinear transient isogeometric analysis of smart piezoelectric functionally graded material plates based on generalized shear deformation theory under thermo-electro-mechanical loads, under review in Computers and Structures.

B. Conference papers

1. **Loc V. Tran,** H. Luong-Van, H. Nguyen-Xuan and M. Abdel Wahab, Thermal post-buckling analysis of functionally graded plates using isogeometric analysis, The Fourteenth East Asia-Pacific Conference on Structural Engineering and Construction (EASEC-14) January 6-8, 2016, Ho Chi Minh City, Vietnam.
2. **Loc V. Tran,** H. Nguyen-Xuan and M. Abdel Wahab, Extended isogeometric analysis in modelling cracked structures. 4th International Conference on Fracture Fatigue and Wear (FFW 2015), 27-28 August 2015, Ghent, Belgium.
3. **Loc V. Tran,** P. Phung-Van, Jaehong Lee, H. Nguyen-Xuan and M. Abdel Wahab, Nonlinear transient isogeometric analysis of laminated composite plates based on higher order plate theory, 11-12 May 2015, CIGOS – Paris 2015.

4. **Loc V. Tran**, P Phung-Van, Vinh Phu Nguyen, M Abdel Wahab, H Nguyen-Xuan, Vibration analysis of cracked plate using higher-order shear deformation theory, The 3rd International Conference on Fracture Fatigue and Wear, 1-3 September 2014, Kitakyushu Japan, Vol. 2, pp. 127-133.
5. **Loc V. Tran**, VP. Nguyen, LV. Hai, TM. Thi and H. Nguyen-Xuan, An assessment of limit loads of cracked structures using extended isogeometric analysis, The Thirteenth East Asia-Pacific Conference on Structural Engineering and Construction (EASEC-13), 11-13 September 2013, Sapporo, Japan.
6. **Loc V. Tran**, Thai Hoang Chien, Nguyen Thoi Trung, Nguyen Xuan Hung, A mixed Nurbs-based isogeometric approach for incompressible media problems, Proceeding of International Conference on Advances in Computational Mechanics (ACOME), 14-16 August 2012, Ho Chi Minh City, Vietnam.